

**Development of personalised lower-limb neuromusculoskeletal models for typically developing paediatric populations and children with cerebral palsy**

**Author**

Davico, Giorgio

**Published**

2020-01-16

**Thesis Type**

Thesis (PhD Doctorate)

**School**

School Allied Health Sciences

**DOI**

[10.25904/1912/1331](https://doi.org/10.25904/1912/1331)

**Downloaded from**

<http://hdl.handle.net/10072/391060>

**Griffith Research Online**

<https://research-repository.griffith.edu.au>



Development of personalised lower-limb  
neuromusculoskeletal models for typically  
developing paediatric populations and children with  
cerebral palsy

Giorgio Davico

*BSc, MSc*

School of Allied Health Sciences  
Menzies Health Institute Queensland  
Griffith University

Submitted in fulfilment of the requirements of the degree of  
Doctor of Philosophy

August 2019





# Abstract

---

Cerebral palsy (CP) is the most common motor disorder in childhood, with an incidence rate of approximately 2 in 1000 newborns. Although starting from a non-progressive lesion occurring in the fetal or infant brain, children with CP present with a wide range of progressive primary and secondary impairments. These include increased muscle tone, contractures, muscular deficits and bony deformities, which if untreated may further lead to progressive loss of locomotor function. Due to CP's multifaceted nature and the patient-specificity of the symptoms, the management of CP is quite complex and standardised treatment plans that suit all patients' needs cannot be defined. Currently, several non-invasive (e.g. casting or strengthening programs) and invasive (e.g. single-event multilevel surgeries) procedures are performed in the attempt to restore typical muscle and motor function. Nonetheless, roughly 25% of the patients are dissatisfied with the treatment outcomes, which often require a second intervention. This may be due to a poor treatment planning, which is primarily based on information gathered via passive muscle tests and gait analysis assessments. Such tests completely disregard the internal biomechanics, i.e. muscle activations, muscle forces and joint contact forces (JCFs).

Although difficult to measure *in vivo*, the internal biomechanics may be estimated *in silico* by employing neuromusculoskeletal (NMSK) models, i.e. virtual digital representations of the human musculoskeletal system. By providing insights on the mechanisms behind the pathology, NMSK models have the potential to improve the management of CP. Moreover, different surgical scenarios may be tested on virtual models prior to entering the operating theatre, allowing for the identification of the most effective and personalised treatment for each patient. Nonetheless, current NMSK models do have limitations. For instance, generic musculoskeletal anatomies, e.g. gait2392 OpenSim model, are commonly employed and scaled with motion capture data to match each participant's dimensions. However, generic anatomies are based on a limited set of healthy elder adult data. Paediatric bones, presenting with more pronounced torsions or with deformities, may have large deviations from those of an adult; even after linear scaling. Inaccurate bony geometries are associated to mislocation of the joint centres, which may affect external joint angles and joint moment estimates. Moreover, generic muscle attachments on ill-scaled bones may be inaccurately positioned, thereby affecting muscle kinematics and muscle function. In addition, muscle-tendon units (MTUs) are

typically represented as Hill-type actuators, whose behaviour is highly dependent on optimal fibre length, tendon slack length and maximal isometric force values. Most commonly, these parameters are linearly scaled along with bones, although this approach has no physiological grounds. As result, MTUs may operate outside the range of physiologically plausible values, and not representing correct muscle function. Furthermore, CP-related MTU abnormalities are often disregarded. Finally, unconstrained static optimisation methods (e.g., static optimisation that minimises muscle activations squared) are typically employed to determine the set of muscle activations to generate the experimental joint moments. However, these methods favour estimation of muscle endurance, minimal muscle activation, the latter also minimising muscle co-contractions, and may not account for muscle dynamics by assuming tendons to be rigid. Static optimisation also estimates similar activation patterns between subjects, and even within subjects when different control is required, which has been proven otherwise. Moreover, abnormal neural solutions, common in observed CP, cannot be generated.

Previous work has focussed on the personalisation of NMSK models to better represent paediatric populations with CP. However, personalisation was mostly introduced using pre-determined factors to scale MTU parameters or based on available literature data. Moreover, only a few features were personalised at once. Therefore, the overarching aim of my thesis was to develop personalised NMSK models of healthy paediatric populations and children with CP, with increasing level of subject-specificity, and to quantify the effect of each personalised feature on the endpoint variables, i.e. muscle excitation patterns and forces, and JCFs estimates.

The first study investigated whether the personalisation of MTU parameters and muscle activation patterns enabled the production of more physiologically plausible internal biomechanics. Two 13 years old identical twin brothers, one typically developing (TD) and one with unilateral spastic CP, were enrolled in the study. For both children, four different NMSK models with incremental level of subject-specificity were generated. The first two models (unCal<sub>SO</sub> and unCal<sub>EMGa</sub>) shared the same musculoskeletal anatomy, which was linearly scaled from a simplified gait2392 generic model and featured morphometrically optimised optimal fibre length (OFL) and tendon slack length (TSL) values. Static optimisation in CEINMS was employed to synthesise muscle activation patterns in unCal<sub>SO</sub>, while unCal<sub>EMGa</sub> used an electromyography (EMG)-assisted approach. A further two models (Cal<sub>EMGa</sub> and Cal<sub>EMGa</sub><sup>MRI</sup>) subsequently calibrated the MTU parameters ( $\pm 5\%$  of their original value) in CEINMS using

experimental EMG data. For the CP child, the initial OFL of selected muscles was decreased by 0.7 before calibration, while the TSL was bound to increase. These alterations were implemented to respectively account for overstretched sarcomeres and longer TSL observed in CP muscles. The last model ( $\text{Cal}_{\text{EMG}a}^{\text{MRI}}$ ) further built on  $\text{Cal}_{\text{EMG}a}$  and featured personalised maximal isometric force values scaled with muscle volumes segmented on magnetic resonance imaging (MRI) scans. The use of an EMG-assisted approach had a greater effect on the ability of the models to track experimental data compared to the calibration of MTU parameters. Nonetheless, when OFL and TSL were not calibrated, knee JCFs estimates did not appear physiologically plausible. The results of this study were included in a full paper submitted as Davico G., Pizzolato C, Lloyd D.G., Obst S.P., Walsh H.P.J., Carty C.P. Increasing level of neuromusculoskeletal model personalisation to investigate joint contact forces in cerebral palsy: a twin case study. *Clinical Biomechanics*.

The second study examined the best methods to accurately reconstruct paediatric lower limb bones for use in NMSK modelling. Medical imaging and motion capture (MOCAP) data from 18 TD children collected in the past five years at Queensland Children's Hospital were used in the study. Ten different combinations of morphing and mesh fitting techniques to reconstruct pelvis, femurs and tibiofibular bones were developed and tested in the open-source software Musculoskeletal Atlas Project (MAP) Client. To determine the minimum required amount of data to achieve acceptable reconstructions, different levels of medical image data incompleteness were provided. The resulting bone reconstructions were compared to the corresponding MRI segmentations using three metrics of similarity: Jaccard index, root mean squared surface-to-surface distance error, and Hausdorff distance. In addition, for each reconstructed pelvis, hip joint centres (HJCs) locations and HJC distance were extracted and compared to the corresponding MRI measurements. The HJC distance was also compared to a clinical MOCAP based measurement, i.e. Harrington regression equation. Our results suggested that non-linear scaling methods should not be used to reconstruct the lower limb bones of children smaller than 145 cm, which would be abnormally shaped. Secondly, the use of medical imaging data, even if incomplete, should be preferred to generate highly accurate bony geometries. Moreover, in small children, HJC-distance may largely differ between MOCAP and reconstruction-based calculations. All research findings from this study were detailed in the invited paper: Davico G., Pizzolato C., Killen B.A., Barzan M., Suwarganda E., Lloyd D.G., Carty C.P. Best methods and data to

reconstruct paediatric lower limb bones for musculoskeletal modelling. *Biomechanics and Modeling in Mechanobiology*, 2019. doi:10.1007/s10237-019-01245-y.

The third study had two main aims. First, was to develop a highly personalised NMSK paediatric model, and second, to determine the individual effects of personalised anatomies, muscle activation patterns and MTU parameters on muscle excitation patterns and forces, and JCFs estimates. Six different NMSK models with incremental levels of subject-specificity were generated for each of the six children (3 TD, 3 with CP) enrolled in the study. For the first time a model generated via the MAP Client was developed and tested. This included personalised bony geometries, and physiologically and physically plausible MTU kinematics (i.e. MTU lengths and moment arms). In addition to the MAP generated anatomies and generically scaled anatomies (simplified gait2392 OpenSim model) were employed for biomechanical simulations of gait. Following the steps of study one, both anatomies were progressively personalised by (1) calibrating MTU parameters and (2) replacing static optimisation methods that minimised muscle activations squared with EMG-assisted approaches to synthesise muscle activations. The calibrated EMG-assisted MAP generated model produced the most physiologically plausible estimates, as (i) it well tracked both external moments and muscle excitations (i.e. EMG linear envelopes), (ii) featured subject-specific bones and (iii) estimated non-zero loading in swing phase. Among all, the use of EMG-assisted methods and personalised musculoskeletal anatomies appeared to have the greatest impact on the endpoint estimates. Nonetheless, the neural solution substantially affected lateral JCF profiles. The paper describing these results will be submitted as Davico G., Killen B.A., Carty C.P., Lloyd D.G., Devaprakash D., Pizzolato C. Developing the new generation of personalised neuromusculoskeletal models to investigate cerebral palsy. *IEEE Transactions on Biomedical Engineering*.

In conclusion, this thesis rigorously assessed what the effects of personalisation are on the endpoint estimates of a NMSK model and provided guidelines to develop more physiologically plausible paediatric musculoskeletal anatomies and models. Particularly, the studies highlighted the weakness and strengths of common clinical measurements and associated methods that may be used to improve the personalisation of NMSK models. The future use of personalised NMSK modelling simulations has the potential to provide knowledge of the internal biomechanics and substantial benefit to the CP paediatric population, by better informing clinical management and by enabling the development of personalised treatments for each patient.

# Acknowledgements

---

I would like to thank everyone who helped me achieving this goal, in one way or another. First of all, I would like to acknowledge my supervisory team. To my principal supervisor Professor David Lloyd, thank you for continuously pushing me above and beyond my limits. Although sometimes I felt overwhelmed, I am extremely grateful for your persistence. I would have never been able to accomplish what I did otherwise. Thank you for always placing good science before easy papers. I am not surprised that all the hard work came to a very nice end. To Dr Christopher Carty, thank you for always supporting me, particularly when everything seemed to go wrong. Thank you for helping me securing the scholarship in first place. All of this would have not been possible without it. To Dr Claudio Pizzolato, thank you for joining my supervisory team. Your technical guidance has been precious and your level of knowledge admirable. Thank you for taking the time to sit with me to help me solving ‘insurmountable’ problems with my simulations.

To Julie Edwards and Chris Stockton, thank you for all the weekends you helped me with data collection. None of this would have been possible without you. To Dr John Walsh, thank you for helping with the recruitment of participants. To all the children and families involved in my research, thank you for taking the time to participate in the studies.

To my family, thank you for always being supportive, no matter the distance or the time difference. To my mum and dad, thank you for the numerous Skype calls filled with good news and fun facts that made me free my mind from time to time. I know it has been difficult for you to have both your sons far away from home, but you always proudly supported our choices. To my brother Luca, thank you for being there for me whenever I needed extra support and for visiting me in Australia. You have always been an example for me, especially in finding the courage to leave everything behind and start a PhD abroad.

To my Australian friends, thank you for making this journey incredible and unforgettable. Special thanks to Daniel, Eva, Bryce, Martin and Kirsten: ‘the Family’. Your friendship and never ending support have been very helpful throughout this journey. I cannot count all the laughs and the amazing moments we spent together, but I know I will carry these wonderful memories with me forever. To my PhD colleagues, Martina, Lexi, Jeremy, Edin, Gavin, Evy, Tamara, Pavlos and Faz, thank you for making the work routine easier to handle, with all the coffee, lunch and afternoon tea breaks filled with fun.

To my close Italian friends, Barbara, Marta, Pablo and Vu, thank you for always being available for a chat or for a get together whenever I was back, even on a short notice. You never let the distance getting between our friendship and you never failed to support me. Special thanks to Barbara and her family. You have been a constant source of energy and confidence for me. Thank you for coming to Australia to check on me and to share some great moments together.

To Barb, thank you for your constant help. You have always been the go-to person within the School, from teaching to PhD related issues. To the GGRS staff, especially to Karen, thank you for your tireless help sorting the bureaucracy for me throughout my candidature, up until the submission date.

To all the other people I met during this journey, especially Edo, Rafa, Lore, Jasmine and Carol, thank you for being part of it and for making me feel a bit more like at home, with nights out, soccer games, fun, and a lot of running. To Memo, thank you for organising the AHS rehab sessions on Fridays. It was a great way to finish off the working week. To Jennifer, thank you for giving me a place to be for the first few months, when I did not know anyone and I had nowhere to go. Your kindness and help have been more than what I could expect.

# Statement of originality

---

This work has not previously been submitted for a degree or diploma in any university. To the best of my knowledge and belief, the thesis contains no material previously published or written by another person except where due reference is made in the thesis itself.

Giorgio Davico

11<sup>th</sup> August 2019



# Publication list

---

## Journal Articles

**Davico, G.**, Pizzolato, C., Lloyd, D.G., Obst, S.J., Walsh, H.P.J., Carty, C.P. Increasing level of neuromusculoskeletal model personalisation to investigate joint contact forces in cerebral palsy: a twin case study. *Clinical Biomechanics*. Submitted.

**Davico, G.**, Pizzolato, C., Killen, B.A., Barzan, M., Suwarganda, E., Lloyd, D.G., Carty, C.P. Best methods and data to reconstruct paediatric lower limb bones for musculoskeletal modelling. *Biomechanics and Modeling in Mechanobiology*. 2019. <https://doi.org/10.1007/s10237-019-01245-y>.

Saxby, D.J., Killen, B.A., Pizzolato, C., Carty, C.P., Diamond, L.E., Modenese, L., Fernandez, J., **Davico, G.**, Barzan, M., Lenton, G.K., Brito da Luz, S., Suwarganda, E., Devaprakash D., Korhonen, R., Alderson, J.A., Besier, T., Barrett, R.S., Lloyd, D.G. Big Data and machine learning to create physics-based personalised computational neuromusculoskeletal models, *Biomechanics and Modeling in Mechanobiology*. Submitted.

**Davico, G.**, Killen, B.A., Carty, C.P., Lloyd, D.G., Devaprakash, D., Pizzolato, C. Developing the new generation of personalised neuromusculoskeletal models to investigate cerebral palsy. *IEEE Transactions on Biomedical Engineering*. In preparation.

Devaprakash, D., Lloyd, D.G., Barrett, R.S., Obst, S.J., Kennedy, B., Adams, K.L., Collings, T.J., **Davico, G.**, Hunter, A., Vlahovich, N., Pease, D.L., Pizzolato, C. Free Achilles tendon geometry and tissue properties in middle distance runners assessed using MRI and three-dimensional ultrasound. *Frontiers in Physiology*. In preparation.

## Conference Papers and Abstracts

### *Podium presentations*

**Davico, G.**, Pizzolato, C., Obst, S.J., Lloyd, D.G., Carty, C.P. *Muscle contributions to knee joint moments in children with cerebral palsy: a twin case study*. 10<sup>th</sup> Australasian Biomechanics Conference, Melbourne, Australia, 2016.

**Davico, G.**, Pizzolato, C., Obst, S.J., Lloyd, D.G., Carty, C.P. *Muscle contributions to knee joint moment and knee joint contact forces during walking in children with cerebral palsy: a twin study*. XXVI Congress of the International Society of Biomechanics, Brisbane, Australia, 2017.

Suwarganda, E.K., Zhang, J., Barzan, M., Killen, B.A., **Davico, G.**, Lloyd, D.G., Diamond, L.E., Saxby, D.J. *Subject-specific bone geometries from sparse imaging using the MAP client*. XXVI Congress of the International Society of Biomechanics, Brisbane, Australia, 2017.

**Davico, G.**, Pizzolato, C., Carty, C.P., Obst, S.J., Lloyd, D.G. *Investigating cerebral palsy using EMG-informed approaches: a twin case study*. 8<sup>th</sup> World Congress of Biomechanics, Dublin, Ireland, 2018.

**Davico, G.**, Killen, B.A., Pizzolato, C., Lloyd, D.G., Barzan, M., Carty, C.P. *Paediatric lower limb bones can be accurately reconstructed via the MAP Client for use in neuromusculoskeletal modelling*. XXVII Congress of the International Society of Biomechanics, Calgary, Canada, 2019. Nominated among the five best oral presentations for the David Winter Young Investigator Award.

**Davico, G.**, Killen, B.A., Carty, C.P., Lloyd, D.G., Devaprakash, D., Pizzolato, C. *Developing the new generation of personalised neuromusculoskeletal models to investigate cerebral palsy*. XXVII Congress of the International Society of Biomechanics, Calgary, Canada, 2019.

# Table of contents

---

|  |       |
|--|-------|
| Abstract .....                               | i     |
| Acknowledgements .....                       | v     |
| Statement of originality .....               | vii   |
| Publication list .....                       | ix    |
| Table of contents .....                      | xi    |
| List of figures .....                        | xv    |
| List of tables .....                         | xxiii |
| List of equations .....                      | xxix  |
| List of abbreviations .....                  | xxxii |
| CHAPTER 1 .....                              | 1     |
| Background.....                              | 1     |
| CP related impairments .....                 | 1     |
| Clinical management of CP .....              | 2     |
| Limitations of current NMSK models .....     | 3     |
| Personalisation of NMSK models .....         | 4     |
| Statement of the problem.....                | 6     |
| Thesis objective .....                       | 7     |
| CHAPTER 2 .....                              | 9     |
| What is cerebral palsy?.....                 | 9     |
| Primary and secondary impairments .....      | 10    |
| Hypertonia and spasticity .....              | 12    |
| Muscle co-contractions.....                  | 13    |
| Muscle morphological changes .....           | 13    |
| Altered muscle composition .....             | 14    |
| Bone and joint deformities .....             | 15    |
| Common gait kinematic deviations in CP ..... | 15    |
| Treatments for CP.....                       | 16    |
| How to inform treatment planning .....       | 17    |

|   |    |
|---|----|
| NMSK modelling .....  | 18 |
| Limitations of commonly used NMSK models.....                       | 20 |
| Personalisation of NMSK models .....                                | 23 |
| Bone geometries .....   | 24 |
| Joint definitions and kinematics .....                              | 24 |
| Muscle morphology and pathways .....                                | 25 |
| Internal MTU parameters .....                                       | 27 |
| Neural solutions.....   | 28 |
| Personalisation for CP .....  | 30 |
| Bony deformities .....  | 30 |
| Altered muscle properties.....                                      | 32 |
| Abnormal muscle activity.....                                       | 33 |
| Spasticity and contractures .....                                   | 33 |
| CHAPTER 3.....  | 35 |
| Data collection.....  | 37 |
| Participants .....  | 37 |
| Data collection protocol.....                                       | 38 |
| Gait laboratory setup .....   | 38 |
| Participant preparation.....  | 40 |
| Gait assessment .....   | 43 |
| MRI acquisition .....   | 43 |
| Data processing .....   | 46 |
| Gait analysis .....   | 46 |
| Segmentation of medical images.....                                 | 46 |
| Development and personalisation of neuromusculoskeletal models..... | 49 |
| Development and personalisation of musculoskeletal anatomy.....     | 51 |
| Model scaling .....   | 51 |
| Subject-specific musculoskeletal anatomies via the MAP Client ..... | 52 |
| Personalisation of MTU parameters .....                             | 58 |
| Model tuning .....  | 58 |
| Calibration of MTU parameters .....                                 | 60 |
| Calibration of MTU parameters for children with CP.....             | 61 |
| Personalisation of muscle activations.....                          | 62 |
| Models execution and biomechanical simulations .....                | 63 |

|  |     |
|--|-----|
| Models summary .....                                     | 65  |
| Statistical analysis .....                               | 67  |
| Models assessment .....                                  | 67  |
| Comparisons between models estimates .....               | 67  |
| Comparisons between pipelines to reconstruct bones ..... | 68  |
| CHAPTER 4 .....  | 69  |
| Abstract.....  | 70  |
| Introduction .....                                       | 71  |
| Methods .....  | 73  |
| Gait analysis data collection and processing .....       | 74  |
| MRI imaging and processing.....                          | 76  |
| MSK base model creation.....                             | 76  |
| NMSK model comparisons .....                             | 77  |
| Data analysis.....                                       | 81  |
| Statistical analysis .....                               | 81  |
| Results .....  | 81  |
| Discussion.....  | 87  |
| Conclusions .....  | 90  |
| Conflicts of interest .....                              | 90  |
| Funding.....   | 90  |
| CHAPTER 5 .....  | 91  |
| Abstract.....  | 92  |
| Introduction .....                                       | 93  |
| Material and Methods .....                               | 96  |
| Participants .....                                       | 96  |
| Data collection and processing .....                     | 96  |
| Bone reconstruction using the MAP Client.....            | 98  |
| Pipeline development .....                               | 100 |
| Pipelines summary.....                                   | 102 |
| Data Analysis.....                                       | 102 |
| Statistical analysis .....                               | 104 |
| Results .....  | 105 |
| Discussion.....  | 116 |
| Conclusions .....  | 121 |

|   |     |
|---|-----|
| CHAPTER 6 .....                                     | 123 |
| Introduction .....                                  | 123 |
| Methods .....                                       | 127 |
| Participants .....                                  | 127 |
| Gait analysis data collection and processing .....  | 127 |
| MRI imaging and processing .....                    | 128 |
| Base musculoskeletal model.....                     | 128 |
| Model personalisation .....                         | 129 |
| Models summary .....                                | 130 |
| Biomechanical simulations.....                      | 131 |
| Data analysis.....                                  | 132 |
| Statistical analysis .....                          | 132 |
| Results .....                                       | 133 |
| Discussion.....                                     | 142 |
| Conclusions .....                                   | 145 |
| CHAPTER 7.....                                      | 147 |
| Thesis summary.....                                 | 147 |
| General modelling implications.....                 | 149 |
| Implications for children with CP .....             | 151 |
| Challenges for clinical implementation.....         | 153 |
| Further limitations .....                           | 154 |
| Technical advancement provided by this thesis ..... | 156 |
| Future directions .....                             | 156 |
| Conclusions .....                                   | 158 |
| Appendix A .....                                    | 159 |
| Appendix B .....                                    | 169 |
| Appendix C .....                                    | 171 |
| Appendix D .....                                    | 173 |
| References .....                                    | 175 |

# List of figures

---

|   |    |
|---|----|
| <b>Figure 1.</b> Schematic of the musculoskeletal alterations associated with CP. Medical imaging data (black boxes) show some common joint deformities and muscle morphological and structural changes observed in CP patients. Top left: feedback loop of events originating from the non-progressive lesion to the brain or motor cortex responsible for the progressive loss of motor function and alterations to musculoskeletal tissues. ....   | 11 |
| <b>Figure 2.</b> Normal gait (a) compared to the most common gait deviations observed in CP, i.e. true equinus (b), pseudo equinus (c), crouch gait (d) and jump knee gait (e). Figures a-e are representative of the mid-stance phase, when the foot is supposed to be in full contact with the ground.....  | 15 |
| <b>Figure 3.</b> (a) generic musculoskeletal anatomy (gait2392 OpenSim model), with virtual markers affixed on anatomical landmarks. (b) experimental motion capture and ground reaction force data employed (1) to scale the generic anatomy to each participant’s dimensions and (2) to compute joint angles and moments during dynamic simulations (c). ....   | 19 |
| <b>Figure 4.</b> Linearly scaled generic opensim geometries (light blue) overlaid to the corresponding MRI segmentations (white) of the pelvis bone (left) and femur (right). The apparent difference in shape, size and curvature between scaled generic and real geometries, which per se does not affect simulations (i.e., bone images are purely for visualisation), may be associated (1) with inaccurate definitions of joint centres, (2) with erroneous joint angle calculations and (3) with inappropriate location of muscle attachments, which can all affect a model’s estimates. .... | 21 |
| <b>Figure 5.</b> Medical imaging techniques employed to extract subject-specific information on muscles and tendons, required to personalise neuromusculoskeletal models. (a) axial MRI image with masks identifying each individual muscle, (b) bi-planar US image of a tendon (yellow contour), (c) 3D free-hand US reconstruction of a tendon, (d) 3D muscle volumes reconstructed from MRI images.....  | 26 |
| <b>Figure 6.</b> Methods to personalise bones. (a) manual segmentation of medical images, (b) mesh fitting techniques and (c) statistical shape modelling. ....   | 31 |

|  |    |
|--|----|
| <b>Figure 7.</b> Workflow employed to estimate muscle and joint contact forces. Experimental motion capture (MOCAP), ground reaction force (GRF), electromyographic (EMG) and magnetic resonance imaging (MRI) data were used to inform the development and personalisation, tuning and calibration of musculoskeletal anatomies and models for biomechanical simulations. ....  | 36 |
| <b>Figure 8.</b> Gait laboratory setup at GU (a) and QCMAS (b). Marker trajectories and ground reaction force data were acquired using a motion capture system and a set of in-ground force plates (orange) while participants performed different locomotor tasks within the motion capture volume. ....  | 39 |
| <b>Figure 9.</b> Participant with 51 retroreflective markers and 12 surface EMG sensors (covered in red tape. E.g., the five circled in figure) were affixed over the body to track the trajectories of each body segment and record lower limb muscle activity during the dynamic tasks. ....   | 42 |
| <b>Figure 10.</b> Examples of full lower limb (a) and high-definition knee MRI (b) scans acquired on one participant. ....   | 44 |
| <b>Figure 11.</b> Post-processing sequences selected to enhance muscle segmentations. (a) fat- and (b) water-suppression, (c) out-of-phase and (d) in-phase Dixon sequences were acquired on the full lower limb Mri scans. ....   | 45 |
| <b>Figure 12.</b> Segmented bony geometries (a) and knee joint structures (d) segmented on full-lower limb and dedicated high-definitions scans, respectively. Unregistered (b) and registered (c) bones. ....   | 47 |
| <b>Figure 13.</b> Three-dimensional view of a subset of lower limb muscles segmented on full lower limb MRI scans (a). Axial view of a thigh (b) and a shank (c) slices on which muscles were manually identified. ....  | 48 |
| <b>figure 14.</b> Levels of subject-specificity implemented in the models. Experimental motion capture, EMG and MRI data, along with literature findings, were used in a staged fashion to progressively increase the level of personalisation of each developed neuromusculoskeletal model. Marker positions were used to scale the template model, EMG signals to calibrate musculotendon (MTU) parameters and medical images to personalise bones, joint, muscle pathways and the maximal isometric force of lower limb muscles. .... | 50 |

|  |    |
|--|----|
| <b>Figure 15.</b> Example of generic base OpenSim model before (a) and after (c) linear scaling. Motion capture data (b) were used to determine each bone scaling factors in the three dimensions. ....  | 51 |
| <b>Figure 16.</b> MAP generated OpenSim skeletal model (a) and personalised muscle pathways with wrapping surfaces in light blue (b).....  | 52 |
| <b>Figure 17.</b> Steps included in the workflow to generate bones in the MAP Client. Linearly scaled MAP mean bone models (white) were firstly registered to the corresponding mri segmentations via iterative-closest-point registration (a to b), then resized (c). Host-mesh fitting (d) and local mesh fitting (e) techniques were finally performed to produce more accurate bone reconstructions. ....  | 54 |
| <b>Figure 18.</b> Nodes (red dots) and elements (numbers) on MAP mean pelvic bone model. ....  | 56 |
| <b>Figure 19.</b> Wrapping surfaces to correct for non-physiological MTU pathways. Example of the rectus femoris muscle, before (a) and after (b) inserting wrapping surfaces on the MAP generated OpenSim model. (c) example of discontinuity in MTU length for the semimembranosus muscle (red) which gets corrected inserting a wrapping surface (blue). ....   | 57 |
| <b>Figure 20.</b> Adapted from Millard et al (2013). Theoretical force-length (a and b) and force-velocity (c) curves which describe the physiological behaviour of muscles in MSK models. (d) Hill-type actuator representation. Each MTU is modelled as a series element (SE) representing the tendon, a contractile element (CE) representing the active muscle fibres and a parallel element (PE) representative of the passive properties of a muscle. The overall MTU length is given by the sum of the tendon length ( $l^t$ ) and muscle fibre length ( $l^m \cos \alpha$ ), which accounts for the orientation of the muscle fibres, i.e. pennation angle ( $\alpha$ ) .... | 59 |
| <b>Figure 21.</b> Neural solutions employed in this thesis. Static optimisation synthesised all excitations to minimise (a) overall squared muscle excitations and (b) joint moments tracking error. The EMG-assisted approach employed experimental EMG data and static optimisation methods to further minimise experimental EMG tracking errors. ....   | 63 |
| <b>Figure 22.</b> Schematic of the static equilibrium problem solved to compute knee joint contact forces, once muscle forces ( $F_{MTU}$ ), muscle moment arms ( $r_{MTU}^{MC}$ ), intercondylar  |    |

distance ( $d^{IC}$ ) and external joint moments around the contact points ( $M_{ext}^{MC/LC}$ ) are known.

..... 64

**Figure 23.** Models accuracy in tracking experimental moments and muscle excitations. Comparison between CEINMS models predictions (i.e., joint moments (a and b) and muscle excitations (c and d)) and corresponding experimental data (i.e., external joint moments and EMG linear envelopes) for a typically developing child (left) and his twin brother with CP (right).  $R^2$  and RMSE values (with relative standard deviation) are reported on the left and right hand-side of each subplot, respectively. Different colours refer to different NMSK models. All results are averaged across three walking trials. Muscle excitations are reported as mean value of the twelve analysed lower limb muscles. Stars indicate statistically significant differences ( $p < 0.05$ ). ..... 82

**Figure 24.** Estimated muscle forces acting on the knee. Estimated muscle forces for the MTUs contributing to the knee adduction-abduction moment, which was used to compute knee joint contact forces. Forces are reported as mean values (solid line)  $\pm$  standard deviation (shaded areas) across 3 trials (red = unCal<sub>SO</sub>, green = unCal<sub>EMGa</sub>, blue = Cal<sub>EMGa</sub> and purple = Cal<sub>EMGa</sub><sup>MRI</sup>) and expressed in bodyweight (BW). ..... 84

**Figure 25.** Total tibiofemoral contact forces estimates. Total tibiofemoral contact forces estimated using the four developed NMSK models. Results are normalised to each subject's bodyweight (BW) to allow for comparisons and reported as mean values. .... 85

**Figure 26.** Comparison of medial, lateral and total tibiofemoral contact forces using static optimisation versus an EMG-assisted approach. Medial, lateral and total tibiofemoral contact forces estimated using static optimisation methods (red) and an EMG-assisted approach (blue), for a child with CP (right side) and his TD twin brother (left). Results are reported as mean values  $\pm$  standard deviation. .... 86

**Figure 27.** Different levels of medical imaging data provided to the MAP Client. Full (a) and sparse (b-c) MRI segmentations used in the MRI-informed pipelines. .... 100

**Figure 28.** Pipelines developed and tested to reconstruct paediatric lower limb bones. Each pipeline, identified by the number above it, comprised different steps, represented in circles. Different colours refer to different methods/techniques employed. Shades of green or blue indicate MOCAP-based and MRI-based methods, respectively. Pipeline 0 was performed in OpenSim on generic geometries from the gait2392 model. Pipeline 1-10 were run in the MAP Client. PC = principal component scaling, LS = linear scaling. .... 101

**Figure 29.** Metrics used to assess the accuracy of reconstructed bones. Volumetric (a) and surface (b) similarity indices between each reconstructed MAP bone and the corresponding MRI segmentation were computed using the reported formulas (bottom right). For the pelvis, colour maps (c) were produced to understand how the surface error was distributed..... 104

**Figure 30.** Volume similarity between MAP reconstructions via scaling approaches and corresponding MRI segmentations for the pelvic, left femoral and left tibiofibular bones. Bar graph reporting Jaccard indices as mean values across the studied population (n=18) for the pipelines solely employing linear or non-linear scaling methods, i.e. P0-6. Different shades of colours were used to separate pipelines performing one only scaling step (blue), or multiple scalings (red and purple). PC = principal component scaling, LS = linear scaling. Symbols denote significant differences: \* compared to OpenSim LS, \*\* compared to MOCAP LS, ^ compared to MRI LS. .... 109

**Figure 31.** Examples of pelvis bone reconstructions for one subject using the developed pipelines. Reconstructed pelvis and relative surface error distribution reported via colour maps, where darker reds denote larger errors, expressed in mm. For completeness, Jaccard indices are reported in the grey circles. The labels PC and LS describe the type of scaling employed, i.e. based on principal components or linear scaling. .... 110

**Figure 32.** Jaccard indices as function of subjects' height. Individual Jaccard indices and corresponding fitted regression lines to show the relationship between reconstruction accuracy and subjects' height for pipelines employing PC-based scaling. Different colours refer to different pipelines. Black dashed lines represent results from pipeline 1 (lower line) and pipeline 9 (upper line), for comparisons. PC = principal component scaling, LS = linear scaling, HMF = host-mesh fitting, LMF = local-mesh fitting..... 111

**Figure 33.** Dependency of hip joint centres location on subject's heights. Hip joint centres estimated from the different pipelines are displayed as spheres of different colours (red to fuchsia) overlaid to the correspondent MRI segmentation. Grey spheres indicate the reference hip joint centres derived from MRI segmentations. Orange circles on the scale at the bottom denote the subjects whose pelvis is displayed..... 114

**Figure 34.** The models' abilities to track experimental data. For each model,  $R^2$  and RMSE values between predicted and experimental ankle joint moment (a), knee joint moment (b) and EMG data (c) were computed. Results are reported as mean across populations, TD (blue) and CP (red). .... 134

**Figure 35.** Examples of knee JCF profiles estimated using the 6 developed NMSK models, for a TD child (a) and a CP child (b). Colors discriminate models based on the definition of musculotendon parameters and neural solution (red = unCal<sub>SO</sub>, blue = Cal<sub>SO</sub>, green = Cal<sub>EMGa</sub>). Line types refers to the musculoskeletal anatomy (solid = personalised in the MAP Client, dashed = scaled generic from OpenSim). ..... 135

**Figure 36.** Comparison of (a) muscle forces and (b) total knee JCF estimates between models. The level of personalisation was incrementally increased by (1) calibrating musculotendon parameters in CEINMS (unCal<sub>SO</sub> to Cal<sub>SO</sub>), and (2) switching neural solution (Cal<sub>SO</sub> to Cal<sub>EMGa</sub>). Estimates from the most physiologically plausible model, i.e. Cal<sub>EMGa</sub><sup>MAP</sup>, were used as gold standard, since no experimental data were available. \* indicate statistically significant differences..... 137

**Figure 37.** Individual peak values for each model and participant. Values are reported as mean (solid line) and standard deviation (shaded area) across 10 walking trials. ... 138

**Figure 38.** Comparison of (a) medial and (b) lateral JCF estimates between models. The level of personalisation was incrementally increased by (1) calibrating musculotendon parameters in CEINMS (unCal<sub>SO</sub> to Cal<sub>SO</sub>), and (2) switching neural solution (Cal<sub>SO</sub> to Cal<sub>EMGa</sub>). Estimates from the most physiologically plausible model, i.e. Cal<sub>EMGa</sub><sup>MAP</sup>, were used as gold standard, since no experimental data were available. \* indicate statistically significant differences..... 139

**Figure 39.** Example of medial and lateral joint contact force estimates for one TD and one CP child. Effect of personalising musculotendon parameters (a) and muscle activation patterns (b). Comparisons between unCal<sub>SO</sub>/Cal<sub>SO</sub> and Cal<sub>SO</sub>/Cal<sub>EMGa</sub> models. Red bands indicate significant differences (p=0.05). ..... 140

**Figure 40.** Example of medial and lateral joint contact force estimates for one TD and one CP child. Effect of personalising musculoskeletal anatomy (a) and combined effect of different levels of personalisation (b). Comparisons between Cal<sub>EMGa</sub>/Cal<sub>EMGa</sub><sup>MAP</sup> and unCal<sub>SO</sub>/Cal<sub>EMGa</sub><sup>MAP</sup> models. Red bands indicate significant differences (p=0.05). .... 141

**Figure 41.** Personalised (a) versus scaled generic (b) anatomy showing how medial and lateral contact points were further apart on MAP models. .... 144

**Figure 42.** Input data for simulations. Normalised linear envelopes of collected EMG data (top), inverse kinematics and inverse dynamics results at the ankle (a, c) and knee joint (b, d) for both participants (blue = TD, red = CP). ..... 164

**Figure 43.** MTU parameters after calibration in CEINMS. Percent variation of optimal fibre and tendon slack lengths values following calibration in CEINMS (blue = Cal<sub>EMGa</sub> vs unCal<sub>EMGa</sub>, yellow = Cal<sub>EMGa</sub><sup>MRI</sup> vs Cal<sub>EMGa</sub>). Note that when developing Cal<sub>EMGa</sub>, for both conditions (i.e., CP and TD), the initial values (i.e. as per unCal<sub>EMGa</sub> model) of OFL were allowed to vary up to  $\pm 5\%$ . On the other hand, TSL bounds were set differently depending on the condition:  $\pm 5\%$  for TD child,  $\pm 10\%$  for CP child. These values were ulteriorly calibrated,  $\pm 2.5\%$  after adjusting maximal isometric forces in model Cal<sub>EMGa</sub><sup>MRI</sup>. ..... 165

**Figure 44.** Experimental joint moment tracking. Ankle and knee joint moments predicted using the four developed NMSK models in comparison to the values experimentally computed via inverse dynamics in OpenSim (black bold line) for both twins (TD on the left, CP on the right). ..... 166

**Figure 45.** Estimated muscle forces for the 34 modelled MTUs. Forces are reported as mean normalised values (solid line)  $\pm$  standard deviation (shaded areas) across 3 trials (red = unCal<sub>SO</sub>, green = unCal<sub>EMGa</sub>, blue = Cal<sub>EMGa</sub> and purple = Cal<sub>EMGa</sub><sup>MRI</sup>) for the TD twin ..... 167

**Figure 46.** Estimated muscle forces for the 34 modelled MTUs. Forces are reported as mean normalised values (solid line)  $\pm$  standard deviation (shaded areas) across 3 trials (red = unCal<sub>SO</sub>, green = unCal<sub>EMGa</sub>, blue = Cal<sub>EMGa</sub> and purple = Cal<sub>EMGa</sub><sup>MRI</sup>) for the twin with CP. .... 168

**Figure 47.** Joint angles and moments comparison between a generic scaled and a MAP generated OpenSim model. The level of agreement was quantified computing the R<sup>2</sup> and root mean square error (RMSE) between models' estimates. .... 173



# List of tables

---

|                 |   |    |
|-----------------|---|----|
| <b>Table 1.</b> | Demographics (mean and standard deviation) of participants. Individual details are provided for the children enrolled in the two experimental studies, in Table 17 and Table 21. ....   | 37 |
| <b>Table 2.</b> | Demographics of participant enrolled in study 2.....  | 38 |
| <b>Table 3.</b> | Gait laboratory equipment used for data collection. ....  | 40 |
| <b>Table 4.</b> | List of motion capture markers affixed over participants’ body for scaling purposes and biomechanical simulations. A total of 51 markers, including four triad clusters and four Plug-in Gait wand markers were used. ....  | 41 |
| <b>Table 5.</b> | List of lower limb muscles from which experimental surface EMG data were collected and corresponding acronym .....  | 42 |
| <b>Table 6.</b> | Summary of the NMSK models developed in this thesis. The top half refers to models developed in study 1, while the bottom half refers to study 3. In both studies, the base musculoskeletal anatomy (unCal models) featured morphometrically tuned musculotendon parameters that were later calibrated in CEINMS with EMG data (Cal models). Both static optimisation (subscript SO) and EMG-assisted (subscript EMGa) approaches were used to estimate muscle forces. In study 1, maximal isometric force ( $F_{\max}^{\text{iso}}$ ) values were further personalised using muscle volumes segmented on MRIs (superscript MRI). In study 3, $F_{\max}^{\text{iso}}$ values were scaled with each participant’s mass (van der Krogt et al., 2016). Personalised musculoskeletal anatomies were developed in the MAP Client and finally implemented in the models (superscript MAP). .... | 66 |
| <b>Table 7.</b> | List of MTUs included in the NMSK models. Thirty-four MTUs, including the major muscles spanning the knee and ankle joints, were modelled. EMGs were collected from 12 MTUs on the left leg of each participant during the gait assessment and used in CEINMS to derive muscle excitations. The activity of three muscles (i.e., biceps femoris short head, semitendinosus and vastus intermedius) was mapped from experimental EMG data assuming that muscles sharing the same innervation have similar excitation patterns. Muscles belonging to each muscle group shared the same strength coefficients (initially set to 1), which were calibrated in $\text{Cal}_{\text{EMGa}}$ and $\text{Cal}_{\text{EMGa}}^{\text{MRI}}$ models. ....   | 74 |

**Table 7 (continued).** List of MTUs included in the NMSK models. Thirty-four MTUs, including the major muscles spanning the knee and ankle joints, were modelled. EMGs were collected from 12 MTUs on the left leg of each participant during the gait assessment and used in CEINMS to derive muscle excitations. The activity of three muscles (i.e., biceps femoris short head, semitendinosus and vastus intermedius) was mapped from experimental EMG data under the assumption that muscles sharing the same innervation have similar excitation patterns. Since no EMG data were available for the nineteen “additional MTUs”, excitation patterns were computed via static optimisation. Muscles belonging to each muscle group shared the same strength coefficients (initially set to 1), which were calibrated in  $Cal_{EMG_a}$  and  $Cal_{EMG_a}^{MRI}$  models. .... 75

**Table 8.** Characteristics of the four developed NMSK models. All models featured scaled-generic bones and joints. However, muscle activation patterns and MTUs parameters (i.e. optimal fibre length, tendon slack length and muscle isometric force) were progressively made subject-specific, combining experimental data, imaging and literature findings, as detailed in the table (“data source” column, on the right). ‘✕’ denotes generic parameters as per gait2392 model or static optimisation to estimate for muscle excitations, while ‘✓’ indicates inclusion of subject-specific characteristic. .... 78

**Table 9.** Demographics of participants. Age and height are reported as mean (standard deviation) across the studied population. .... 96

**Table 10.** Landmarks positions of the MOCAP markers. Anatomical landmarks name and location of the 51 retro-reflective markers affixed on each participants’ body. .... 97

**Table 11.** Pipelines summary. List of morphing techniques employed and time required to complete each pipeline per subject. PC = principal components. .... 103

**Table 12.** Volume and surface similarity metrics for pipelines solely employing linear or non-linear scaling methods. Jaccard index (JI), root mean square distance error (RMSE) and Hausdorff distance values are reported as mean (standard deviation) across the population. Values highlight the pipeline which provided the worst (red) results. For the pipelines employing MRI data, the letter in superscript indicates the level of segmentation incompleteness: ‘j’ stands for joint scans segmentations while ‘s’ indicates sparse segmentations. .... 106

**Table 13.** Volume and surface similarity metrics for pipelines employing linear or non-linear scaling methods in combination with mesh fitting techniques. Jaccard index (JI), root mean square distance error (RMSE) and Hausdorff distance values are reported as

mean (standard deviation) across the population. Values highlight the pipelines which provided the best (blue) results. For the pipelines employing MRI data, the letter in superscript indicates the level of segmentation incompleteness: ‘j’ stands for joint scans segmentations while ‘s’ indicates sparse segmentations. .... 107

**Table 14.** Statistics of linear regression models. R-squared values ( $R^2$ ),  $\beta$  coefficient (i.e. slope) and p-values ( $p$ ) for the regression lines fit to the individual Jaccard indices of pelvic, femoral and tibiofibular bones reconstructed using non-linear scaling methods. Higher slope values indicate more pronounced size-effect on volume similarity. The colour code reflects the legend in Figure 32. .... 108

**Table 15.** Hip joint centres location and percent distance errors. Euclidean distances between left/right hip joint centres (HJC) and percent absolute inter-HJC distance error between MRI segmentations and registered pelvis reconstructions. Location errors are expressed in mm, while inter-HJC distance errors are reported as percent values. Hip joint centres distance was also calculated using Harrington equation, commonly used in clinical practice, and measured on MRI segmentations. Results are reported as mean (standard deviation). Significant differences ( $p < 0.05$ ) with respect to MRI measurements and from Harrington equation are indicated by the symbols  $\wedge$  and  $*$  respectively. Superscript letters denote the level of MRI data sparsity: ‘j’ stands for joint scans segmentations, while ‘s’ indicate sparse segmentations..... 115

**Table 16.** List of methods employed to personalise neuromusculoskeletal models, based on experimental, literature or models data. Personalised features include: musculoskeletal anatomy, muscle pathways, optimal fibre length (OFL), tendon slack length (TSL), maximal muscle isometric force ( $F_{iso}^{max}$ ) and muscle activation patterns... .. 126

**Table 17.** Demographics of the studied population, which included three children with cerebral palsy (CP, GMFCS I-II) and 3 age-matched typically developing (TD) controls. .... 127

**Table 18.** List of neuromusculoskeletal models developed in this study. .... 131

**Table 19.** Physiological plausibility score. For each model, a score up to 6 was assigned based on the number of participants (dots) for whom the selected feature/condition was present/met. Population specific, i.e. for typically developing (TD, blue) and cerebral palsy (CP, red) children, and overall scores per model were calculated. The model

associated to the highest score ( $Cal_{EMGa}^{MAP}$ ) was considered to be the most physiologically plausible model. .... 136

**Table 20.** Intercondylar distance, in generic scaled and personalised anatomies..... 144

**Table 21.** Demographics of participants. Two identical twin brothers of comparable size and weight were enrolled in this study. The co-contraction index (CCI) was computed between knee flexors (i.e., SM, BF, MG, LG) and extensors (i.e. VL, VM, RF) muscles and defined in agreement with previous work (Knarr et al. 2012) as:  $(EMG_{flex} + EMG_{ext}) \frac{\min(EMG_{flex}, EMG_{ext})}{\max(EMG_{flex}, EMG_{ext})}$ , where  $EMG_{flex/ext}$  is the summed normalised linear envelope of the knee flexors/extensors. Values are reported as mean±standard deviation across the four processed trials..... 159

**Table 22.** Markers placement. Name and location of the 51 retro reflective MRI compatible markers placed on anatomical landmarks over the trunk, pelvis, thigh, shank and foot segments. .... 160

**Table 23.** Knee joint moments and muscle excitations tracking ability of different NMSK models. Values (i.e.  $R^2$  and RMSE) are reported as mean across three trials ± standard deviation (SD). For muscles excitations, results are reported as mean values of 12 individual MTUs (Table 7)..... 161

**Table 24.** Segmented muscle volumes. Muscle volumes manually segmented on full lower limb MRI scans. Five muscles (in bold) presented with substantial volume reductions between participants (i.e., volume difference > 22.5%, accounting for volume reduction by 20% + segmentation error 2.5%). Please refer to Table 7 for muscle acronyms. .... 162

**Table 25.** Muscle maximal isometric force values. Comparison between generic values ( $Cal_{EMGa}$ ) and MRI based values ( $Cal_{EMGa}^{MRI}$ )..... 163

**Table 26.** Difference in femur neck-shaft angle between MRI segmentations and bone reconstructions for the 18 participants, listed in order of height. Three-dimensional angles were computed in 3-Matic (Materialise, Leuven, BE) between the principal axis of two cylinders fitted to neck and shaft of the femoral geometry, respectively. P0 = linearly scaled OpenSim generic bones, P1 = linearly scaled MAP generic geometries, P2 = non-linearly scaled MAP generic geometries, P9 = most accurate MAP reconstructions (see results). .... 171

**Table 27.** Knee and ankle joint axis orientation with respect to the global coordinate system (MRI coil). Joint axes were defined according to ISB recommendations, based on anatomical landmarks. Angles were computed from the corresponding rotation matrix and are reported as mean values across the 18 participants, for five of the 21 developed pipelines (i.e., P0, P1, P2, P7 and P9). MRI = manual segmentations (gold standard), P0 = linearly scaled OpenSim generic bones, P1 = linearly scaled MAP generic geometries, P2 = non-linearly scaled MAP generic geometries, P7/9 = most accurate MAP reconstructions..... 172



# List of equations

---

|                    |     |
|--------------------|-----|
| Equation (1).....  | 59  |
| Equation (2).....  | 60  |
| Equation (3).....  | 60  |
| Equation (4).....  | 62  |
| Equation (5).....  | 64  |
| Equation (6).....  | 64  |
| Equation (7).....  | 79  |
| Equation (8).....  | 80  |
| Equation (9).....  | 129 |
| Equation (10)..... | 131 |
| Equation (11)..... | 132 |



# List of abbreviations

---

2D – Two-dimensional

3D – Three-dimensional

ANOVA – Analysis of Variance

ASIS - Anterior superior iliac spine

BoNT – Botulinum NeuroToxin

CEINMS – Calibrated EMG-Informed Neuromusculoskeletal Modelling Software

CP – Cerebral palsy

CT – Computed tomography

DICOM - Digital Imaging and COmmunications in Medicine

DOF – Degree of freedom

EOS – Electro Optic System

EMG - Electromyography

GMFCS – Gross Motor Function Classification System

GRA - Gracilis

GRF – Ground reaction force

GU – Griffith University

HD – High-definition

HJC – Hip joint centre

HMF – Host-mesh fitting

ISB – International Society of Biomechanics

JCF – Joint contact force

JJ – Jaccard Index

LG – Lateral gastrocnemius

LMF – Local-mesh fitting

MAL – Moment arm length

MAP – Musculoskeletal Atlas Project

MG – Medial gastrocnemius

MOCAP – Motion capture

MOPSO – Multi objective particle swarm optimisation

MRI – Magnetic resonance imaging

MSK - Musculoskeletal

MTL – Muscle-tendon length

MTU – Musculotendon unit

NMSK - Neuromusculoskeletal

OFL – Optimal fiber length

PC – Principal component

QCH – Queensland Children’s Hospital

QCMAS – Queensland Children’s Motion Analysis Service

RF – Rectus femoris

RMSE – Root mean square error

SDR – Selective dorsal rhizotomy

SPM – Statistical parametrical mapping

SPSS - Statistical Package for Social Science

SSM – Statistical shape model

STL - Stereolithography

SWS – Selected walking speed

TD – Typically developing

TFL – Tensor fasciae latae

TSL – Tendon slack length

US - Ultrasound



# CHAPTER 1

---

## Introduction

### Background

Cerebral palsy (CP) is a progressive disorder of the neuromuscular system resulting from a non-progressive damage to the immature brain during early development (Bax et al. 2005; Keith et al. 1959; Rosenbaum et al. 2007). The incidence of CP has remained relatively stable over recent decades (Cans 2000; Smithers-Sheedy et al. 2016). It is estimated that CP affects approximately 2-4 in 1000 newborns per year and over 17 million children worldwide, which makes CP the most common physical disability in childhood. Depending on severity and location of the brain damage different forms of physical and movement impairment can manifest and may affect one or both sides of the body. CP may also be associated with epilepsy and/or cognitive, sensory, urogenital and endocrinal impairments (Odding et al. 2006). Based on the type of motor impairment, CP is classified as spastic, dyskinetic or ataxic. However, in many cases patients present with a mixture of the three (Gage 2009). Motor function in CP is typically graded using the 5-point ordinal Gross Motor Function Classification System (GMFCS)(Palisano et al. 1997). In this grading system, level 1 is associated with children who are able to perform gross motor skills without limitations while level 5 is normally assigned to children presenting with restricted voluntary control of movement, limited motor functions and inability to move independently (Palisano et al. 1997).

### CP related impairments

Many researchers have postulated that the brain insult prior to or during birth leads to altered muscle growth in children with CP (Gough and Shortland 2012). Significant volume deficits, from 10 to 58% (Barrett and Lichtwark 2010), measured using magnetic resonance imaging (MRI) or ultrasound, have been reported in the affected lower limb muscles of children with CP compared to their healthy counterparts. These smaller volumes were accompanied by significant shortening of the muscle belly and were

generally more evident in the bi-articular hamstrings (Handsfield et al. 2015; Noble et al. 2014; Oberhofer et al. 2010). Hypertonia and spasticity, together with contractures and changes in muscle composition (Foran et al. 2005; Lieber et al. 2004; Pitcher et al. 2015) further lead to reduced functional abilities in CP children. Moreover, since activity participation in this population is reported to be less than in typical developing peers (Hanna et al. 2009), motor function tend to worsen in time as muscles do not receive the necessary stimulation to grow.

In addition, the abovementioned alterations in muscle activity and morphology may hinder the capacity for lower limb muscles to produce the forces necessary to achieve typical gait. Noticeable changes in gait kinematics might initially be masked in some individuals with mild CP who are able to compensate using the redundancy in the musculoskeletal system. However, as severity of CP increases a number of common gait impairments may emerge including; reduced knee flexion in swing, increased hip and knee flexion during stance, increased ankle plantarflexion or ankle dorsiflexion during stance and an internal foot progression angle (Wren et al. 2005). These atypical gait kinematics and associated aberrant muscle forces can excessively overload joints and ultimately induce progressive deformation of developing bones due to bone remodelling (Frost 2003). Secondary abnormalities such as bone deformities can emerge and subsequently contribute to further gait decline.

## **Clinical management of CP**

Since normal neuro-muscular control cannot be restored in patients with CP, surgical and/or rehabilitative interventions are tailored to correct deformities, restore joint range of motion, stabilise joints and balance muscle power (Kriger 2006; Theroux and DiCindio 2014) in order to improve function and to restore typical gait. To this end, single event multi-level orthopaedic surgery is the preferred intervention and may include: muscle lengthening, tendon transfer, guided growth (Wang et al. 2019), and/or osteotomy (Gage 1990; Novak et al. 2013). Unfortunately, the decision making process is not straightforward. Due to the specificity of the symptoms and the differences in the grade of impairment from patient to patient, a standardised treatment plan is likely to be sub-optimal. Clinical management of CP is currently based on clinical examinations, clinical history and imaging. These methods may provide valuable information, but do not provide a clear understanding of dynamic function or the underlying mechanisms specific to the pathology (Desloovere et al. 2006). Clinical motion analysis may be used to assist in designing the appropriate treatment plan (Chang et al. 2010; DeLuca 1991; DeLuca et

al. 1997; Sangeux and Armand 2015). However, despite proven benefits to patients' quality of life when gait analysis recommendations were followed (Wren et al. 2011), in a consistent number of cases (23%) some key gait parameters did not change or even worsened (Filho et al. 2008) after surgery; suggesting the need for additional tools to acquire useful information on the pathology. In this scenario, neuro-musculoskeletal (NMSK) modelling emerges as an asset to complement clinical motion analysis findings (van der Krogt et al. 2016). NMSK models can provide estimates of the internal loads (i.e., muscle and joint contact forces, JCFs) acting on selected joints (Arnold et al. 2010; Garijo et al. 2017; Gerus et al. 2013; Saxby et al. 2016), which may be used first to inform clinical decision making (Arnold and Delp 2005) and second to potentially anticipate gait kinematic decline. Harmful joint loading that might eventually lead to deformity and subsequent kinematic decline in asymptomatic patients may in fact be detected. Moreover, virtual surgeries may be tested on the models prior to entering the operating theatre, enabling to identify the most appropriate treatment for each patient.

## **Limitations of current NMSK models**

Although promising, current NMSK models present with a number of limitations that may curb their translation to clinical practice. Firstly, musculoskeletal anatomies are commonly scaled from generic template models, which are representative of one (or few) healthy older adult subjects. Hence, despite being relatively fast and simple to build, scaled-generic models may not accurately describe healthy paediatric populations, let alone pathologic conditions (e.g., CP or other gait disorders) who present with a range of musculoskeletal deformities. Furthermore, paediatric bone geometries change with growth in typically developing (TD) children and in children with CP and consequently, comparison of individual longitudinal data, using generic models, might mask changes in gait dynamics. Inaccurate representations of the musculoskeletal anatomy may lead to errors in calculations: bone deformities (Bosmans et al. 2014) and bone (mis)alignment (Heller et al. 2003; Lerner et al. 2014) have a substantial effect on the computed joint contact forces (JCFs). Erroneous estimates of joint angles and moments may also be produced due to the misplacement of joint centres. Moreover, as muscle attachments on bones could also be erroneously located, musculotendon kinematics may be affected as well (Arnold et al. 2000; Scheys et al. 2008a).

Further to poor bone representations and associated inaccuracies, few modelling assumptions may contribute to observe non-physiological muscle behaviour. For example, there is no scientific evidence supporting the idea that internal parameters

governing muscle function do scale linearly with bones or muscle lengths (Ward et al. 2007; Ward et al. 2005). This assumption may hinder muscle function (Carbone et al. 2016), as linearly scaled values may fall outside known physiologically plausible ranges (Modenese et al. 2016). Theoretical force-length and force-velocity curves describing muscle behaviour (Arnold et al. 2013; Millard et al. 2013) may not be respected. In addition, unconstrained optimisation methods (e.g., static optimisation that minimises muscle activations squared)(Anderson and Pandy 2001a; Anderson and Pandy 2001b; Buchanan and Shreeve 1996), which are based on *a priori* criteria, are commonly employed due to their simplicity to estimate muscle activation patterns. Depending on the criteria selected, the underlying assumption is that the central nervous system favours the maximisation of endurance, minimisation of excitation, or smallest muscle forces while activating muscles to perform a certain task (Crowninshield and Brand 1981). As a consequence, these criteria discourage the estimation of muscle co-contraction, thereby erroneously describing muscle activity in healthy populations (Saxby et al, 2016; Lloyd and Besier, 2003; Pizzolato et al , 2015), let alone in children with CP, who present with highly abnormal muscle excitations and high levels of co-contraction (Prosser et al. 2010; Steele et al. 2015). Moreover, static optimisation has been proven to yield unsatisfactory results compared to subject-specific muscle-activation patterns (Hoang et al. 2019; Lloyd and Besier 2003; Veerkamp et al. 2019) and/or subject-specific strength adjustments (Knarr and Higginson 2015) in determining muscle forces.

Altogether these modelling inaccuracies may lead to the misinterpretation of clinical findings, which could not be tolerated if NMSK models are employed to inform surgeries. Personalisation is crucial (Hicks et al. 2015; Valente et al. 2014), particularly to describe CP that may present with a variety of symptoms and impairments (Bar-On et al. 2015; Mathewson and Lieber 2015; Odding et al. 2006). More importantly, each individual is affected to a different extent (Handsfield et al. 2015) and the number of musculoskeletal structures involved may vary from patient to patient. To this end, several steps forward in the personalisation of NMSK models have been made over the last years (Fernandez et al. 2016; Sartori et al. 2017a).

## **Personalisation of NMSK models**

Depending on the availability of experimental data, personalisation may be introduced in different ways (Arnold and Delp 2005; da Luz et al. 2017; Fox et al. 2018; Gerus et al. 2013; Hoang et al. 2018; Modenese et al. 2018; Schwartz and Lakin 2003; Steele et al. 2012; van der Krogt et al. 2016; Veerkamp et al. 2019; Wesseling et al. 2019).

For instance, subject-specific skeletal anatomies can be generated via manual or (semi-)automatic segmentation of medical imaging data, e.g. MRI's (da Luz et al. 2017; Scheys et al. 2008b) or computed tomography (CT) scans. However, this is a costly and time-consuming process. Alternatively, data mining methods, such as statistical shape modelling (Bahl et al. 2019; Nolte et al. 2016; Rajamani et al. 2007; Suwarganda et al. 2019; Zhang et al. 2014a) and mesh fitting techniques (Oberhofer et al. 2019), may be employed. These methods offer the possibility of fast, automated and accurate reconstructions of bones from limited experimental data.

Secondly, MTU parameters that are difficult to collect *in vivo* may be personalised via tuning (Modenese et al. 2016; Winby et al. 2008) and calibration (Hoang et al. 2018; Meyer et al. 2017; Pizzolato et al. 2015; Serrancolí et al. 2016) of linearly scaled values. Particularly, morphometric scaling (i.e., tuning) aims to ensure physiological muscle behaviour, while calibration uses experimental data to constrain MTU parameters within known physiological limits. More complex methods were proposed to extract personalised muscle parameters (Gerus et al. 2015; Manal and Buchanan 2004; Mathewson et al. 2015; Panizzolo et al. 2016), directly from medical imaging data. For example, freehand 3D ultrasound techniques were used to measure the architectural properties of muscles (i.e. pennation angle, fascicle length and physiological cross-sectional area) (Sartori et al. 2017b) and indirectly calculate muscle volumes and lengths (Barber et al. 2009), but this approach is only limited to superficial muscles. When modelled, abnormalities due to CP are commonly implemented applying pre-determined scaling factors based on previously reported literature data. Hence, values are not subject-specific, unlike the symptoms of CP. Similarly, the maximal isometric force value, which limits the capability of a muscle to generate force, may be scaled with participants' mass, height or the product mass\*height (Kainz et al. 2018; van der Krogt et al. 2016). However, these methods do not account for muscle size heterogeneity (Handsfield et al. 2015). Alternatively, when medical imaging data are available, segmented muscle volumes (Handsfield et al. 2014) or volumes derived from regression equations (Noble et al. 2017) can be used to recalculate maximal isometric force values.

Finally, several approaches were proposed to produce personalised muscle activation patterns. These include (i) EMG-informed approaches (Lloyd and Besier 2003; Meyer et al. 2017; Pizzolato et al. 2015; Sartori et al. 2012), which employ experimental muscle signals, (ii) synergy-based methods (Bianco et al. 2017; Meyer et al. 2016; Steele et al. 2015) and (iii) stochastic approaches (Martelli et al. 2015).

Nonetheless, to date, there is a lack of studies combining more than one level of personalisation on a single NMSK model. This is due to the need for specialised software and niche skillset required to develop and to personalise models. However, new technology is becoming available to rapidly generate patient-specific NMSK models. For example, the open-source Musculoskeletal Atlas Project (MAP) Client (Zhang et al. 2014b) aims to generate full lower limbs models from sparse MRI scans, using data mining methods (e.g., statistical shape modelling) and mesh fitting techniques to fill in the missing bone segments with information gathered from an anatomical repository. This promises a faster way to build NMSK models from medical images and reduce the amount of images collected (Bahl et al. 2019; Suwarganda et al. 2019), but the efficacy of using the MAP Client for paediatric populations has yet to be demonstrated. The MAP Client also enables the personalisation of a generic OpenSim model (Delp et al. 2007; Delp et al. 1990) with subject-specific anatomies. This may facilitate the integration of the MAP Client with other open-source software, i.e. OpenSim and CEINMS, which are commonly employed to develop and to personalise NMSK models for biomechanical simulations of gait. Although personalisation may be crucial to produce physiologically plausible estimates of internal biomechanics, it is not yet clear what the contribution of different levels of personalisation is on model's estimates of muscle forces and JCFs.

## **Statement of the problem**

There is abundance of scientific evidence detailing the impairments and abnormalities secondary to CP. Yet, the NMSK mechanisms behind the manifested pathologies are not completely understood. Clinical assessments and tests employed to inform the management of CP do provide useful information on external biomechanics, but fail to capture specific key features that would enable the delivery of effective personalised treatments. Additional parameters (e.g., muscle and joint contact forces), may be estimated using NMSK models and could uncover harmful internal forces before gait decline. This additional information has the potential to transform clinical decision making. Nonetheless, currently available models most probably fail to encapsulate enough subject-specific information to produce physiologically plausible estimates, possibly leading to the misinterpretation of clinical findings.

# Thesis objective

The main goal of this thesis was to develop personalised NMSK models of typically developing paediatric populations and children with CP. These models, which incorporate physiologically plausible MTU parameters, subject-specific muscle activation patterns and image-based musculoskeletal anatomies, may enable to capture pathology-related abnormalities. To this end, three studies were implemented as part of this thesis. The first and last studies aimed to develop NMSK models with increasing level of personalisation in order to quantify the individual contribution of each feature on models' performances and estimates. The second study focussed on the processes to generate subject-specific paediatric lower limb bony geometries for use in NMSK modelling. There were three specific aims:

1. To develop NMSK models with incremental level of complexity and subject-specificity to investigate the effect of (i) MTU parameters calibration, (ii) neural solutions and (iii) maximal isometric muscle force scaling on models' ability to track experimental data and to capture individual (and pathological) differences between two identical twin brothers, where one was typically developing and one with CP (GMFCS I). A linearly scaled generic model of each participant was generated for comparisons.
2. To determine the minimal amount of experimental data and the best (combination of) methods to accurately reconstruct pelvic, femoral and tibiofibular bones in typically developing paediatric populations. Three metrics of volumetric and surface similarity between reconstructed and MRI-segmented bones were computed to assess the reconstruction accuracy of each of the ten tested combinations.
3. To develop a personalised paediatric NMSK model informed with experimental motion capture, medical imaging and EMG data to estimate muscle forces and knee JCF during gait in children with CP (GMFCS I-II) and age- and size-matched typically developing participants. Furthermore, to quantify the individual and combined effect of musculoskeletal anatomy personalisation on model predictions, five additional models with different (and lower) level of subject-specificity were developed.

Three independent research studies were designed to address the threefold aims of this thesis and are here presented in journal article format. The thesis comprises seven

chapters overall, including this introduction and three experimental chapters relative to the implemented studies. In details:

*Chapter 1* provides a succinct and general introduction to the topics of this thesis and introduces the aims of the research work.

*Chapter 2* provides information on the aetiology and pathophysiology of CP and describes the state of the art in NMSK modelling, highlighting the limitations of commonly employed models and the current gaps in literature.

*Chapter 3* presents all methods and procedures employed in this thesis for data collection and processing, including information on participants' recruitment and details on the personalisation process and statistical tests performed. The content of this chapter may be included in a methodological paper detailing the steps involved in the development and personalisation of a paediatric NMSK model.

*Chapter 4* describes the development of four paediatric NMSK models with incremental level of personalisation, specifically designed to better characterise CP and to further the knowledge of the effects of pathology-related abnormalities on the internal biomechanics. This chapter addresses the first specific aim of this thesis and it is now under review in *Clinical Biomechanics*.

*Chapter 5* presents different ways to reconstruct accurate paediatric lower limb bones for use in NMSK modelling applications and proposes guidelines to achieve optimal results. This chapter addresses the second specific aim of this thesis and has been accepted with minor concerns in *Biomechanics and Modeling in Mechanobiology*, where it was invited for publication on a special issue.

*Chapter 6* describes the implementation and use of a MAP Client generated paediatric lower limb NMSK model to study normal and pathological gait. This chapter addresses the third specific aim of this thesis, and investigates the individual contribution of MTU parameters, neural solution and musculoskeletal anatomy personalisation on muscle forces and JCF estimates. A manuscript will be prepared for submission to *IEEE Transactions on Biomedical Engineering*.

*Chapter 7* contextualises the research findings of this thesis within the current literature and expands on the implications of the work, addressing feasibility and translational potential of NMSK modelling. Limitations and future directions are finally discussed.

# CHAPTER 2

---

## Literature review

### What is cerebral palsy?

Cerebral palsy (CP) is the most common motor disorder in childhood. Recent data from the Australian Cerebral Palsy Register (Report of the Australian Cerebral Palsy Register, Birth Years 1993-2006 February, 2013) and the Surveillance of Cerebral Palsy in Europe (Surveillance of Cerebral Palsy in Europe (SCPE) Scientific report 1998 - 2018 November, 2018) reports showed a CP prevalence rate of approximately 2 in 1000 live births, in agreement with a previous meta-analysis reporting a worldwide incidence rate around 2.11/1000 births (Oskoui et al. 2013). However, population-based studies have shown rates ranging from 1 to 4.1/1000 births (Galea et al. 2019; Touyama et al. 2016; van Naarden Braun et al. 2016). More importantly, although constant until the early 2000s (McIntyre et al. 2011), the number of CP cases reduced in the last decades (Sellier et al. 2016) along with advancement in medicine and technology. Initially, CP was defined as *'a persisting but not unchanging disorder of movement and posture, appearing in the early years of life and due to a non-progressive disorder of the brain'* (Keith et al. 1959). However, its definition was soon extended to comprise all developmental disorders of performance and behaviour that often accompany musculoskeletal and postural disorders (Bax et al. 2005; Morris 2007; Rosenbaum et al. 2007). More generally, nowadays, CP is used as an umbrella term to identify a number of motor impairments originating from a non-progressive damage to the immature brain occurring before or at birth, or within the first 2 years of age. In addition to motor impairment, CP may be associated with epilepsy and/or cognitive, sensory, urogenital and endocrinal impairments (Jan 2006), however the focus of this chapter is on the consequences of the brain damage on motor impairment.

Based on both severity and location of the brain damage, different forms of physical and movement impairments can manifest in CP patients who may be affected on one or both sides of the body. For this reason, CP is commonly classified by the type of motor impairment as spastic, dyskinetic or ataxic. Spastic CP, which is the most prevalent type (in 80% of the patients), is characterised by tight and stiff muscles. Dyskinetic and

ataxic CP, that equally share the remaining 20% of the cases, are instead characterised by involuntary movements and incoordination or shaky movements, respectively. Nonetheless, in many cases patients present with a mixture of the above (Odding et al. 2006) and their motor impairment is broadly classified using the Gross Motor Function Classification System (GMFCS) (Palisano et al. 1997). The GMFCS is a five-level objective functional scale used to grade the residual motor abilities of a person. Level I is associated with individuals able to perform gross motor skills without limitations, while level V is normally assigned to subjects presenting with restricted voluntary control of movement, limited motor functions and inability to move independently.

## **Primary and secondary impairments**

Contributing to the loss of motor abilities, a wide range of neuromuscular alterations and structural changes of the musculoskeletal system are typical in CP patients (Shortland 2017). For example, Barrett and Lichtwark (2010) reported significant alterations of morphological, structural and mechanical properties in CP muscles, which are primarily characterised by an abnormal activity resulting from the damage to the upper motor neurons (Gage 2009)(Figure 1). Both upper and lower limbs may be involved. However, in the present chapter we will focus only on lower limb muscle and joint impairments, as these are directly responsible for the gait deviations observed in CP children.

CP-related musculoskeletal alterations are classified as primary or secondary impairments. Primary impairments have a neurological origin and are likely caused by the abnormal motor control, reduced number of effective motor units and increased excitability of alpha and gamma neurons. Primary impairments include increased and aberrant muscle activity, e.g. hypertonia and spasticity (Bar-On et al. 2015) and muscle weakness (Mockford and Caulton 2010).

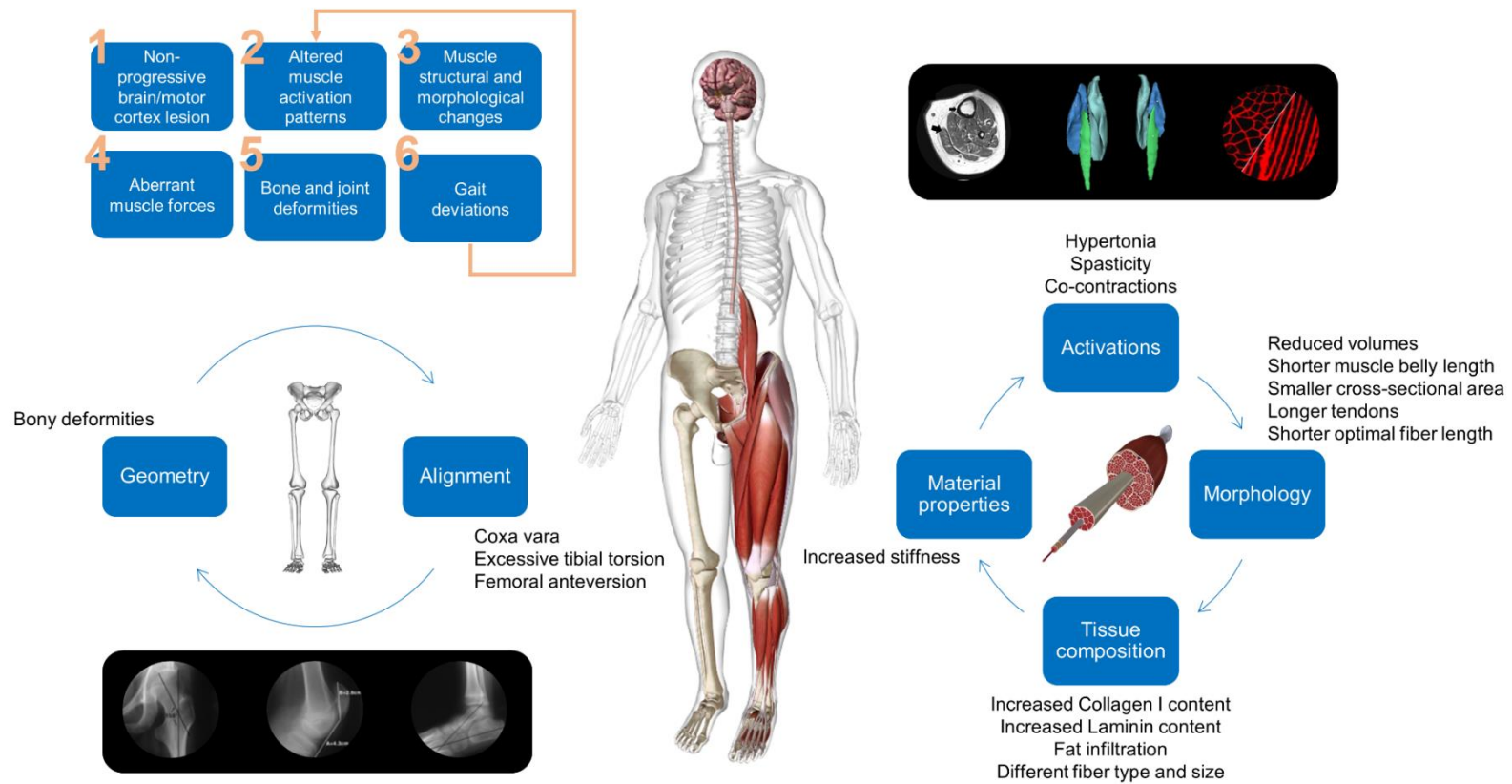


**Figure 1.** Schematic of the musculoskeletal alterations associated with CP. Medical imaging data (black boxes) show some common joint deformities and muscle morphological and structural changes observed in CP patients. Top left: feedback loop of events originating from the non-progressive lesion to the brain or motor cortex responsible for the progressive loss of motor function and alterations to musculoskeletal tissues.

## **Hypertonia and spasticity**

Clinically, the term hypertonia refers to an increased resistance to passive motion due (1) to hyper-reflexia, i.e. excessive reflex responses caused by the enhanced excitability of motor neurons, which occurs in CP patients secondary to the brain damage and (2) to alterations in the soft tissues (Nielsen et al. 2005; Trompetto et al. 2014). The main contributors to hypertonia in CP are believed to be the aberrant muscle activations induced by spasticity (Cans 2000; Morrell et al. 2002), which is the most prevalent symptom in CP patients. Spasticity has been described as a velocity-dependent increase in resistance to passive movement (Lance 1980) caused by exaggerated tonic stretch reflexes. In clinical practice, spasticity is typically measured via physical examinations (Scholtes et al. 2006) involving passive muscle tests and classified according to the modified Ashworth (Bohannon and Smith 1987) or the modified Tardieu scales (Boyd and Graham 1999). However, poor correlation has been found between the above clinical spasticity scores and gait data (Desloovere et al. 2006; Fleuren et al. 2010). Consequently, instrumented measures (Bar-On et al. 2013) involving simultaneous electromyography (EMG) data, angular velocity and external torques recordings, were introduced; allowing for a more precise quantification of the effects of spasticity (Damiano et al. 2002). Yet, the contribution of spasticity to hypertonia remains unclear and difficult to assess (Bar-On et al. 2015). Few studies have investigated the relationship between muscle activity and muscle stretch velocity during dynamic tasks. Their results showed that increased muscle activations in CP children tend to occur when the muscles are stretching more rapidly (Bar-On et al. 2014; Crenna 1998; Crenna 1999; van der Krogt et al. 2009; van der Krogt et al. 2010). Computational simulations further supported the idea of spasticity being a velocity-dependent mechanism. van der Krogt and colleagues (2016) were able to accurately predict passive knee motion in CP by implementing a velocity-dependent feedback to simulate spasticity. However, a recent study suggested that spasticity may have a force-dependent nature (Falisse et al. 2018), as the developed neuromusculoskeletal models more accurately predicted experimental data when a force-dependent, as opposed to a velocity-dependent, spasticity model was implemented.

## **Muscle co-contractions**

In addition to an increased muscle tone, higher levels of co-contraction have been reported in the muscles of children with CP compared to their typically developing (TD) peers (Damiano 1993; Damiano et al. 2000; Granata et al. 2000; Leonard et al. 1991; Lorentzen et al. 2019), particularly while performing extension movements and at faster walking speeds (Vaughan et al. 1992). In CP patients, this may be partially explained by the higher thresholds required to activate the intracortical inhibitory circuits (Frisk et al. 2019). However, co-contractions, per se, cannot be classified as abnormalities. Everyday, the central nervous system adopts different strategies to activate muscles in order to complete a specific task or movement. At times, to achieve a higher degree of precision (Damiano 1993) simultaneous activations of antagonist muscles, referred to as muscle co-contractions, are employed. Although this mechanism is associated with an increased energy expenditure, it also results in an overall enhanced joint stiffness (Nielsen 1998), which may help protecting the ligaments and increasing joint stability to overcome muscle weakness. For the above reasons, co-contractions are not necessarily decreased with skill development (Ford et al. 2008); sometimes may even increase. However, when excessive, co-contractions may hinder movement. This is the case of children with spastic CP, who tend to walk with stiff legs, presumably to increase their stability. Interestingly, Lorentzen and colleagues (2019) observed similar amount of tibialis anterior/soleus co-contraction in children with CP and TD children below the age of 10-12 years during toe walking. Nonetheless, in the TD group the co-contraction level declined with age and maturation.

## **Muscle morphological changes**

Secondary impairments are not directly caused by the brain lesion, but develop in response or together with primary impairments. Examples are muscle morphological deficits (Barrett and Lichtwark 2010) and increased muscle and joint stiffness due to altered muscle composition. Many researchers have postulated that the brain insult prior to or during birth may further lead to altered muscle growth (Gough and Shortland 2012). Spastic muscles are often smaller in size, i.e. volume and cross sectional area, and have a shorter belly length compared to healthy muscles (Barrett and Lichtwark 2010). Reported volume losses range between 10 and 58% across muscles and studies, with the distal musculature generally affected to a greater extent (Barrett and Lichtwark 2010). Particularly, the shank muscles, i.e. gastrocnemii and soleus muscles, appear to be heavily

involved with an overall volume loss of around 30-40% (Fry et al. 2004; Handsfield et al. 2015; Lampe et al. 2006; Noble et al. 2014; Oberhofer et al. 2010). However, CP targets muscles on a subject-specific base: independently on the grade of impairment, volume loss is heterogeneous (Fry et al. 2004; Handsfield et al. 2015) across muscles and individuals. Moreover, there is strong evidence in literature supporting the idea that observed volume deficits more likely result from reduced cross-sectional areas (reductions greater than 20%)(Elder et al. 2003) rather than shorter muscle lengths (Barrett and Lichtwark 2010). In addition, ultrasonography studies (Barber et al. 2009; Barber et al. 2011; Barber et al. 2012; Gao et al. 2011; Pitcher et al. 2015; Wren et al. 2010) showed that the whole muscle-tendon unit (MTU) is affected by CP. Children with CP have longer tendons in the triceps surae compared to their typically developing (TD) peers (Barber et al. 2012; Gao et al. 2011; Hösl et al. 2015; Wren et al. 2010). Nonetheless, while Barber and colleagues (2012) reported similar tendon stiffness in CP patients and healthy controls, others found a significant decrease in passive tendon stiffness in children with CP (Kruse et al. 2017).

### **Altered muscle composition**

At a tissue level, muscle biopsies revealed differences in muscle fibre type and size between spastic and healthy muscles (Foran et al. 2005). Moreover, the quality of the muscular tissue is poorer as confirmed via ultrasound (US) imaging (Pitcher et al. 2015). Fat infiltration (Johnson et al. 2009; Whitney et al. 2017) and tissue atrophy (Castle et al. 1979), due to disuse, are common in CP muscles and typically come along with an increased concentration of fibrous tissue, i.e. larger presence of collagen I and laminin, in the extracellular matrix connecting muscle fibres (Lieber et al. 2003; Lieber et al. 2004), which are associated with increased muscle stiffness. Also, Smith and colleagues (2011), using laser diffraction techniques, were able to measure the length of the sarcomeres, i.e. the fundamental force-producing unit in a muscle, which they found to be overstretched due to spasticity. This could possibly explain muscle stiffness and weakness, as sarcomeres would be operating far from the range of optimal lengths, which would elicit maximal force production in response to a small and fast contraction, as it is in healthy muscles (Shortland 2017).

## Bone and joint deformities

Bony structures may also be affected (Morrell et al. 2002). The aberrant muscle forces combined with muscle and joint stiffness may lead to abnormal joint contact force profiles, which could induce progressive deformation of bones due to bone remodelling. Common bony deformities include excessive tibial torsion, femoral anteversion and coxa valga (i.e. increased femoral neck-shaft angle). On top of these, children with CP present with a range of joint abnormalities, thought to primarily arise from muscle contractures and bone misalignment. Examples are hip subluxation, patella alta, knee flexion contracture, genu recurvatum (i.e. knee hyperextension), varus and valgus heel and equinus deformity (Figure 1, bottom left).

## Common gait kinematic deviations in CP

Secondary impairments associated with CP tend to worsen over time leading to a progressive loss of motor function (Bell et al. 2002; Graham and Selber 2003; Johnson et al. 1997), which progressively affects activities of daily living, such as gait. Typical gait deviations in CP, including prevalence, are: reduced knee flexion in swing (80%), increased knee (69%) and hip (65%) flexion during stance (i.e., crouch gait), internal foot progression angle (64%) and increased ankle plantarflexion (i.e., toe walking) or ankle dorsiflexion during stance (61%) (Winters 1987; Wren et al. 2005)(Figure 2). Despite these progressive gait impairments, a large percentage of children with CP are classified as independent walkers, although they have a higher risk of tripping and falling and subsequent injuries (Aiona and Sussman 2004).

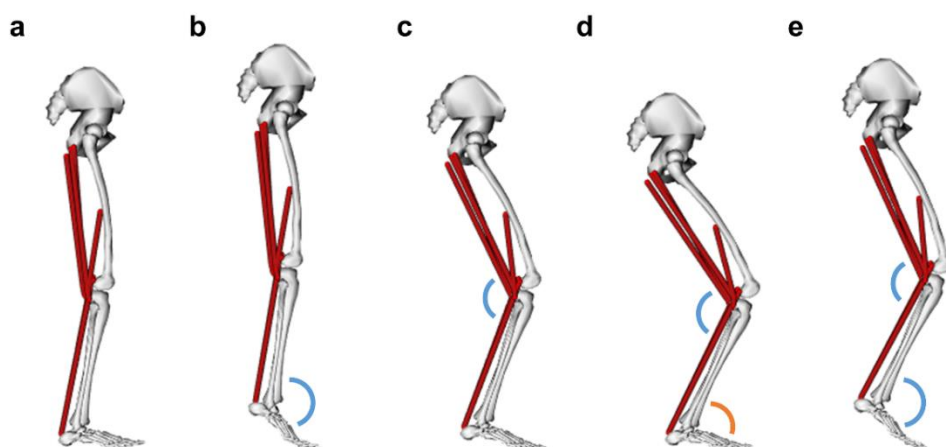


**Figure 2.** Normal gait (a) compared to the most common gait deviations observed in CP, i.e. true equinus (b), pseudo equinus (c), crouch gait (d) and jump knee gait (e). Figures a-e are representative of the mid-stance phase, when the foot is supposed to be in full contact with the ground.

## Treatments for CP

Several different procedures are currently available for the management and treatment of CP (Novak et al. 2013; Steinbok 2006). However, since normal neuro-muscular control cannot be restored, surgical and/or rehabilitative interventions are tailored to correct deformities, stabilise joints and balance muscle power (Kriger 2006; Pollock 1962; Sprague 1992; Theroux and DiCindio 2014) in order to improve joint and muscle function. Depending on the stage of maturation of the patients, the symptoms and the severity of the pathology, different surgical plans may be put in place (Damiano et al. 2009).

Conservative treatments (Verrotti et al. 2006) include physiotherapy, casting, orthoses and oral pharmacological treatments, and represent the first line of intervention due to their non-invasive nature. Physiotherapy aims to restore gross motor skills and functional mobility as well as to improve muscle strength. Casting of the lower limbs, generally performed from an early age (Papavasiliou 2009), is meant to alleviate hypertonia, spasticity and muscle contractures that are responsible for restrained movements and joint deformities such as the equinovarus foot deformity (Mortenson and Eng 2003). On the other hand, the use of orthoses facilitates correct bony and joint alignment helping to achieve more typical gait patterns.

To reduce the effects of spasticity, intramuscular injection of Botulinum NeuroToxin (BoNT) or intrathecal administration of Baclofen may also be prescribed to temporarily inhibit the neural response of specific muscles (Koman et al. 2003). Despite proven short term results, particularly when combined with other conservative treatments (Molenaers et al. 2010), repeated Botulinum injections may be associated with deficit in muscle size and morphology in children with CP (Barber et al. 2013; Gough 2009; Schroeder et al. 2009; Williams et al. 2013). Moreover, both techniques require a high level of precision to ensure correct delivery in order to minimise side effects.

Neurosurgical techniques, such as selective dorsal rhizotomy (SDR) are also extensively performed to reduce spasticity in children with CP. SDR involves the separation of dorsal and ventral roots of the alpha motor neurons at different levels of the spinal cord, in order to reduce the excitation of those motor neurons involved with the muscle groups identified as spastic (Steinbok 2007). Proven benefits have been reported in terms of joint kinematics, joint kinetics and more importantly muscle forces after SDR (Kainz et al. 2019).

When conservative or pharmacological treatments are no longer effective, targeted surgery (for single-joint involvement), or multi-level surgery is the preferred intervention and may include muscle-tendon lengthening (Rutz et al. 2011), split or full tendon transfer, guided growth, joint capsule release (Beals 2001), and/or osteotomy (Fasano et al. 1978; Gage 1990; Novak et al. 2013). While muscle and tendon surgeries are generally performed to restore joint range of motion (Abel et al. 1999; Thomason et al. 2011), osteotomies aim to correct for bone deformities and joint misalignment.

## **How to inform treatment planning**

Most of the above procedures have permanent effects and, in some cases (e.g. SDR), cannot be reversed. Therefore, an appropriate treatment planning is desirable. Unfortunately, the decision-making process is not straightforward (Rosenbaum and Stewart 2004). Clinical examinations, together with clinical history and static medical imaging are routinely employed to gather valuable information (O'Shea 2008). This information alone is not sufficient to understand dynamic function or the underlying mechanisms specific to CP (Desloovere et al. 2006; Steele et al. 2017). To this end, clinical motion analysis, commonly referred to as three-dimensional (3D) gait analysis, is used to assist in designing the appropriate treatment plan, which cannot be standardised to all patients (Chang et al. 2010; Cook et al. 2003; DeLuca 1991; DeLuca et al. 1997; Gage 1983; Lee et al. 1985; Sangeux and Armand 2015), who present with subject-specific impairments. In a gait laboratory, marker trajectories and ground reaction forces, together with EMG signals from selected muscles of interest, are collected and used to calculate joint kinematics and joint moments and to study muscle activity. As such, 3D gait analysis enables a comprehensive understanding of the (altered) external biomechanics. Nonetheless, despite proven benefits to patients' quality of life when gait analysis recommendations were followed (Wren et al. 2011), in a consistent number of cases (23%) some key gait parameters did not change or even worsened (Filho et al. 2008) after surgery; suggesting the need for additional tools to acquire useful information on the pathology prior to treatment.

Neuromusculoskeletal (NMSK) models may fill the missing gap, by complementing the assessment of CP with quantitative measures and estimates of the internal biomechanics, i.e. muscle forces and joint contact forces (Arnold and Delp 2005; Valente et al. 2014; van der Krogt et al. 2016), which may be used (1) to get a better understanding of the NMSK mechanisms behind the presenting pathology (Blemker et al. 2007), and (2) as an early bio-markers of joint overloading. Moreover, a NMSK model

can replicate personalised musculoskeletal anatomy (Fernandez et al. 2016), including accurate representation of bones, muscle attachments and muscle pathways, which may enable accurate analyses of muscle moment arms (MMA) and muscle tendon lengths (MTL) that can be used to inform surgery (e.g. bony realignment or tendon transfer). Virtual testing of prostheses and orthoses (Ackland et al. 2017) as well as surgeries (Chao et al. 2007) maybe also possible, potentially allowing for more optimal surgical planning, therefore improving procedural outcomes.

## **NMSK modelling**

A NMSK model is a mathematical and computational representation of the human body and its internal structures, e.g. muscles and bones, which are interconnected by joints. Since muscles are also modelled, their function can be investigated and the force they produce can be quantified. Moreover, NMSK models may be used for virtual, or *in silico*, surgery (Fregly et al. 2012b), i.e. testing of surgical scenarios on a computational model, thereby providing clinicians and surgeons with a tool to test the effect of different interventions virtually and outside the operating theatre. This is of practical importance in the treatment of CP (Arnold and Delp 2005), as many surgical treatments are not reversible, therefore suboptimal surgeries would cause long term detriment.

Biomechanical simulations employing NMSK models commonly use experimental data to move the model in space and to compute joint angles and joint moments (Figure 3). At each time frame, the relative angles between articulating bodies (e.g. femur and tibia) are determined either directly from the 3D trajectories of the markers associated with each body, i.e. direct kinematic approach, or by adjusting the model's joint angles to best match the modelled with the experimental markers positions, i.e. inverse kinematics approach (Kainz et al. 2016; Lu and O'Connor 1999). The joint kinematics are then combined with the ground reaction force data to compute joint moments, most commonly via inverse dynamics methods (Kadaba et al. 1990). A bottom-up approach is followed, with the external moments around the foot and ankle joint, on which the ground reaction forces act directly, being solved for first. Once joint angles are determined, MTU kinematics, i.e. MTLs and MMAs, can also be readily estimated, e.g. using OpenSim (Delp et al. 2007; Seth et al. 2018) or AnyBody (Damsgaard et al. 2006).

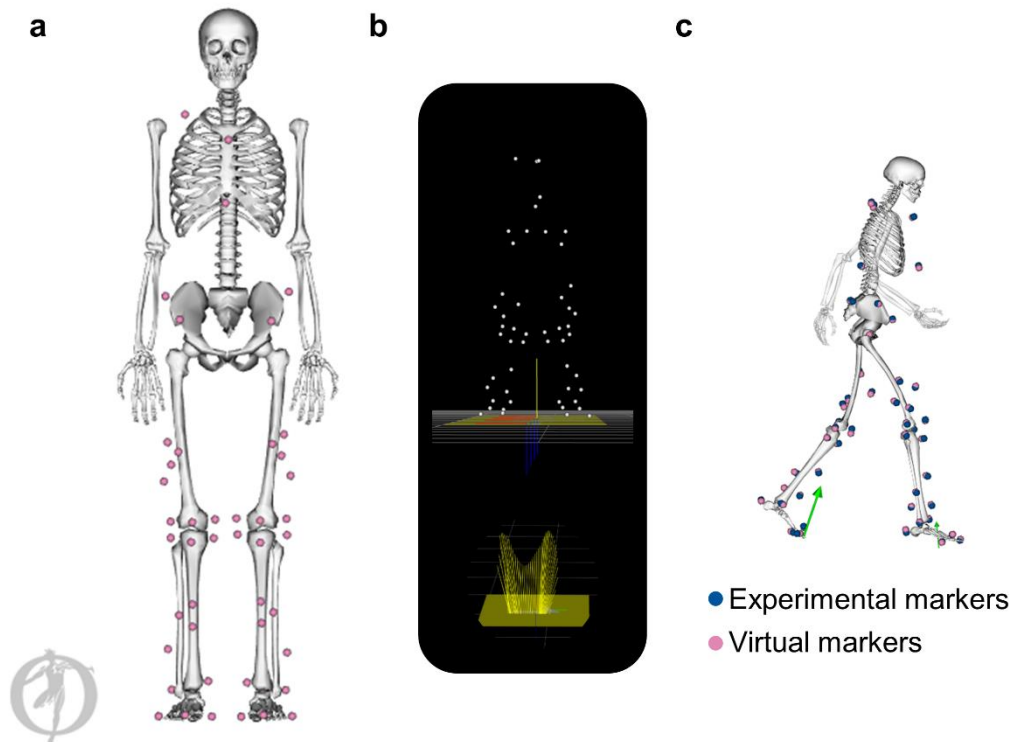


**Figure 3.** (a) Generic musculoskeletal anatomy (gait2392 OpenSim model), with virtual markers affixed on anatomical landmarks. (b) Experimental motion capture and ground reaction force data employed (1) to scale the generic anatomy to each participant's dimensions and (2) to compute joint angles and moments during dynamic simulations (c).

NMSK models employ different algorithms to compute muscle activations patterns, and subsequently muscle forces, used to perform a task. For example, static or dynamic optimisation estimate muscle activation based on *a priori* criteria and objective functions to minimise the overall muscle activity, muscle energy expenditure, or muscle forces, depending on the criteria chosen (Anderson and Pandy 2001a). Alternatively, EMG-informed approaches can be adopted (Lloyd and Besier 2003; Pizzolato et al. 2015; Sartori et al. 2012), which employ experimental EMG data to compute muscle activations. Of note, MTUs behaviour, and consequently muscle activation and force estimates, strongly depend on the parameters defining the muscle models, i.e. tendon slack length, optimal fibre length, pennation angle and muscle maximal isometric force values. Muscles are commonly represented as the parallel of a contractile element and an elastic element, in series with an elastic component representative of the tendon (Hill 1938); although more complex muscle models have also been developed (Dao and Tho 2018; Haeufle et al. 2014). Ultimately, the previously calculated muscle forces, MMAs and external joint moments can be combined to determine joint contact forces (JCFs) (Gerus et al. 2013; Saxby et al. 2016; Winby et al. 2009).

## **Limitations of commonly used NMSK models**

Despite their great potential, the generation and execution of NMSK models have a number of methodological challenges. For instance, commonly used musculoskeletal anatomies are linearly scaled from template anatomies, which are available on open-source, e.g. OpenSim (Delp et al. 2007), or purchased, e.g. AnyBody (Damsgaard et al. 2006), software packages for biomechanical analyses. Because OpenSim is open and free, it has widespread use in the international biomechanics field and so will be the focus of this review, although much of the discussion is relevant to other NMSK modelling packages. In OpenSim, the 3D scaling factors for each bone are typically computed as the ratio of two Euclidean distances, which are measured between selected pairs of virtual (i.e., on the model) and experimental (i.e., from MOCAP data) markers. Alternatively, the user can define arbitrary scaling factors, derived from medical images or anthropometrical measurements. Although the resulting scaled model well approximates the overall dimensions of each individual, the underlying anatomy (i.e., joint centres, joint axes, and muscle attachments and pathways) may be incorrect. Template models, such as the gait2392 model in OpenSim (Delp et al. 1990), are based on data from one or few healthy adult subjects which may not be representative of developing paediatric populations or children with musculoskeletal disorders. Thus, linear scaling methods may not well capture bone deformities, e.g. Perthes disease or deformity subsequent to a slipped capital femoral epiphysis, and bone (mis)alignment, e.g. tibia torsion or increased femoral neck-shaft angle, which are not present on the generic geometries. Moreover, erroneous marker positioning on the subject in the gait laboratory may further lead to scaling inaccuracies (Bosmans et al. 2014), e.g. abnormal pelvis width (Figure 4). These may affect joint pose estimation during scaling as hip, knee and ankle joint centres could be inappropriately located, leading to incorrect joint angles and joint moments calculations (Kainz et al. 2017a; Reinbolt et al. 2007).

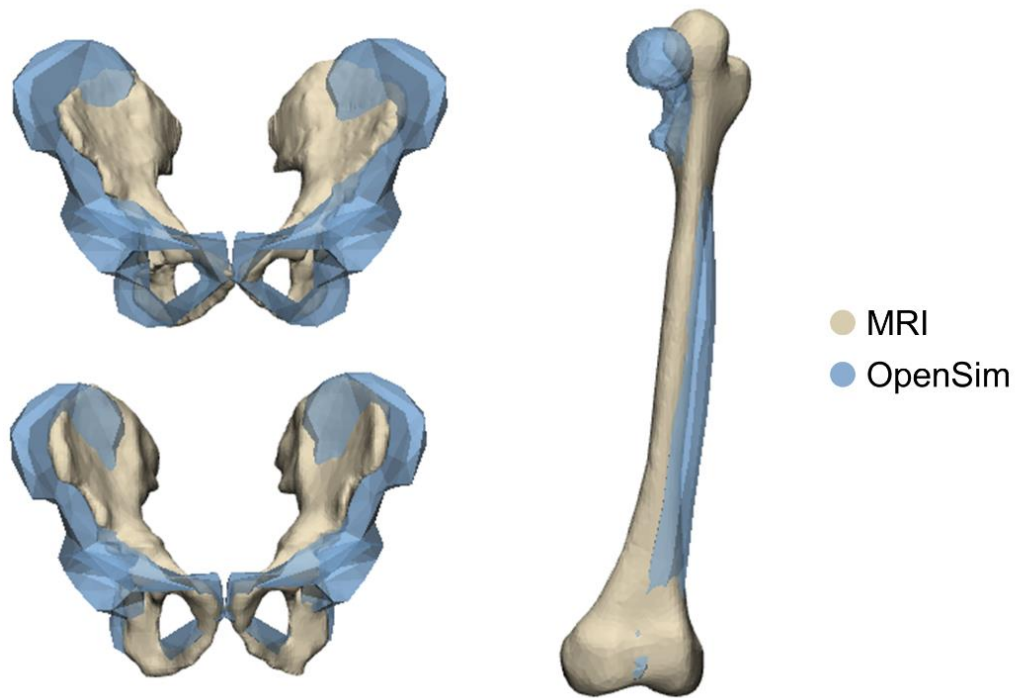


**Figure 4.** Linearly scaled generic OpenSim geometries (light blue) overlaid to the corresponding MRI segmentations (white) of the pelvis bone (left) and femur (right). The apparent difference in shape, size and curvature between scaled generic and real geometries, which per se does not affect simulations (i.e., bone images are purely for visualisation), may be associated (1) with inaccurate definitions of joint centres, (2) with erroneous joint angle calculations and (3) with inappropriate location of muscle attachments, which can all affect a model’s estimates.

Linear scaling of NMSK models may be inappropriate way to model MTU kinematics. In NMSK models, muscles are commonly represented as lines connecting two fixed points, i.e. origin and insertion, located on specific bony landmarks, representative of anatomical muscle attachments. Additional via points or wrapping surfaces are inserted between origin and insertions to constrain MTU pathways and avoid non-physiological behaviours, e.g. muscle penetration into bones which may occur at specific joint angles. During the scaling process, muscle path points are scaled along with the bone to which they are attached. However, while the relative position of muscle attachments on bones is preserved, the intermediate points/wrapping surfaces of bi-articular muscle pathways may be inappropriately located as all bones are individually scaled. Therefore, muscle length and moment arms curves may present discontinuities, which introduce errors in muscle force estimates. Moreover, the original location of

muscle path points on the generic models (e.g., gait2392) were either derived from small cadaveric datasets and then manually selected and positioned in the model (Delp et al. 2007; Delp et al. 1990). As such, these path points may not be anatomically correct (Arnold et al. 2001; Duda et al. 1996), affecting muscle moment arms calculations (Scheys et al. 2008a; Wesseling et al. 2019).

It is incorrect to assume that the internal MTU parameters, i.e. optimal fibre length (OFL) and tendon slack length (TSL), scale linearly with bone lengths (Ward et al. 2005) or MTU length (Ward et al. 2007). Consequently, as muscles are commonly modelled as Hill-type actuators, their estimated muscle function, which depends on both TSLs and OFLs (Arnold et al. 2013; Baxter et al. 2019; Heine et al. 2003; Winby et al. 2008), may be compromised (Garner and Pandy 2003). Inappropriate OFL and TSL values may hinder computation of physiological MTU behaviour, i.e. which abides/follows to theoretical force-length and force-velocity curves.

Further to the abovementioned inappropriate anatomical scaling methods, commonly used NMSK models are limited by the methods employed to solve for the muscle redundancy problem, i.e. to determine the unique set of muscle activation patterns that produce specific (experimental) joint moments. Since several combinations of muscle activations may generate a certain joint moment, the mechanical problem has multiple solutions. Therefore, optimisation functions based on *a priori* criteria are implemented to reduce the solution space to one solution, ideally representative of the real set of muscle activations. Among all, static optimisation that minimises the sum of squared muscle activations to produce the measured joint moments, is the most widely used optimisation function. The underlying assumption of static optimisation is that the human body organises muscles activation to minimise muscle excitation, forces or energy expenditure depending on the chosen criteria (Crowninshield and Brand 1981). These assumptions are likely incorrect for healthy children, and particularly for children with neuromuscular disorders, such as CP, whose motor control is affected and who often present with muscle spasticity and/or heightened co-contractions. As a result, muscle excitations and activations generated via static optimisation do not accurately represent experimental EMG data in in timing (i.e. on/offset), or amplitude (Hoang et al. 2019; Kainz et al. 2019).

Although each of the above errors appear to have a small effect by itself, one should realise that taken altogether these inaccuracies may produce large effects on the final output of a model, particularly on muscle force estimates (Valente et al. 2014). Muscle dynamics and MTU kinematics, both affecting individual muscle forces and

contributions, respectively depend on MTU parameters, and muscle geometries and pathways that may be erroneously identified on linearly scaled generic models. Contrarily, JCF estimates per se appear to be less sensitive to such uncertainty (Valente et al. 2014). Nonetheless, as muscle forces and JCFs are related one another, errors in muscle force estimates are likely transferred to JCF estimates. This cannot be considered acceptable if the outcome measures are to be used to inform surgeries (e.g., tendon transfer or osteotomies), which are often irreversible.

Fortunately, musculoskeletal anatomy in NMSK models can be personalised by incorporating medical imaging. Furthermore, experimental EMG data can be used to reduce the solution space and solve for the muscle redundancy problem, possibly enabling physiologically more plausible internal biomechanics. Finally, alternative methods, e.g. dynamic optimisation (Anderson and Pandy 2001a) or EMG-informed approaches (Falisse et al. 2017; Lloyd and Besier 2003; Pizzolato et al. 2015; Sartori et al. 2014) have been proposed to overcome the inherent limitations of (unconstrained) static optimisation methods.

It is accepted within the biomechanics research community that NMSK model personalisation is important (Bahl et al. 2019; Bosmans et al. 2015; Demers et al. 2014; Gerus et al. 2013; Konrath et al. 2016; Lenaerts et al. 2008; Lerner et al. 2014; Marra et al. 2015; Serrancolí et al. 2016; Winby et al. 2009). Unfortunately, the acquisition and segmentation of medical images is time consuming and costly, and specialised skillsets and software are required to create image-based subject-specific models. Therefore, at present, the feasibility of incorporating personalised NMSK modelling into clinical practice to inform clinical decision making for CP is low. In the next section, currently available methods to personalise NMSK models are detailed to provide an overview of the current state-of-the-art, and highlight potential future research pathways.

## **Personalisation of NMSK models**

As mentioned above, the personalisation of a NMSK model may extend to many features (Hicks et al. 2015; Sartori et al. 2017a). These include musculoskeletal anatomy, internal and external MTU parameters and muscle activation patterns, which can be personalised using experimental data (e.g. EMG, imaging or MOCAP data) and literature data from *in-vivo* and *in-vitro* studies or previously developed models.

## **Bone geometries**

Subject-specific bones may be generated via manual or automatic segmentation of medical images (e.g. MRIs or CT) (da Luz et al. 2017; Modenese et al. 2018; Scheys et al. 2008b; Wesseling et al. 2019). Alternatively, statistical shape modelling and morphing techniques may be employed to reconstruct anatomically accurate bony geometries from sparse imaging datasets (Bahl et al. 2019; Blemker et al. 2007; Nolte et al. 2016; Oberhofer et al. 2019; Suwarganda et al. 2019; Zhang et al. 2014a) or MOCAP data (Oberhofer et al. 2019), reducing time and costs associated with the acquisition and segmentation of medical images. Personalised geometries could then replace scaled generic geometries, resulting in a better representation of each individual's skeletal anatomy, as abnormal morphologies and possible bone misalignments would be modelled. Associated benefits would go beyond mere visual aspects. Gait simulations are affected by inaccurate joint geometries (Lerner et al. 2014), as the location of both joint centres (Kainz et al. 2017a) and joint contact points could be erroneous in generic models. Moreover, subject-specific inertial parameters, i.e. centre of mass and moment of inertia, can be extracted from medical images. Knowing the density of each tissue, e.g. muscles and bones, and the overall volume of a body segment, e.g. shank, one can derive mass values and subsequently estimate subject-specific inertial properties, which were shown to vary quite considerably from scaled generic values (Reinbolt et al. 2007). However, implementing subject-specific inertial parameters may not have significant effects on joint moments estimates (Reinbolt et al. 2007).

## **Joint definitions and kinematics**

Medical imaging data, particularly MRIs, can further be employed to personalise joints, and not only from a purely anatomical view point. For instance, bony landmarks identified on segmented geometries are used to define local body and joint coordinate frames, which are, in turn, employed to accurately determine joint position and orientation in space. Furthermore, high-fidelity MRI scans enable the identification and segmentation of the other anatomical structures, e.g. ligaments and cartilages, that together with bones govern joint kinematics. This additional information can be used to accurately estimate joint kinematics, which in current scaled-generic NMSK models is often oversimplified. Abduction/adduction and internal/external rotations and translations in space, i.e. secondary kinematics, are typically neglected or expressed as a function of the primary kinematics, i.e. flexion/extension, which can be readily and accurately determined from

MOCAP data. Although popular, generic splines, which are derived from cadaveric data, do not well represent real *in-vivo* kinematics and, more importantly, may lead to bone-to-bone penetration when subject-specific bones replace (scaled) generic geometries. Alternatively, medical images may be employed to scale generic splines (Arnold et al. 2000) or to define personalised joint mechanisms of different complexity (da Luz et al. 2017; Dzialo et al. 2018; Franci et al. 2009; Gasparutto et al. 2012; Kainz et al. 2017a; Modenese et al. 2018; Sancisi and Parenti-Castelli 2011; Sancisi et al. 2011; Valente et al. 2015). However, more complex joint mechanisms require (1) the identification of several input parameters that have large effects on joint kinematic solutions, and (2) a considerable computational effort to solve the mechanical problem. Nonetheless, implementing subject-specific joints kinematics is likely to affect MTU kinematics, i.e. muscle lengths and moment arms (Navacchia et al. 2017).

## **Muscle morphology and pathways**

As with bones and joint structures, muscle volumes can also be manually or semi-automatically segmented on MRI's (Figure 5a and d) (Handsfield et al. 2014; Oberhofer et al. 2010), although this can be a time-consuming process. Unlike bones, the separation of individual muscles may be difficult as muscle boundaries may not be easily identified on medical images due to poor contrast between neighbouring tissues. This is particularly problematic in paediatric data where the musculoskeletal system may not be not fully developed. To facilitate the segmentation of muscles, atlas-based approaches have been proposed (Pellikaan et al. 2014; Scheys et al. 2009). However, these rely on the previous definition of population-specific atlases and their results may be sensitive to the parameters of the selected MRI sequences.

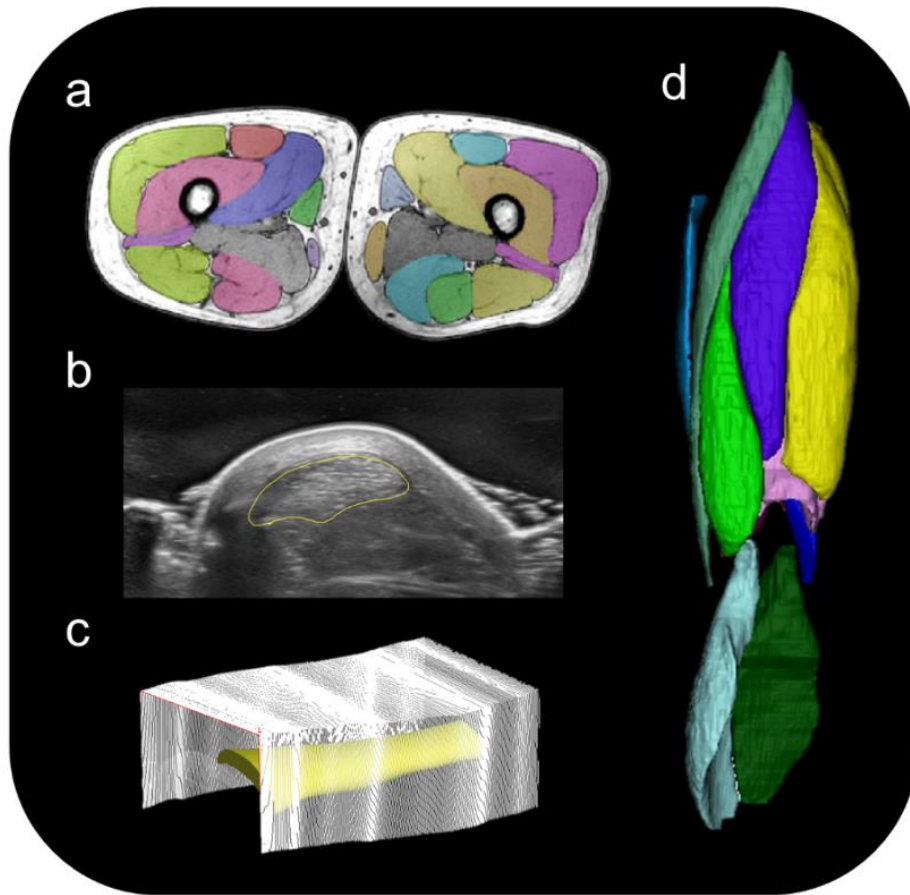


**Figure 5.** Medical imaging techniques employed to extract subject-specific information on muscles and tendons, required to personalise neuromusculoskeletal models. (a) Axial MRI image with masks identifying each individual muscle, (b) bi-planar US image of a tendon (yellow contour), (c) 3D free-hand US reconstruction of a tendon, (d) 3D muscle volumes reconstructed from MRI images.

Alternatively, muscle and tendons can be reconstructed from bi-planar US images (Figure 5b) or employing 3D free-hand US techniques (Figure 5c)(Nuri et al. 2017; Nuri et al. 2018; Obst et al. 2014; Schless et al. 2018). Independently on the imaging modality, segmented muscle morphologies provide subject-specific information on muscle size, i.e. volume, length and cross-sectional areas, and shape, which can be used to personalise both the force producing abilities and the pathways of all modelled muscles, ultimately improving MTU kinematics (Lenaerts et al. 2008; Scheys et al. 2011b).

When medical imaging data are not available, muscle volumes may be estimated from regression equations (Handsfield et al. 2014; Noble et al. 2017). However, one should be aware that disorder-specific muscle deficits, which in the case of CP may also be heterogeneous (Handsfield et al. 2015), would not be captured, as the proposed regression equations were derived from healthy populations. Without prior knowledge on

muscle volumes, the maximal isometric force of each MTU may be scaled from the generic template values based on the mass of each subject (van der Krogt et al. 2016), MTU lengths ratios and/or dynamometric measurements (Kainz et al. 2018).

Personalised muscle pathways need to be implemented, i.e. muscle origins, insertions and intermediate pathways. Atlas-based approaches were recently adopted to morph generic muscle path points from various database (i.e., one subject's data, gait2392 or SOMSO anatomical model) to subject-specific bone geometries which were previously segmented on MRI's (Modenese et al. 2018) or reconstructed via statistical shape modelling techniques (Oberhofer et al. 2019), e.g. using the Musculoskeletal atlas Project (MAP) Client (Zhang et al. 2014b). To further improve MTU kinematics, intermediate path points were either manually adjusted (Modenese et al. 2018) based on literature data or located using a weighted vector average method (Carleton 2018), which accounted for bone shape and size changes while preserving the original relative position with respects to bones. These resulted in non-physiological muscle behaviour (Killen 2019). To overcome the above limitations, Killen and colleagues (2019) developed an automated framework, within the MAP Client, to facilitate the personalisation of MTU pathways. In this, all via points were replaced by wrapping surfaces, initially fit to specific anatomical regions, and subsequently optimised to ensure continuous and physiological MTU kinematics using a Multiple-Objective Particle Swarm Optimisation algorithm (MOPSO).

## **Internal MTU parameters**

Other internal MTU parameters, i.e. OFL and TSL, cannot be easily measured *in-vivo* (Herzog et al. 1991). Nonetheless, the generic values, after being scaled, can be tuned (Manal and Buchanan 2004; Modenese et al. 2016; Winby et al. 2008) and/or calibrated within physiological ranges using other measured data (Hoang et al. 2019; Hoang et al. 2018; Meyer et al. 2017; Pizzolato et al. 2015). Tuning consists in optimising the scaled generic TSL and OFL values to enforce a physiological MTU behaviour throughout the full range of motion. At each joint angle, while preserving the overall MTU length, OFL and TSL values are minimally adjusted to ensure that the force-length and force-velocity curves implemented in the template model and defining muscle function are respected (Modenese et al. 2016). Different approaches can be used to this extent (Winby et al. 2008). On the other hand, calibration employs experimental joint moments and EMG data to further adjust OFL and TSL values, along with other MTU parameters, so that these fall within known physiological ranges (Falisse et al. 2017; Hoang et al. 2018; Meyer et

al. 2017; Pizzolato et al. 2015; Sartori et al. 2012; Shao et al. 2009). Models employing calibrated parameters have shown to estimate (1) knee joint contact forces showing excellent agreement with experimental measures from instrumented implants (Gerus et al. 2013), and (2) more physiologically plausible hip joint contact forces compared to uncalibrated models (Hoang et al. 2018). Previous measured data, e.g. experimental JCFs from instrumented implants, can also be used for calibration purposes (Serrancolí et al. 2016), further constraining the parameters of a model. Alternative approaches to optimise MTU parameters include stochastic methods, such as Monte Carlo simulations (Reed et al. 2015).

## **Neural solutions**

While the above steps enable to create the digital replica of a person, the concept of personalisation in NMSK modelling extends beyond the definition of anatomically correct representations of the musculoskeletal system. As muscle forces and JCFs are common end-point variables of biomechanical simulations, the neural solutions employed to resolve the muscle redundancy problem play a major role. In general, neural solutions have been obtained using static or dynamic optimisation, statistical, or EMG-driven, approaches, which all have certain limitations.

Several studies demonstrated the inability of unconstrained static optimisation to reproduce muscle co-contraction and atypical neuromuscular strategies (Kautz et al. 2000; Lloyd and Besier 2003). Moreover, commonly used static optimisation approaches assume that the tendon is rigid, neglecting muscle-dynamics. To address the criticisms to static optimisation in general, a forward dynamics approach was introduced, i.e. dynamic optimisation (Anderson and Pandy 2001a; Prilutsky and Zatsiorsky 2002). In this, the objective function, which minimised the metabolic energy expenditure to perform a task, is solved once for the whole trial, and muscles are not allowed to turn on and off instantaneously. Additionally, first order derivatives are used to describe the muscle excitation-to-activation relationship, providing a more physiological characterisation of muscle properties. Computed muscle activations for muscles with compliant tendons (e.g. plantarflexors) may be significantly affected (De Groote et al. 2016). However, solving a dynamic optimisation problem is computationally expensive and time consuming. Moreover, for walking, dynamic optimisation produced similar results to static optimisation (Anderson and Pandy 2001b), and was still unable to well predict individual muscle activation patterns.

A completely different statistically-based approach to determine muscle activity was recently proposed by Martelli and colleagues (2015). They employed Bayesian statistics and Markov chain Monte Carlo methods to reconstruct and explore the spectrum of plausible muscle synergies, therefore eliminating any *a priori* assumptions on the sensorimotor behaviour. However, this was still limited to not knowing the final neural solution used by the individual.

Alternatively, EMG-driven approaches, which use experimental EMG data to determine muscle excitations inputs, can be employed. Despite their potential and proven efficacy in estimating measured (knee) JCFs (Fregly et al. 2012a), EMG-driven methods were initially limited by the number of experimental EMG data that could be collected, and therefore modelled. To overcome these problems, Sartori and colleagues (2012) proposed a method to map the excitation of additional MTUs from available experimental data, based on the assumption that muscles with common innervation have similar excitations patterns. Others used muscle synergies to reconstruct missing EMG signals (Bianco et al. 2017; Meyer et al. 2016). However, EMG signals can exhibit noise and cross talk that needs to be addressed.

More recently, new EMG-informed methods have been developed to further expand the number of modelled MTUs while accounting for EMG errors, thereby generating more comprehensive NMSK models. To this end, two additional neural solutions were implemented in the Calibrated EMG-informed Neuromusculoskeletal Modelling Software (CEINMS) (Pizzolato et al. 2015; Sartori et al. 2012): the Hybrid and EMG-assisted modes. These combined both experimental EMG data and static optimisation methods to reconstruct the full set of MTUs excitations. However, while in the Hybrid mode static optimisation is only used to synthesise the excitations of all MTUs without experimental data, the EMG-assisted solution additionally employs static optimisation to minimally adjust the EMG-driven excitations. The resulting NMSK models were able to better track experimental joint moments along with EMG data (Hoang et al. 2019; Hoang et al. 2018; Kainz et al. 2019; Pizzolato et al. 2015; Veerkamp et al. 2019), and consequently more closely approximated measured (knee) JCFs compared to models employing other neural solutions (Hoang et al. 2019; Hoang et al. 2018; Pizzolato et al. 2015).

It appears clear that personalisation may have a key role in the development of NMSK models able to capture disorder-specific abnormalities. Such models will: possibly lead to a better understanding of neuromuscular pathologies, such as CP, which present with subject-specific features. However, the implementation of CP-related

abnormalities into NMSK models may not be straightforward. The next section will provide a succinct summary of the state of art of NMSK model personalisation with regards to CP and paediatric populations, to highlight what is commonly done, what is missing and current issues.

## **Personalisation for CP**

Over the last decades, impelled by the need for a full understanding of the biomechanical implications of CP, considerable steps forward in the development of personalised NMSK models of (TD paediatric populations and) children with CP have been made.

### **Bony deformities**

Several studies focussed on ways to incorporate bone deformities into NMSK models. In these, lower limb bony geometries were personalised using two main approaches: (1) deforming generic geometries based on clinical observations and measurements or previously reported findings (Hicks et al. 2007; Schwartz and Lakin 2003) and (2) developing personalised bony geometries via segmentation of medical images, i.e. CT scans, MRIs, US and EOS (Figure 6a)(Arnold et al. 2001; Bosmans et al. 2016; Lenaerts et al. 2008; Modenese et al. 2018; Oberhofer et al. 2019; Passmore et al. 2018; Sangeux et al. 2009; Scheys et al. 2008b). While deforming generic geometries is relatively easy and less time-consuming than manually segmenting bones on medical images, the latter provide a more accurate representation of each subject's anatomy (Figure 6a). However, the implementation of subject-specific image-based geometries into NMSK models is not trivial and requires niche and specialist skills and software. Particularly, muscle path points are not automatically included in the image-based models. In previous work, muscle attachments and via-points were either (1) derived from previous models (Modenese et al. 2018), i.e. OpenSim gait2392, and morphed via non-rigid registrations to subject-specific bones or (2) manually or semi-automatically identified on MRIs (Scheys et al. 2006). Other than laborious, this process is likely to result in in-bone penetrations and discontinuous MTU kinematics (Killen 2019).

To reduce time consumption, mesh fitting techniques (Figure 6b) were recently used to morph generic NMSK models to subject-specific medical imaging data solely based on anatomical landmarks (Oberhofer et al. 2019), therefore removing the need for manual segmentation. Alternatively, semi-automated workflows developed in the MAP Client (Zhang et al. 2014b) may be employed (1) to generate accurate paediatric lower limb bones via the combination of statistical shape modelling (Figure 6c) and mesh fitting

techniques and (2) to customise a generic gait2392 OpenSim model with subject-specific bone geometries and personalised MTU pathways (Carleton 2018; Killen 2019). However, to date, no such methods have been used to reconstruct paediatric lower limb models.

Modelling deformities has several implications on the results of biomechanical simulations. Although joint kinematics and kinetics are only slightly affected (Gerus et al. 2013; Lenaerts et al. 2008; Scheys et al. 2011a), MTU kinematics is significantly altered (Bosmans et al. 2016; Correa et al. 2011; Hicks et al. 2007; Scheys et al. 2011b; Wesseling et al. 2019). Secondary to the relocation of muscle path points due to the presence of deformities, MALs and MTLs calculated on generic models differ from those calculated on subject specific NMSK models. However, while including femoral deformities severely affected hip muscles MALs (Scheys et al. 2011b; Scheys et al. 2008a; Wesseling et al. 2019), modelling excessive tibial torsion did not impact ankle muscles kinematics to the same extent (Hicks et al. 2007). Moreover, since the relative contribution of muscle forces is also altered (Gerus et al. 2013; Wesseling et al. 2019), generic and subject-specific models produce different estimates of JCFs both at the hip (Bosmans et al. 2014; Wesseling et al. 2019) and the knee (Gerus et al. 2013) joints.

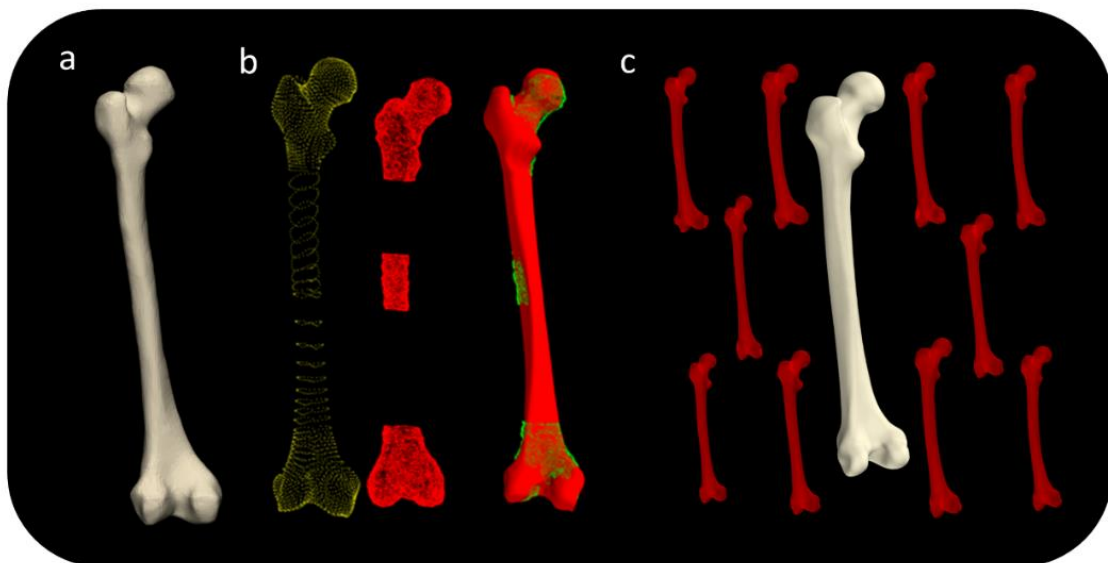


**Figure 6.** Methods to personalise bones. (a) Manual segmentation of medical images, (b) mesh fitting techniques and (c) statistical shape modelling.

## Altered muscle properties

In addition to bone deformities, one can model CP-induced muscle alterations, i.e. muscle weakness, spasticity and morphological changes. Muscle weakness, common in CP, can be modelled by reducing the maximal isometric force values, which define the force producing ability of muscles. Several scaling methods have been suggested in literature. In previous work, pre-determined percent reductions based on literature findings were imposed (Fox et al. 2018; Ong et al. 2019; Steele et al. 2012). However, despite providing insights on the effects of muscle weakness on gait parameters, such reductions were likely not representative of each individual case, defying the purpose of personalisation. Others scaled the maximal isometric force values based (1) on children's mass (van der Krogt et al. 2016), (2) on the ratios of both MTU lengths and mass from scaled and generic models (Correa et al. 2011) or (3) on measurements from dynamometric tests (Kainz et al. 2018). Alternatively, the maximal isometric force values can be recalculated using muscle volumes derived from regression equations (Handsfield et al. 2014; Noble et al. 2017) or segmented on medical images, i.e. MRIs (Handsfield et al. 2014; Konrath et al. 2016), in combination with muscle specific tensions from literature (O'Brien et al. 2010; Weijs and Hillen 1985). However, it must be noted that on paediatric data muscle segmentation is very time-consuming. In addition, the methods employed to scale maximal isometric force values seem to have little effects on the resulting muscle force and JCFs estimates (Modenese et al. 2018).

Personalised OFL and TSL values can be estimated via complex mathematical approaches (Gerus et al. 2015; Li et al. 2009; Manal and Buchanan 2003; Manal and Buchanan 2004; Winby et al. 2008). Unfortunately, these rely on experimental imaging data that is rarely collected *in-vivo* in clinical settings. Therefore, internal MTU parameters are often simply linearly scaled from generic template models and subsequently tuned via a morphometric scaling (Hainisch et al. 2012; Modenese et al. 2016; Winby et al. 2008) to ensure physiological muscle behaviour. CP-induced alterations, which significantly affect muscle function, are either disregarded or implemented by adjusting the scaled and optimised parameters to reflect literature findings. For example, TSLs may be increased to model tendon lengthening shown to occur in CP muscles (Fox et al. 2018). Once again, these scaling factors are typically pre-determined and not based on subject-specific information. To better approximate OFLs and TSLs, generic values may be additionally calibrated using EMG-informed approaches (Hoang et al. 2018; Pizzolato et al. 2015; Sartori et al. 2012). That is, the

scaled and optimised internal muscle parameters are adjusted and constrained between known physiological ranges to improve models' ability to track experimental data, e.g. measured EMG signals or external forces (Falisse et al. 2017; Hoang et al. 2019; Hoang et al. 2018; Pizzolato et al. 2015; Serrancolí et al. 2016).

## **Abnormal muscle activity**

Although clear that muscle activity in CP patients is altered, i.e. characterised by abnormal muscle activations and high levels of co-contraction, little has been done to account for this in the simulations. In NMSK modelling muscle forces are commonly determined using static optimisation (Steele et al. 2012; van der Krogt et al. 2012; Wesseling et al. 2019), which minimises the squared sum of muscle activations to perform a movement (Anderson and Pandy 2001b). As result, co-contractions are discouraged, and similar neural solutions are produced for both healthy and pathological populations. Atypical muscle control may not be captured (Hoang et al. 2018; Lloyd and Besier 2003). However, in the last decade, EMG-informed approaches, which directly employ experimental EMG data to solve for the muscle redundancy problem, gained popularity. Recent work from Kainz and colleagues (2019) showed that EMG-informed NMSK models compared to models using static optimisation better reproduced experimental data. Other studies (Veerkamp et al. 2019) also reported muscle forces from both approaches, clearly showing differences between healthy and pathological populations when EMG-informed models were used .

## **Spasticity and contractures**

A spasticity model was recently proposed (Falisse et al. 2018) to better understand the effects of spasticity on motor impairments due to CP. In this, the (passive) sensory response due to exaggerated stretch reflexes was determined using three different approaches, respectively based on: (1) muscle fibre length and velocity, (2) muscle fibre length, velocity and acceleration or (3) muscle forces, which were estimated via EMG-driven forward simulations. All parameters determining the sensory response were then optimised to reduce the EMG tracking error during controlled passive movements. The force-related spasticity model was able to explain the abnormal muscle activity observed in CP during gait tasks. As such, it may be used in future to simulate and to study pathological gait via forward simulations.

Forward simulations were recently employed to investigate the effect of muscle contractures in CP (Ong et al. 2019). In this case, plantarflexor weakness and contracture

in the models were respectively induced by reducing the maximal isometric force and the optimal fibre lengths values of the soleus and/or gastrocnemii muscles. When the properties of the soleus muscle were altered, the models tended to walk in a more crouched position, possibly linking crouch gait to equinus walk. However, the study had a few limitations. For example, the objective functions implemented to generate muscle activations did not account for altered neural inputs, which are common in CP. Nonetheless, this study highlighted the tremendous potential of forward simulations, which in the future may enable a better understanding of pathological conditions.

In conclusion, over the last decades tremendous work has been done to incorporate subject specific features of CP in NMSK models. Researchers extensively investigated the impact of different levels of personalisation on the endpoint variables for both TD and CP paediatric populations. However, there still remain some gaps in literature. Despite the abundance of experimental imaging data and literature findings, internal MTU parameters are still difficult to personalise. Moreover, to date only one work (Pitto et al., 2019) proposed ways to comprehensively incorporate different personalised features in a single NMSK, which however was not employed to estimate joint contact forces and used muscle synergies to reconstruct muscle activations. Therefore, it is still not clear how sensitive the endpoint variables (i.e., particularly JCF estimates) are to each component of personalisation. Finally, workflows to generate subject-specific NMSK models, which would facilitate their implementation and use in research and clinical settings, are yet to be developed.

# CHAPTER 3

---

## General Methods

This chapter describes all data collection, data processing, and neuromusculoskeletal modelling procedures utilised in this thesis. The experimental data, which included motion capture (MOCAP), electromyography (EMG) and magnetic resonance imaging (MRI) data, were collected in two different facilities on a total of seventeen participants. Eight participants recruited for the first data collection underwent gait analysis at Griffith University (GU) and MRI acquisition at the QScan Radiology Clinic (Southport, QLD, Australia). The remaining nine participants underwent gait assessment at the Queensland Children Motion Analysis Service (QCMAS) and MRI examination at the Queensland Children's Hospital (QCH) in the Department of Medical Imaging and Nuclear Medicine (Brisbane, QLD, Australia). Data collection and processing protocols (see section below) were consistent across facilities. All data were processed to extract information on each participant's musculoskeletal anatomy, gait characteristics, and muscle activity and were later combined to develop and inform paediatric neuromusculoskeletal models with increasing levels of personalisation. Subsequently, biomechanical simulations were run to estimate muscle forces and knee joint contact forces (JCFs) (Figure 7). Finally, statistical analyses were used to determine the physiological accuracy of each model, i.e., how well the model could track experimental data, and to compare estimates of internal biomechanics quantities across models.

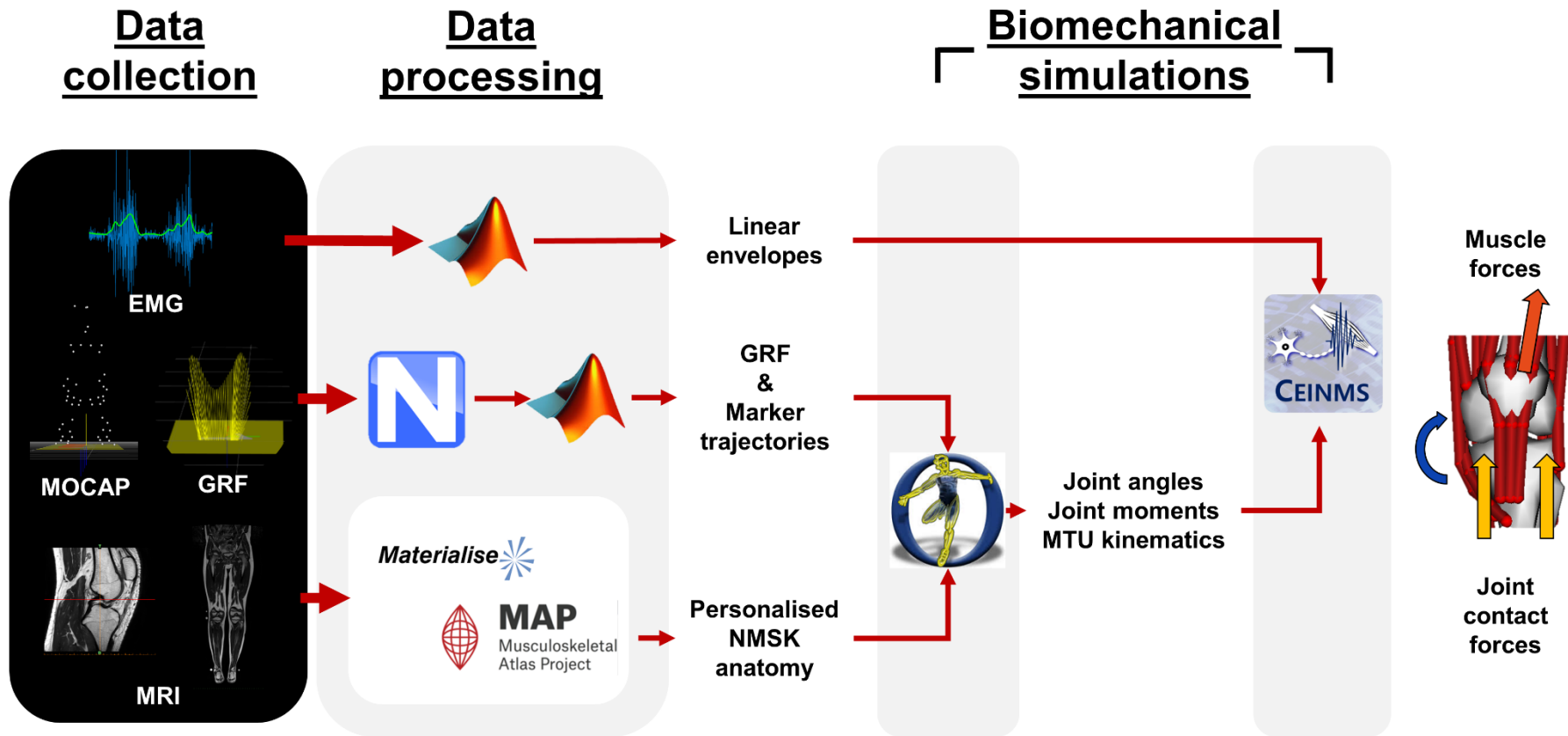


**Figure 7.** Workflow employed to estimate muscle and joint contact forces. Experimental motion capture (MOCAP), ground reaction force (GRF), electromyographic (EMG) and magnetic resonance imaging (MRI) data were used to inform the development and personalisation, tuning and calibration of musculoskeletal anatomies and models for biomechanical simulations.

# Data collection

## Participants

Seventeen participants were recruited as part of this thesis: eight children with spastic cerebral palsy (CP), who were independent walkers and graded level I-II according to the Gross Motor Function Classification System (GMFCS)(Palisano et al. 1997), and nine typically developing (TD) children (Table 1). Participants were matched according to overall group characteristics (i.e. age, height and weight). The dataset comprised two sets of identical twins, two brothers (aged 13) and two sisters (aged 6), where one sibling had spastic CP and the other was TD.

**Table 1.** Demographics (mean and standard deviation) of participants. Individual details are provided for the children enrolled in the two experimental studies, in Table 17 and Table 21.

|                                    | <b>CP</b>     | <b>TD</b>     |
|------------------------------------|---------------|---------------|
|                                    | <b>(n=8)</b>  | <b>(n=9)</b>  |
| <b>Sex</b><br><b>(male/female)</b> | 6/2           | 4/5           |
| <b>Age (years)</b>                 | 10.75 (3.39)  | 10.59 (2.90)  |
| <b>Mass [kg]</b>                   | 35.70 (13.60) | 37.24 (14.97) |
| <b>Height [m]</b>                  | 1.428 (0.225) | 1.424 (0.190) |

Inclusion criteria for the CP group were (1) age between five and 17 years old, (2) diagnosis of CP affecting any of the lower limbs and (3) ability to walk independently (GMFCS I-II). Patients were excluded if in the six months prior to the test they had received any botulinum toxin injections, bony surgeries and/or muscle-tendon surgeries (Fasano et al. 1978; Gage 1990; Gage 2009; Novak et al. 2013). Healthy age-matched control participants, with no medical history of neuromusculoskeletal disorders who were free from lower limb injury in the six months before data collection, were recruited from the local community. Prior to MRI each participants' guardians were provided with a safety questionnaire to identify and exclude participants unable to undergo the MRI assessment (e.g., claustrophobic or with metallic implants). The study was approved by the Children's Health Queensland Hospital and Health Services human research ethics committee (HREC/13/QRCH/197) and the GU human research ethics committee (AHS/42/14/HREC & AHS/38/15/HREC) and written informed consent from the children's guardians was provided.

For the second study (Chapter 5), where only data from TD paediatric populations were used, the combined TD dataset (GU + QCMAS) was further expanded to include 10 additional TD children enrolled in previous research studies (Table 2) ('Young people with old knees'. Ethics: PES/36/10/HREC (GU), 0932864.3 (University of Melbourne)).

**Table 2.** Demographics of participant enrolled in study 2.

|                             | <b>TD<sub>GU+QCMAS</sub></b> | <b>TD<sub>OtherStudies</sub></b> |
|-----------------------------|------------------------------|----------------------------------|
|                             | <b>(n=9)</b>                 | <b>(n=10)</b>                    |
| <b>Sex</b><br>(male/female) | 4/5                          | 5/5                              |
| <b>Age (years)</b>          | 10.59 (2.89)                 | 11.36 (2.50)                     |
| <b>Mass [kg]</b>            | 37.24 (14.97)                | 39.38 (11.10)                    |
| <b>Height [m]</b>           | 1.424 (0.190)                | 1.494 (0.135)                    |

## Data collection protocol

The data collection protocol was consistent between the two facilities and comprised of a three-dimensional (3D) gait assessment followed by MRI data acquisition, both performed on the same day. Gait analyses were carried out in the gait laboratories at GU and at QCMAS, while MRI images were acquired at the QScan and QCH MRI clinics, respectively.

## Gait laboratory setup

The GU gait laboratory (Figure 8a) was equipped with a 14-camera motion capture system (Vicon, Oxford Metrics, Oxford, United Kingdom. 200Hz) which was integrated with 4 force plates (Advanced Mechanical Technology Inc., Watertown, MA, USA. AMTI. 1000Hz) embedded in the ground and an instrumented treadmill (Bertec Corporation, Columbus, OH). Similarly, the QCMAS laboratory was equipped with a 10-camera motion capture system (Vicon, Oxford Metrics, Oxford, United Kingdom. 100Hz) and 4 in-ground AMTI force plates (1000Hz), which were sized to accommodate shorter strides of paediatric compared to adult participants (510 mm x 465 mm, Figure 8b). In addition, a 16-channel Cometa Aurion Zero Wire surface EMG system (Cometa Systems, Milan, IT. 1000Hz) was present in both facilities.

On each data collection day, prior to data acquisition, all equipment (Table 3) was tested to identify and resolve possible technical issues, then the gait laboratory was calibrated. Standard motion capture system calibration procedures were followed to

ensure complete coverage of the capture volume, i.e., 3D space around the force plates where participants were to perform different locomotor tasks. Next, the origin of the capture volume was defined, and the position of each force plate was checked to make sure the system correctly detected their location in space.

Finally, all force plates were zeroed, both manually and from the motion capture software, and a test walking trial was collected to visually verify point of application, shape and magnitude of the recorded ground reaction forces (GRFs).



**Figure 8.** Gait laboratory setup at GU (a) and QCMAS (b). Marker trajectories and ground reaction force data were acquired using a motion capture system and a set of in-ground force plates (orange) while participants performed different locomotor tasks within the motion capture volume.

**Table 3.** Gait laboratory equipment used for data collection.

|                              | <b>GU</b>                                   | <b>QCMAS</b>                                |
|------------------------------|---|---|
| <b>Motion capture system</b> | 14xVicon cameras                            | 10xVicon cameras                            |
| <b>Force plates</b>          | 4xAMTI                                      | 4xAMTI                                      |
| <b>EMG system</b>            | 16 channels -<br>Cometa Aurion<br>Zero Wire | 16 channels -<br>Cometa Aurion<br>Zero Wire |

## **Participant preparation**

Upon arrival, an experienced physiotherapist measured each participants' height, mass, bilateral leg length, knee varus/valgus angles with a manual goniometer in standing, in addition to knee and ankle widths. All parameters were entered in Vicon Nexus 2.5 (Vicon, Oxford Metrics, Oxford, UK) and stored for later use. A set of retro-reflective spherical markers (radius = 14mm) were when affixed on anatomical body landmarks (Figure 9 and Table 4). The marker set was composed by 35 individual markers and 4 triad clusters. To these, four wand markers (i.e., Plug-in-Gait markers) that were routinely used at QCMAS for gait assessments were also added. Markers were placed in accordance with Barzan (2019).

Skin was prepared by the physiotherapist by gently shaving and cleansing specific areas with an alcohol swap. A minimum of 12 surface EMG sensors were placed on selected muscles of the lower limb (Table 5) according to SENIAM guidelines (Merletti et al. 2006). Appropriate EMG sensors placement was assessed by asking the participants to perform simple movements, which required the activation of specific muscles or muscle groups. Finally, hypoallergenic sports tape (Coban, 3M Australia, NSW, Australia) was wrapped around thigh and shank segments to hold all surface EMG sensors in place during motion (red tape in Figure 9), thus reducing movement artefacts. For CP patients, the most affected limb was instrumented. By contrast, for all TD participants EMG signals were collected from the right limb, in accordance with our previous research.

**Table 4.** List of motion capture markers affixed over participants' body for scaling purposes and biomechanical simulations. A total of 51 markers, including four triad clusters and four Plug-in Gait wand markers were used.

| <b>Body segment</b> | <b>Marker name</b> | <b>Anatomical landmark</b>         |
|---------------------|--------------------|------------------------------------|
| Back                | C7                 | 7 <sup>th</sup> Cervical Vertebra  |
|                     | T10                | 10 <sup>th</sup> Thoracic Vertebra |
|                     | CLAV               | Clavicle                           |
|                     | STRN               | Sternum                            |
|                     | RBAK               | Right thorax                       |
| Pelvis              | R/LASI             | Anterior superior iliac spine      |
|                     | R/LIC              | Lateral iliac crest                |
|                     | R/LPSI             | Posterior superior iliac spine     |
| Knee                | R/LKNE             | Lateral femoral condyle            |
|                     | R/LPAT             | Patella                            |
|                     | R/LMKNE            | Medial femoral condyle             |
|                     | R/LLTC             | Lateral tibial trochanter          |
|                     | R/LTTUB            | Tibial tuberosity                  |
|                     | R/LMTC             | Medial tibial trochanter           |
| Foot                | R/LANK             | Lateral malleolus                  |
|                     | R/LHEE             | Calcaneus                          |
|                     | R/LMMAL            | Medial malleolus                   |
|                     | R/LMT1             | 1 <sup>st</sup> metatarsal         |
|                     | R/LTOE             | 2 <sup>nd</sup> metatarsal         |
|                     | R/LMT5             | 5 <sup>th</sup> metatarsal         |
| Thigh               | R/LTH1-3           | Thigh triad cluster                |
|                     | R/LTHI             | Thigh wand marker                  |
| Shank               | R/LTIB1-3          | Tibia triad cluster                |
|                     | R/LTIB             | Tibia wand marker                  |

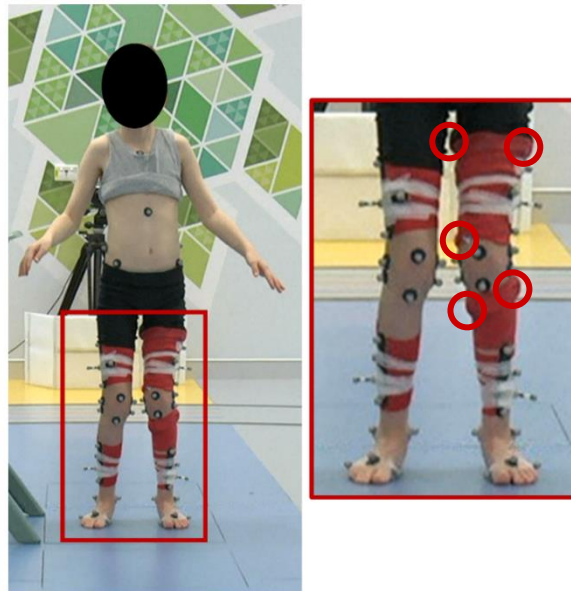


**Figure 9.** Participant with 51 retroreflective markers and 12 surface EMG sensors (covered in red tape. E.g., the five circled in figure) were affixed over the body to track the trajectories of each body segment and record lower limb muscle activity during the dynamic tasks.

**Table 5.** List of lower limb muscles from which experimental surface EMG data were collected and corresponding acronym

| <b>Muscle name</b>                          | <b>Acronym</b> |
|---|----------------|
| <b>Biceps femoris long head</b>             | BFLH           |
| <b>Gracilis</b>                             | GRA            |
| <b>Lateral gastrocnemius</b>                | LG             |
| <b>Medial gastrocnemius</b>                 | MG             |
| <b>Rectus femoris</b>                       | RF             |
| <b>Sartorius</b>                            | SR             |
| <b>Semimembranosus</b>                      | SM             |
| <b>Soleus</b>                               | SOL            |
| <b>Tensor fasciae latae</b>                 | TFL            |
| <b>Tibialis anterior</b>                    | TA             |
| <b>Vastus lateralis</b>                     | VL             |
| <b>Vastus medialis</b>                      | VM             |
| <b>Additional muscles recorded at QCMAS</b> |                |
| <b>Peroneus brevis</b>                      | PB             |
| <b>Peroneus longus</b>                      | PL             |

## **Gait assessment**

After preparation, participants were instructed to stand still on a single force plate in the capture volume with feet shoulder width apart, and arms raised to the side (see Figure 9), while a static trial was collected (Cappozzo et al, 1995). Then, a series of dynamic tasks were performed. These included three squats, three jumps and several overground walking trials. In addition, at GU, as part of a broader study, participants performed a series of 30s long walking trials on the instrumented treadmill, at three different speeds: self-selected walking speed (SWS), SWS+10% and SWS+30%.

The 3D marker trajectories (acquired at 200 Hz and 100 Hz, at GU and QCMAS, respectively) and analogue signals (i.e., GRF and EMG data, 1000 Hz) were simultaneously acquired. In order to record their typical gait patterns, while performing the overground walking trials all participants were instructed to walk naturally at a self-selected speed, looking straight ahead. The overground walking task was repeated until a minimum of 10 clean force plate strikes with the instrumented leg were recorded.

## **MRI acquisition**

Following gait assessment, for safety reasons all triad clusters, wand and trunk markers were removed, while the remaining 30 anatomical markers were replaced by MRI compatible markers with liquid centre (Campbell et al. 2009). Upon arrival to the MRI clinic, a radiographer assessed each participant's suitability to undergo MRI scanning. Then, participants were let inside the MRI collection room and asked to lay on the sliding bed in supine position. MRI coils were then positioned over the lower body to focus the magnetic field on the area of interest. Full lower limb, i.e., from pelvis to toes, and a dedicated high-definition (HD) knee joint MRI scans were acquired (Figure 10).

For the data collection at GU, all medical imaging data were acquired on a 3T Philips Insigna scanner (Phillips, the Netherlands). Full-length bones and pelvis were imaged using a 3D T1- weighted sequence (slice thickness: 1.0 mm, spatial resolution:  $0.79 \times 0.79 \text{ mm}^2$ ) while knee joint regional areas were acquired on a 3D proton density sequence (slice thickness: 0.6 mm, spatial resolution:  $0.28 \times 0.28 \text{ mm}^2$ ).

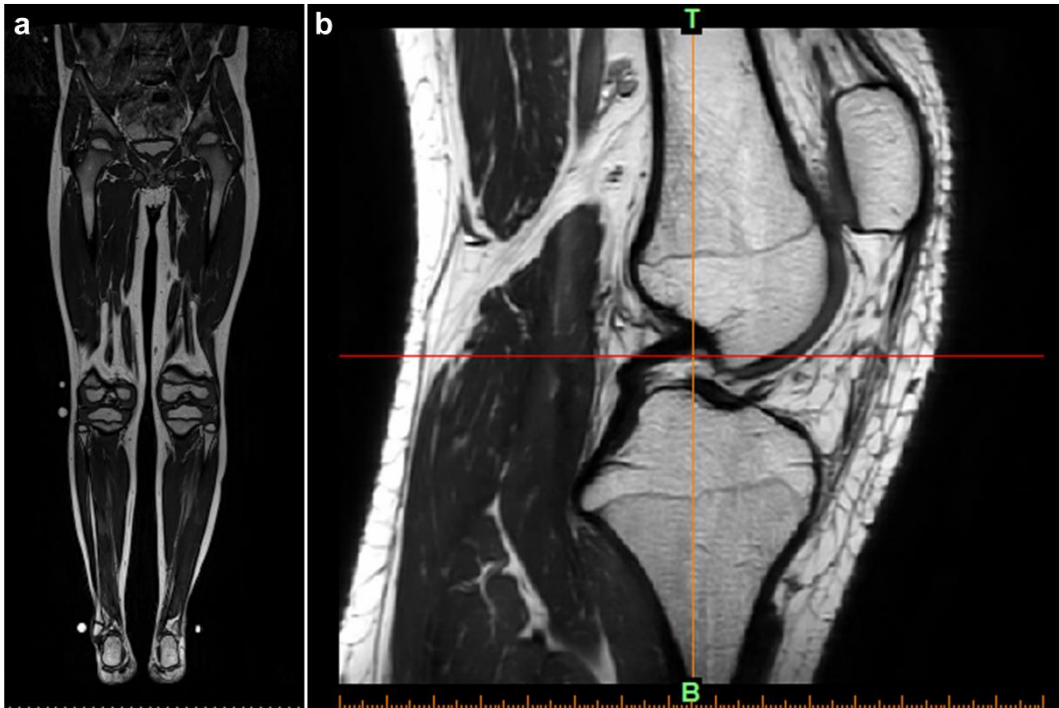


**Figure 10.** Examples of full lower limb (a) and high-definition knee MRI (b) scans acquired on one participant.

In comparison, two different MRI machines were used at QCH. Full lower limb scans were acquired on a 1.5T SIEMENS MAGNETOM Avanto fit syngo MR VE11B scanner (SIEMENS, Germany) to capture images from the iliac crests to the malleoli (3D PD SPACE sequence, slice thickness: 1.0 mm, spatial resolution:  $0.83 \times 0.83 \text{mm}^2$ ), while the dedicated knee joint scans were acquired on a 3T SIEMENS MAGNETOM Skyra scanner (SIEMENS, Germany) in the three planes using a T2-weighted sequence (i.e., 3D SPC T2, slice thickness: 0.53 mm, spatial resolution:  $0.53 \times 0.53 \text{mm}^2$ ). Four additional post-processing sequences were run on the full lower limb scans. Fat- and water-suppression, in-phase- and out-of-phase Dixon sequences (Ma 2008) were selected to highlight muscles boundaries thus facilitating segmentation of muscles (Figure 11 a-d).

Sequence parameters for the HD scans were optimised to identify bony structures, ligaments and cartilages of the knee joint on the leg which was instrumented during gait assessment. The scanning time depended on the size of each participant and overall ranged between 25 to 35 minutes per scan. All MRI data were finally exported in DICOM format.

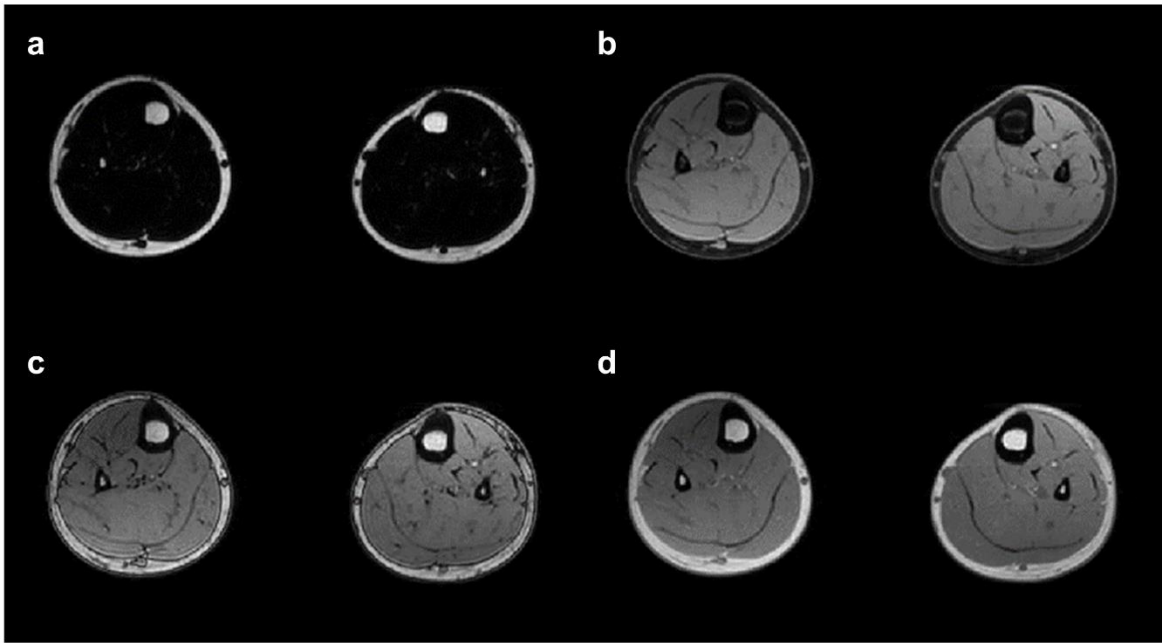


**Figure 11.** Post-processing sequences selected to enhance muscle segmentations. (a) Fat- and (b) water-suppression, (c) out-of-phase and (d) in-phase Dixon sequences were acquired on the full lower limb MRI scans.

# Data processing

## Gait analysis

Motion capture data were cleaned and labelled in Vicon Nexus 2.5, then processed in MATLAB using the MOtoNMS toolbox (Mantoan et al. 2015). Both marker trajectory and GRF data were filtered using a 4<sup>th</sup> order 6 Hz low-pass Butterworth zero-lag filter. EMG signals were band-pass filtered (zero-lag double-pass 4<sup>th</sup> order Butterworth, 20-400 Hz), full-wave rectified, low-pass filtered (zero-lag double-pass 4<sup>th</sup> order Butterworth, 6 Hz) and then normalised to each muscle's maximal excitation identified across all walking and heel raising tasks (Devaprakash et al. 2016). While processing the static pose trial, hip, knee and ankle joint centres were computed to enable the subsequent scaling of musculoskeletal anatomies. Specifically, the Harrington equation (Harrington et al. 2007) was used to determine left and right hip joint centres, while the mid-point between medial and lateral condyle markers and medial and lateral malleoli markers were selected as knee and ankle joint centres, respectively.

## Segmentation of medical images

The Research Innovation Suite software package (Materialise, Leuven, BE) was used for MRI data processing. This included the image segmentation software Mimics Research and the software 3-Matic.

The MRI data, stored in DICOM format, were firstly imported in Mimics Research 20, then saved as new Mimics working projects and subsequently anonymised. Images were automatically ordered and displayed according to their position in space expressed in the local coordinate system of the MRI coil. On selected slices, the Multiple Slice Edit tool was used to draw the contours of each structure of interest (i.e., lower limb bones). Contours delineation was performed more finely (i.e., every other slice) in the presence of complex or rapidly changing shapes (e.g., femur epiphyses) and more coarsely (i.e., one in five slices) elsewhere. Automatic interpolation filled the gaps between consecutive manual segmentations. On each segmented slice, all pixels enclosed in a contour were assigned to a bi-dimensional mask, specific to a structure. Finally, 3D objects were built off the resulting 2D masks. Wrapping (smallest detail: pixel size; gap closing distance: 2x pixel size) and smoothing (first order Laplacian method, smoothing factor: 0.8, iterations: 20) functions were employed to ensure surface smoothness while preserving originally segmented contours. All 3D structures were then exported as point

clouds in stereolithography (stl) format. Pelvis and bilateral full-length lower limb bones (i.e., left and right femurs, tibia/fibulas, patellas and feet bones) were segmented on full lower limb MRI scans (Figure 12a). Knee bone regions (i.e., distal femur, proximal tibia/fibula and patella) were further segmented on the dedicated high-definition (HD) knee joint scans (Figure 12d). Since full lower limb and HD knee joint scans were acquired with the knee in a slightly different position due to the presence of the dedicated knee coil, the STL Registration tool in Mimics was used to perform an iterative closest point (ICP) registration (Besl and McKay 1992) to align bony structures (Figure 12).

Registered volumes were imported in 3-Matic where rigid transformations were applied to re-orient the global coordinate system as per the International Society of Biomechanics (ISB) convention (Wu et al. 2002). The x-, y- and z-axes defining the antero-posterior, proximal-distal and medio-lateral directions respectively, were finally directed forward, upward and right.

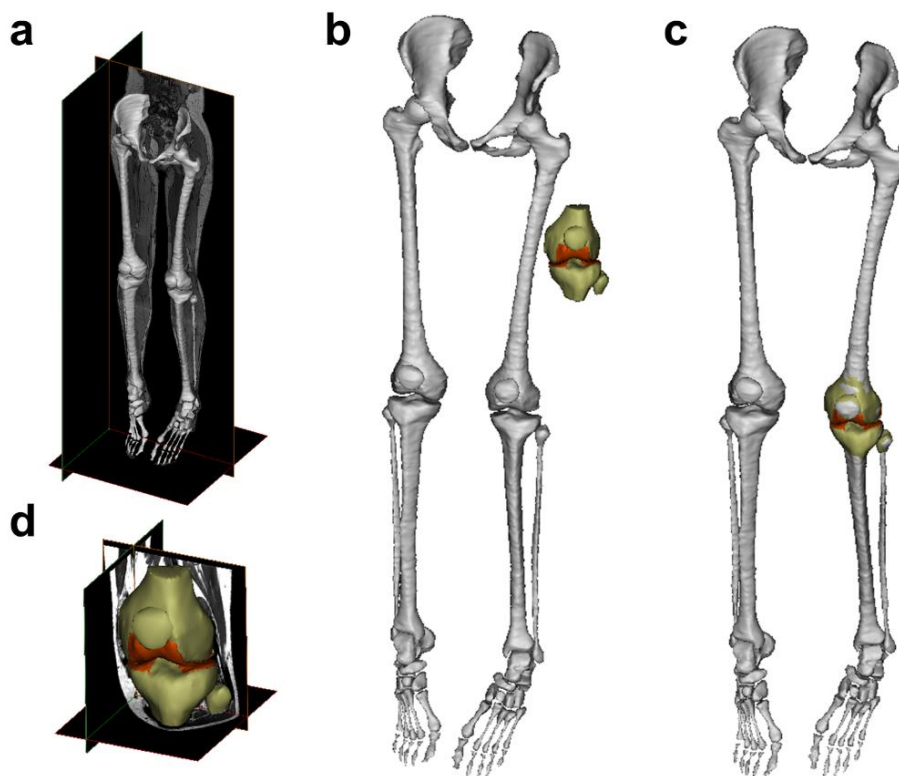


**Figure 12.** Segmented bony geometries (a) and knee joint structures (d) segmented on full-lower limb and dedicated high-definitions scans, respectively. Unregistered (b) and registered (c) bones.

For a subset of participants, fifteen muscles of the lower limb were manually segmented from the MRI's (Figure 13). Segmented muscles included the primary MTUs spanning the knee and ankle joints (i.e., muscles in Table 5 plus biceps femoris long head, semitendinosus and vastus intermedius). Out-of-phase Dixon scans were chosen for muscles segmentations as muscle boundaries were more clearly defined than on any of the other collected sequences. Once again, the Multiple Slice Edit tool was primarily used to draw contours on every other axial plane slice. However, in some instances, e.g., for shank muscles, it was necessary to work on multiple planes to ensure a proper muscle volume segmentation using the 3D Live Wire tool. Two-dimensional masks were then interpolated and 3D objects were generated, then wrapped as detailed above.

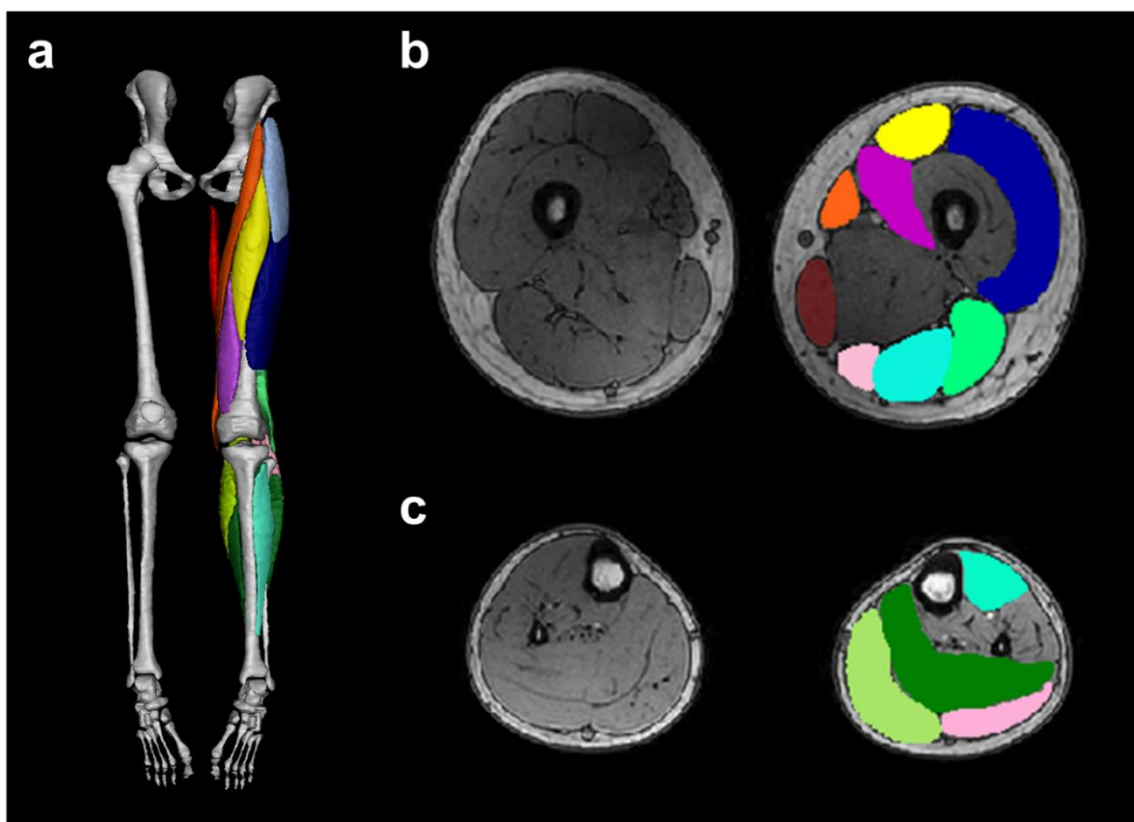


**Figure 13.** Three-dimensional view of a subset of lower limb muscles segmented on full lower limb MRI scans (a). Axial view of a thigh (b) and a shank (c) slices on which muscles were manually identified.

# Development and personalisation of neuromusculoskeletal models

Experimental MOCAP, EMG and MRI data along with literature findings were used to develop personalised neuromusculoskeletal (NMSK) models with incremental levels of subject-specificity. Personalisation extended to: (1) musculoskeletal anatomy, i.e. bones and MTU pathways, (2) MTU parameters, i.e., optimal fibre length, tendon slack length and maximal isometric force, and (3) muscle activation patterns.

A simplified version of the OpenSim gait2392 generic model (Delp et al. 1990) was selected as base musculoskeletal anatomy (Sartori et al. 2012; Saxby et al. 2016). The base model included thirty-four muscle-tendon units (MTU) per leg (Sartori et al. 2012) and a two-point contact knee mechanism to allow for the calculation of knee JCFs (Gerus et al. 2013; Saxby et al. 2016; Winby et al. 2009). The exact location for the contact points, which were inserted on the tibial plateaus where femoral and tibial bones touched, was determined using a regression equation based on adult MRI data (Winby et al. 2009). Following a step-wise approach (Figure 14), the base model was then progressively personalised.

To facilitate comprehension, the entire customisation process is hereby described in three separate subsections: (i) development and personalisation of musculoskeletal anatomy, (ii) model tuning and calibration of MTU parameters and (iii) model execution and biomechanical simulations.

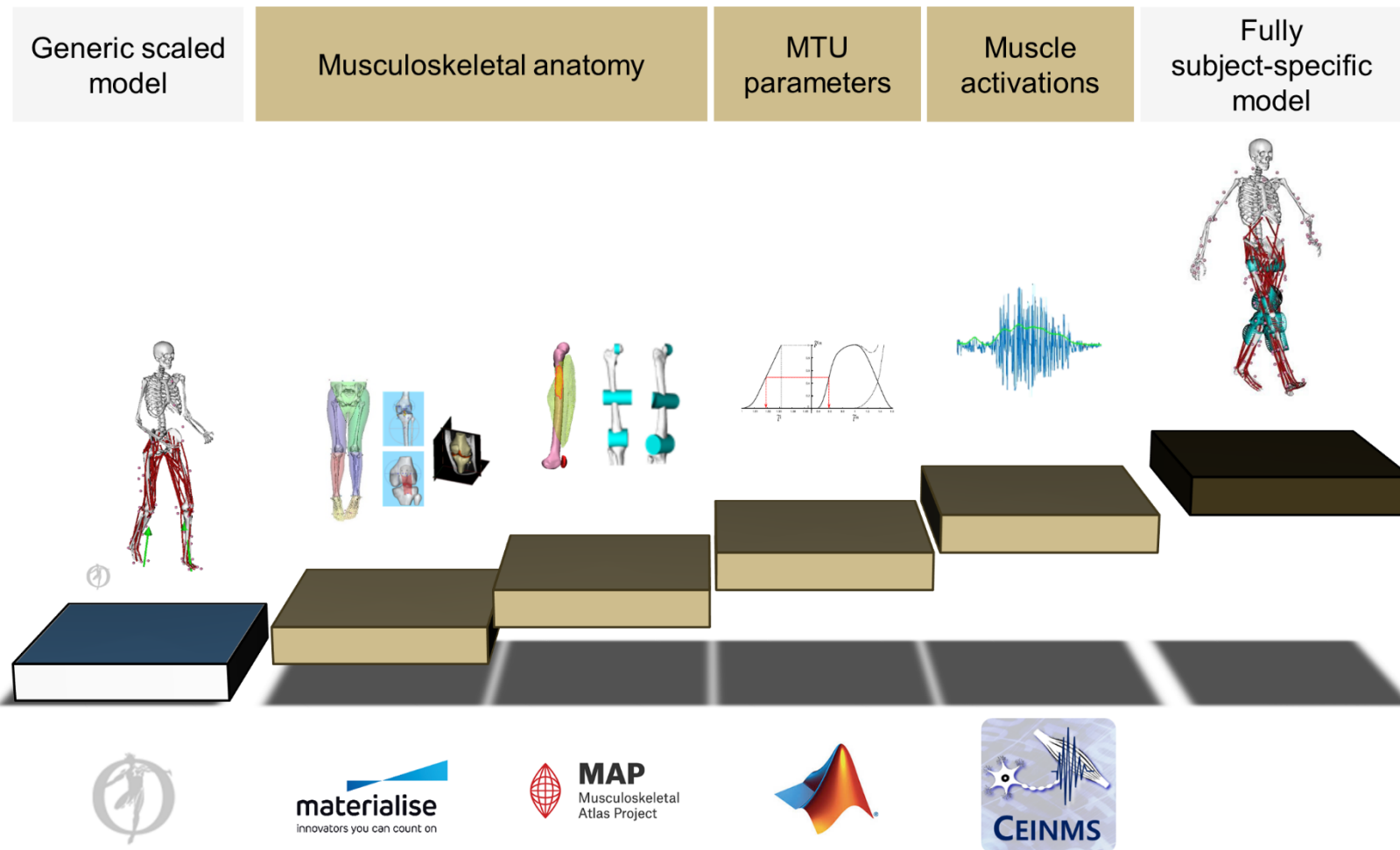


**Figure 14.** Levels of subject-specificity implemented in the models. Experimental motion capture, EMG and MRI data, along with literature findings, were used in a staged fashion to progressively increase the level of personalisation of each developed neuromusculoskeletal model. Marker positions were used to scale the template model, EMG signals to calibrate musculotendon (MTU) parameters and medical images to personalise bones, joint, muscle pathways and the maximal isometric force of lower limb muscles.

# Development and personalisation of musculoskeletal anatomy

## Model scaling

As common practice in modelling for biomechanical simulations (Hicks et al. 2015), the base musculoskeletal anatomy was initially linearly scaled (Figure 15) to match each participant's dimensions. However, erroneous representations of the human anatomy due to inappropriate scaling may affect joint angles (Kainz et al. 2017a), joint torques and muscle kinematics estimates (Scheys et al. 2008b), possibly leading to misinterpretation of clinical findings. To ensure proper scaling, individual scaling factors for each bone were calculated as the ratio of Euclidean distances between pairs of MOCAP markers and corresponding virtual landmarks on the OpenSim base model. Marker pairs for scaling were selected in accordance to Kainz' recommendations (Kainz et al. 2017b) and included (1) iliac crests markers (i.e., left and right ASIS), (2) hip joint centres computed via the Harrington formula and (3) knee and ankle joint centres defined as the mid distance between medial and lateral knee condyle and malleoli markers respectively. Muscle origin, insertion and via points which defined MTU pathways were scaled together with the bones they were attached to.

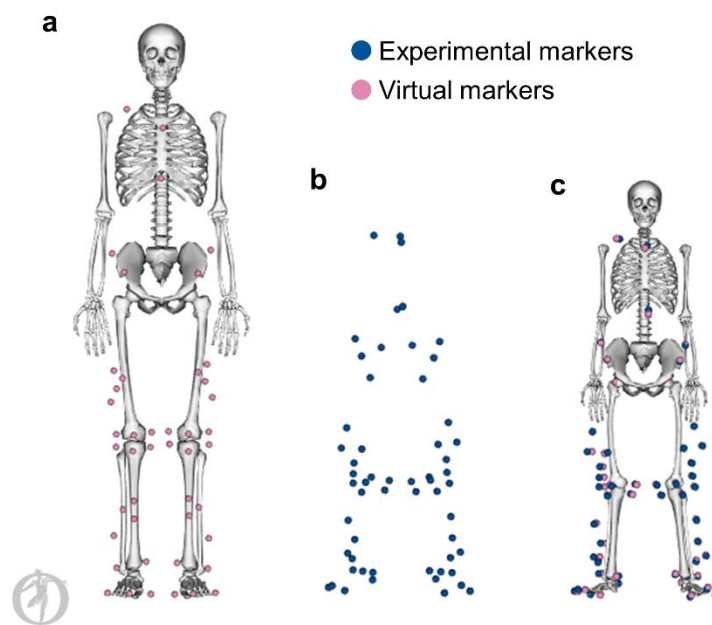


**Figure 15.** Example of generic base OpenSim model before (a) and after (c) linear scaling. Motion capture data (b) were used to determine each bone scaling factors in the three dimensions.

## Subject-specific musculoskeletal anatomies via the MAP Client

Acknowledging the limitations of linearly scaled generic models (see Chapter 2), subject-specific image-based paediatric MSK anatomies were later developed via the Musculoskeletal Atlas Project (MAP) Client (Zhang et al. 2014b). The MAP Client is an open-source software which combines statistical shape modelling (SSM) and morphing techniques (e.g., free form deformations) to reconstruct pelvic, femoral, tibiofibular, and patellar bones. Medical images and MOCAP data can be provided to inform the bone reconstruction process. Moreover, the MAP Client enables the customisation of a generic gait2392 OpenSim (Delp et al. 1990) model for use in NMSK modelling and simulations (Killen 2019). The resulting MAP Client generated OpenSim models include subject-specific bony geometries and personalised muscle pathways (Figure 16).

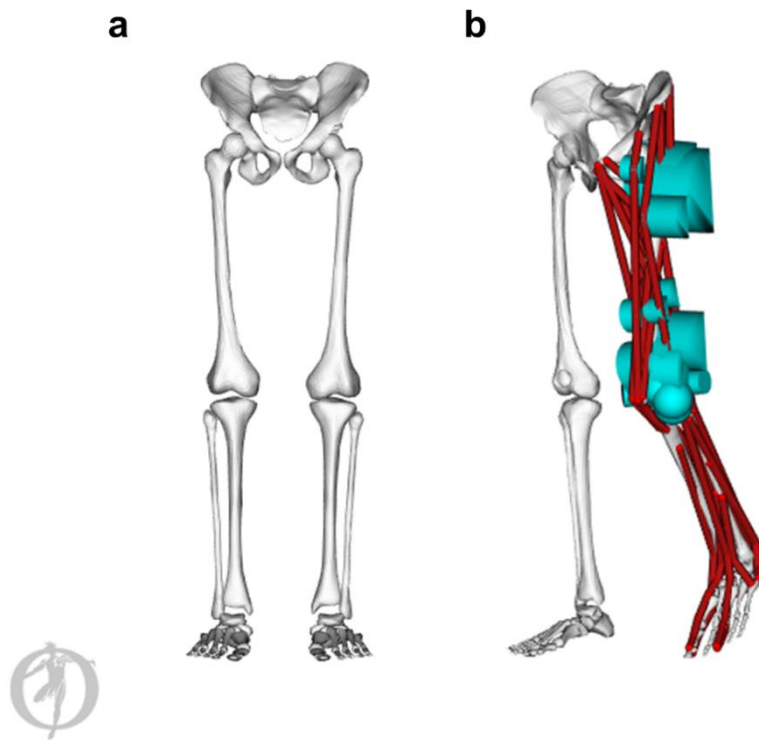


**Figure 16.** MAP generated OpenSim skeletal model (a) and personalised muscle pathways with wrapping surfaces in light blue (b).

## Subject-specific bones

Within the MAP Client, several pipelines, i.e., combination of techniques, may be used to generate bones depending on the availability of experimental data (Chapter 5). In this thesis, personalised pelvic, femoral, patellar and tibiofibular bones for all MAP generated MSK models were reconstructed employing both MOCAP and MRI data. Firstly, for each bone of interest, the corresponding mean MAP statistical shape model, resulting from a database of 26 lower limbs and over 200 femurs, was linearly scaled using experimental MOCAP data (i.e., static trial). Similar to linear scaling in OpenSim, all scaling factors were computed as the ratio of Euclidean distances between virtual markers on the mean MAP model and corresponding MOCAP marker positions. Marker pairs to scale each bone dimensions were defined in accordance with established recommendations (Kainz et al. 2017b).

Once scaled, MAP generated bone geometries were registered to the corresponding MRI segmentations via an ICP registration step (Besl and McKay 1992), then resized to ensure adequate bone sizing (Figure 17a-b-c). Subsequently, host-mesh fitting (HMF) and local-mesh fitting (LMF) techniques were employed one after the other to progressively minimise the surface-to-surface distance error between MAP and MRI point clouds and enhance reconstruction accuracy (Figure 17e-f). To ensure the best fit to experimental imaging data, both steps were iterated five times with different penalty weights which were employed to preserve surface smoothness and to avoid abnormal element curvature (Suwarganda et al. 2019).

The HMF step was performed first and resulted in a gross bone shape refinement. A set of rigid transformations were applied to all points enclosed in the MAP host-mesh, i.e., the bounding box surrounding each point cloud data. These transformations allowed for a close match between MAP and corresponding MRI host-meshes. Contrarily, the LMF step worked on a point-to-point basis: the distance between each point on the MAP mesh and its closest point on the registered MRI mesh was minimised, thus enabling a local mesh refinement. The resulting reconstructed bones were highly accurate when compared to MRI segmentations. The Jaccard index, used to quantify volume similarity, was consistently higher than 0.8, which was previously considered a good level of accuracy (Suwarganda et al. 2019).

Statistical shape models of foot bone geometries were not available in the MAP Client and consequently could not be morphed using the methods outlined above. Feet bones were instead linearly scaled by the average scale factor of all MAP generated lower limb bones.

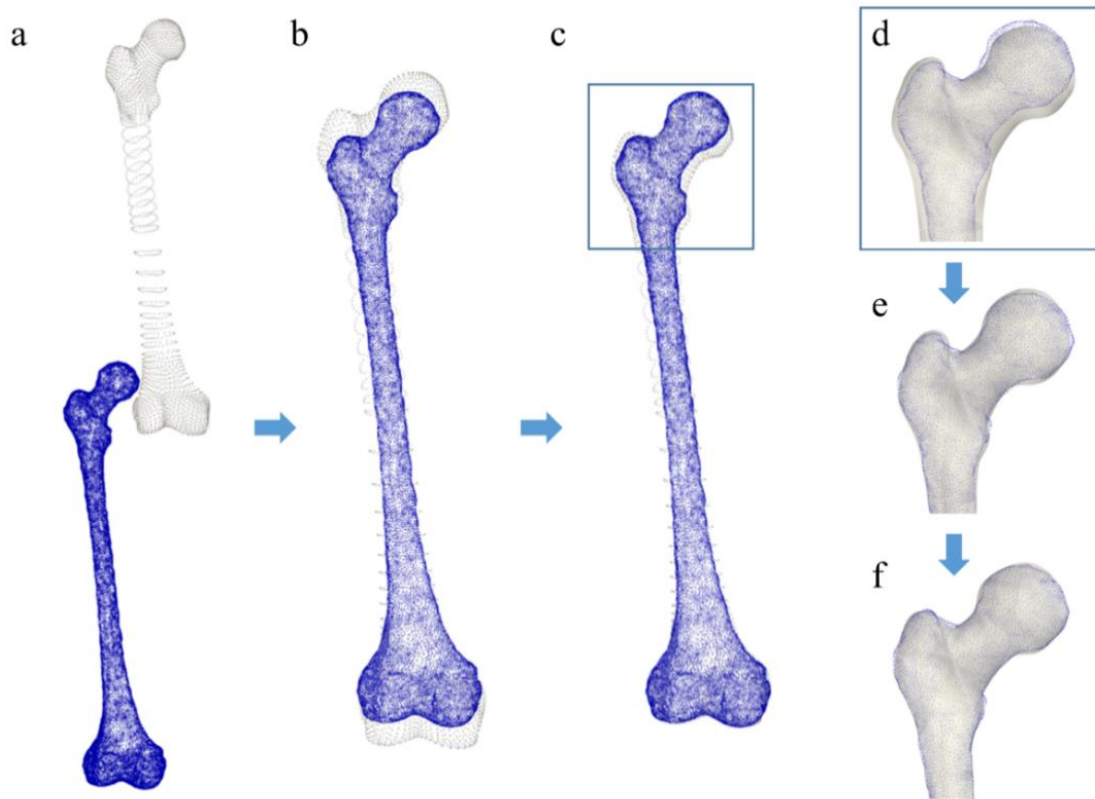


**Figure 17.** Steps included in the workflow to generate bones in the MAP Client. Linearly scaled MAP mean bone models (white) were firstly registered to the corresponding MRI segmentations via iterative-closest-point registration (a to b), then resized (c). Host-mesh fitting (d) and local mesh fitting (e) techniques were finally performed to produce more accurate bone reconstructions.

## **Joints definition**

All MAP generated OpenSim models featured generic ankle and hip joints equivalent to the corresponding joints on the gait2392 model (Delp et al. 1990), which was used as template for the customisation process in the MAP Client. On the other hand, the knee joint was represented as a 1 degree-of-freedom (DOF) hinge joint with translations in the x (anterior/posterior) and y (superior/inferior) directions prescribed as function of the knee flexion angle to preserve a minimal distance between femur and tibia. Furthermore, a fixed patello-femoral joint was included. As result, the patellar body was kinematically constrained to move along with the tibial body.

## **Subject-specific MTU pathways: definition and optimisation**

Each bone model generated in the MAP Client was defined by a specific number of nodes and elements (Figure 18). Musculotendon units' attachments on bones (i.e., origin and insertion points) were assigned to specific nodes, the location of which was derived from the anatomical SOMSO model (Marcus Sommer SOMSO Modelle, Sonneberg, Germany. [www.somso.de](http://www.somso.de)). Hence, when the MAP bone models were morphed to match MRI segmentations the muscle origins and insertions were moved accordingly.

In OpenSim models, musculotendon pathways are additionally constrained within physiological limits using via points. The position in space of via points is either defined as a constant translation from a body reference system, or expressed as function of a specific DOF angle. Sometimes, via points may not be required throughout the full range of motion. In these cases, conditional via points that are active at specific joint angles may be preferred. In the MAP Client, all via points were morphed using a weighted average vector method that considered shape changing and scaling factors resulting from the bone customisation process (Carleton, 2018).

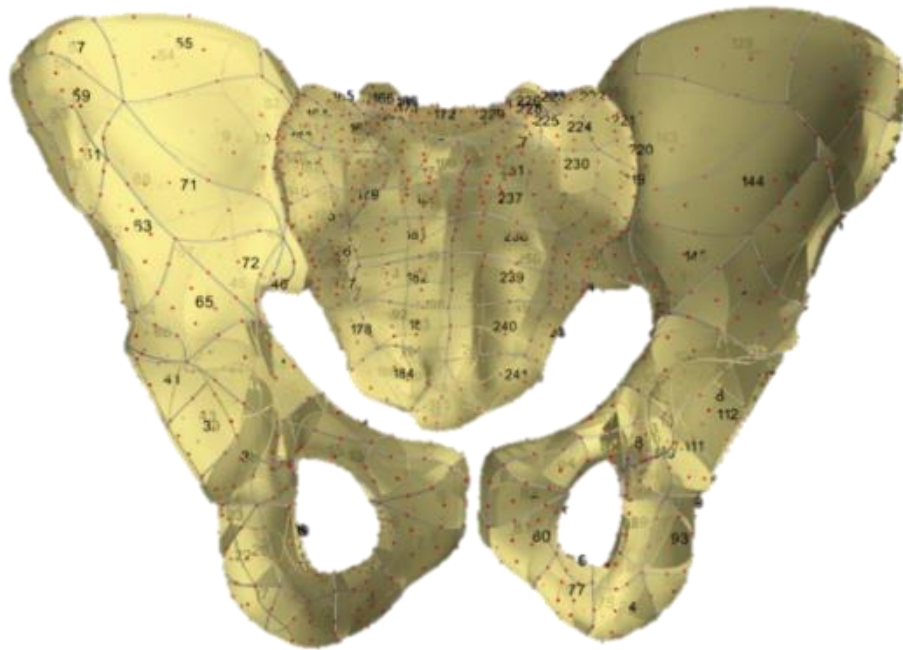


**Figure 18.** Nodes (red dots) and elements (numbers) on MAP mean pelvic bone model.

However, using the weighted average vector method resulted in discontinuous MTU length and moment arms curves. Therefore, wrapping surfaces were instead used for the muscles spanning the knee joint. Wrapping surfaces are analytical shapes (e.g., cylinders or spheres) which cannot be penetrated by a MTU pathway. When a MTU pathway comes in contact with a wrapping surface, it smoothly wraps around it, via the shortest path (Sherman et al. 2013). Specific bony landmarks on the MAP bone models were selected to locate the initial position of each wrapping surface, the size of which was determined by geometrical primitives (e.g., cylinders or spheres) fitted to the corresponding anatomical regions (e.g., femur condyles). The use of wrapping surfaces partly resolved non-physiological in-bone penetrations (Figure 19). Nonetheless, few residual inaccuracies (i.e., discontinuities in MTU kinematics and inappropriate wrapping paths) were still present due to suboptimal wrapping surfaces sizing, positioning and orientation.

To minimise discontinuities and ensure proper wrapping paths, a particle swarm optimisation (PSO) routine in Python was used to automatically refine the parameters defining each wrapping surface to produce smooth and physiologically plausible MTU kinematics (Killen 2019). For each MTU, a cumulative score, resulting from the sum of different penalty and objective functions, was iteratively computed and minimised. Penalty functions were introduced to detect errors in MTU lengths, moment arms and pathways. These included (1) a moment arm polarity penalty to prevent from non-

physical MTU behaviours (e.g., extensor muscles acting as flexors), (2) a wrapping penalty to enforce appropriate surface wrapping and (3) a penetration penalty to discourage in-bone muscle penetration. The objective functions were employed (1) to ensure continuity and smoothness of both MTU lengths and moment arms throughout the full range of motion and (2) to produce MTU kinematics which closely correlated to the patterns of cadaveric and previous generic OpenSim models data.

To reduce computational time, the optimisation problem was parallelised, i.e., each MTU was optimised independently, but concurrently. Optimisation was performed on the Gowonda high-performance computing cluster (HPC) at Griffith University and required approximately 12 hours per subject to be completed. Updated wrapping surfaces parameters were subsequently implemented in each MAP generated OpenSim model. Still, in few cases, the optimised wrapping surfaces were associated with non-physiological behaviours, which were resolved by manually adjusting size and position of the wrapping objects.

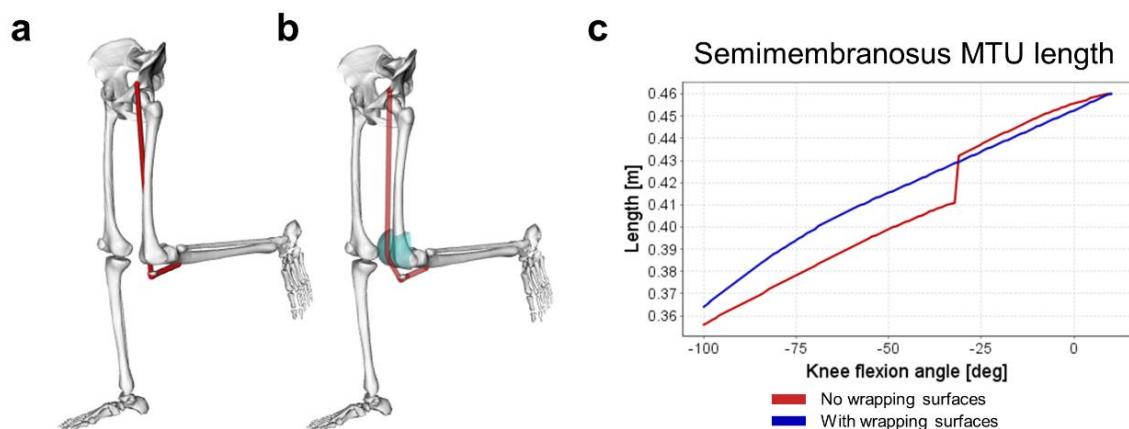


**Figure 19.** Wrapping surfaces to correct for non-physiological MTU pathways. Example of the rectus femoris muscle, before (a) and after (b) inserting wrapping surfaces on the MAP generated OpenSim model. (c) Example of discontinuity in MTU length for the semimembranosus muscle (red) which gets corrected inserting a wrapping surface (blue).

## **Additional features**

Some additional steps were required before the personalised and optimised NMSK models could be used for biomechanical simulations. Firstly, the set of virtual markers attached to each MAP generated model had to be replaced with the full experimental marker set, which was copied, for each subject, from the corresponding linearly scaled OpenSim base model. To refine marker positioning the marker placer function was subsequently run in OpenSim. Finally, the two-point contact knee mechanism had to be added to the model. The element-based nature of each MAP bone model facilitated the placement of medial and lateral contact points, which were positioned on the tibial plateaus where the distance between femoral and tibial bodies in the default OpenSim position (i.e., all joint angles equal to zero) was minimal.

## **Personalisation of MTU parameters**

### **Model tuning**

Once the musculoskeletal anatomies, generic scaled or personalised, were developed, adjustments were made to ensure a physiological MTU behaviour, which respected the force-length-velocity relationship defining muscle function (Figure 20a-c).

In this thesis, the Calibrated-EMG Informed NeuroMusculoSkeletal (CEINMS) modelling software (Pizzolato et al. 2015; Sartori et al. 2012) was used to estimate muscle forces. In CEINMS, muscles were represented as modified Hill-type actuators (Figure 20d). As such, their function (Figure 20a-c) strongly depended on the internal MTU parameters, especially optimal fibre length (OFL) and tendon slack length (TSL) (Buchanan and Shreeve 1996; Manal and Buchanan 2004; Winby et al. 2008).

Linearly scaled values were likely to be not physiologically correct, as OFL and TSL do not linearly scale along with MTU length or bones (Ward et al. 2007; Ward et al. 2005). Therefore, a morphometric scaling (Modenese et al. 2016; Winby et al. 2008) was performed to tune OFL and TSL values for all modelled MTUs. At each joint angle, OFL and TSL values were optimised to enforce force-length and force-velocity curves on the scaled model to match the corresponding theoretical curves on a generic unscaled reference model.

However, the morphometric scaling did not guarantee for the OFL and TSL values to be within physiologically plausible ranges, possibly affecting muscle dynamics.

Muscle forces in CEINMS were estimated solving for the following equation:

$$F^m = cF^{max} [f_a(\tilde{l}_m) \cdot f_v(\tilde{v}_m) \cdot a + f_p(\tilde{l}_m) + d_m \cdot \tilde{v}_m] \cdot \cos\varphi \quad (1)$$

where  $F^m$  is the muscle force,  $F^{max}$  is the maximal isometric force,  $c$  is the strength coefficient (specific to each muscle or muscle group) used to constrain the ability of muscles to generate force,  $a$  is the activation,  $d_m$  is the muscle dumping element introduced to avoid singularities when  $a = 0$  or  $F^{max} = 0$ ,  $\tilde{l}_m$  is the normalised fibre length,  $\tilde{v}_m$  is the normalised muscle velocity and  $\varphi$  is the pennation angle. Inappropriate definitions of MTU parameters could hinder muscle function.

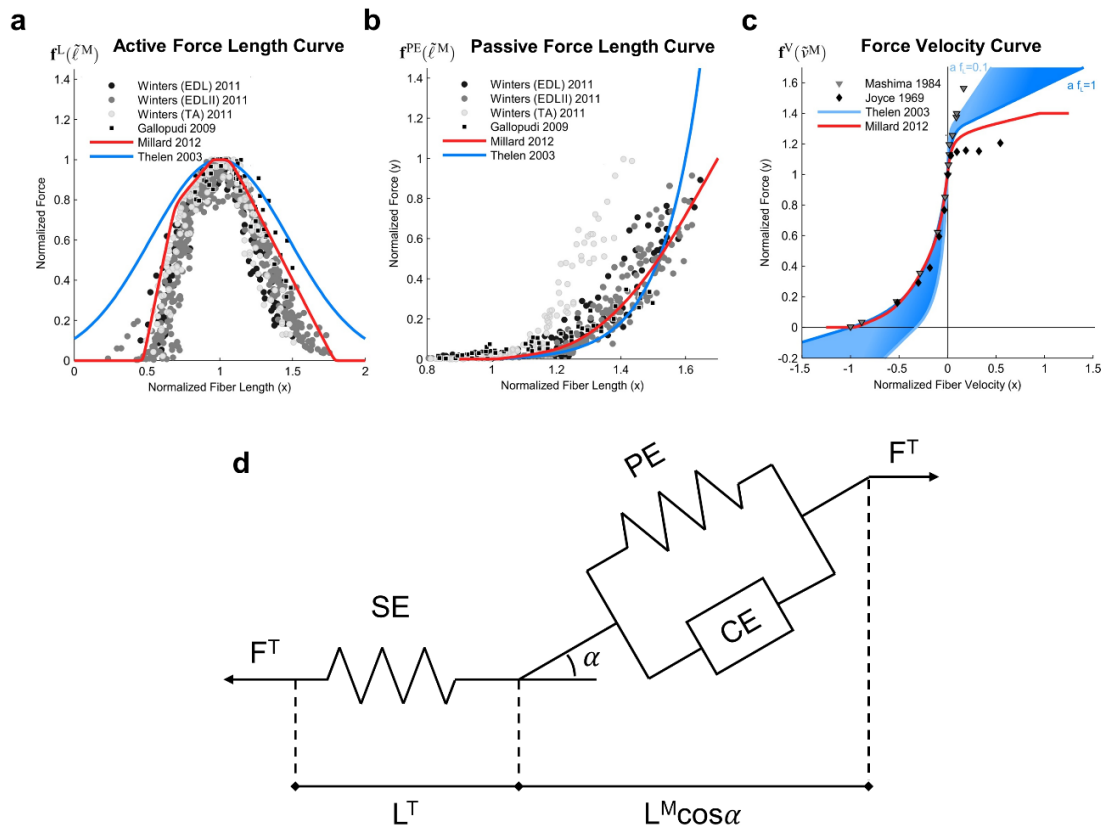


**Figure 20.** Adapted from Millard et al (2013). Theoretical force-length (a and b) and force-velocity (c) curves which describe the physiological behaviour of muscles in MSK models. (d) Hill-type actuator representation. Each MTU is modelled as a series element (SE) representing the tendon, a contractile element (CE) representing the active muscle fibres and a parallel element (PE) representative of the passive properties of a muscle. The overall MTU length is given by the sum of the tendon length ( $L^T$ ) and muscle fibre length ( $L^M \cos \alpha$ ), which accounts for the orientation of the muscle fibres, i.e. pennation angle ( $\alpha$ )

## Calibration of MTU parameters

A calibration step was later performed in CEINMS to further tune and personalise MTU parameters. Calibration enhanced each model's ability to track experimental joint torques and EMG data, therefore to reproduce more physiologically plausible internal biomechanics (Hoang et al. 2018; Pizzolato et al. 2015). A selection of walking, and heel raising trials were used in the calibration process. During calibration, the initial MTU parameters, which were extracted from each linearly and morphometrically scaled OpenSim model, were allowed to vary within a specified range of absolute or percent values (e.g., 90%-110%) in order to minimise experimental joint moment tracking errors (Hoang et al. 2018; Pizzolato et al. 2015; Sartori et al. 2014). Since the ratio of TSL and MTU lengths have previously been found to be preserved with aging (O'Brien et al. 2010), scaled MTU parameters were considered to be reasonably valid to represent a healthy paediatric population. Therefore, calibration only allowed for a  $\pm 5\%$  variation of initial OFL and TSL values to minimally correct for modelling inaccuracies. Additionally, the strength coefficient values, which control the ability of muscles to generate force, were also calibrated. All strength coefficients were initially set to 1 and bound to vary between 0.5 and 1.5. Muscles belonging to the same functional group were required to share the same strength coefficient.

Finally, different approaches were used to personalise muscles' maximal isometric force ( $F_{iso}^{max}$ ) values, based on the available experimental data. In study 1 (Chapter 4), muscle volumes segmented on MRIs were employed to update  $F_{iso}^{max}$  values, which were otherwise not scaled together with the musculoskeletal anatomy. The following formula was used:

$$F_{iso}^{max} = \sigma \frac{V^m}{l_0^m} \quad (2)$$

where  $V^m$  was the muscle volume from MRIs,  $l_0^m$  was the calibrated OFL and  $\sigma$  was the muscle specific tension, which was set to  $55 \text{ N/cm}^2$  (O'Brien et al. 2010) for all muscles. Minimal adjustments of MTUs parameters were then performed via a second calibration step in CEINMS ( $\pm 2.5\%$  variation), which did not alter the strength coefficients. Conversely, in study 3 (Chapter 6), the generic  $F_{iso}^{max}$  values were scaled based on the mass of each participant (van der Krogt et al. 2016), using the formula below:

$$F_{SS}^{max} = F_G^{max} \left( m_{SS} / m_G \right)^{2/3} \quad (3)$$

where  $m_{SS}$  is the mass of the participant, while  $m_G$  and  $F_G^{max}$  are the mass and maximal isometric force values from the unscaled template model.

## Calibration of MTU parameters for children with CP

Muscles in children with CP are generally smaller in volume and shorter in length compared to those in typical children (Barrett and Lichtwark 2010; Noble et al. 2014). Although muscle deficits are heterogeneous and become more apparent with the level of severity, plantarflexors, quadriceps and hamstrings muscles are usually more affected (Handsfield et al. 2015; Pitcher et al. 2018). These CP induced difference in muscle are attributed to smaller OFL's, due to a reduced number of sarcomeres in series (Lieber et al. 2004; Mathewson and Lieber 2015; Mathewson et al. 2015; Smith et al. 2011), and to longer TSL's (Barber et al. 2009; Barrett and Lichtwark 2010).

In study 1 (Chapter 4), muscle volumes, segmented from the MRI's of identical twins, were used to define whether a muscle was significantly affected by CP. A muscle was considered to be affected in the CP twin if it had a volume <80% of the corresponding muscle in the TD twin. This was the case for MG, LG, TFL, GRA and RF muscles, in line with previous literature (Handsfield et al. 2015). Hence, for these five muscles, to simulate over-stretched sarcomeres due to spasticity, the initial OFL values were scaled by a factor of 0.7. The scaling factor was derived from sarcomere lengths reported in literature (Mathewson and Lieber 2015; Smith et al. 2011), which were shown to be on average 1.4 ( $= \frac{3.69 \mu\text{m}}{2.63 \mu\text{m}} = \frac{\overline{l_{CP}^{sarc}}}{\overline{l_{TD}^{sarc}}}$ ) times longer in CP muscles compared to corresponding healthy muscles. In fact, for a given muscle fibre length, if the sarcomere length increases, the number of sarcomeres in series (i.e. OFL) reduces. Precisely, the amount of shortening is inversely related to the over-stretch:

$$\frac{\overline{l_{CP}^{sarc}}}{\overline{l_{TD}^{sarc}}} = 1.4 \rightarrow \frac{OFL_{CP}}{OFL_{TD}} = \frac{1}{1.4} = 0.71 \approx 0.7$$

where  $\overline{l^{sarc}}$  and  $\overline{OFL}$  are the mean in vivo sarcomere and optimal fibre lengths respectively.

The adjusted OFL values were subsequently calibrated in CEINMS to allow for a  $\pm 5\%$  variation to account for individual differences. TSL values for all muscles were not modified before calibration. However, they were allowed a 0 to 10% increase in the original value during calibration to simulate longer TSL, which is common in CP. Strength coefficients were calibrated similarly in both CP and TD participants.

## Personalisation of muscle activations

The last level of personalisation concerned the neural solution employed to synthesise muscle activations. In CEINMS, two different approaches, both implementing elastic tendons, were used (Figure 21): (i) Static optimisation and (ii) EMG-assisted modes (Pizzolato et al. 2015; Sartori et al. 2014; Sartori et al. 2012). Static optimisation synthesised all MTUs excitations to minimise the sum of squared muscle activations and joint torques tracking errors ( $E_{Moment}$ ). On the other hand, the EMG-assisted approach employed both experimental EMG data, minimally adjusted via static optimisation to minimise  $E_{Moment}$ , and muscle excitations synthesised via static optimisation. To increase the number of experimentally driven MTUs, additional muscle excitations were mapped from the collected EMG dataset assuming that muscles sharing same innervation have similar excitations (Sartori et al. 2012).

In this thesis, a static optimisation method that minimises the sum of squared muscle activations was chosen as the benchmark, as it is commonly used in biomechanical simulations (Modenese et al. 2018; Steele et al. 2012). However, static optimisation is based on the a priori assumption that muscles favour endurance over performance by minimising the overall activation (Crowninshield and Brand 1981). This principle may already not be valid for healthy populations (Kautz et al. 2000), let alone for children with CP (Kainz et al. 2019). Therefore, the EMG-assisted approach was later employed, as it enabled to capture co-contractions (Hoang et al. 2019) and abnormal muscle activity. In both cases, the following objective function was solved frame by frame:

$$f = \alpha E_{Moment} + \beta E_{sumExc} + \gamma E_{EMG} \quad (4)$$

where  $E_{sumExc}$  is the sum of squared muscle excitations;  $E_{Moment}$ , and  $E_{EMG}$  are the errors between experimental and estimated normalised joint moments and muscle excitations respectively;  $\alpha$ ,  $\beta$  and  $\gamma$  are weighting factors differently set for each neural solution. For static optimisation,  $\alpha$ ,  $\beta$  were set to 1 and 2, respectively, with  $\gamma$  set to 0. For the EMG-assisted mode,  $\alpha$ ,  $\beta$  and  $\gamma$  were automatically optimised to balance between muscle excitations and joint moments tracking errors.

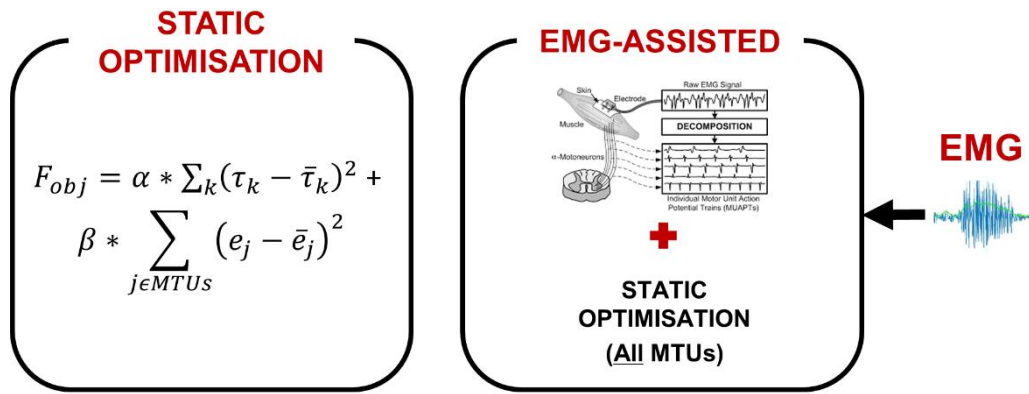


**Figure 21.** Neural solutions employed in this thesis. Static optimisation synthesised all excitations to minimise (a) overall squared muscle excitations and (b) joint moments tracking error. The EMG-assisted approach employed experimental EMG data and static optimisation methods to further minimise experimental EMG tracking errors.

## Models execution and biomechanical simulations

Biomechanical simulations were performed on generic scaled and personalised OpenSim MSK anatomies, after morphometric scaling of the MTU parameters. Joint kinematics, joint kinetics and muscle kinematics were computed in OpenSim 3.3 (Delp et al. 2007) on a series of dynamic trials including walking, heel raising and jumping tasks, using the Inverse Kinematics, Inverse Dynamics and Muscle Analysis tools respectively. The number and type of trials for which experimental MOCAP and GRF data were provided varied study by study. All simulations were batch processed in Batch OpenSim Processing Scripts (BOPS) (Mantoan and Reggiani 2015) to ensure consistency and to reduce time consumption and human errors. Moreover, SimTK guidelines to assess the validity of our models and results were followed and threshold criteria were met (Hicks et al. 2015).

Joint angles, joint moments and MTU kinematics results from OpenSim were provided to CEINMS which was used (1) to calibrate the MTU parameters of each model (see “Model tuning and calibration of MTU parameters” section) and (2) to estimate muscle activations and muscle forces (Pizzolato et al. 2015; Sartori et al. 2015; Sartori et al. 2012). Medial ( $JCF^{MC}$ ) and lateral ( $JCF^{LC}$ ) knee contact forces were finally computed by solving at each time frame the following static equilibrium problem (Figure 22):

$$JCF^{LC/MC} = \frac{(M_{MTU}^{MC/LC} - M_{ext}^{MC/LC})}{d_{IC}} \quad (5)$$

where  $M_{ext}^{MC/LC}$  is the external moment around the medial/lateral contact point,  $M_{MTU}^{MC/LC}$  is the overall muscle torque acting on the medial/lateral knee compartment, and  $d_{IC}$  is the intercondylar distance (i.e. between contact points). Muscle torques were calculated as:

$$M_{MTU}^{MC/LC} = \sum_{i=0}^n F_{MTU}^i r_{MTU}^{MC/LC^i} \quad (6)$$

where  $F_{MTU}^i$  is the force generated by the  $i$ -th MTU (estimated in CEINMS), and  $r_{MTU}^{MC/LC^i}$  is the  $MTU_i$  moment arm to the medial/lateral contact point (computed in OpenSim).

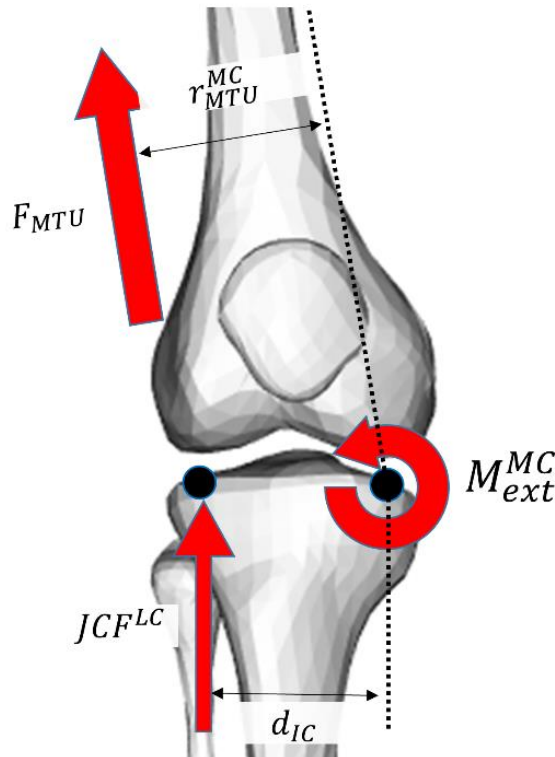


**Figure 22.** Schematic of the static equilibrium problem solved to compute knee joint contact forces, once muscle forces ( $F_{MTU}$ ), muscle moment arms ( $r_{MTU}^{MC}$ ), intercondylar distance ( $d_{IC}$ ) and external joint moments around the contact points ( $M_{ext}^{MC/LC}$ ) are known.

## Models summary

Seven different levels of personalisation were implemented in the NMSK models developed as part of this thesis (Table 6). These levels of personalisation were independently investigated to determine the effects of each personalised feature on the endpoint variables, and were subsequently combined to produce NMSK models of increasing subject specificity.

In study 1, the twofold aims were (1) to assess whether the calibration of MTU parameters was required to estimate physiologically plausible internal biomechanics and (2) to determine the impact of different neural solutions, namely EMG-assisted and static optimisation approaches, on the study of neuromuscular disorders, such as CP. Four NMSK models were developed (Table 6, top): unCal<sub>SO</sub> and unCal<sub>EMGa</sub>, which shared the same scaled and tuned musculoskeletal anatomy, derived from the template model, but employed different neural solutions to solve for muscle forces; Cal<sub>EMGa</sub> which featured calibrated OFLs and TSLs and Cal<sub>EMGa</sub><sup>MRI</sup> that had personalised  $F_{iso}^{max}$  values scaled by muscle volumes segmented on MRIs.

In study 3, a personalised NMSK model featuring personalised bony geometries and muscle pathways was developed using the MAP Client (Cal<sub>SO/EMGa</sub><sup>MAP</sup>) and compared to a generic scaled gait2392 model (Cal<sub>SO/EMGa</sub>) (Table 6, bottom). All models were tuned and calibrated in CEINMS to adjust MTU parameters and executed employing both static optimisation and EMG-assisted approaches. Calibration was deemed necessary to reduce inaccuracies associated with linear scaling of MTU parameters for paediatric participants who are significantly smaller than the template generic model. The  $F_{iso}^{max}$  values were scaled based on each participant's mass.

**Table 6.** Summary of the NMSK models developed in this thesis. The top half refers to models developed in study 1, while the bottom half refers to study 3. In both studies, the base musculoskeletal anatomy (unCal models) featured morphometrically tuned musculotendon parameters that were later calibrated in CEINMS with EMG data (Cal models). Both static optimisation (subscript SO) and EMG-assisted (subscript EMGa) approaches were used to estimate muscle forces. In study 1, maximal isometric force ( $F_{\max}^{\text{iso}}$ ) values were further personalised using muscle volumes segmented on MRIs (superscript MRI). In study 3,  $F_{\max}^{\text{iso}}$  values were scaled with each participant's mass (van der Krogt et al. 2016). Personalised musculoskeletal anatomies were developed in the MAP Client and finally implemented in the models (superscript MAP).

| Model                                   | Personalised features |           |                         |                    |
|---|-----------------------|-----------|-------------------------|--------------------|
|   | MSK anatomy           | OFL & TFL | $F_{\max}^{\text{iso}}$ | Muscle activations |
| <b>unCal<sub>SO</sub></b>               | ✗                     | ✗         | ✗                       | ✗                  |
| <b>unCal<sub>EMGa</sub></b>             | ✗                     | ✗         | ✗                       | ✓                  |
| <b>Cal<sub>EMGa</sub></b>               | ✗                     | ✓         | ✓                       | ✗                  |
| <b>Cal<sub>EMGa</sub><sup>MRI</sup></b> | ✗                     | ✓         | ✓                       | ✓                  |
| <b>unCal<sub>SO</sub></b>               | ✗                     | ✗         | ✓                       | ✗                  |
| <b>unCal<sub>SO</sub><sup>MAP</sup></b> | ✓                     | ✗         | ✓                       | ✗                  |
| <b>Cal<sub>SO</sub></b>                 | ✗                     | ✓         | ✓                       | ✗                  |
| <b>Cal<sub>SO</sub><sup>MAP</sup></b>   | ✓                     | ✓         | ✓                       | ✗                  |
| <b>Cal<sub>EMGa</sub></b>               | ✗                     | ✓         | ✓                       | ✓                  |
| <b>Cal<sub>EMGa</sub><sup>MAP</sup></b> | ✓                     | ✓         | ✓                       | ✓                  |

## **Statistical analysis**

In study one and study three, which focussed on the development and personalisation of NMSK models, statistical tests were conducted (i) to assess each developed NMSK model, (ii) to compare muscle and joint contact force estimates between models and (iii) to determine the individual contribution of different levels of personalisation on the models' outcomes. On the other hand, in study two that focussed on bone reconstructions, statistical tests were used to identify the best combination of methods to accurately reconstruct paediatric lower limb bones.

All statistical analyses were conducted in the IBM SPSS Statistics for Windows (IBM Corp, Armonk, NY) v25 for study one, in IBM SPSS v25 and Python 2.7 for study two, and in Python 3.6 for study three.

## **Models assessment**

Different metrics were used to assess each model's ability to reproduce experimental EMG and joint kinetic data. R-squared values and root mean square errors (RMSE) were computed for knee and ankle joint moments and muscle excitations to quantify the level of agreement between each CEINMS prediction and corresponding experimental data. Values were calculated individually for each of the collected muscles and reported as mean across all muscles. Data were initially checked for normality and if distributions were normal, a one-way (study one) or mixed (study three) repeated measures ANOVA test with Bonferroni correction was used to determine whether increasing the level of subject-specificity of NMSK model was associated with improvements in muscle excitations tracking. If data were not normally distributed, a Friedman test was conducted, followed by post hoc analysis with Wilcoxon signed-rank tests with Bonferroni adjustments. Statistical significance was set to  $p = 0.05$ .

## **Comparisons between models estimates**

Muscle forces and knee JCF profiles were compared between the developed models. In study 1, due to the limited number of subjects and trials analysed, the endpoint variables were only qualitatively compared. On the other hand, in study 3, to highlight when during the gait cycle different NMSK models produced significantly different estimates of knee JCFs, paired t-tests were conducted via statistical (non)parametric mapping in Python 3.6 (Pataky 2012). Additionally, the first and second characteristic peaks of total knee JCF were qualitatively compared. Finally, to determine the effect of each level of subject

specificity on the endpoint variables, muscle forces and (total, medial and lateral) knee JCF estimates were compared between models computing  $R^2$  and RMSE values (using  $Cal_{EMG_a}^{MAP}$  estimates as gold standard). Data were checked for normality. If data distributions were normal, mixed repeated measures ANOVA tests were performed in Pingouin (Vallat 2018). Alternatively, a Friedman test was conducted, followed by post hoc analysis with Wilcoxon signed-rank tests with Bonferroni adjustments. Statistical significance was set to  $p = 0.05$ .

## **Comparisons between pipelines to reconstruct bones**

The level of agreement between bones reconstructed using the twenty-one developed pipelines and the corresponding MRI segmentations was quantified using (1) the Jaccard index (i.e., index of shape similarity between volumes), (2) the root mean square of the distance error between closest points on each MAP generated and corresponding MRI point cloud, and (3) the Hausdorff distance (i.e., maximum distance error between point clouds). For the pelvic bone, the reconstruction accuracy was further assessed by computing (1) left and right hip joint centre location error compared to the MRI measurement and (2) left-to-right HJC distance, as surrogate measure of hip width, which was also compared to a marker-based measure (i.e., Harrington regression equation). Data were checked for normality. If data were normally distributed, repeated measures ANOVA tests were conducted. Alternatively, the equivalent non-parametric Friedman test followed by Wilcoxon signed rank tests were performed. To account for multiple comparisons, the significance level, initially set to  $p < 0.05$ , was recalculated implementing Bonferroni corrections.

## CHAPTER 4

---

# **Increasing level of neuromusculoskeletal model personalisation to investigate joint contact forces in cerebral palsy: a twin case study**

### *Acknowledgement of co-authorship*

This chapter includes a co-authored paper that has been re-formatted for this thesis. The bibliographic details/status of the co-authored paper, including all authors, are:

Davico, G., Pizzolato, C, Lloyd, D.G., Obst, S.J., Walsh, H.P.J., Carty, C.P. Increasing level of neuromusculoskeletal model personalisation to investigate joint contact forces in cerebral palsy: a twin case study. *Clinical Biomechanics*. (Submitted)

I made a substantial contribution in the conception and design of this study, data collection, analysis and interpretation of data, drafting and revising of the final manuscript.

Student/ Corresponding author: Giorgio Davico

Principal supervisor: David G Lloyd

# Abstract

**Background:** Cerebral palsy is a complex neuromuscular disorder that affects the sufferers in multiple different ways. Neuromusculoskeletal models are promising tools that can be used to plan patient-specific treatments for cerebral palsy. However, current neuromusculoskeletal models are typically scaled from generic adult templates that poorly represent paediatric populations. Furthermore, muscle activations are commonly computed via optimisation methods, which may not reproduce co-contraction observed in cerebral palsy. Alternatively, calibrated EMG-informed approaches within OpenSim can capture pathology-related muscle activation abnormalities, possibly enabling more feasible estimations of muscle and joint contact forces.

**Methods:** Two identical twin brothers, aged 13, one with unilateral cerebral palsy and the other typically developing, were enrolled in the study. Four neuromusculoskeletal models with increasing subject-specificity were built in OpenSim and CEINMS combining literature findings, experimental motion capture, EMG and MR data for both participants. The physiological and biomechanical validity of each model was assessed by quantifying its ability to track experimental joint moments and muscle excitations.

**Findings:** All developed models accurately tracked external joint moments; however EMG-informed models better tracked muscle excitations compared to neural solutions generated by static optimisation. Calibrating muscle-tendon unit parameters with EMG data allowed for more physiologically plausible knee joint contact forces estimates. Further scaling the maximal isometric force of muscles with MR-derived muscle volumes did not affect model predictions.

**Interpretation:** Given their ability to identify atypical knee joint contact forces profiles and accurately reproduce experimental data, calibrated EMG-informed models should be preferred over generic models using optimisation methods in informing the management of cerebral palsy.

# Introduction

Cerebral palsy (CP) is the most common motor disorder in childhood, with an incidence of 2.1 per 1000 live births in Australia (Smithers-Sheedy et al. 2016). CP is caused by a non-progressive brain lesion that impairs neuromuscular control and leads to progressive changes in muscle composition (Lieber et al. 2004), muscle morphology (Barrett and Lichtwark 2010), subsequent bony deformity (Morrell et al. 2002), and movement impairment (Smithers-Sheedy et al. 2016). Ambulant children with CP (GMFCS, I-III) are typically referred for clinical gait analyses to identify joint level kinematic and kinetic deviations from a typical population. Clinical gait analysis results are interpreted alongside the findings of physical examination (e.g., joint passive range of motion, muscle strength, spasticity) and medical imaging to develop a surgical and/or conservative management plan.

Neuromusculoskeletal (NMSK) modelling is becoming an increasingly popular extension of clinical gait analysis as it allows investigation of individual muscle contributions to movement and joint contact forces (JCF) during gait (Steele et al. 2012). Despite these opportunities, the value of NMSK modelling in the clinical management of CP remains unclear, as modelling assumptions may distort clinical interpretation (van der Krogt et al. 2012). For example, the activation patterns in NMSK models are commonly estimated using optimisation approaches that minimise the overall energy consumption or total muscle activation squared (Anderson and Pandy 2001b) to perform a specific movement, disregarding altered activation patterns which are typical in CP (Prosser et al. 2010). Furthermore, commonly implemented NMSK models scaled the individual's anatomy from generic healthy adult models, which is likely an oversimplification for typical children, let alone children with CP who present with altered muscle composition and morphology, and bony anatomy (Barber et al. 2011; Correa et al. 2011; Hicks et al. 2015).

Muscles in children with CP have reduced volumes, due to shortened muscle-tendon lengths and/or reduced cross-sectional areas (Barrett and Lichtwark 2010). Such deficits vary across subjects and muscles (Handsfield et al. 2015), with distal muscles being typically more affected and volume loss increasing with the level of physical impairment. Fat infiltration is also common in CP, further contributing to muscle weakness (Lieber et al. 2004). Additionally, tendon slack length (TSL) and optimal fibre length (OFL) are altered in CP. A 10% increase in TSL was observed in the calf muscles of children with spastic CP in comparison to TD peers (Barber et al. 2012). Similarly,

sarcomeres of spastic muscles are stretched compared to healthy muscles, with values increasing with severity (Mathewson and Lieber 2015; Shortland 2017) suggesting shorter OFL in CP-affected muscles. Neglecting any of these features may affect model predictions and diagnostic interpretations for children with CP (van der Krogt et al. 2012).

Muscles in NMSK models are often represented as Hill-type actuators and their behaviour strongly depends on muscle-tendon unit (MTU) parameters, such as TSL, muscle OFL and maximal isometric force ( $F_{max}^{iso}$ ) (Heine et al. 2003; Manal and Buchanan 2004). These parameters can be (1) directly measured via ultrasound (Gerus et al. 2015; Panizzolo et al. 2016; Sartori et al. 2017b) or MR imaging (Blemker et al. 2007), (2) calibrated (Garner and Pandy 2003; Hoang et al. 2018; Lloyd and Besier 2003) or (3) scaled (Hainisch et al. 2012) using experimental or literature data. Nonetheless, direct measurements are difficult to obtain (Herzog et al. 1991), calibration may require data which is not always available, while properly scaling MTU parameters can be complicated (Winby et al. 2008). Appreciating that muscle properties differ in children compared to adults, Hainisch and colleagues (Hainisch et al. 2012) proposed an approach to scale TSL and OFL based on tendon and muscle elongations from a generic adult model (Delp et al. 1990). While this approach may be valid for typically developing (TD) populations, it is likely not appropriate for children with CP as evidenced above. Few studies have simulated CP-induced muscle weakness or muscle contracture by respectively reducing  $F_{max}^{iso}$  (van der Krogt et al. 2012), shortening TSL (Fox et al. 2018) or reducing OFL values (Delp et al. 1995) in their respective generic NMSK models. These model modifications resulted in different simulated muscle recruitment strategies to achieve typical gait and provided valuable insight into the potential challenges that children with CP may face. However, all previous work is limited by the methods employed to scale MTU parameters. For example, muscle volumes derived from magnetic resonance images (MRI) (Handsfield et al. 2014) may provide a more accurate solution to scale  $F_{max}^{iso}$  compared to pre-defined scaling factors (Fox et al. 2018; van der Krogt et al. 2012), although this does not account for the aberrant muscle activation patterns commonly observed in children with CP.

Altered muscle activity in children with CP is characterised by increased total muscle activation and higher levels of co-contraction compared to their TD peers (Prosser et al. 2010). Co-contraction is quantified by measuring the simultaneous activation of agonist and antagonist muscles (e.g., knee flexors and extensors) and calculating co-contraction indices between the EMG linear envelopes (Knarr et al. 2012). However, although EMG signals are repeatable in both TD and CP paediatric populations (Steele et

al. 2019), the poor repeatability of the co-contraction indices in these populations means these metrics maybe undependable to assess group differences in muscular control (Mohr et al. 2018). Besides, the mechanical action generated by muscle' activation and co-contraction cannot be assessed using EMG alone, for which NMSK modelling is required.

In NMSK modelling, different methods are available to simulate muscle activity and solve for muscle forces. Optimisation-based methods, such as computed muscle control (CMC) (Thelen et al. 2003a) or static optimisation (Anderson and Pandy 2001b), are based on *a priori* objective criterion, and may not reproduce co-contraction (Lloyd and Besier 2003) that is evident in the EMG of patients with CP. Alternatively, EMG-informed methods (Lloyd and Besier 2003; Meyer et al. 2017; Pizzolato et al. 2015; Sartori et al. 2014), use experimental EMG data to capture pathology-related muscle activation abnormalities, possibly enabling more physiologically plausible estimation of muscle forces and JCFs (Hoang et al. 2018). Furthermore, one can calibrate the NMSK model's parameters to represent the individual, which is commonly done in EMG-informed methods. Nonetheless, to date, calibrated EMG-informed approaches have not been used to simulate the gait of children with CP.

The present study aimed to: (i) determine the impact of increased NMSK model subject-specificity on tracking of experimental joint moments and muscle excitations for two identical twin brothers (one typically developed and one with CP), and (ii) compare lower limb muscle force and knee JCF estimates between a NMSK model with muscle excitation patterns estimated solely via static optimisation and subject-specific NMSK models employing an EMG-informed approach. We hypothesised that: (i) an EMG-informed NMSK model would provide more accurate estimates of joint moments and muscle excitations compared to a NMSK model informed using static optimisation, (ii) a progressive increase in the subject-specificity of NMSK muscle properties would progressively improve the tracking of joint moment and muscle excitation estimates when implementing an EMG-informed NMSK model, and (iii) the use of an EMG-informed approach would enable a clearer discernment between typical and pathological muscle forces and JCF patterns and magnitudes, allowing for a better assessment of CP compared to static optimisation methods.

## Methods

Two identical twin brothers (aged 13, Table 21, Appendix A), one with (left) unilateral CP (GMFCS I) and the other TD, participated in the study. The CP twin exhibited

prolonged ankle plantarflexion throughout the stance phase of the gait cycle (i.e., true equinus patterns, clusters 5 and 8 according to Papageorgiou’s classification (2019)). The study was approved by the institutional Research Ethics Committee and informed consent was provided.

## Gait analysis data collection and processing

The 3D gait analysis assessment was performed in a gait laboratory. An experienced physiotherapist placed 51 retro-reflective MRI-compatible surface markers on anatomical landmarks (Table 22, Appendix A). After skin cleansing, twelve wireless bi-polar EMG sensors (Zerowire, Aurion, Milan, IT. 1000 Hz) were placed on selected left lower limb muscles (Table 7) and fastened using hypoallergenic sports tape.

**Table 7.** List of MTUs included in the NMSK models. Thirty-four MTUs, including the major muscles spanning the knee and ankle joints, were modelled. EMGs were collected from 12 MTUs on the left leg of each participant during the gait assessment and used in CEINMS to derive muscle excitations. The activity of three muscles (i.e., biceps femoris short head, semitendinosus and vastus intermedius) was mapped from experimental EMG data assuming that muscles sharing the same innervation have similar excitation patterns. Muscles belonging to each muscle group shared the same strength coefficients (initially set to 1), which were calibrated in  $Cal_{EMG_a}$  and  $Cal_{EMG_a}^{MRI}$  models.

| <b>MTUs with experimental EMG data</b> |                |                   |                     |
|--|----------------|-------------------|---------------------|
| <b>Muscle name</b>                     | <b>Acronym</b> | <b>EMG source</b> | <b>Muscle Group</b> |
| <b>Biceps femoris long head</b>        | BFLH           | BFLH              | 5                   |
| <b>Gracilis</b>                        | GRA            | GRA               | 8                   |
| <b>Lateral gastrocnemius</b>           | LG             | LG                | 7                   |
| <b>Medial gastrocnemius</b>            | MG             | MG                | 7                   |
| <b>Rectus femoris</b>                  | RF             | RF                | 8                   |
| <b>Sartorius</b>                       | SR             | SR                | 5                   |
| <b>Semimembranosus</b>                 | SM             | SM                | 5                   |
| <b>Soleus</b>                          | SOL            | SOL               | 10                  |
| <b>Tensor fasciae latae</b>            | TFL            | TFL               | 8                   |
| <b>Tibialis anterior</b>               | TA             | TA                | 9                   |
| <b>Vastus lateralis</b>                | VL             | VL                | 11                  |
| <b>Vastus medialis</b>                 | VM             | VM                | 11                  |
| <b>Mapped MTUs</b>                     |                |                   |                     |
| <b>Biceps femoris short head</b>       | BFSH           | BFLH              | 6                   |
| <b>Semitendinosus</b>                  | ST             | SM                | 5                   |
| <b>Vastus intermedius</b>              | VI             | (VM+VL)/2         | 11                  |

**Table 7 (continued).** List of MTUs included in the NMSK models. Thirty-four MTUs, including the major muscles spanning the knee and ankle joints, were modelled. EMGs were collected from 12 MTUs on the left leg of each participant during the gait assessment and used in CEINMS to derive muscle excitations. The activity of three muscles (i.e., biceps femoris short head, semitendinosus and vastus intermedius) was mapped from experimental EMG data under the assumption that muscles sharing the same innervation have similar excitation patterns. Since no EMG data were available for the nineteen “additional MTUs”, excitation patterns were computed via static optimisation. Muscles belonging to each muscle group shared the same strength coefficients (initially set to 1), which were calibrated in  $Cal_{EMG_a}$  and  $Cal_{EMG_a}^{MRI}$  models.

| <b>Additional MTUs</b>   |                |                   |                     |
|--------------------------|----------------|-------------------|---------------------|
| <b>Muscle name</b>       | <b>Acronym</b> | <b>EMG source</b> | <b>Muscle Group</b> |
| <b>Adductor longus</b>   | ADDL           | -                 | 1                   |
| <b>Adductor brevis</b>   | ADDB           | -                 | 1                   |
| <b>Adductor magnus 1</b> | AMAG1          | -                 | 1                   |
| <b>Adductor magnus 2</b> | AMAG2          | -                 | 1                   |
| <b>Adductor magnus 3</b> | AMAG3          | -                 | 1                   |
| <b>Gluteus maximus 1</b> | GMAX1          | -                 | 2                   |
| <b>Gluteus maximus 2</b> | GMAX2          | -                 | 2                   |
| <b>Gluteus maximus 3</b> | GMAX3          | -                 | 2                   |
| <b>Gluteus medium 1</b>  | GMED1          | -                 | 3                   |
| <b>Gluteus medium 2</b>  | GMED2          | -                 | 3                   |
| <b>Gluteus medium 3</b>  | GMED3          | -                 | 3                   |
| <b>Gluteus minimum 1</b> | GMIN1          | -                 | 3                   |
| <b>Gluteus minimum 2</b> | GMIN2          | -                 | 3                   |
| <b>Gluteus minimum 3</b> | GMIN3          | -                 | 3                   |
| <b>Iliacus</b>           | IL             | -                 | 4                   |
| <b>Peroneus brevis</b>   | PB             | -                 | 9                   |
| <b>Peroneus longus</b>   | PL             | -                 | 9                   |
| <b>Peroneus tertius</b>  | PT             | -                 | 9                   |
| <b>Psoas</b>             | PSO            | -                 | 4                   |

Marker trajectories were collected using a 12-camera motion capture system (Vicon Motion System, Oxford, UK. 100 Hz) while the subjects performed a static standing task, overground walking at their preferred walking speed (i.e. 0.8m/s for both twins) and heel raising trials. Simultaneously, ground reaction forces were measured from

two ground-mounted force platforms (Advanced Mechanical Technology Inc., Watertown, MA, USA. 1000 Hz).

Motion capture data were cleaned and labelled in Vicon Nexus 2.3, then processed in MATLAB using the MOtoNMS toolbox (Mantoan et al. 2015). Both marker trajectory and ground reaction force data were filtered using 4<sup>th</sup> order 6 Hz low-pass Butterworth zero-lag filter. EMG signals were band-pass filtered (zero-lag double-pass 4<sup>th</sup> order Butterworth, 20-400 Hz), full-wave rectified, low-pass filtered (zero-lag double-pass 4<sup>th</sup> order Butterworth, 6 Hz) and then normalised to each muscle's maximal excitation identified across all walking and heel raising tasks (Devaprakash et al. 2016), which produced the EMG linear envelopes (Figure 42, Appendix A).

## **MRI imaging and processing**

Following gait analysis, participants had full lower limb MRI scans taken at a nearby medical imaging clinic. Images were acquired on a 3T Ingenia scanner (Philips Healthcare, Best, The Netherlands) using an axial T1-weighted 3D fast field echo sequence (slice thickness: 1.0 mm, resolution: 0.79x0.79x1.0 mm<sup>3</sup>).

Fifteen muscles per leg were manually segmented from the MRI's using the Mimics Research Suite v17 (Materialise, Leuven, BE) from which muscles volumes were reconstructed (Table 24, Appendix A). These included the primary MTUs spanning the knee and ankle joints (i.e., MTUs with experimental EMG data and mapped MTUs in Table 7).

## **MSK base model creation**

The base MSK model was a simplified version of the gait2392 OpenSim model (Delp et al. 1990), which included 34 muscles per leg (Sartori et al. 2012) (Table 7). In addition, a two-point contact knee joint was added to the model to enable the calculation of medial and lateral tibiofemoral JCFs (Saxby et al. 2016). The base model was linearly scaled to each participant's dimensions using anatomical markers positions, with MTU parameters of TSL and OFL linearly scaled and morphologically optimised (Modenese et al. 2016) to ensure a MTU physiological behaviour throughout the full range of motion. Although this represents a scaled adult musculoskeletal model, its use for children without neuromuscular disorders is justified because the ratio between TSLs and MTU lengths is preserved with aging (O'Brien et al. 2010). However,  $F_{max}^{iso}$  values were not automatically scaled with body segment lengths, but given that our subjects' weights and heights were close to those of gait2392 (Table 21, Supplementary material) the original gait2392

values were considered a good approximation. The stance phases (i.e., heel-strike to toe-off of the left foot) of four walking trials per subject were analysed in OpenSim using inverse kinematics, inverse dynamics, and muscle analysis tools to compute joint angles, joint moments (Figure 42, Supplementary material), MTU lengths and moment arms.

## **NMSK model comparisons**

The stance phase data calculated using the base model, and experimental muscle excitations, were then used as inputs for the OpenSim toolbox, CEINMS (Pizzolato et al. 2015; Sartori et al. 2014), to estimate muscle forces using different neural solutions and levels of model subject-specificity. Four different models (Table 8) with incrementally increased levels of subject-specificity were tested: (1) scaled generic OpenSim model with muscle excitation patterns estimated using static optimisation methods (*unCal<sub>SO</sub>*), (2) scaled generic OpenSim model with muscle excitation patterns estimated via an EMG-informed approach (*unCal<sub>EMG<sub>a</sub></sub>*), (3) scaled generic OpenSim model with EMG-calibrated MTUs parameters that employed an EMG-informed approach (*Cal<sub>EMG<sub>a</sub></sub>*) and (4) scaled generic OpenSim model with EMG-calibrated MTUs parameters and corrected maximal isometric muscle forces based on MRIs that employed an EMG-informed approach (*Cal<sub>EMG<sub>a</sub></sub>*<sup>MRI</sup>).

**Table 8.** Characteristics of the four developed NMSK models. All models featured scaled-generic bones and joints. However, muscle activation patterns and MTUs parameters (i.e. optimal fibre length, tendon slack length and muscle isometric force) were progressively made subject-specific, combining experimental data, imaging and literature findings, as detailed in the table (“data source” column, on the right). ‘✘’ denotes generic parameters as per gait2392 model or static optimisation to estimate for muscle excitations, while ‘✓’ indicates inclusion of subject-specific characteristic.

|                                      | GENERIC             | SUBJECT-SPECIFIC      |                     |                                    | DATA SOURCE       |
|--------------------------------------|---------------------|-----------------------|---------------------|------------------------------------|-------------------|
|                                      | unCal <sub>so</sub> | unCal <sub>EMGa</sub> | Cal <sub>EMGa</sub> | Cal <sub>EMGa</sub> <sup>MRI</sup> |                   |
| Muscle Activation Patterns           | ✘                   | ✓                     | ✓                   | ✓                                  | Experimental EMGs |
| Optimal Fibre & Tendon Slack Lengths | ✘                   | ✘                     | ✓                   | ✓                                  | Literature & EMGs |
| Maximal Isometric Force              | ✘                   | ✘                     | ✘                   | ✓                                  | Literature & MRIs |
| Bones & Joints                       | ✘                   | ✘                     | ✘                   | ✘                                  | OpenSim           |

Our first two models, *unCalsO* and *unCal<sub>EMG</sub>a*, both used the base model's musculoskeletal anatomy. However, to solve for muscle excitation patterns, and subsequent muscle forces and knee JCFs, different neural algorithms were employed in CEINMS (Pizzolato et al. 2015; Sartori et al. 2014). *unCalsO* solely used static optimisation which minimised sum squared excitations ( $E_{sumEXC}$ ) and sum squared tracking errors between experimental (inverse dynamic) and NMSK model estimated joint moments ( $E_{Moment}$ ) to synthesise all the muscles excitations. In contrast, *unCal<sub>EMG</sub>a* employed the EMG-assisted approach to account for the CP child's abnormal muscle activation patterns (including co-contraction) and the personalised activation patterns of TD child. The EMG-assisted approach in CEINMS uses static optimisation to improve joint moments predictions (i.e. minimising  $E_{Moment}$ ) by minimally adjusting the EMG linear envelopes and synthesising excitations of muscles without EMGs, on a frame-by-frame basis (Hoang et al. 2018; Pizzolato et al. 2015; Sartori et al. 2014). In this optimisation, the objective function ( $f_{EMG-assisted}$ ) minimises  $E_{sumEXC}$ ,  $E_{Moment}$  and the sum squared tracking errors between the experimental and adjusted EMG linear envelopes ( $E_{EMG}$ ), i.e.

$$f_{EMG-assisted} = \alpha E_{Moment} + \beta E_{sumEXC} + \gamma E_{EMG} \quad (7)$$

where the weighting factor  $\alpha$  was set to 1, while  $\beta$  and  $\gamma$  were optimised to obtain a balance between the minimised tracking errors for the EMG linear envelopes and experimental joint moments (Hoang et al. 2018; Pizzolato et al. 2015; Sartori et al. 2014). In comparison, for static optimisation  $\gamma$  was set to zero, while  $\alpha$  and  $\beta$  were set to 1 and 2 respectively.

Calibrated EMG-informed models, *Cal<sub>EMG</sub>a* and *Cal<sub>EMG</sub>a<sup>MRI</sup>*, were specifically developed to account for the musculoskeletal differences between the TD and CP participants' MTU parameters. This was a two-step process in CEINMS: 1) model calibration to the individual, and then 2) model execution where muscle excitation patterns were estimated using EMG-assisted approach as described above (Pizzolato et al. 2015; Sartori et al. 2014). Calibration in general, used two trials, one walking and one heel raising, to adjust the EMG-to-muscle activation parameters, TSL and OFL values, and muscle group strength coefficients (see Table 7 muscle groupings) to reduce the error between experimental (i.e., from OpenSim's inverse dynamics) and NMSK model predicted (i.e., from CEINMS) ankle plantarflexion, knee flexion, hip flexion and hip adduction moments. In calibration, the NMSK model's only inputs were the EMG linear envelopes and MTU kinematics estimated by OpenSim muscle analysis tool.

In  $Cal_{EMGa}$ , TSL and OFL were set differently for each participant. For the TD participant, calibration adjusted the TSL and OFL within  $\pm 5\%$  of the base model values, while for both participants, their muscle group strength coefficients were bound between 0.5 and 1.5 (Figure 43, Supplementary material). For the CP participant, the initial OFLs were taken from the base model ( $unCal_{EMGa}$ ) and adjusted for only those muscles whose segmented volumes ( $V_{CP}$ ) were at least 20% smaller than the corresponding muscles in the TD participant ( $V_{TD}$ ), i.e. the medial and lateral gastrocnemii, tensor fasciae latae, gracilis and rectus femoris muscles. The adjusted CP OFL initial values were reduced by 0.7 (refer to Appendix B for details) to simulate the effect of overstretched sarcomeres observed in contracted muscles (Mathewson and Lieber 2015). For a given fibre length, an increase in sarcomeres length would mean less sarcomeres in series, therefore a reduced OFL. From this, the model was then calibrated in CEINMS to allow for a  $\pm 5\%$  OFL variation (Figure 43, Appendix A), while allowing TSLs to increase from 0 to 10% (10% as reported in literature (Barber et al. 2012)), for all muscles, to simulate tendon lengthening shown to occur in CP (Barber et al. 2009; Barrett and Lichtwark 2010). Once calibrated, the models were executed using an EMG-assisted approach (Pizzolato et al. 2015; Sartori et al. 2014).

A final level of personalisation ( $Cal_{EMGa}^{MRI}$ ) was deemed necessary to account for volumetric muscle deficits associated with the morphological alterations in children with CP (see Table 24, Appendix A for differences between the TD and CP participant). To this end,  $Cal_{EMGa}^{MRI}$  featured subject-specific  $F_{max}^{iso}$  values (Table 25, Appendix A) for the primary MTUs spanning the knee and ankle joints (i.e., the fifteen segmented muscles per participant), in addition to the previously updated and calibrated MTU parameters of  $Cal_{EMGa}$ .  $F_{max}^{iso}$  was determined by:

$$F_{iso}^{max} = \sigma \frac{V^m}{l_0^m} \quad (8)$$

where  $V^m$  is the muscle volume from MRIs,  $l_0^m$  is the OFL calculated as per  $Cal_{EMGa}$  and  $\sigma$  is the muscle specific tension, which was set to  $55 \text{ N/cm}^2$  (O'Brien et al. 2010) for all muscles. Based on the participants height we used the muscle specific tension reported for men ( $55 \pm 11 \text{ N cm}^{-2}$ ), which is  $<2\%$  larger, and essentially same value, as reported for boys ( $54 \pm 14 \text{ N cm}^{-2}$ ) (O'Brien et al. 2010). After setting the  $F_{max}^{iso}$  values, a final re-calibration step was performed to minimally adjust MTUs parameters within  $\pm 2.5\%$  (Figure 43, Appendix A), while not adjusting the muscle strength coefficients. After model calibration to individual, the models were executed again using the EMG-assisted approach described above (Pizzolato et al. 2015; Sartori et al. 2014).

## Data analysis

All estimates were time normalised to the stance phase duration and averaged across three walking trials. Additionally, joint moments, muscle forces and JCFs results were amplitude-normalised to body weight (BW). Root mean square error (RMSE) and coefficient of determination ( $R^2$ ) between experimental and predicted muscle excitations and joint moments were computed to assess the physiological and biomechanical validity of each NMSK model. Computed muscle forces and JCFs were qualitatively compared via time-series plots.

## Statistical analysis

Prior to any statistical analysis, all data were checked for normality conducting the Shapiro-Wilk test in the Statistical Package for Social Science (SPSS) software. If the data distribution were normal, a one-way repeated measures ANOVA test with Bonferroni correction was used to determine whether increasing the level of subject-specificity of NMSK model was associated with improvements in muscle excitations tracking ( $R^2$  and RMSE, versus experimental data). Otherwise, a Friedman test was conducted, followed by post hoc analysis with Wilcoxon signed-rank tests with Bonferroni adjustments. Values were calculated individually for each of the 12 collected muscles and reported as mean across all muscles. All statistical analyses were performed in the SPSS software (v25), with statistical significance being  $P < 0.05$ .

## Results

All models accurately reproduced experimental knee joint moments (Figure 23a-b and Figure 44, Appendix A). The CP participant's  $R^2$  values were close to 1.0, while the TD child's  $R^2$  values ranging between 0.944 (SD 0.073) and 0.986 (SD 0.004) (Table 23 and Figure 44, Appendix A), depending on the model. Additionally, for both TD and CP participants', RMS errors were smaller than 0.053 Nm/kg.

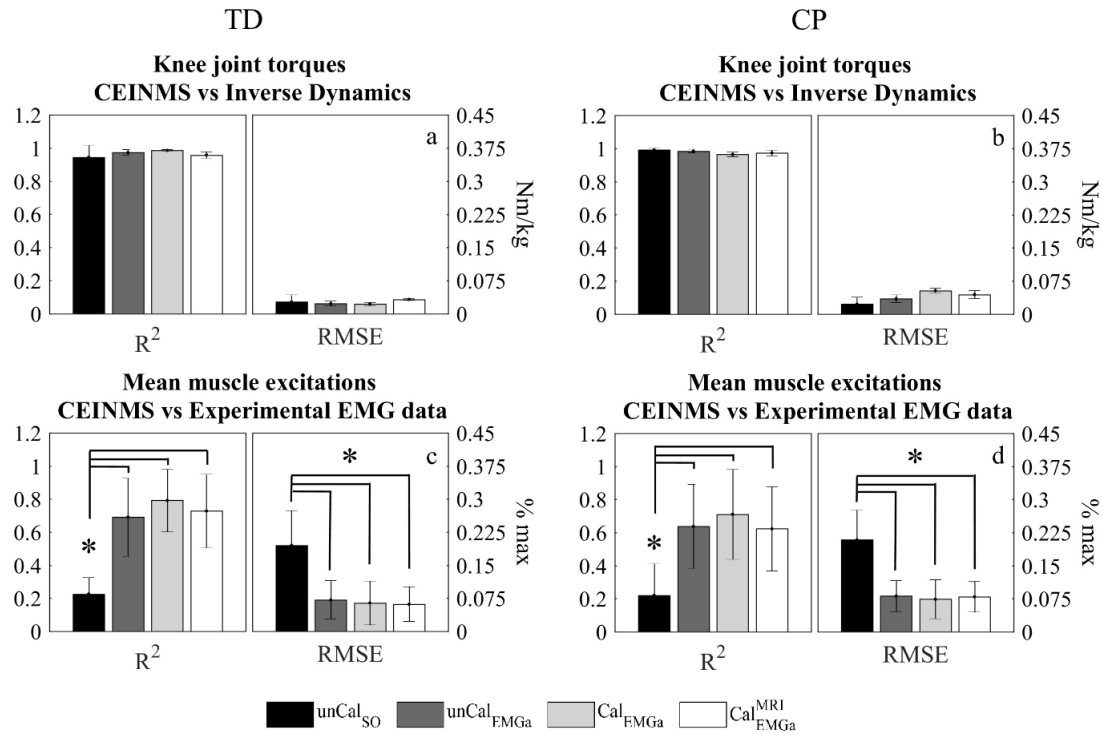


**Figure 23.** Models accuracy in tracking experimental moments and muscle excitations. Comparison between CEINMS models predictions (i.e., joint moments (a and b) and muscle excitations (c and d)) and corresponding experimental data (i.e., external joint moments and EMG linear envelopes) for a typically developing child (left) and his twin brother with CP (right).  $R^2$  and RMSE values (with relative standard deviation) are reported on the left and right hand-side of each subplot, respectively. Different colours refer to different NMSK models. All results are averaged across three walking trials. Muscle excitations are reported as mean value of the twelve analysed lower limb muscles. Stars indicate statistically significant differences ( $P < 0.05$ ).

Regarding muscle excitations, there were no differences in  $R^2$  values between  $unCal_{EMGa}$ ,  $Cal_{EMGa}$  and  $Cal_{EMGa}^{MRI}$  for both participants ( $R^2 \geq 0.691$  and  $R^2 \geq 0.623$ , for the TD and CP participant respectively). On the other hand,  $unCal_{SO}$  produced significantly poorer estimates of experimental EMG data ( $R^2 = 0.226$ , for TD, and  $R^2 = 0.221$ , for CP) compared to the EMG-assisted models ( $P \leq 0.002$ ). Additionally,  $unCal_{SO}$  was associated with the largest muscle excitations RMSEs among the four models, for both participants ( $P < 0.002$  versus  $unCal_{EMGa}$ ,  $Cal_{EMGa}$ ,  $Cal_{EMGa}^{MRI}$ ).

Muscle forces for the MTUs crossing the knee joint (Figure 24. All estimated muscle forces are reported in Figure 45 and Figure 46, Appendix A) were generally larger in magnitude using the three EMG-assisted models (i.e.,  $unCal_{EMGa}$ ,  $Cal_{EMGa}$  and

$Cal_{EMGa}^{MRI}$ ), in comparison to  $unCal_{SO}$ , which solely employed static optimisation. Only exception being the MG muscle, for which  $Cal_{EMGa}$  and  $Cal_{EMGa}^{MRI}$  produced smaller forces compared to both uncalibrated models. In the CP condition, total knee JCF estimates were lowest for much of stance phase in  $unCal_{SO}$  (Figure 25), compared to the other models.  $unCal_{EMGa}$  produced the largest total JCFs predictions for both TD and CP, while  $Cal_{EMGa}$  and  $Cal_{EMGa}^{MRI}$  produced similar total JCF profiles, which were lower than predictions from  $unCal_{EMGa}$  and higher than predictions from  $unCal_{SO}$ . The most subject-specific NMSK model ( $Cal_{EMGa}^{MRI}$ ) and the generic model ( $unCal_{SO}$ ) generated considerably different normalised JCFs (Figure 26) for the child with CP.

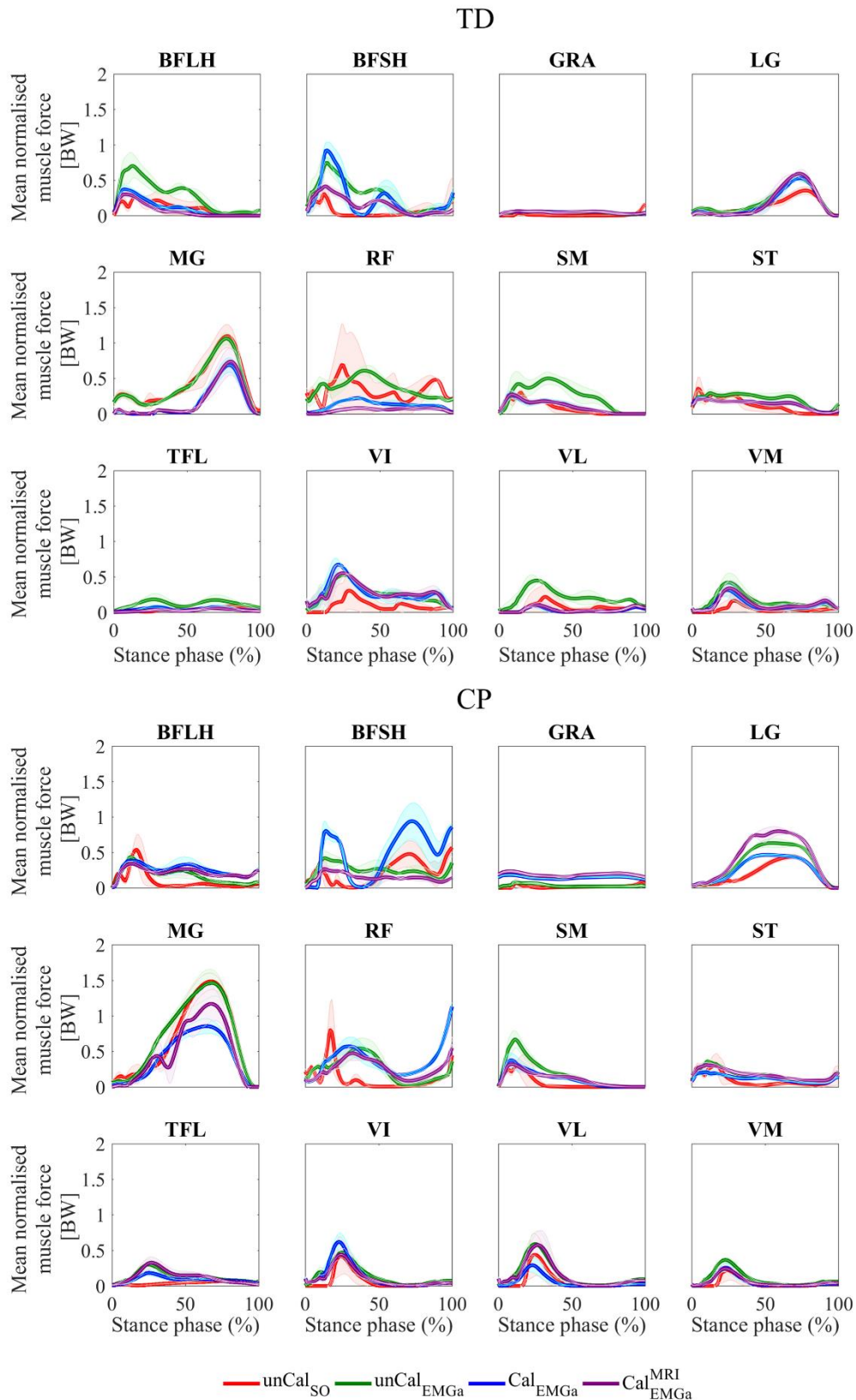


**Figure 24.** Estimated muscle forces acting on the knee. Estimated muscle forces for the MTUs contributing to the knee adduction-abduction moment, which was used to compute knee joint contact forces. Forces are reported as mean values (solid line)  $\pm$  standard deviation (shaded areas) across 3 trials (red = unCal<sub>SO</sub>, green = unCal<sub>EMGa</sub>, blue = Cal<sub>EMGa</sub> and purple = Cal<sub>EMGa</sub><sup>MRI</sup>) and expressed in bodyweight (BW).

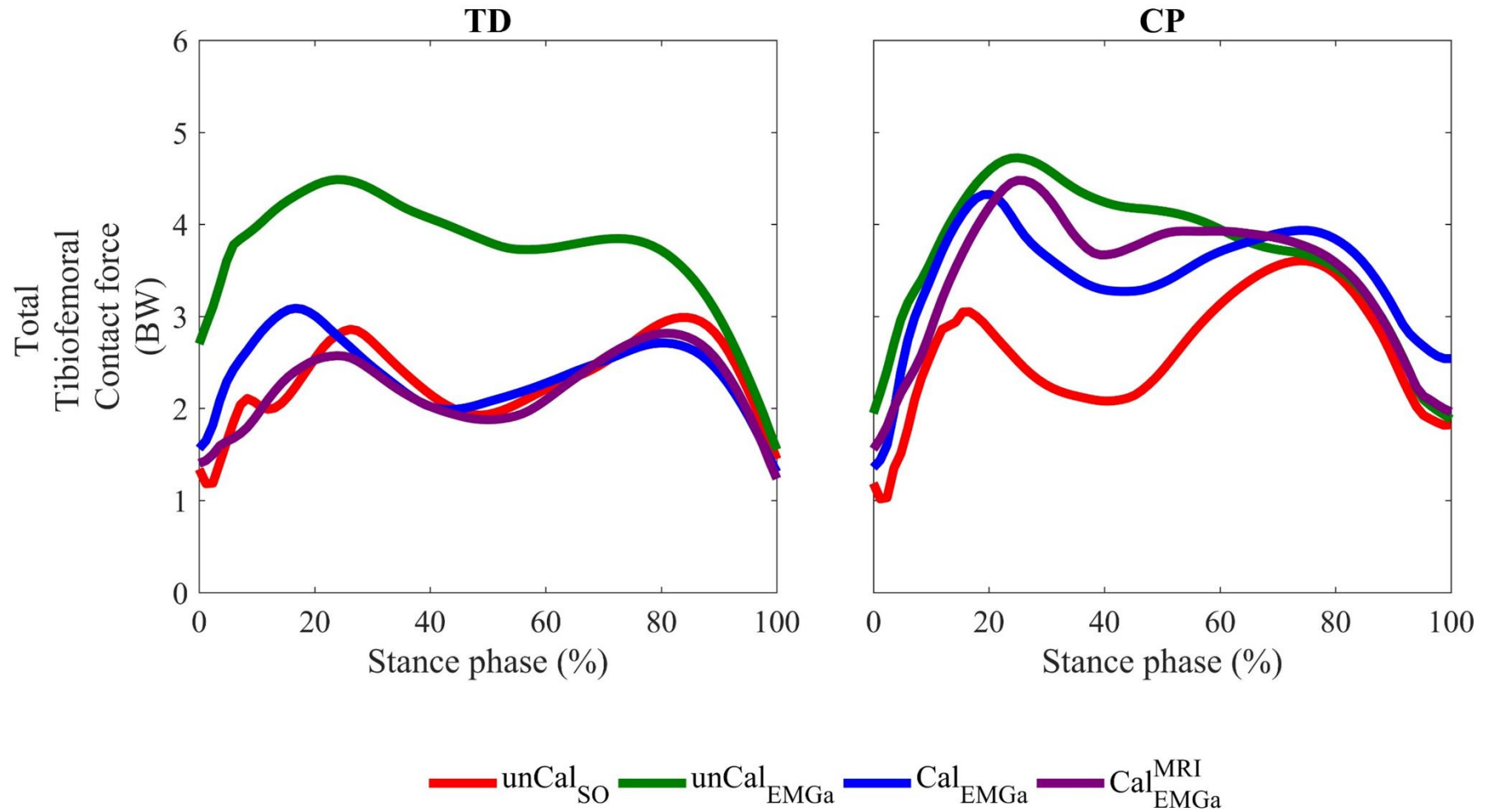


**Figure 25.** Total tibiofemoral contact forces estimates. Total tibiofemoral contact forces estimated using the four developed NMSK models. Results are normalised to each subject’s bodyweight (BW) to allow for comparisons and reported as mean values.

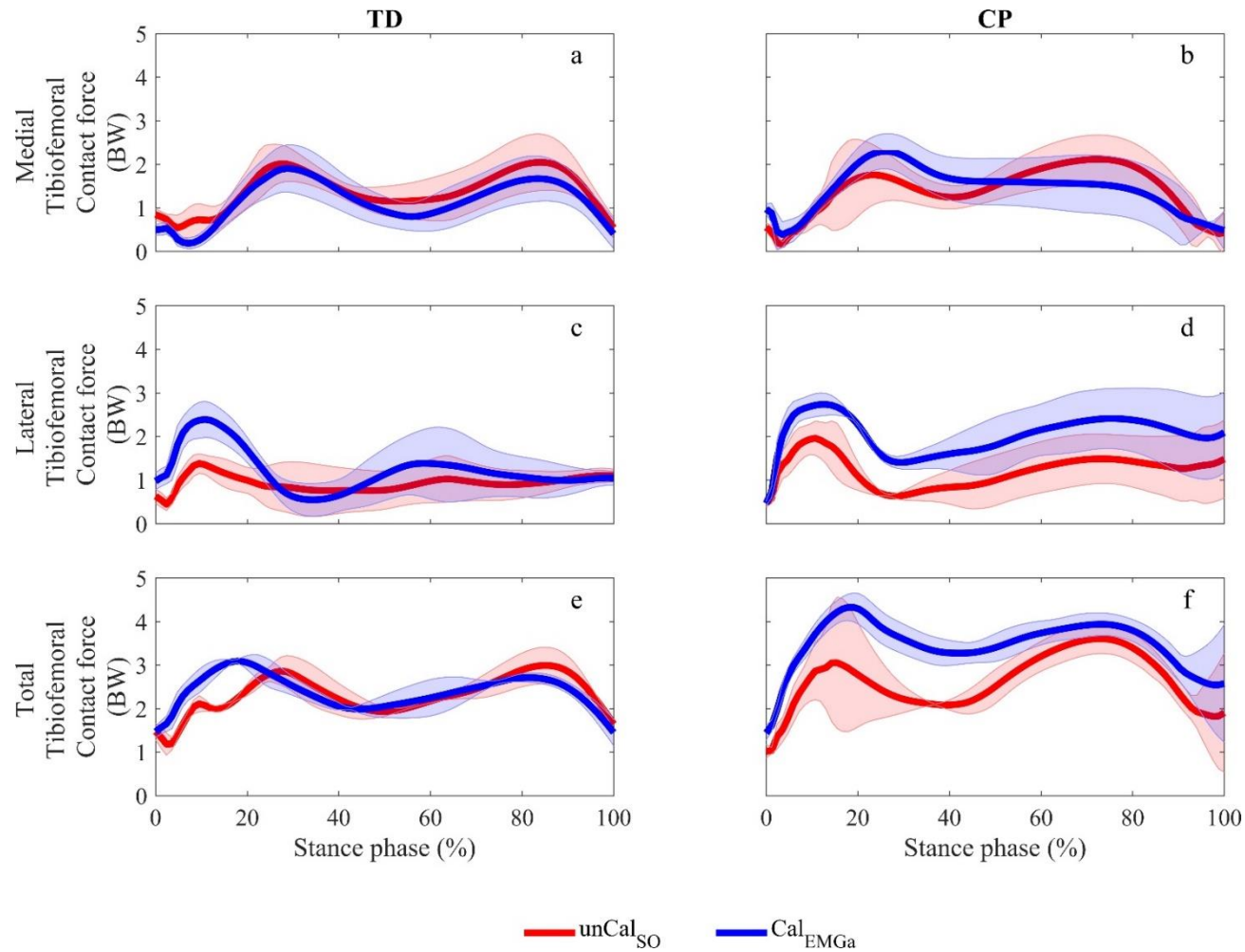


**Figure 26.** Comparison of medial, lateral and total tibiofemoral contact forces using Static optimisation versus an EMG-assisted approach. Medial, lateral and total tibiofemoral contact forces estimated using static optimisation methods (red) and an EMG-assisted approach (blue), for a child with CP (right side) and his TD twin brother (left). Results are reported as mean values  $\pm$  standard deviation.

## Discussion

Four NMSK models with increasing levels of subject-specificity were developed and implemented to simulate the gait of a child with unilateral spastic CP (GMFCS I) and the gait of his typically developed twin brother. Each model was assessed according to experimental joint moments and muscle excitations tracking accuracy, and estimates of physiologically plausible muscle forces and JCFs. For the first time an EMG-assisted approach was used with staged levels of MTU subject-specificity to estimate knee JCFs in a TD child and a child with CP. The unique recruitment of identical twin participants allowed for exact matching of genetics and age. Additionally, both children had been exposed to similar physical activity opportunities and had comparable height and weight (Table 21, Appendix A).

In partial agreement with our first hypothesis, the EMG-assisted models (*unCal<sub>EMG<sub>a</sub></sub>*, *Cal<sub>EMG<sub>a</sub></sub>* and *Cal<sub>EMG<sub>a</sub></sub>*<sup>MRI</sup>) better tracked muscle excitations compared to *unCal<sub>SO</sub>*, which only employed static optimisation. However, there were no differences between models in the tracking of external knee joint moments (Figure 23). High correlation values between experimental and estimated joint moments ( $R^2 > 0.94$ ) were obtained with all four NMSK models, demonstrating how both static optimisation methods and EMG-assisted approaches were able to match external joint moments. For *Cal<sub>EMG<sub>a</sub></sub>* and *Cal<sub>EMG<sub>a</sub></sub>*<sup>MRI</sup>, this was ensured by the joint moment error minimisation step embedded in the CEINMS calibration process (Pizzolato et al. 2015). Nonetheless, good joint moment tracking did not necessarily correspond to accurate predictions of experimental muscle excitations. When linearly scaled-generic MTU parameters were used in conjunction with static optimisation methods (*unCal<sub>SO</sub>*) experimental EMG data were not well reproduced ( $R^2 < 0.23$ , as opposed to  $R^2 \geq 0.62$  using *unCal<sub>EMG<sub>a</sub></sub>*, *Cal<sub>EMG<sub>a</sub></sub>* and *Cal<sub>EMG<sub>a</sub></sub>*<sup>MRI</sup>), suggesting that static optimisation methods may not produce physiological muscle activation patterns when tracking external joint moments. In contrast, the EMG-assisted models were able to accurately track both experimental joint moments and muscle excitations, suggesting a more physiologically feasible solution to the musculoskeletal redundancy problem, and likely better estimates of muscle forces and JCFs.

In contrast to our second hypothesis, *unCal<sub>EMG<sub>a</sub></sub>*, *Cal<sub>EMG<sub>a</sub></sub>* and *Cal<sub>EMG<sub>a</sub></sub>*<sup>MRI</sup> exhibited a similar level of accuracy in tracking experimental joint moments and EMG data. This could misleadingly suggest that increasing the level of subject-specificity by personalising MTUs parameters (i.e., TSL, OFL and/or maximal isometric force) did not

add value to the model. However, improving subject-specificity did affect the predicted muscle forces and JCFs. When TSL and OFL were not calibrated (*unCal<sub>EMGa</sub>*), estimated muscle forces were in most cases large compared to the other EMG-assisted models predictions (Figure 24), leading to large knee JCFs estimates (Figure 25). This was clearer on the TD models, further highlighting the limitations of linearly scaled MTU parameters to accurately characterise paediatric muscles, particularly in healthy populations. Conversely, *Cal<sub>EMGa</sub>* and *Cal<sub>EMGa</sub><sup>MRI</sup>* produced similar and more physiological JCF profiles when compared to published in-vivo knee joint load data (Fregly et al. 2012a), which, for our TD subject, were also comparable both in magnitude and shape to *unCal<sub>SO</sub>* outputs and in-line with previous findings (Steele et al. 2012). Finally, although we expected *Cal<sub>EMGa</sub><sup>MRI</sup>* to be more representative of each subject due to its highest level of subject-specificity (Table 8), there were only small difference in estimated JCF profiles between *Cal<sub>EMGa</sub>* and *Cal<sub>EMGa</sub><sup>MRI</sup>*. Therefore, *Cal<sub>EMGa</sub>* might be a preferred option, as it does not require collection and segmentation of full lower limb MRIs to inform muscle parameters in the musculoskeletal model. In this case, strength reduction thresholds from dynamometry testing, as opposed to the 20% volume reduction threshold on MRI, could be used as a surrogate measure to identify MTUs that require OFL adjustment to represent CP affected muscle.

In agreement with our third hypothesis, the use of an EMG-informed approach with calibrated MTU parameters enabled us to discern between TD and CP knee JCFs, particularly in early stance during load acceptance (Figure 26). Conversely, static optimisation produced similar results between the two participants, which was an interesting finding given the differences observed in (1) joint angles and joint moments and (2) the linear envelopes of collected EMG data between the two conditions (Figure 42, Appendix A). In addition, for both participants, the *unCal<sub>SO</sub>* model tended to underestimate loading on the lateral compartment of the knee joint compared to the *Cal<sub>EMGa</sub>* model (Figure 26c-d), suggesting an inability of static optimisation to reproduce muscle co-contraction (Lloyd and Besier 2003) in healthy children and children with CP. Finally, inspection of muscle force profiles revealed similar profiles between the two subjects when static optimisation was adopted, but different, both in magnitude and profile (e.g., MG and LG muscles, Figure 24), when using an EMG-assisted approach. The ability to accurately estimate (knee) JCFs may be of particular relevance in the study and management of CP. Internal quantities, such as JCFs, may be used as biomarkers of disease progression and/or of the risk of developing osteoarthritis (Richards et al. 2018),

both impacting on an individual's quality of life. Moreover, estimated JCFs may serve as boundary data for dedicated surgery and implant design (Bergmann et al. 2016).

There are limitations to this study that need consideration. First, estimated muscle forces and JCFs were qualitatively compared, as only two participants were included in the analysis. Extending the investigation to a larger cohort would help supporting current findings and provide further understanding of the level of subject-specificity required. However, the strength of this study was using identical twins that allowed near exact matching, in terms of age, height, weight, genetics and exposure to similar physical activity opportunities. Previous research has focussed on twins with CP (van Drongelen et al. 2013) using standard clinical gait analysis. However, our research added the collection of EMG and MRI data to inform the development of four NMSK models with increasing levels of complexity, which is a large technical achievement for the field. Second, the overall number of processed trials per subject (i.e., four stance phases) was limited, collecting only walking and heel raising tasks in an effort to reduce the physical burden on the CP participant. This may have resulted in inadequately optimised morphological parameters if only using single-joint single-DOF in model calibration (Falisse et al. 2017) and a local optimisation method. However, we performed multi-joint and multi-DOF calibration with a global optimiser (i.e. simulated annealing) in CEINMS, which was previously shown to produce excellent parameter calibration with limited trials (Sartori et al. 2012). Third, EMG signals from more and/or different muscles should be acquired during the data collection to ensure a more comprehensive and accurate EMG mapping. However, to accommodate this issue, we used EMG-assisted modelling that accounted for muscles without EMG using a hybrid of EMG-driven and static optimisation, while ensuring excitations that produced a dynamically consistent model (Sartori et al, 2014; Pizzolato et al 2015). Fourth, the 20% threshold of volume deficiency (between TD and CP) to identify affected muscles was based on previously reported muscle volume reduction in CP (Barrett and Lichtwark 2010; Handsfield et al. 2015). However, this value may vary according to the severity of CP and across lower limb muscles. Furthermore, more advanced imaging methods (Lichtwark et al. 2017; Mathewson et al. 2015) may better inform the choice of the scaling factor for the OFLs, here set to 0.7 based on literature data. More accurate representations of the underlying anatomy and physiology may be achieved incorporating additional subject-specific detail to the models, such as MRI derived bones and joint models (da Luz et al. 2017), and muscle pathways. Finally, in this study we modelled the foot as a single-segment body, which may be an over simplification in the presence of foot deformities or altered mid-

foot motion. However, this was not the case of the enrolled twin with CP. Therefore, the model presented likely reflected his ankle kinematics and triceps surae length changes during gait.

## Conclusions

Personalisation, as implemented in models  $Cal_{EMGa}$  and  $Cal_{EMGa}^{MRI}$ , appears to be crucial to better reproduce the internal biomechanics of the human body and consequently to produce physiologically plausible estimates of both muscle forces and JCFs. To this end, EMG-informed approaches should be preferred over optimisation methods, especially in the study of neuromuscular disorders such as CP, given the inability of static optimisation to accurately reproduce atypical muscle activity. In agreement with previous work (Hoang et al. 2018) we found it is essential to calibrate linearly scaled-generic MTUs parameters in order to avoid abnormal muscle forces and JCFs production, even in healthy populations. Finally, the validity of a NMSK model cannot be solely assessed based on its ability to reproduce external joint measurements. All models proved to be able to track experimental torque data despite showing different levels of accuracy in tracking muscle excitations as well as dissimilar muscle forces and JCFs estimates.

## Conflicts of interest

All authors declare no conflicts of interest.

## Funding

The authors would like to acknowledge the funding support for this research. CC was supported by an Advance Queensland Research Fellowship. GD would like to acknowledge Griffith University and Menzies Health Institute Queensland for the PhD scholarship.

## CHAPTER 5

---

# **Best methods and data to reconstruct paediatric lower limb bones for musculoskeletal modelling**

### *Acknowledgement of co-authorship*

This chapter includes a co-authored paper that has been re-formatted for this thesis. The bibliographic details/status of the co-authored paper, including all authors, are:

Davico, G., Pizzolato, C., Killen, B.A., Barzan, M., Suwarganda, E., Lloyd, D.G., Carty, C.P. Best methods and data to reconstruct paediatric lower limb bones for musculoskeletal modelling. *Biomechanics and Modeling in Mechanobiology*. 2019. <https://doi.org/10.1007/s10237-019-01245-y>.

I made a substantial contribution in the conception and design of this study, data collection, analysis and interpretation of data, drafting and revising of the final manuscript.

Student/ Corresponding author: Giorgio Davico

Principal supervisor: David G Lloyd

# Abstract

**Background:** In biomechanical simulations, generic linearly scaled musculoskeletal anatomies are commonly used to represent children, often neglecting or oversimplifying subject-specific features that may affect model estimates. Inappropriate bone sizing may influence joint angles due to erroneous joint centre identification. Alternatively, subject-specific image-based musculoskeletal models allow for more realistic representations of the skeletal system. To this end, statistical shape modelling (SSM) and morphing techniques may help reconstructing bones rapidly and accurately. Specifically, the Musculoskeletal Atlas Project (MAP) Client, which employs magnetic resonance imaging (MRI) and/or motion capture data to inform SSM and non-rigid morphing techniques, proved able to accurately reconstruct adult pelvis and femur bones. Nonetheless, to date, the above methods have never been applied to paediatric data.

**Methods:** In this study, paediatric pelvis, femurs and tibiofibular bones of 18 typically developing children were reconstructed using the MAP Client. Ten different combinations of SSM and morphing techniques, i.e., pipelines, were developed. Generic bone geometries from the gait2392 OpenSim model were linearly scaled for comparisons. Jaccard index, root mean square distance error and Hausdorff distance were computed to quantify reconstruction accuracy. For the pelvis bone, colour maps were produced to identify areas prone to inaccuracies and hip joint centres (HJC) location was compared. Finally, percent difference between MRI- and MAP-measured left-to-right HJC distances was computed.

**Findings:** Pipelines informed by MRI data, alone or in combination with motion capture data, accurately reconstructed paediatric lower limb bones (i.e. Jaccard index  $> 0.8$ ). Scaled OpenSim geometries provided the least accurate reconstructions. Principal component-based scaling methods produced size-dependent results, which were worse for smaller children.

# Introduction

Musculoskeletal (MSK) models are powerful tools that can be used to investigate the internal biomechanics of the human body (Delp et al. 2007; Marra et al. 2015). Combined with experimental data (e.g., ground reaction forces and motion capture, MOCAP, data). MSK models can simulate locomotion (Delp et al. 2007) and estimate muscle forces and joint contact forces (JCF) (Moissenet et al. 2014). MSK models thus provide an alternative to invasive methods, such as instrumented implants (Fregly et al. 2012a), and have the potential to assist clinical decision making via virtual surgery planning (Delp et al. 1990; Fregly et al. 2012b) and predictive simulations (Jonkers et al. 2003). Nonetheless, there are a number of considerations that need to be taken into account when interpreting results from MSK modelling simulations.

Commonly used MSK models are based on generic skeletal anatomies gathered from small cohorts of healthy older adult (male) subjects (Delp et al. 1990). Routine personalisation involves linear scaling to resize generic bony geometries to each individual's dimensions. However, the further an individual's anthropometry differs from the generic model (e.g., small stature, deformity), the more likely their scaled model will be an inaccurate anatomical representation. Inaccurate bony geometries will consequently affect joint definitions by altering the location of joint centres (Bahl et al. 2019; Gerus et al. 2013; Lenaerts et al. 2008), which in turn will affect joint angle and joint moment calculations (Kainz et al. 2017a). Furthermore, muscle attachments may be inappropriately positioned (Duda et al. 1996), leading to erroneous muscle-tendon units (MTU) length and moment arm estimates (Scheys et al. 2011b; Scheys et al. 2008a) ultimately affecting predicted muscle function (Garijo et al. 2017; Heller et al. 2003; Passmore et al. 2018). Fortunately, subject-specific image-based MSK models (Blemker et al. 2007; Bosmans et al. 2014; Murray et al. 1998; Passmore et al. 2018) may overcome these problems.

Subject-specific bone reconstructions can be obtained via segmentation of medical images (Blemker et al. 2007; da Luz et al. 2017). Magnetic resonance imaging (MRI) and computed tomography (CT) are commonly employed for qualitative and quantitative assessment of bones in clinical settings (Eckstein et al. 2006; Hong et al. 2000; Oei et al. 2016). Alternatively, new technologies, such as EOS (Melhem et al. 2016) and 3D ultrasound (Parmar et al. 2010; Treece et al. 2003), may be used for imaging purposes to reduce time, costs and exposure to radiation. However, segmenting medical images is often a manual and time-consuming process, with the exception of CT scan

segmentation that can be fully automated (Cootes et al. 1995; Krčah et al. 2011). Nonetheless, MRI images are more appealing for many MSK modelling applications compared to CT scans, which are characterised by inferior soft tissue contrast (Sharma and Aggarwal 2010) that prevents individual muscles segmentation. Moreover, cartilage, ligaments and other soft tissues may not be visible on CT scans (Hayashi et al. 2016). Upon segmentation, reconstructed three-dimensional bony geometries may be employed to generate subject-specific skeletal models (Valente et al. 2017), enabling the investigation of subject-specific joint kinematics and joint kinetics (da Luz et al. 2017). However, muscle origin and insertion points are not embedded in such bone models (i.e. the reconstructed three-dimensional bony geometries). Therefore, if muscle forces and JCFs are to be studied, muscle attachments and muscle pathways would need to be manually defined or morphed from a pre-existing dataset. Internal parameters (e.g. muscle forces), which are critical for clinical decision making (Steele et al. 2017), cannot be studied otherwise. To this end, MRI images may be used to assist in the process (Scheys et al. 2011b; Scheys et al. 2006; Scheys et al. 2009; Scheys et al. 2008b), possibly reducing time consumption and increasing precision. Statistical shape modelling (SSM) and morphing techniques, such as host-mesh fitting (HMF) and local-mesh fitting (LMF) (Fernandez et al. 2004), are alternative methods to manual segmentation of bones from medical images. The open-source software Musculoskeletal Atlas Project (MAP) Client (Zhang et al. 2014b) combines SSM and fitting methods to reconstruct lower limb bones and allows for the customisation of the gait2392 OpenSim MSK model (Delp et al. 1990) with personalised bony geometries. Furthermore, since each MAP generated bone embeds information on muscles attachments, the resulting customised MSK model can be directly employed to estimate muscle forces and JCFs. Within the MAP Client, mean statistical shape bone models, resulting from a database of 26 adult lower limbs (and over 200 femurs), are typically morphed along a set of principal components (PCs) in order to minimise the error between correspondent landmarks/measurements on the mean model and on experimental data (i.e., medical images or MOCAP data). However, all PCs currently implemented in the MAP Client were extracted from the above adult dataset. As such, the MAP Client may not be able to accurately reconstruct paediatric bones whose shapes and sizes are not comprised in the training adult population. To improve bone reconstructions (i.e., increase accuracy of bone models), segmentations of medical images (be those MRI or CT scans) may be used to inform and guide the morphing process via HMF and LMF techniques. The underlying idea is that the more data provided, the better the reconstructions. Nevertheless, incomplete segmentations potentially provide

sufficient information to accurately reconstruct adult femur and pelvis geometries (Nolte et al. 2016; Suwarganda et al. 2019; Zhang and Besier 2017). To date, the accuracy of paediatric bone models produced from the MAP Client has not been investigated

We systematically set out four aims to determine the most accurate methods to reconstruct paediatric pelvis (without sacrum), femurs and tibiofibular bones using SSM and morphing techniques. (1) Determine whether linear or non-linear approaches are best for scaling lower limb paediatric bones, (2) determine whether incomplete sets of MRI data could be used to improve scaled bone geometries, (3) investigate the benefits of including mesh fitting methods to correct for possible inaccuracies derived from scaling approaches and (4) investigate the effect of reconstruction inaccuracies on hip joint centre estimates. To this end, we implemented ten different combinations of morphing techniques, henceforth referred to as pipelines, in the MAP Client that were informed by MOCAP data only, MRI data only or by a combination of both MOCAP and MRI data. Furthermore, both complete and sparse segmentations were evaluated to identify the minimum MRI data required for accurate scaling (according to Suwarganda and colleagues (2019)). We hypothesised that (H1) pipelines employing PC-based methods would not produce satisfactory results compared to previous results (Nolte et al. 2016; Suwarganda et al. 2019) when applied to a paediatric population, (H2) incomplete sets of medical images would be sufficient to enable accurate bone reconstructions (i.e. shape similarity index  $> 0.8$  when compared to MRI segmentations), (H3) providing both MOCAP and MRI segmentations would improve results and (H4) that pelvis reconstruction accuracy, as determined by hypotheses H1-3, would be related to improved hip joint centre estimates.

# Material and Methods

## Participants

Data from 18 typically developing children were included in the study (Height:  $144.78 \pm 16.24$  cm, age:  $10.78 \pm 2.78$  years, Table 9). All procedures were approved by the institutional Research Ethics Committee and informed consent was provided.

**Table 9.** Demographics of participants. Age and height are reported as mean (standard deviation) across the studied population.

| <b>Subject<br/>[ID]</b> | <b>Height<br/>[cm]</b> | <b>Age<br/>[years]</b> |
|-------------------------|------------------------|------------------------|
| <b>TD01</b>             | 116                    | 6.5                    |
| <b>TD02</b>             | 117                    | 6                      |
| <b>TD03</b>             | 123.5                  | 8                      |
| <b>TD04</b>             | 132.5                  | 8.5                    |
| <b>TD05</b>             | 133                    | 8                      |
| <b>TD06</b>             | 134                    | 9                      |
| <b>TD07</b>             | 138.5                  | 10.5                   |
| <b>TD08</b>             | 141                    | 10                     |
| <b>TD09</b>             | 144                    | 11                     |
| <b>TD10</b>             | 148                    | 12                     |
| <b>TD11</b>             | 150                    | 11                     |
| <b>TD12</b>             | 153                    | 12                     |
| <b>TD13</b>             | 154                    | 12                     |
| <b>TD14</b>             | 157                    | 12                     |
| <b>TD15</b>             | 161                    | 12                     |
| <b>TD16</b>             | 163                    | 15                     |
| <b>TD17</b>             | 168.5                  | 18                     |
| <b>TD18</b>             | 172                    | 15                     |
| <b>Mean(SD)</b>         | 144.78(16.24)          | 10.78(2.78)            |

## Data collection and processing

Fifty-one retro-reflective MRI-compatible surface markers were placed on anatomical landmarks (Table 10) by an experienced motion capture physiotherapist. Marker trajectories were collected using a 10-camera motion capture system (Vicon Motion

System, Oxford, UK. 100 Hz) with subjects standing in T-pose (Cappozzo et al. 1995). Motion capture data were cleaned and labelled in Vicon Nexus 2.5, then processed in MATLAB using the MOtoNMS toolbox (Mantoan et al. 2015). Trajectories were filtered using a 4<sup>th</sup> order 6 Hz low-pass Butterworth zero-lag filter. Finally, hip, knee and ankle joint centres were computed for scaling purposes. Hip joint centres (HJCs) were determined using the Harrington equation (Harrington et al. 2007), which is commonly used in clinical gait analysis as it provides the most accurate *in vivo* estimates (Kainz et al. 2015). Knee and ankle joint centres were defined as the midpoint between medial and lateral knee condyles and medial and lateral malleoli markers, respectively.

**Table 10.** Landmarks positions of the MOCAP markers. Anatomical landmarks name and location of the 51 retro-reflective markers affixed on each participants' body.

| <b>Body segment</b> | <b>Marker name</b> | <b>Anatomical landmark</b>         |
|---------------------|--------------------|------------------------------------|
| Back                | C7                 | 7 <sup>th</sup> Cervical Vertebra  |
|                     | T10                | 10 <sup>th</sup> Thoracic Vertebra |
|                     | CLAV               | Clavicle                           |
|                     | STRN               | Sternum                            |
|                     | RBAK               | Right back                         |
| Pelvis              | L/RASI             | Anterior superior iliac spine      |
|                     | L/RIC              | Lateral iliac crest                |
|                     | L/RPSI             | Posterior superior iliac spine     |
| Knee                | L/RKNE             | Lateral femoral condyle            |
|                     | L/RPAT             | Patella                            |
|                     | L/RMKNE            | Medial femoral condyle             |
|                     | L/RLTC             | Lateral tibial trochanter          |
|                     | L/RTTB             | Tibial tuberosity                  |
|                     | L/RMTC             | Medial tibial trochanter           |
| Foot                | L/RANK             | Lateral malleolus                  |
|                     | L/RHEE             | Calcaneus                          |
|                     | L/RMMAL            | Medial malleolus                   |
|                     | L/LMT1             | Big toe                            |
|                     | L/RTOE             | 2 <sup>nd</sup> toe                |
|                     | L/RMT5             | 5 <sup>th</sup> toe                |
| Thigh               | L/RTHI             | Thigh wand marker                  |
|                     | L/RTH1-3           | Thigh triad cluster                |
| Shank               | L/RTIB             | Tibia wand marker                  |
|                     | L/RTB1-3           | Tibial triad cluster               |

Medical imaging data were acquired as part of separate research projects on two different MRI scanners. Fifteen participants' images were acquired on a Magnetom Siemens 1.5 T (thickness: 1.0mm, voxel size: 0.83x0.83x1.0 mm<sup>3</sup>), while for the remaining 3 children, a Philips Insigna 3T was used (slice thickness: 1.0 mm, voxel size:

0.79x0.79x1.0 mm<sup>3</sup>). In both cases, full lower limb MRI scans were acquired with the subjects laying supine, employing sequences specifically optimised for identification of bone contours.

Bony structures were manually segmented from MRI data using the Mimics Research Suite v20 (Materialise, Leuven, Belgium). For each participant, the pelvis (excluding sacrum), left femur, and left tibiofibular bones were segmented using the multiple slice edit tool to define bone borders from which the volume was determined. To balance quality of segmentations and time consumption, bone contours were segmented finely (i.e., every other slice) in correspondence of complex shapes (e.g., femur head or the whole pelvis structure) and coarsely along the bone shafts where changes in shape were minimal and automatic contour interpolation could work well. All segmentations were then exported in stereolithography (STL) format.

## **Bone reconstruction using the MAP Client**

The open-source plug-in-based software MAP Client (Zhang et al. 2014b) was used to reconstruct paediatric lower limb bones by combining several SSM and morphing techniques. These included linear and non-linear PC scaling, HMF and LMF.

Linear scaling was informed by either MOCAP or MRI data. When using MOCAP data, linear scaling was performed as per OpenSim guidelines (Delp et al. 2007; Hicks et al. 2015). Selected bony landmarks (i.e., left and right anterior superior iliac spine; hip, knee and ankle joint centres) were used to calculate the scaling factors for each bone dimension by computing the ratio of Euclidean distances between virtual anatomical landmarks on the MAP model and corresponding MOCAP markers. Landmarks pairs for scaling were defined as per Kainz and colleagues' (2017b) recommendations. When using MRI data, linear scaling was performed using an iterative closest point algorithm, in which the SSMs were rigidly scaled to minimise the root mean square distance error (RMSE) between closest points on the MAP bone and on the corresponding MRI segmentation meshes. Although a better match in size was ensured, the original shape and curvature of the mean MAP SSMs were not altered.

Medical imaging and MOCAP data were also used to drive non-linear PC scaling. In this case, a user-defined number of PCs were employed to determine the directions along which to deform each mean MAP SSM. The goal was to minimise the distance error between (i) MOCAP markers and corresponding virtual landmarks on the morphed MAP model or (ii) nodal points on MRI and MAP bone point clouds, for MOCAP- and MRI-informed pipelines respectively. Principal components were used to explore the

whole range of shape variations within the MAP atlas, enabling a better fit of SSMs to experimental data. In accordance with previous studies (Nolte et al. 2016; Suwarganda et al. 2019), non-linear scaling employed four PCs to morph pelvis and femur bones and eight PCs for the tibiofibular bone when informed by MRI data. On the other hand, non-linear scaling methods informed by MOCAP data, which morphed all lower limb bones at once, used five PCs. Five PCs were identified as ideal to minimise distance error while using a least number of components since only small reductions in distance errors were observed when reconstructing adult pelvis and femur bones after increasing the number of PCs from four to five. User defined weighting factors (i.e., Mahalanobis distance) were set to guide the morphing process aiming to achieve a low final RMSE (i.e., below 2 mm), which ensured that the resulting morphed SSM properly fit experimental data, providing an acceptable approximation of the real bone.

Mesh fitting techniques were finally used to refine bone reconstructions. Both HMF and LMF fitting methods aimed to reduce nodal points distance errors between MAP bone models and corresponding MRI segmentations. HMF primarily improved on the overall shape of the bone by morphing nodal points while preserving the relative distance between them. LMF worked on a point-by-point base allowing for localised refinements. In a coarse-to-fine refinement fashion, HMF was performed prior to LMF. Method-specific weights and penalties (i.e., 2D and 3D Sobolev and boundary normal smoothing terms) were employed to preserve natural shapes and smoothness (Suwarganda et al. 2019).

## Pipeline development

The identification of the best combination of methods to generate paediatric lower limb bones with the minimal amount of data and highest level of accuracy followed a step-wise process composed of four main tests. The first test involved comparing linear and non-linear PC scaling approaches using MOCAP or MRI to assess which method resulted in best bone reconstruction. The second test assessed how different levels of MRI data sparsity (Figure 27) affected bone reconstruction. The third test assessed whether shape and curvature reconstruction inaccuracies could be corrected via pipelines involving combinations of morphing techniques (Figure 28). The fourth and final test assessed the error between HJC estimated by each pipeline and real HJC as determined from MRI data.

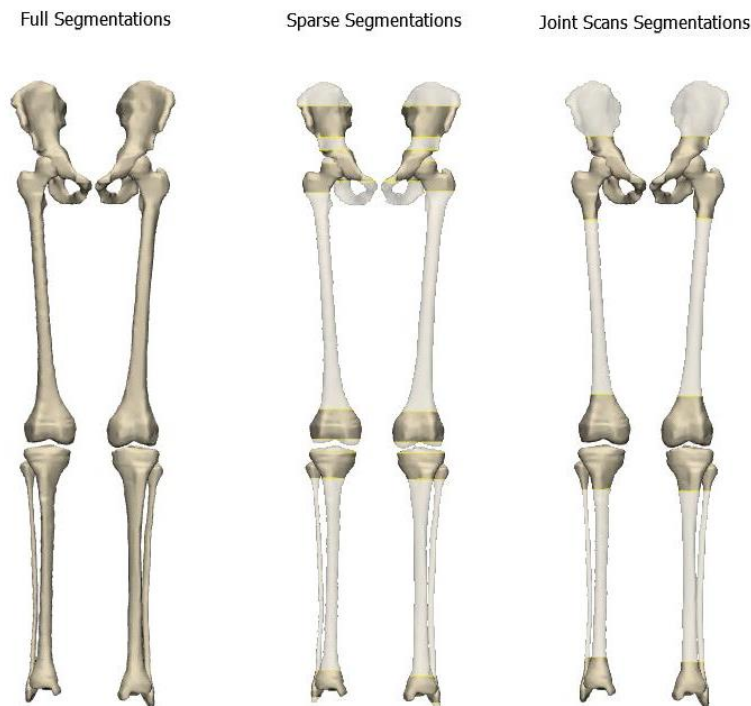


**Figure 27.** Different levels of medical imaging data provided to the MAP Client. Full (a) and sparse (b-c) MRI segmentations used in the MRI-informed pipelines.

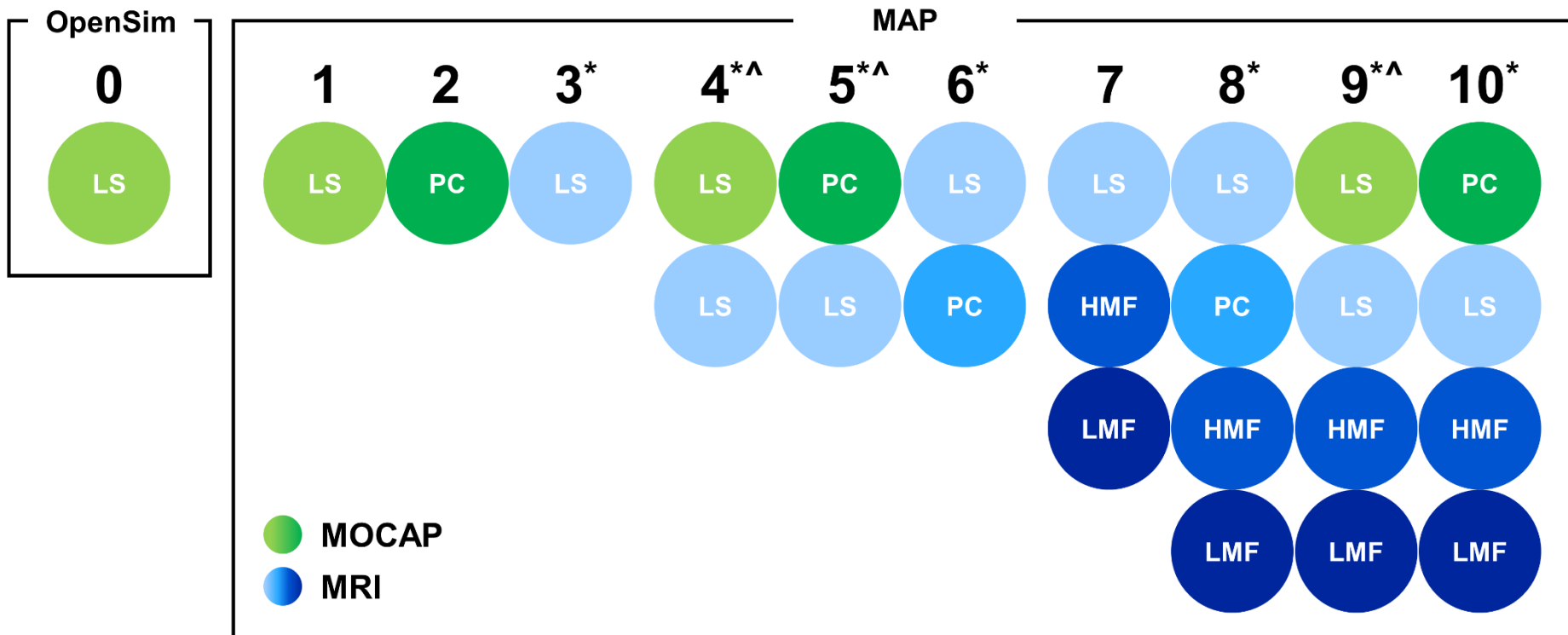


**Figure 28.** Pipelines developed and tested to reconstruct paediatric lower limb bones. Each pipeline, identified by the number above it, comprised different steps, represented in circles. Different colours refer to different methods/techniques employed. Shades of green or blue indicate MOCAP-based and MRI-based methods, respectively. Pipeline 0 was performed in OpenSim on generic geometries from the gait2392 model. Pipeline 1-10 were run in the MAP Client. PC = Principal component scaling, LS = Linear scaling.

## Pipelines summary

Ten different pipelines (Figure 28) were developed to explore the scenarios where only MOCAP data, only medical imaging data, or both, were available. Moreover, to identify the minimal amount of imaging data required to accurately reconstruct paediatric bones, both sparse and complete segmentations (Figure 27) were used to inform the MAP Client. For additional comparisons, in pipeline 0 all bones were reconstructed using OpenSim's MOCAP linear scaling approach on generic bone templates from the gait2392 model (Delp et al. 1990). For consistency, the same landmarks pairs were selected in OpenSim and the MAP Client to compute each bone's linear scaling factors. All pipelines were run on a desktop computer (i.e., Intel Core i5 @ 3.50GHz, 4 Cores), and in general, the more steps included in a pipeline, the longer the computational time required to reconstruct all bones of interest (Table 11).

## Data Analysis

Bones reconstructed using the MAP Client were compared to the corresponding full MRI segmentations using different metrics (Figure 29). First, the Jaccard index (JI) defined as the ratio between the intersection and the union of two volumes was used to determine volume similarity (Figure 29a). Second, the RMSE was computed to quantify surface reconstructions inaccuracies. Third, the Hausdorff distance, defined as the maximal surface-to-surface distance error between point clouds (Figure 29b), was used to identify inaccurate reconstructions. Furthermore, for the pelvis bone, which was characterised by a more complex structure in comparison to femurs and tibia/fibulas, visual checks were performed to understand how the distance error was distributed on the bone surface (i.e., evenly or in specific locations). To this end, colour maps of the MAP-to-MRI distance error were produced (Figure 29c). Finally, HJC (left and right) locations were determined and compared to the centres of the spheres fitted to the acetabula on MRI segmentations. The inter-HJCs distance and percent error between MRI and MAP Client measurements were also calculated and compared to results from Harrington's regression equation, commonly used in clinical practice. Finally, to determine possible effects of participants' size on bone reconstruction accuracy when using non-linear PC scaling methods, a linear regression model (numpy polyfit module in Python 2.7) was fitted to individual JI values for all reconstructed lower limb bones. The slope of each regression line (i.e.,  $\beta$ ),  $R^2$  and p values were computed to extract further information on the quality of the fit.

**Table 11.** Pipelines summary. List of morphing techniques employed and time required to complete each pipeline per subject. PC = Principal components.

| Pipeline | MOCAP          |                       | MRI            |                       |                         | Time<br>(Pelvis, Femurs<br>and Tibia/Fibulas) |
|----------|----------------|-----------------------|----------------|-----------------------|-------------------------|---|
|          | Linear scaling | Non-linear PC scaling | Linear scaling | Non-linear PC scaling | Mesh fitting techniques |   |
| 0        | ✓              |                       |                |                       |                         | 10-15 min                                     |
| 1        | ✓              |                       |                |                       |                         | 10-15 min                                     |
| 2        |                | ✓                     |                |                       |                         | 15-20 min                                     |
| 3        |                |                       | ✓              |                       |                         | ~4 h  |
| 4        | ✓              |                       | ✓              |                       |                         | ~4 h  |
| 5        |                | ✓                     | ✓              |                       |                         | ~4 h  |
| 6        |                |                       | ✓              | ✓                     |                         | ~5 h  |
| 7        |                |                       | ✓              |                       | ✓                       | 10-12 h                                       |
| 8        |                |                       | ✓              | ✓                     | ✓                       | 12-14 h                                       |
| 9        | ✓              |                       | ✓              |                       | ✓                       | 10-12 h                                       |
| 10       |                | ✓                     | ✓              |                       | ✓                       | 10-12 h                                       |

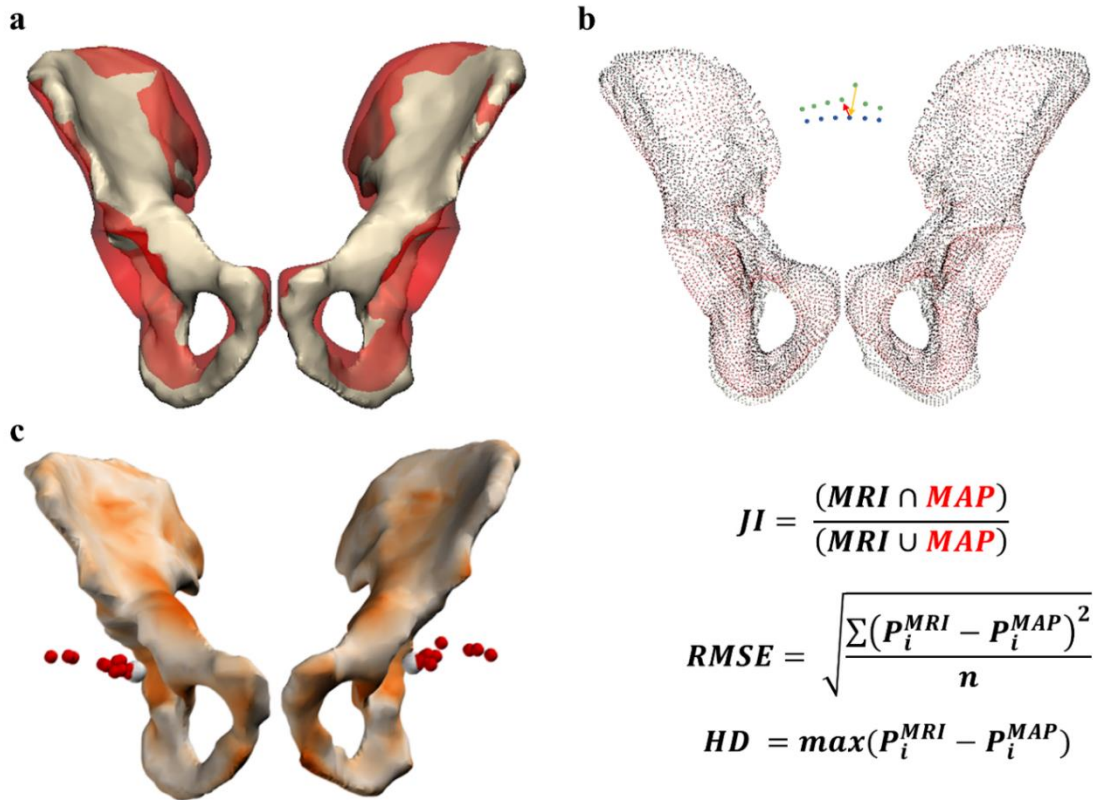


**Figure 29.** Metrics used to assess the accuracy of reconstructed bones. Volumetric (a) and surface (b) similarity indices between each reconstructed MAP bone and the corresponding MRI segmentation were computed using the reported formulas (bottom right). For the pelvis, colour maps (c) were produced to understand how the surface error was distributed.

## Statistical analysis

All data were tested for normality. If the data distributions were normal, comparisons between pipelines were performed via repeated measures ANOVA tests. Otherwise, the equivalent non-parametric tests (i.e., Friedman test followed by Wilcoxon signed rank tests) were used. To account for multiple comparisons, the significance level, initially set to  $p < 0.05$ , was recalculated implementing Bonferroni corrections. All analyses were performed in the Statistical Package for the Social Sciences version 25 (SPSS Inc., Chicago, USA).

## Results

All results are reported in Table 12, Table 13, Table 14 and Table 15. The first test involved the comparison of linear and non-linear PC scaling methods. For all tested bones, pipeline 3, solely employing linear scaling approaches and MRI data, produced more accurate geometries than pipeline 5, which combined linear and non-linear scaling methods, and pipelines 0-2, which were informed by MOCAP data alone (Figure 30). Pipeline 4 performed similarly to pipeline 3, while pipeline 6, despite being associated with the highest mean JI (Figure 30, Table 12 and Table 13) for pelvis and femurs, generated abnormally shaped pelvis and tibiofibular geometries for small children (Figure 31 and Figure 32). This size-dependency was also noticed in results from pipelines 2 and 5, both employing non-linear PC scaling methods: the smaller the child, the worse the reconstruction (regression lines fitted to individual JIs showed  $R^2 = 0.60$  and  $0.80$  for pelvis,  $R^2 = 0.55$  and  $0.73$  for tibia/fibula, using pipelines 2 and 5, respectively, versus  $R^2 \sim 0$  from pipeline 1. Figure 32 and Table 14). Specifically, for children smaller than 145 cm, non-linear scaling methods produced less accurate reconstructions than linear scaling approaches and vice versa for taller participants (Figure 31, Figure 32 and Table 14). Visual checks of the pelvis reconstructions revealed that, for small children, more natural shapes were produced when MAP Client geometries were scaled linearly rather than non-linearly (Figure 31). Also, iliac crests and ischia (i.e., posterior inferior iliac spines, close to the acetabulum) were the areas of the pelvis more prone to reconstruction inaccuracies (Figure 31). Moreover, linearly scaled femurs and tibia/fibulas from OpenSim were the furthest distance away from the actual bone segmentations ( $JI_{Femur} = 0.54 \pm 0.05$ ,  $JI_{TibiaFibula} = 0.55 \pm 0.06$  versus  $JI_{Femur} > 0.65 \pm 0.05$  and  $JI_{TibiaFibula} > 0.61 \pm 0.12$ . Table 12 and Table 13). On the other hand, the pelvis bone was equally poorly reconstructed by all MOCAP based pipelines, as evidenced by the overall lowest volume ( $JI_{Pelvis} = 0.20 \pm 0.08$ ,  $0.26 \pm 0.08$  and  $0.26 \pm 0.13$ ; from pipeline 0, 1 and 2, respectively) and largest surface ( $RMSE \geq 8$  mm and Hausdorff distance  $\geq 25.8$  mm. Table 12&Table 13) similarity indices.

**Table 12.** Volume and surface similarity metrics for pipelines solely employing linear or non-linear scaling methods. Jaccard index (JI), root mean square distance error (RMSE) and Hausdorff distance values are reported as mean (standard deviation) across the population. Values highlight the pipeline which provided the worst (red) results. For the pipelines employing MRI data, the letter in superscript indicates the level of segmentation incompleteness: ‘j’ stands for joint scans segmentations while ‘s’ indicates sparse segmentations.

| Pipeline             | Pelvis            |                    |                     | Femur             |                   |                     | Tibia/Fibula      |                   |                     |
|----------------------|-------------------|--------------------|---------------------|-------------------|-------------------|---------------------|-------------------|-------------------|---------------------|
|                      | JI                | RMSE [mm]          | HD [mm]             | JI                | RMSE [mm]         | HD [mm]             | JI                | RMSE [mm]         | HD [mm]             |
| <b>0</b>             | <b>0.20(0.08)</b> | <b>12.57(1.63)</b> | <b>36.39 (9.32)</b> | <b>0.54(0.05)</b> | <b>7.43(1.13)</b> | <b>17.58 (3.00)</b> | <b>0.55(0.06)</b> | <b>8.16(1.22)</b> | <b>20.33 (2.87)</b> |
| <b>1</b>             | 0.26(0.08)        | 8.45(3.10)         | 31.37(10.77)        | 0.65(0.05)        | 4.75(1.20)        | 14.98(4.46)         | 0.63(0.08)        | 4.27(1.20)        | 13.30(3.47)         |
| <b>2</b>             | 0.26(0.13)        | 8.00(2.63)         | 25.79(8.28)         | 0.67(0.07)        | 4.29(0.78)        | 14.56(3.34)         | 0.64(0.09)        | 3.79(1.10)        | 15.24(9.96)         |
| <b>3<sub>s</sub></b> | 0.50(0.05)        | 4.00(0.81)         | 14.73(2.23)         | 0.66(0.06)        | 4.00(1.01)        | 12.58(3.63)         | 0.69(0.07)        | 2.86(0.55)        | 8.95(2.55)          |
| <b>3</b>             | 0.51(0.06)        | 3.88(0.75)         | 14.56(2.33)         | 0.72(0.05)        | 3.62(0.57)        | 11.36(1.44)         | 0.72(0.06)        | 2.75(0.45)        | 8.58(2.01)          |
| <b>4<sub>j</sub></b> | 0.47(0.07)        | 4.38(1.20)         | 17.13(4.71)         | 0.69(0.05)        | 3.61(0.59)        | 11.72(1.66)         | 0.70(0.06)        | 2.79(0.49)        | 8.72(2.26)          |
| <b>4<sub>s</sub></b> | 0.50(0.05)        | 4.12(0.91)         | 15.69(3.35)         | 0.67(0.05)        | 3.81(0.64)        | 12.02(1.66)         | 0.68(0.07)        | 3.03(0.94)        | 9.57(3.60)          |
| <b>4</b>             | 0.51(0.05)        | 3.89(0.70)         | 14.16(0.05)         | 0.71(0.05)        | 3.77(0.57)        | 11.50(1.33)         | 0.71(0.06)        | 2.76(0.44)        | 8.89(2.05)          |
| <b>5<sub>j</sub></b> | 0.31(0.11)        | 7.12(2.85)         | 26.69(9.85)         | 0.69(0.08)        | 3.67(0.87)        | 12.90(3.09)         | 0.63(0.11)        | 3.64(1.03)        | 14.37(8.28)         |
| <b>5<sub>s</sub></b> | 0.37(0.13)        | 5.66(1.70)         | 19.07(6.69)         | 0.67(0.09)        | 3.82(0.95)        | 13.18(2.68)         | 0.61(0.12)        | 3.86(1.55)        | 13.98(7.99)         |
| <b>5</b>             | 0.38(0.12)        | 5.39(1.53)         | 17.61(4.66)         | 0.70(0.07)        | 3.81(0.78)        | 13.31(2.80)         | 0.65(0.09)        | 3.58(1.10)        | 14.47(10.34)        |
| <b>6<sub>s</sub></b> | 0.59(0.05)        | 3.45(0.38)         | 16.53(2.69)         | 0.68(0.19)        | 4.17(2.98)        | 16.16(11.83)        | 0.65(0.19)        | 4.90(5.17)        | 17.75(14.81)        |
| <b>6</b>             | 0.63(0.05)        | 3.05(0.44)         | 14.64(2.58)         | 0.79(0.08)        | 2.92(0.79)        | 12.36(3.66)         | 0.70(0.19)        | 4.62(5.13)        | 15.66(14.42)        |

**Table 13.** Volume and surface similarity metrics for pipelines employing linear or non-linear scaling methods in combination with mesh fitting techniques. Jaccard index (JI), root mean square distance error (RMSE) and Hausdorff distance values are reported as mean (standard deviation) across the population. Values highlight the pipelines which provided the best (blue) results. For the pipelines employing MRI data, the letter in superscript indicates the level of segmentation incompleteness: ‘j’ stands for joint scans segmentations while ‘s’ indicates sparse segmentations.

| Pipeline              | Pelvis            |                   |                    | Femur             |                   |                   | Tibia/Fibula      |                   |                   |
|-----------------------|-------------------|-------------------|--------------------|-------------------|-------------------|-------------------|-------------------|-------------------|-------------------|
|                       | JI                | RMSE [mm]         | HD [mm]            | JI                | RMSE [mm]         | HD [mm]           | JI                | RMSE [mm]         | HD [mm]           |
| <b>7</b>              | <b>0.89(0.03)</b> | <b>1.58(0.51)</b> | <b>10.05(3.40)</b> | <b>0.96(0.01)</b> | <b>1.78(0.47)</b> | <b>8.56(2.34)</b> | <b>0.94(0.01)</b> | <b>1.56(0.35)</b> | <b>6.82(2.52)</b> |
| <b>8<sub>s</sub></b>  | 0.74(0.05)        | 2.69(0.34)        | 15.60(3.64)        | 0.72(0.19)        | 3.87(3.00)        | 15.34(11.78)      | 0.68(0.18)        | 4.79(5.17)        | 17.65(15.11)      |
| <b>8</b>              | 0.83(0.04)        | 1.95(0.37)        | 12.37(3.72)        | 0.92(0.03)        | 2.22(1.10)        | 11.18(6.83)       | 0.83(0.19)        | 4.15(5.27)        | 15.17(14.83)      |
| <b>9<sub>j</sub></b>  | 0.64(0.09)        | 3.69(1.21)        | 18.57(4.87)        | 0.87(0.04)        | 2.16(0.49)        | 9.37(2.11)        | 0.84(0.04)        | 1.88(0.29)        | 7.59(2.34)        |
| <b>9<sub>s</sub></b>  | 0.76(0.04)        | 2.83(0.69)        | 16.39(4.80)        | 0.78(0.03)        | 2.80(0.44)        | 10.56(1.37)       | 0.79(0.05)        | 2.18(0.48)        | 8.29(2.98)        |
| <b>9</b>              | <b>0.89(0.03)</b> | <b>1.53(0.40)</b> | <b>9.75(2.84)</b>  | <b>0.96(0.01)</b> | <b>1.79(0.47)</b> | <b>8.57(2.29)</b> | <b>0.94(0.01)</b> | <b>1.55(0.36)</b> | <b>6.77(2.51)</b> |
| <b>10<sub>s</sub></b> | 0.56(0.16)        | 5.91(2.69)        | 31.12(12.71)       | 0.80(0.05)        | 2.82(0.57)        | 12.36(4.47)       | 0.76(0.09)        | 2.75(1.12)        | 12.60(7.42)       |
| <b>10</b>             | 0.84(0.08)        | 1.98(0.60)        | 13.84(6.03)        | 0.94(0.04)        | 1.98(0.56)        | 10.14(3.31)       | 0.88(0.09)        | 2.27(1.28)        | 12.06(8.12)       |

**Table 14.** Statistics of linear regression models. R-squared values ( $R^2$ ),  $\beta$  coefficient (i.e. slope) and p-values ( $p$ ) for the regression lines fit to the individual Jaccard indices of pelvic, femoral and tibiofibular bones reconstructed using non-linear scaling methods. Higher slope values indicate more pronounced size-effect on volume similarity. The colour code reflects the legend in Figure 32.

| Pipeline                      | Pelvis |                    |        | Femur |                    |        | Tibia/Fibula |                    |        |       |
|-------------------------------|--------|--------------------|--------|-------|--------------------|--------|--------------|--------------------|--------|-------|
|                               | $R^2$  | $\beta$<br>(slope) | $p$    | $R^2$ | $\beta$<br>(slope) | $p$    | $R^2$        | $\beta$<br>(slope) | $p$    |       |
| 1                             | 0.007  | -0.0004            | 0.736  | 0.008 | -0.0003            | 0.731  | 0.005        | 0.0003             | 0.784  |       |
| Non-linear PC scaling methods | 2      | 0.600              | 0.0059 | 0.000 | 0.351              | 0.0024 | 0.010        | 0.450              | 0.0037 | 0.002 |
|                               | 5      | 0.787              | 0.0066 | 0.000 | 0.158              | 0.0016 | 0.103        | 0.552              | 0.0041 | 0.000 |
|                               | 6      | 0.350              | 0.0019 | 0.010 | 0.206              | 0.0021 | 0.058        | 0.689              | 0.0096 | 0.000 |
|                               | 8      | 0.672              | 0.0022 | 0.000 | 0.651              | 0.0016 | 0.000        | 0.630              | 0.0091 | 0.000 |
|                               | 10     | 0.660              | 0.0040 | 0.000 | 0.504              | 0.0017 | 0.001        | 0.733              | 0.0047 | 0.000 |
| 9                             | 0.124  | 0.0006             | 0.152  | 0.391 | 0.0006             | 0.006  | 0.557        | 0.0006             | 0.000  |       |

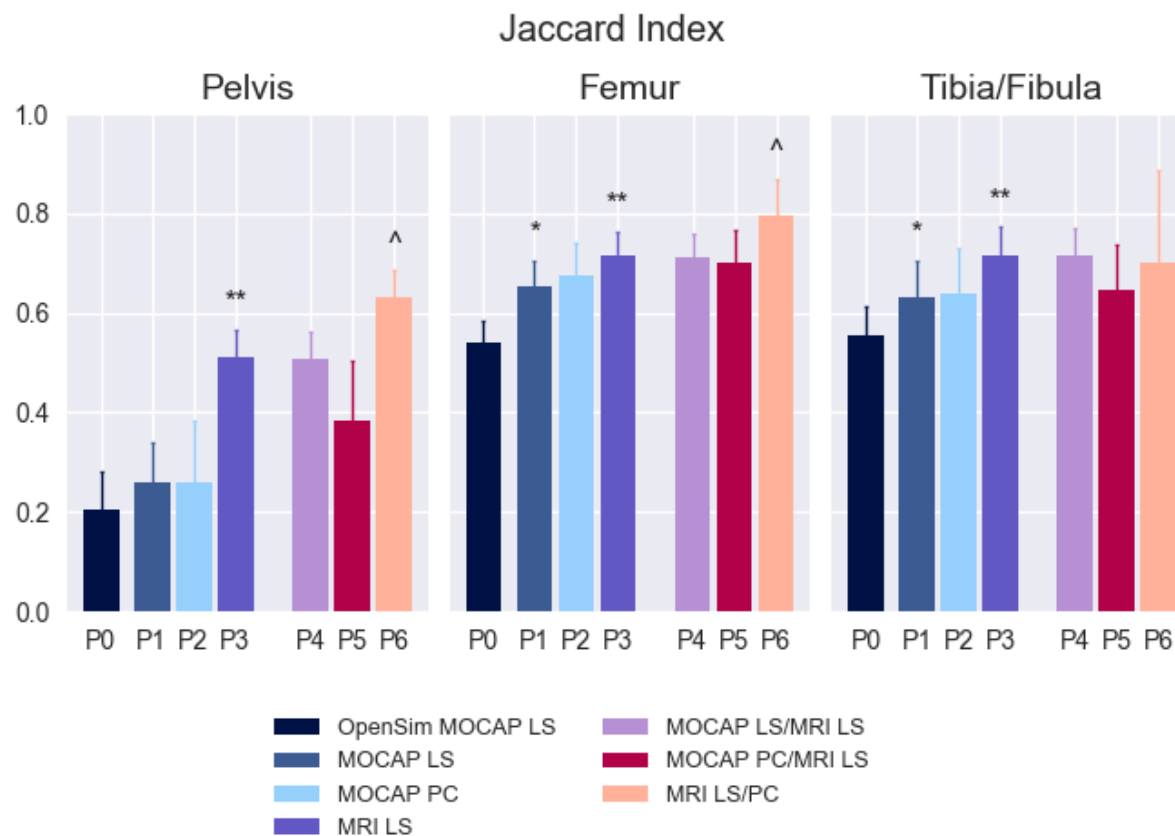


**Figure 30.** Volume similarity between MAP reconstructions via scaling approaches and corresponding MRI segmentations for the pelvic, left femoral and left tibiofibular bones. Bar graph reporting Jaccard indices as mean values across the studied population (n=18) for the pipelines solely employing linear or non-linear scaling methods, i.e. P0-6. Different shades of colours were used to separate pipelines performing one only scaling step (blue), or multiple scalings (red and purple). PC = Principal component scaling, LS = Linear scaling. Symbols denote significant differences: \* compared to Opensim LS, \*\* compared to MOCAP LS, ^ compared to MRI LS.

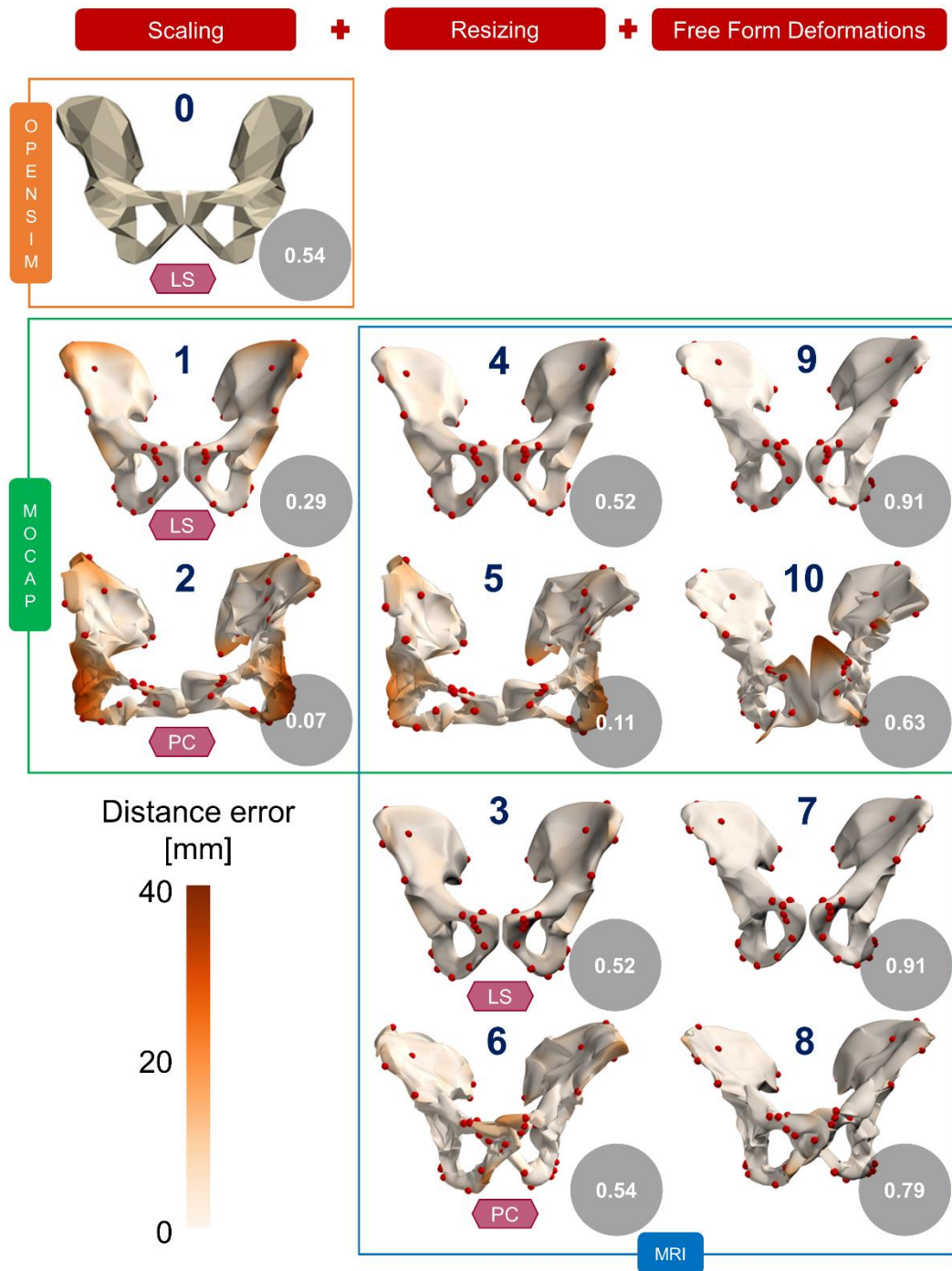


**Figure 31.** Examples of pelvis bone reconstructions for one subject using the developed pipelines. Reconstructed pelvis and relative surface error distribution reported via colour maps, where darker reds denote larger errors, expressed in mm. For completeness, Jaccard indices are reported in the grey circles. The labels PC and LS describe the type of scaling employed, i.e. based on principal components or linear scaling.

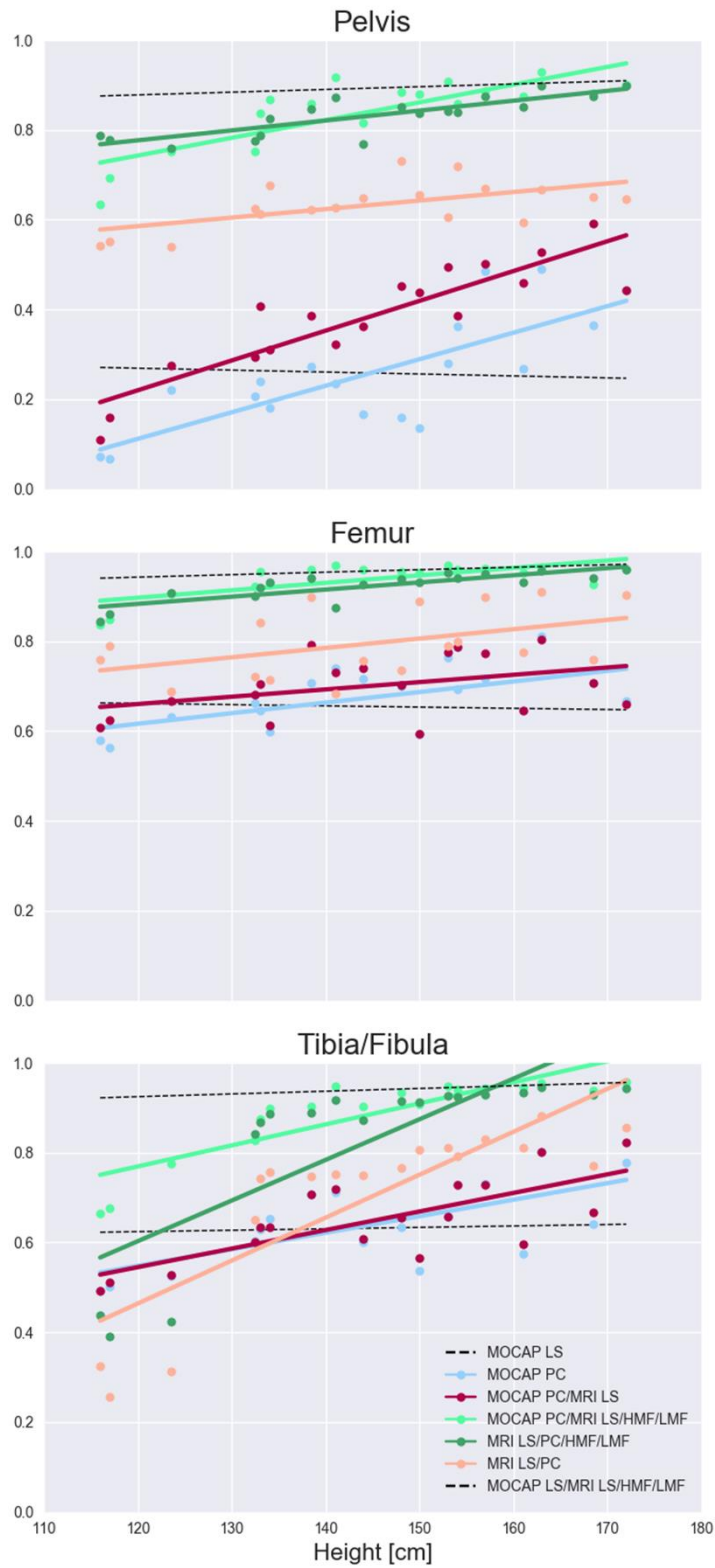


**Figure 32.** Jaccard indices as function of subjects' height. Individual Jaccard indices and corresponding fitted regression lines to show the relationship between reconstruction accuracy and subjects' height for pipelines employing PC-based scaling. Different colours refer to different pipelines. Black dashed lines represent results from pipeline 1 (lower line) and pipeline 9 (upper line), for comparisons. PC = Principal component scaling, LS = Linear scaling, HMF = Host-mesh fitting, LMF = Local-mesh fitting.

The second test assessed the effect of MRI data sparsity on bone reconstruction. On the two best pipelines from test one (i.e., pipeline 3 and 4), different levels of incompleteness were tested (Figure 27 and Table 12). The use of complete MRI segmentations was generally associated with higher similarity indices compared to both incomplete medical imaging datasets (Table 12 and Table 13). However, for the pelvis, there were no statistically significant differences between reconstructions from sparse and full segmentations ( $p > 0.5$ ), while joint scans produced poorer results ( $p < 0.018$ ). Conversely, for femurs and tibia/fibulas, joint scans enabled to reconstruct bones with higher levels of accuracy compared to sparse scans ( $J\text{I}_{\text{Femur}}^{\text{joint}} = 0.69 \pm 0.05$  versus  $J\text{I}_{\text{Femur}}^{\text{sparse}} = 0.67 \pm 0.05$  and  $J\text{I}_{\text{TibiaFibula}}^{\text{joint}} = 0.70 \pm 0.06$  versus  $J\text{I}_{\text{TibiaFibula}}^{\text{sparse}} = 0.68 \pm 0.07$ ).

The third test assessed whether freeform deformation techniques could correct shape and curvature inaccuracies observed in bone reconstructed via pipelines 4-6 (Table 13). Pipeline 7, solely informed by MRI-data and employing linear scaling, HMF and LMF techniques, produced highly accurate bone geometries (Table 12 and Table 13). Pipelines 9 and 10, which were informed by MOCAP data and MRI segmentations, also produced very accurate reconstructions for all tested bones ( $J\text{I}_{\text{Pelvis}} = 0.89 \pm 0.03$  and  $0.84 \pm 0.08$ ,  $J\text{I}_{\text{Femur}} = 0.96 \pm 0.01$  and  $0.94 \pm 0.04$ ,  $J\text{I}_{\text{TibiaFibula}} = 0.88 \pm 0.09$  and  $0.94 \pm 0.01$ ). However, Wilcoxon signed-rank tests showed that employing a linear scaling step, in pipeline 9, as opposed to a PC scaling step, in pipeline 10, significantly improved reconstructions ( $Z = +3.288$ ,  $p = 0.001$ ). RMSE values were progressively smaller when more information was provided (Table 12 and Table 13). The smallest RMSEs (i.e.,  $1.53 \pm 0.39$  mm,  $1.79 \pm 0.47$  mm and  $1.55 \pm 0.36$  mm for pelvis, femur and tibia/fibula respectively) were obtained combining MOCAP and MRI linear scaling, HMF and LMF techniques (i.e. pipeline 9). On each reconstructed pelvis (Figure 31), the largest distance error, decreased in value when more data were provided to the MAP Client (i.e., pipelines 9-10 versus pipelines 1-2 and complete versus incomplete segmentations, Table 12 and Table 13). The most accurate geometries were produced employing full segmentations, however joint scans and sparse segmentations provided enough information to accurately reconstruct long bones and pelvis, respectively (i.e., JI around or above 0.8).

The fourth test assessed the ability of each pipeline to accurately estimate HJC location. Hip joint centres mislocation varied quite considerably across pipelines (Figure 33). When no segmentations were provided the error was the largest ( $17.66 \pm 6.76$  mm,  $16.65 \pm 7.27$  mm and  $15.10 \pm 5.26$  mm for left HJCs; similar values were found for the right HJCs). On the other hand, pipelines 7 and 9 were associated with the smallest location errors, i.e.  $3.09 \pm 1.47$  mm and  $3.01 \pm 1.57$  mm respectively (Table 15). For taller children,

HJCs estimates from the different pipelines were clustered around the reference locations identified on MRI segmentations. Nonetheless, the smaller the participant, the larger the differences between pipelines (Figure 33). The absolute percent inter-HJC distance error between MRI and reconstructed pelvis was largest for MOCAP linearly scaled geometries, both in OpenSim and the MAP Client (i.e.,  $22.31\pm 10.38\%$  and  $22.33\pm 11.43\%$ , respectively), decreasing (i.e.,  $\leq 9.26\pm 6.03\%$ ) when medical images were provided and minimal (i.e.,  $1.92\pm 1.70\%$ ) in pipeline 6 which was solely informed via MRIs (Table 15). Finally, pipelines 7 and 9 also produced significantly better estimates of left-to-right HJC distance compared to Harrington's regression equation (Harrington et al. 2007), which is commonly used in clinical gait analysis.

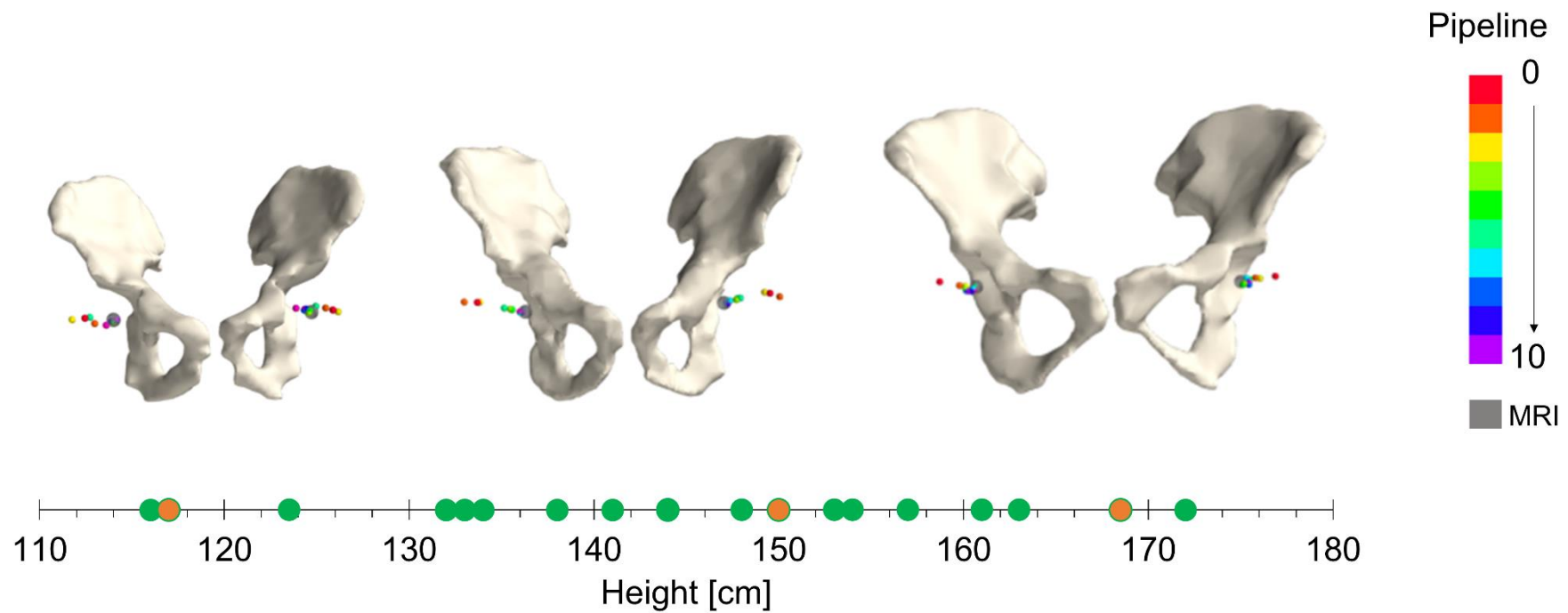


**Figure 33.** Dependency of hip joint centres location on subject's heights. Hip joint centres estimated from the different pipelines are displayed as spheres of different colours (red to fuchsia) overlaid to the correspondent MRI segmentation. Grey spheres indicate the reference hip joint centres derived from MRI segmentations. Orange circles on the scale at the bottom denote the subjects whose pelvis is displayed.

**Table 15.** Hip joint centres location and percent distance errors. Euclidean distances between left/right hip joint centres (HJC) and percent absolute inter-HJC distance error between MRI segmentations and registered pelvis reconstructions. Location errors are expressed in mm, while inter-HJC distance errors are reported as percent values. Hip joint centres distance was also calculated using Harrington equation, commonly used in clinical practice, and measured on MRI segmentations. Results are reported as mean (standard deviation). Significant differences ( $p < 0.05$ ) with respect to MRI measurements and from Harrington equation are indicated by the symbols <sup>^</sup> and \* respectively. Superscript letters denote the level of MRI data sparsity: ‘j’ stands for joint scans segmentations, while ‘s’ indicate sparse segmentations

| Pipeline          | Left HJC error [mm] | Right HJC error [mm] | Inter-HJC distance Error (%) |
|-------------------|---------------------|----------------------|------------------------------|
| <b>Harrington</b> | -                   | -                    | 14.00(9.20)                  |
| <b>0</b>          | 15.10(5.26)         | 15.20(7.46)          | 21.26(11.78)                 |
| <b>1</b>          | 17.66(6.76)         | 17.60(7.25)          | 22.31(10.38) <sup>^</sup>    |
| <b>2</b>          | 16.65(7.27)         | 16.69(7.90)          | 22.33(11.43)                 |
| <b>3s</b>         | 4.44(1.57)          | 5.00(2.73)           | 3.15(2.7)*                   |
| <b>3</b>          | 5.69(1.87)          | 5.83(2.99)           | 5.14(3.28)                   |
| <b>4j</b>         | 5.73(3.04)          | 6.54(2.79)           | 4.21(3.88)*                  |
| <b>4s</b>         | 8.60(6.90)          | 7.12(3.51)           | 6.28(6.25)                   |
| <b>4</b>          | 7.36(2.98)          | 8.39(4.17)           | 9.26(6.03)                   |
| <b>5j</b>         | 4.68(2.58)          | 5.27(3.01)           | 3.53(2.85)*                  |
| <b>5s</b>         | 5.06(2.11)          | 5.62(2.93)           | 3.79(2.86)*                  |
| <b>5</b>          | 6.04(2.06)          | 5.58(2.74)           | 5.14(3.41)                   |
| <b>6s</b>         | 3.40(1.36)          | 4.25(2.11)           | 1.98(1.87)*                  |
| <b>6</b>          | 3.50(1.44)          | 3.75(2.22)           | 1.92(1.71)*                  |
| <b>7</b>          | 3.01(1.57)          | 3.08(1.87)           | 2.96(1.68)*                  |
| <b>8s</b>         | 2.86(1.20)          | 2.70(1.75)           | 2.36(1.56)*                  |
| <b>8</b>          | 3.12(1.22)          | 2.77(1.75)           | 2.39(1.56)*                  |
| <b>9j</b>         | 3.22(2.42)          | 2.99(1.90)           | 2.93(1.81)*                  |
| <b>9s</b>         | 3.16(1.98)          | 2.98(2.43)           | 3.05(2.14)*                  |
| <b>9</b>          | 3.10(1.47)          | 3.08(1.80)           | 3.06(1.59)*                  |
| <b>10s</b>        | 7.48(4.32)          | 7.44(5.42)           | 7.99(7.61)                   |
| <b>10</b>         | 4.25(2.54)          | 3.58(1.75)           | 2.59(1.95)*                  |

<sup>^</sup> significantly larger than Harrington regression equation

\*significantly lower than Harrington regression equation

## Discussion

In this paper, for the first time, the MAP Client was used to reconstruct paediatric lower limb bones. Ten different pipelines were developed and tested to determine the (i) most effective combination of morphing methods and (ii) amount of experimental data to be provided to ensure accurate bone reconstructions. Pipelines 7 and 9, which employed linear scaling methods and mesh fitting techniques, produced bony geometries with overall highest volume and surface similarity indices that, for the pelvis, were also associated with accurate estimates of HJC locations. Moreover, in agreement with our first two hypotheses, (1) non-linear scaling methods were not able to accurately morph lower limb bones for small children and (2) sparse and joint scans both enabled acceptable level of accuracy for pelvis and long bones. On the other hand, the use of MOCAP data did not improve reconstruction accuracy, as pipeline 7 and 9 performed similarly.

As hypothesised, pipelines using non-linear PC approaches to scale bone geometries, e.g. pipeline 6, did not produce accurate reconstructions of paediatric lower limb bones. Abnormal pelvic and tibiofibular shapes were generated for children shorter than 145 cm (Figure 31). Particularly, iliac crests and ischia, which correspond to the inferior and posterior regions of the pelvis, were the least accurately reconstructed regions (Figure 31) of the pelvic bone. This finding is of practical importance for MSK modelling as several muscle attachments are located on the surface of these regions. Such size-dependent behaviour (Figure 32) likely resulted from using PCs derived from an adult database (i.e., comprising subjects 160 to 180 cm tall), which presumably did not adequately describe variations within the shorter paediatric population. Nonetheless, for children taller than 145 cm, non-linear PC scaling produced more accurate reconstructions than linear scaling (Figure 32 and Table 14). Therefore, for children of height above 145 cm, we recommend the use of pipeline 2 to reconstruct paediatric lower limb bones if medical imaging data are not available, while for children shorter than 145 cm, pipeline 1 is preferred. More natural shapes, particularly for the pelvis and tibia/fibula, were produced for shorter children when linear scaling approaches were employed (Figure 31 and Figure 32, Table 12). Conversely, when MRI data are available, pipelines 3 should be preferred as it proved to better reconstruct paediatric lower limb bones compared to all MOCAP-based pipelines (Figure 30 and Table 12). Linearly scaled OpenSim generic geometries were the least accurate overall ( $JI = 0.20 \pm 0.08$ ,  $0.54 \pm 0.05$  and  $0.55 \pm 0.06$  for pelvis, femur and tibia/fibula, respectively), suggesting that caution

needs to be taken when interpreting the results from a generic OpenSim model that is scaled to the dimensions of a paediatric participant.

The use of full MRI segmentations to inform bone morphing, as expected, was associated with the most accurate reconstructions. Nonetheless, incomplete imaging datasets, which require less time and costs to be acquired, may provide sufficient information (Table 12 and Table 13) to accurately scale and morph bones without employing HMF and LMF techniques. However, different considerations need to be taken for each bone. For instance, the pelvis can vary considerably between individuals, even in healthy populations. Therefore, information from different areas (e.g., iliac crests, acetabula, ischia) may need to be provided to ensure accurate reconstructions, as reported by Suwarganda and colleagues (2019) and as shown in the present results. The use of joint scans, which did not carry information on the iliac crests, resulted in significantly poorer pelvis geometries compared to both sparse and full segmentations, which produced comparable results (Table 12 and Table 13). On the other hand, for femurs and tibia/fibulas, joint scans produced more accurate geometries than sparse segmentations. The possible reason being that joint scans included the whole bone epiphyses (Figure 27), which may yield the largest degree of complexity compared to bone shafts for both femurs and tibia/fibulas. However, more information may be required for pathologic populations presenting with deformity that impacts the mid-shaft (e.g., femoral torsion).

Combining MOCAP- and MRI-informed linear scaling, HMF and LMF methods, i.e. pipeline 9, led to the most accurate reconstructions of paediatric pelvis, femurs and tibiofibular bones both in terms of volume ( $JI_{Pelvis} = 0.89 \pm 0.03$ ,  $JI_{Femur} = 0.96 \pm 0.01$ ,  $JI_{TibiaFibula} = 0.94 \pm 0.01$ ) and surface ( $RMSE_{Pelvis} = 1.53 \pm 0.40$  mm,  $RMSE_{Femur} = 1.79 \pm 0.47$  mm,  $RMSE_{TibiaFibula} = 1.55 \pm 0.36$  mm) similarity to the MRI segmentations. More importantly, results were not size-dependent: low  $R^2$  values (equal to 0.12, 0.39 and 0.56, Table 13) and minimal slopes were associated with the regression lines fitted to the Jaccard indices for pelvis, femur and tibia/fibulas reconstructions (Figure 32 and Table 14). However, similar results were achieved with pipeline 7, which did not include the first MOCAP-based linear scaling step (Table 12, Table 13 and Table 15), demonstrating that MRI data alone may be sufficient to generate accurate reconstructions. Moreover, pipeline 8, which employed non-linear PC scaling and has previously been associated with the highest JI for adult bones (Suwarganda et al. 2019), did not lead to similarly good results on paediatric data (e.g.,  $JI_{Pelvis}^{Paed} = 0.83 \pm 0.04$  versus  $JI_{Pelvis}^{Adult} = 0.93 \pm 0.02$ ), most likely due to the use of PCs derived from an adult dataset. Once again, the use of full segmentations to inform the morphing process resulted in very high levels of accuracy,

reported above, for all bones. However, in pipelines 7 and 9, good results ( $JI > 0.8$ ) were also achieved when providing incomplete sets of medical images (Table 12 and Table 13). For long bones, which are characterised by simpler geometry compared to the pelvis bone, joint scans seemed to carry enough information to enable accurate reconstructions. Contrarily, for the pelvis, imaging data from the upper portion was still required for best results. Indeed, employing HMF and LMF techniques appeared to be crucial to capture specific features of paediatric bones. For example, femoral neck geometry, which is known to change during growth, was notably different on femurs reconstructed using pipeline 0, pipeline 1 and pipeline 2 compared to manual segmentation (Table 26 in Appendix C).

The benefits of employing imaging data to inform the morphing process and the limits of MOCAP-based pipelines to produce accurate reconstructions were further highlighted in the fourth test which focussed on the pelvis bone. Pipelines 0-2 performed similarly to one another, i.e. poorly, and were associated with larger HJCs location errors ( $\geq 15.10 \pm 5.26$  mm. Table 15) and abnormal inter-HJCs distances (i.e., up to 22% difference to the distance measured on MRI segmentations) compared to the other tested pipelines. However, in agreement with previously reported data (Bahl et al. 2019), HJC estimates were more accurate when imaging data were provided to inform the scaling and morphing processes (Table 15). Moreover, pipeline 0 and pipeline 9 produced results on opposite sides of the spectrum, with linearly scaled OpenSim geometries being the least accurate reconstructions overall and pipeline 9 the most accurate. Our results (Table 15) also showed that left-to-right HJC distances measured on the bones reconstructed using pipelines 6-9 were significantly closer to the MRI measurements compared to the both estimates from linearly scaled OpenSim bone models and via Harrington's regression equation (Harrington et al. 2007), which is the current gold standard in paediatric clinical motion analysis. Therefore, caution should be used in clinical gait analysis when computing HJCs location and distances using generic OpenSim scaling methods or via regression equations (e.g., Harrington formula), especially for smaller children (Figure 33). Such findings cannot be neglected when generating bones for use in MSK modelling applications, since errors in HJCs location may propagate to hip and knee joint angles calculations (Kainz et al. 2017a), possibly affecting subsequent joint kinetics computations and leading to misinterpretation of clinical findings. In addition, the orientation in space of knee and ankle joint axis varied based on the final bone geometry (Table 27 in Appendix C). Joint kinematics and kinetics may consequently be affected.

It must be appreciated that accurately reconstructing pelvic, femoral and lower leg bones requires a large time investment (Table 11). For example, pipeline 9, which produced the most accurate reconstructions, took up to 7 hours per subject to run, including both computational time and the time to collect experimental MOCAP data, plus two to four hours for bone segmentations. On the other hand, pipelines 0-2, solely employing MOCAP data, required less than fifteen minutes to complete. However, pipeline 0 in OpenSim, which is commonly used in research on paediatric populations and clinical practice, produced the worst reconstructions for all tested bones. Notably, the use of sparse segmentations allowed for reduced running time (~6 hours overall) without compromising reconstruction accuracy (e.g.,  $J_{\text{Pelvis}} > 0.80$ ). Importantly, the computational time here reported (up to 7 hours) may decrease in the future by using high-performance computers as opposed to standard office desktop machines. In addition, the reconstructed bones may be readily employed to generate personalised MSK models within the MAP Client within 30 mins, as muscle origin and insertion points would be already embedded in the three-dimensional geometries. In contrast, available methods to manually or semi-automatically add muscle attachments would take up to 2 hours to complete one model (Scheys et al. 2006). Finally, the ability to produce an accurate MAP Client bone model using medical image data only (pipeline 7) will facilitate investigation of human biomechanics ‘outside the lab’ through the use of inertial sensors (Pizzolato et al. 2017).

This study has limitations. Firstly, manual segmentations were used as gold standard to quantify bone reconstruction accuracy. Although all segmentations were checked for inaccuracies, residual errors may have been present on the final segmented geometries, possibly affecting results. Secondly, Jaccard indices are highly influenced by misalignment between MRI segmentations and correspondent MAP Client reconstructions. Despite a rigid registration process was used to minimise the RMSE between the point clouds, misalignment may have not been completely removed, negatively affecting results. Thirdly, reported RMSE and Hausdorff distance values were calculated between pairs of closest points identified on the MAP Client and MRI segmentation meshes and computed in two ways, i.e. MAP-to-MRI and MRI-to-MAP, to account for errors due to inappropriate point picking. However, although the MAP Client meshes were discretised in order to have the same number of nodes as the corresponding MRI segmentations, the points may have not been similarly distributed, leading to larger distance errors in specific areas. It must be noted that both MRI and MAP Client meshes were finer at the bone extremities and coarser on the shafts for femurs and tibia-fibulas,

while uniformly dense for the pelvis. Also, in some instances, MOCAP-based linear scaling failed to correctly resize the mean MAP Client model of the pelvis. This problem mainly affected pelvis width and may have been caused by the way multiple scaling factors are applied to a geometry within the MAP Client or erroneous experimental markers placements. To reduce the impact of MOCAP-based scaling errors, anthropometric measurements, e.g., pelvis width/depth, could be further provided to the MAP Client to better inform the scaling process. Furthermore, to be consistent between participants, PC-scaling, HMF and LMF steps were iterated the same number of times across subjects and bones. However, this number may have not been ideal for all subjects, leading to suboptimal results. In addition, PC-based pipelines in this study used adult PCs, which were likely not ideal for paediatric bones. Future work should focus on populating a paediatric database to extract PCs capable of explaining the shape variations within a paediatric population. Finally, this paper primarily focussed on the geometry of bones, which represents only one part of the modelling problem. Nonetheless, this is a mandatory and crucial aspect that needed to be addressed prior to investigating the effect of abnormal bone shapes on a model's predictions. Future studies are needed to investigate how joint kinematics and kinetics, muscle forces and joint contact forces are affected by inaccuracies in bony morphologies and joint axis orientations.

## Conclusions

Accurate reconstructions of paediatric pelvis, femur and tibiofibular bones can be generated combining SSM and morphing techniques. However, different approaches should be taken based on participants' height and availability of experimental data. For children of stature below 145 cm, non-linear scaling methods should be avoided until a population-specific database from which to extract paediatric PCs is available. Pipelines which employ linear scaling approaches and that incorporate medical imaging data, should be selected to achieve optimal results. Contrarily, for taller children, PC-based pipelines may produce accurate results. In general, informing the morphing process with segmentations of medical images (via HMF and LMF) ensures accurate bone reconstructions. Full segmentations would ensure optimal results, however joint scans may be sufficient to reconstruct both femurs and tibia/fibulas, while for the pelvis bone to be accurately modelled more information (e.g. on the iliac crests) should be provided. Finally, MOCAP data alone to inform bone reconstruction may be insufficient and may lead to large HJCs location errors, ultimately affecting joint angles and joint moments estimates in MSK modelling simulations.



# CHAPTER 6

---

## **Developing the new generation of personalised neuromusculoskeletal models to investigate cerebral palsy**

This chapter investigates the individual contribution of musculotendon parameters, neural solution and musculoskeletal anatomy personalisation on muscle and knee joint contact forces estimates during gait in a typically developing paediatric population and in children with CP. The manuscript describing these results will be submitted as Davico, G., Killen, B.A., Carty, C.P., Lloyd, D.G., Devaprakash, D., Pizzolato, C. *Developing the new generation of personalised neuromusculoskeletal models to investigate cerebral palsy*. IEEE Transactions on Biomedical Engineering.

### **Introduction**

Neuromusculoskeletal (NMSK) models are virtual, digital and mathematical representations of the human anatomy, wherein bones are commonly described as rigid bodies interconnected by joints and actuated by muscles. When combined with motion capture (MOCAP) and ground reaction force data, NMSK models can be used for biomechanical analysis of gait and several other locomotor tasks and daily activities (e.g. running, sit-to-stand tasks and side stepping). Importantly, NMSK models can estimate internal biomechanical quantities, such as muscle and joint contact forces, that are difficult or unethical to measure *in vivo*. As such, NMSK models have been employed to better understand the underpinning neuromuscular mechanisms that manifest the pathologies observed in cerebral palsy and improve their clinical management (Arnold and Delp 2005).

Despite the evolution of NMSK modelling techniques, extreme care should be taken in interpreting the results of biomechanical simulations, as NMSK models relies on

numerous assumptions (Hicks et al. 2015; Valente et al. 2014). These include: (1) generic musculoskeletal anatomy based on limited number of cadaveric specimens, (2) simplified joint kinematics and (3) muscle activation patterns generated via optimisation methods which are based on *a priori* criteria. In NMSK modelling musculoskeletal anatomy is commonly linearly scaled from generic template models (Delp et al. 1990). However, musculotendon (MTU) parameters, i.e. tendon slack and optimal fibre length, do not linearly scale with bones or muscle lengths (Ward et al. 2007; Ward et al. 2005). Hence, muscle function, which strongly depends on these parameters (Buchanan and Shreeve 1996; Carbone et al. 2016; Winby et al. 2008), may be affected. Moreover, generic bony geometries poorly represent real bones (Bahl et al. 2019; Suwarganda et al. 2019). As such, joint centres, particularly the hip joint centre, may be inappropriately located (Bahl et al. 2019; Kainz et al. 2017b), thus affecting joint angles calculations (Kainz et al. 2017a) and subsequent joint moments estimates. Additionally, location of muscle attachments may be inaccurate due to morphological differences between generic and real bones, affecting MTU kinematics (Lenaerts et al. 2008; Scheys et al. 2008a), and consequently muscle forces estimates. Lastly, muscle activations are commonly synthesised using optimisation algorithms, e.g. static optimisation (Crowninshield and Brand 1981). Depending on the optimisation criteria selected, the underlying assumption is that the central nervous system favours the maximisation of endurance, minimisation of excitation, or smallest muscle forces while activating muscles to perform a certain task, which cannot account for co-contractions and abnormal muscle activity typical of individuals with neuromuscular pathologies. Resulting knee joint contact forces profiles may show zero loading in swing phase (Modenese et al. 2018). However, this is in contrast with experimental data from instrumented implants (Fregly et al. 2012a).

To overcome the above limitations, several personalised NMSK models with different levels of complexity and subject-specificity have been developed over the years (Arnold and Delp 2005; da Luz et al. 2017; Fox et al. 2018; Gerus et al. 2013; Hoang et al. 2018; Modenese et al. 2018; Schwartz and Lakin 2003; Steele et al. 2012; van der Krogt et al. 2016; Veerkamp et al. 2019; Wesseling et al. 2019). In these, personalisation was introduced in various ways (Table 16). Subject-specific skeletal anatomies have been reconstructed from CT or MRI scans via manual or semiautomatic segmentations (da Luz et al. 2017; Scheys et al. 2006) or generated via statistical shape modelling (Nolte et al. 2016; Zhang et al. 2014a) and morphing techniques (Oberhofer et al. 2019). Muscle attachments,

which may not be visible on medical images, have been morphed to personalised geometries using atlas-based approaches (Pellikaan et al. 2014); while via-points or wrapping surfaces (Modenese et al. 2018; Wesseling et al. 2019) were manually inserted to constrain muscle pathways. Moreover, optimal fibre and tendon slack lengths, which may not be readily measured *in vivo* (Herzog et al. 1991), have been (1) tuned to ensure physiological muscle behaviour (Modenese et al. 2016; Winby et al. 2008), and/or (2) calibrated within physiological ranges (Hoang et al. 2018; Pizzolato et al. 2015; Serrancolí et al. 2016). The maximal isometric force of muscles has often been scaled as function of participants' mass and/or height (Kainz et al. 2018; Noble et al. 2017; van der Krogt et al. 2016) or with segmented muscle volumes when medical images were available (Handsfield et al. 2014). Nonetheless, muscle weakness and altered mechanical properties due to CP have commonly been based on literature data (Fox et al. 2009; Steele et al. 2012). Finally, several methods were proposed to synthesise muscle activation patterns. These included dynamic optimisation (Anderson and Pandy 2001a), computed muscle control (Thelen et al. 2003b), electromyography(EMG)-informed approaches (Lloyd and Besier 2003; Pizzolato et al. 2015; Sartori et al. 2012) and synergy-based methods (Meyer et al. 2016).

However, in previous work most of the above features were implemented independently one another. Therefore, it is not clear what the combined effect of different levels of personalisation is on muscle and joint contact forces estimates. Hence, in this study we developed six different NMSK models with incremental levels of personalisation, with a twofold aim. Firstly, to determine which model was physiologically more plausible. Secondly, to quantify the individual effect of personalised (i) MTU parameters, (ii) neural solution, and (iii) musculoskeletal anatomy on the outcome variables. We hypothesised twofold. First, corresponding with the higher the level of personalisation, the models would produce more physiologically plausible outcome estimates. Second, considering the limitations of static optimisation and the differences between generic scaled and image-based geometries, personalising neural solution and musculoskeletal anatomy would affect models' estimates more than calibrating MTU parameters.

**Table 16.** List of methods employed to personalise neuromusculoskeletal models, based on experimental, literature or models data. Personalised features include: musculoskeletal anatomy, muscle pathways, optimal fibre length (OFL), tendon slack length (TSL), maximal muscle isometric force ( $F_{\text{iso}}^{\text{max}}$ ) and muscle activation patterns.

|                | <b>Skeletal anatomies</b>      | <b>Muscle pathways</b> | <b>OFL&amp;TSL</b>   | <b><math>F_{\text{iso}}^{\text{max}}</math></b> | <b>Muscle activations</b>                        |
|----------------|--------------------------------|------------------------|----------------------|---|--|
| <b>Methods</b> | Segmentation of medical images | Atlas-based approaches | Morphometric scaling | Scaling with mass                               | Dynamic optimisation                             |
|                | Statistical shape modelling    | Via points             | Calibration          | Scaling with height                             | Computed muscle control                          |
|                | Mesh fitting techniques        | Wrapping surfaces      | Experimental data    | Scaling with muscle volumes                     | EMG-informed approaches<br>Synergy-based methods |

# Methods

## Participants

Three children with unilateral CP (Gross Motor Function Classification System I-II. Age:  $8.35 \pm 2.01$  years, height:  $1.25 \pm 0.12$  m, mass:  $23.30 \pm 5.33$  kg) and three typically developing (TD) age- and size-matched control participants (age:  $7.98 \pm 1.75$  years, height:  $1.23 \pm 0.10$  m, mass:  $24.47 \pm 6.02$  kg) were enrolled in the study (Table 17). The study was approved by the Children's Health Queensland Hospital and Health Services human research ethics committee and informed consent was provided by each participant's guardian or parent.

**Table 17.** Demographics of the studied population, which included three children with cerebral palsy (CP, GMFCS I-II) and 3 age-matched typically developing (TD) controls.

|             | Age<br>[years] | Height<br>[m] | Mass<br>[Kg] | Diagnosis  | GMFCS |
|-------------|----------------|---------------|--------------|------------|-------|
| <b>TD01</b> | 10.45          | 1.385         | 32.90        | -          | -     |
| <b>TD02</b> | 6.55           | 1.170         | 21.30        | -          | -     |
| <b>TD03</b> | 6.96           | 1.160         | 19.00        | -          | -     |
| <b>CP01</b> | 6.50           | 1.135         | 18.00        | Hemiplegic | I     |
| <b>CP02</b> | 11.16          | 1.425         | 30.60        | Diplegic   | II    |
| <b>CP03</b> | 7.39           | 1.195         | 21.30        | Diplegic   | I     |

## Gait analysis data collection and processing

A 3D gait analysis assessment was performed in the gait laboratory at Queensland Children Motion Analysis Service (QCMAS, Brisbane, QLD, Australia), where an experienced physiotherapist placed 51 retro-reflective motion capture markers on anatomical landmarks (see Chapter 3 of this thesis, General Methods) and twelve wireless bi-polar EMG sensors (Zerowire, Aurion, Milan, IT. 1000 Hz) on selected muscles of the left lower limb (see Chapter 3 of this thesis, General Methods).

The gait lab was equipped with a 10-camera motion capture system (Vicon Motion System, Oxford, UK. 100 Hz) to record 3D marker trajectories, and 4 in-ground force platforms (Advanced Mechanical Technology Inc., Watertown, MA, USA. 1000 Hz) to

simultaneously measure the ground reaction forces while the participants performed dynamic tasks. An additional static trial was collected while the participants were standing in a T-pose.

Motion capture data were cleaned and labelled in Vicon Nexus 2.6, then processed in MATLAB using the MOTO-NMS toolbox (Mantoan et al. 2015). Both marker trajectory and ground reaction force data were filtered using 4<sup>th</sup> order 6 Hz low-pass Butterworth zero-lag filter. EMG signals were band-pass filtered (zero-lag double-pass 2<sup>th</sup> order Butterworth, 30-400 Hz), full-wave rectified, low-pass filtered (zero-lag double-pass 2<sup>th</sup> order Butterworth, 6 Hz) and then normalised to each muscle's maximal excitation identified across walking, heel raising and jumping tasks (Devaprakash et al. 2016).

## **MRI imaging and processing**

Following gait analysis, participants had MRI scans taken at the Queensland Children's Hospital (QCH, Brisbane, QLD, Australia). All motion capture markers placed on anatomical landmarks were replaced by MRI compatible markers, filled with a liquid visible on MRI, while the remaining upper body and cluster markers were removed. Full lower limb MRI scans, i.e. from the iliac crests to the malleoli, were acquired on a 1.5 T SIEMENS MAGNETOM Avanto fit syngo MR VE11B scanner (SIEMENS, Germany) using a 3D PD SPACE sequence (slice thickness: 1.0 mm, spatial resolution: 0.83x0.83mm<sup>2</sup>). Lower limb bony geometries, including pelvis, femurs, patellae, tibiae and fibulas, were manually segmented on the MRI scans using the Mimics Research Innovation Suite (v19).

## **Base musculoskeletal model**

A simplified gait2392 OpenSim model (Delp et al. 1990) was selected as base musculoskeletal anatomy. The base model included 34 MTUs per leg (Sartori et al. 2012), a single degree-of-freedom (DOF) knee mechanism with generic splines defining knee flexion/extension and a two-point contact knee mechanism for the calculation of knee JCFs (Saxby et al. 2016). Medial and lateral contact points were positioned on the tibial plateaus based on a regression equation (Winby et al. 2009).

To match each participant's size, the base musculoskeletal anatomy was linearly scaled with motion capture data according to Kainz' recommendations (2017b). However, since the population under study was significantly shorter and smaller than the subjects

represented by the generic OpenSim model, linearly scaled MTU parameters were further tuned. Specifically, we employed a morphometric scaling (Modenese et al. 2016) to optimise optimal fibre and tendon slack length values, thus ensuring a physiological muscle behaviour throughout the full range of motion. Maximal isometric force values were scaled based on each participant's mass, using the formula proposed by van der Krogt and colleagues (2016):

$$F_{SS}^{\max} = F_G^{\max} (m_{SS}/m_G)^{2/3} \quad (9)$$

where  $m_{SS}$  is the mass of the participant, while  $m_G$  and  $F_G^{\max}$  are the mass and maximal isometric force values from the unscaled template model.

## Model personalisation

The base model was progressively personalised to feature subject-specific image-based anatomies, tuned and calibrated MTU parameters and muscle activation patterns derived from EMG data.

Subject-specific bony geometries were reconstructed combining statistical shape modelling and morphing techniques (see Chapter 5). Personalised musculoskeletal anatomies were generated using the free and open-source software Musculoskeletal Atlas Project (MAP) Client (Zhang et al. 2014b). Personalised bones were then employed to customise a generic gait2392 OpenSim model (Delp et al. 1990) for use in biomechanical simulations. Feet bone geometries, for which a statistical shape model was not available in the MAP Client, were linearly scaled from the generic gait2392 model. During the customisation process, the pathways of all muscles spanning the knee joint were also personalised. Muscle origin and insertion points, whose location on the mean models was based on the SOMSO anatomical model, were morphed together with the bone meshes. A set of wrapping surfaces (i.e. analytical shapes) were then fitted to selected anatomical regions to constrain muscle pathways, thus avoiding in-bone muscle penetrations and ensuring smooth MTU kinematics throughout the range of motion (Killen 2019). The resulting MAP Client generated models featured personalised bones and physiologically and physically plausible muscle pathways. The knee joint was modelled as a 1 DOF hinge joint mechanism, where anterior/posterior and superior/inferior translations were prescribed to preserve a fixed distance between femur and tibia; the patellar body was locked to and moved along with the tibial body, via a fixed patello-femoral joint; while hip and ankle joints were defined as in the generic gait2392 OpenSim template model. A two-point contact knee

mechanism was finally implemented to enable the estimation of knee JCFs (Saxby et al. 2016; Winby et al. 2009). In this case, medial and lateral contact points were positioned on the tibial plateaus where femur and tibia, with the model in default position (i.e. all joint angles equal to 0 degrees), were the closest.

Scaled and tuned MTU parameters were further adjusted via a calibration process in the Calibrated EMG-informed Neuromusculoskeletal Modelling Toolbox (CEINMS)(Pizzolato et al. 2015; Sartori et al. 2012), which employed experimental EMG signals to constrain values within physiological limits. The aim was to improve each model's ability to track experimental joint moments and EMG data. During calibration, which was performed using four of the processed trials, optimal fibre and tendon slack length values were allowed to vary by  $\pm 5\%$  from their original value. The strength coefficients that were used in CEINMS to control the force producing capability of each muscle were bound between 0.5 and 1.5. For two subjects (TD03 and CP01) who were twin sisters as well as the shortest and lightest participants in the studied population, a  $\pm 10\%$  variation was implemented to ensure physiological muscle function.

Within CEINMS, two different neural solutions were employed to resolve the muscle redundancy problem. Initially, in consistency with previous literature and for comparisons, the whole set of muscle excitations was synthesised via static optimisation. This minimised the sum of muscle activations squared in order to produce the experimental joint moments. Later on, an EMG-assisted approach, which combined experimental EMG data and muscle excitation synthesised via static optimisation, was employed to personalise the muscle activation patterns.

## **Models summary**

A total of 6 different NMSK models with incremental level of subject-specificity were developed in this study (Table 18). The least personalised model (unCalso) featured a generic scaled musculoskeletal anatomy, morphometrically tuned MTU parameters,  $F_{\max}^{\text{iso}}$  values scaled with each participant's mass and employed static optimisation methods to solve for muscle forces. This model was progressively personalised by (1) calibrating MTU parameters with EMG data (renamed Cal), (2) replacing static optimisation with an EMG-assisted approach to resolve the muscle redundancy problem (subscript EMGa), and (3) updating the musculoskeletal anatomy with personalised bones and MTU pathways via the MAP Client (superscript MAP).

**Table 18.** List of neuromusculoskeletal models developed in this study.

| Model                              | Personalised features |           |                         |                    |
|------------------------------------|-----------------------|-----------|-------------------------|--------------------|
|                                    | MSK anatomy           | OFL & TFL | $F_{\max}^{\text{iso}}$ | Muscle activations |
| unCal <sub>SO</sub>                | ✗                     | ✗         | ✓                       | ✗                  |
| Cal <sub>SO</sub>                  | ✗                     | ✓         | ✓                       | ✗                  |
| Cal <sub>EMGa</sub>                | ✗                     | ✓         | ✓                       | ✓                  |
| unCal <sub>SO</sub> <sup>MAP</sup> | ✓                     | ✗         | ✓                       | ✗                  |
| Cal <sub>SO</sub> <sup>MAP</sup>   | ✓                     | ✓         | ✓                       | ✗                  |
| Cal <sub>EMGa</sub> <sup>MAP</sup> | ✓                     | ✓         | ✓                       | ✓                  |

## Biomechanical simulations

Biomechanical simulations were performed on both generic and personalised musculoskeletal anatomies in OpenSim (v 3.3) (Delp et al. 2007), where joint angles, joint moments and MTU kinematics were calculated using the Inverse Kinematics, Inverse Dynamics, and Muscle Analysis tools, respectively. OpenSim's results were then provided to the CEINMS toolbox to guide the calibration process, when required, and to estimate muscle forces using the two neural solutions. In both cases, the following objective function was solved frame by frame:

$$f = \alpha E_{\text{Moment}} + \beta E_{\text{sumExc}} + \gamma E_{\text{EMG}} \quad (10)$$

where  $E_{\text{sumExc}}$  is the sum of squared muscle excitations;  $E_{\text{Moment}}$ , and  $E_{\text{EMG}}$  are the errors between experimental and estimated joint moments and muscle excitations respectively;  $\alpha$ ,  $\beta$  and  $\gamma$  are weighting factors differently set depending on the neural solution. For static optimisation,  $\alpha$  and  $\beta$  were set to 1 and 2 respectively, with  $\gamma$  set to 0. In contrast, for the EMG-assisted approach the weighting factors were optimised to balance between muscle excitations and joint moments tracking errors (Pizzolato et al, 2015). Finally, considering the knee joint as planar, at each time point knee JCFs could be estimated solving for the following static equilibrium problem (Winby et al. 2009):

$$JCF^{LC/MC} = \frac{(M_{MTU}^{MC/LC} - M_{ext}^{MC/LC})}{d_{IC}} \quad (11)$$

where  $M_{ext}^{MC/LC}$  is the external moment around the medial/lateral contact point,  $M_{MTU}^{MC/LC}$  is the overall muscle torque acting on the medial/lateral knee compartment, and  $d_{IC}$  is the intercondylar distance (i.e. between contact points).

## Data analysis

The ability of each model to reproduce physiologically plausible internal biomechanics was assessed by quantifying their ability to track experimental joint moments and EMG data and to predict non-zero loading in swing phase. For each of the 12 muscles experimentally collected, r-squared values ( $R^2$ ) and root mean square errors (RMSE) between CEINMS predictions and surface EMG data were calculated and reported as mean (standard deviation). Same metrics were used to compare ankle and knee joint moments estimates from CEINMS and the corresponding OpenSim Inverse Dynamics results. For the total knee JCFs, both the force profile throughout the gait cycle and the magnitude of the first and second peaks were compared. After each test, a score was assigned to each model based on their performance: 1 point per participant for whom the above criteria were met. The model which obtained the highest overall score was considered to be the most physiologically plausible, and was thereon used as gold standard to compare muscle forces, total, medial and lateral JCF estimates. The level of agreement with the most physiologically plausible model was measured once again computing the  $R^2$  and RMSE values. This enabled the quantification of the individual effect of each level of personalisation on the endpoint variables.

## Statistical analysis

Data were checked for normality. If data distributions were normal, a mixed ANOVA was performed to compare  $R^2$  and RMSE values between models and within populations (i.e. TD and CP). Post-hoc analyses were conducted using paired t-tests implementing Bonferroni corrections to account for multiple comparisons. If data were not normally distributed, the  $R^2$  and RMSE were compared using a Friedman test for repeated measures followed by a Wilcoxon signed-rank test. Finally, statistical parametrical mapping (SPM) was employed to compare medial and lateral knee JCF profiles. Paired T-tests or the

equivalent non-parametrical tests were conducted to identify when during the gait cycle different models produced significantly different estimates of JCFs. For all tests, statistical significance was initially set to  $p = 0.05$ . All analysis were conducted in Python 3.6, using the Pingouin (Vallat 2018) and spm1d (Pataky 2012) modules.

## Results

Joint kinematics and kinetics produced by generic and MAP generated NMSK models showed a high level of agreement (i.e., knee flexion angle:  $R^2 \sim 0.95$ , RMSE  $\sim 4$  deg; knee flexion moment:  $R^2 > 0.85$ , RMSE  $\sim 0.08$  Nm/Kg. Figure 47, Appendix D).

All models well tracked inverse dynamics' ankle ( $R^2 > 0.97 \pm 0.02$ ) and knee ( $R^2 > 0.85 \pm 0.13$ ) joint moments (Figure 34). Significant differences in  $R^2$  values were revealed by the ANOVA test (1) between models ( $p = 0.0015$ ) in tracking the ankle plantarflexion moment, and (2) between populations ( $p = 0.047$ ) in tracking the knee flexion moment. Specifically,  $\text{Cal}_{\text{EMGa}}^{\text{MAP}}$  less accurately tracked ankle joint moments compared to  $\text{unCal}_{\text{SO}}^{\text{MAP}}$  and  $\text{Cal}_{\text{SO}}$  models, while all six NMSK models better tracked knee joint moments for TD compared to CP participants (on average  $R_{\text{TD}}^2 = 0.93 \pm 0.05$ ,  $R_{\text{CP}}^2 = 0.88 \pm 0.08$ ). Low RMSEs ( $< 0.08$  Nm/Kg) were measured for both ankle and knee joint moments, across models and subjects. Ankle plantarflexion tracking errors were significantly lower in paediatric CP models ( $p < 0.0001$ ). Discrepancies between experimental and tracked joint moments were mostly observed around heel strike (first frames) and toe-off ( $\sim 60\%$  gait cycle).

For both TD and CP children, the first four NMSK models, which employed static optimisation methods to synthesise muscle excitations, were unable to accurately track experimental EMG data ( $R^2 < 0.30 \pm 0.23$ , RMSE  $> 0.09 \pm 0.03$ ). Contrarily,  $\text{Cal}_{\text{EMGa}}$  and  $\text{Cal}_{\text{EMGa}}^{\text{MAP}}$  produced significantly more accurate estimates ( $R^2 > 0.58 \pm 0.25$ , RMSE  $< 0.07 \pm 0.04$ ,  $p < 0.0001$ ). A significant main effect of the level of personalisation (i.e., model) was found on models' ability to track EMG signals. Indeed, replacing static optimisation with an EMG-assisted approach to solve for muscle forces had a significantly larger effect on the ability of models to track EMG data, compared to personalising the musculoskeletal anatomy (Figure 34c).

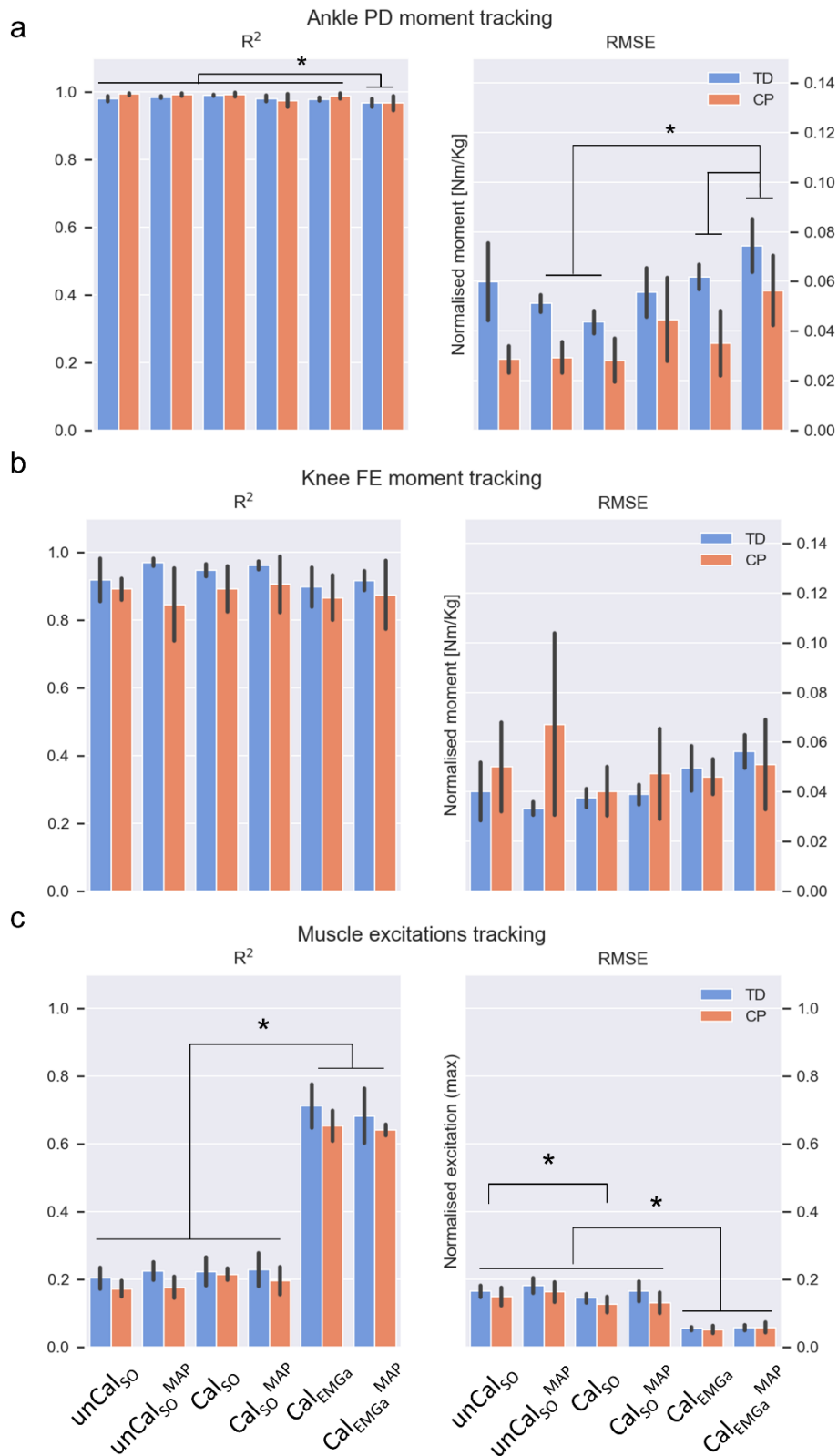


**Figure 34.** The models' abilities to track experimental data. For each model,  $R^2$  and RMSE values between predicted and experimental ankle joint moment (a), knee joint moment (b) and EMG data (c) were computed. Results are reported as mean across populations, TD (blue) and CP (red).

From a qualitative standpoint, MAP generated models produced lower knee JCF estimates compared to the corresponding scaled generic models, for all children (Figure 35). Moreover, excluding  $\text{Cal}_{\text{SO}}^{\text{MAP}}$  model, models featuring personalised musculoskeletal anatomies predict physiological non-zero loading conditions in swing phase for five out of six children. Similar results were achieved using  $\text{unCal}_{\text{SO}}$  models.

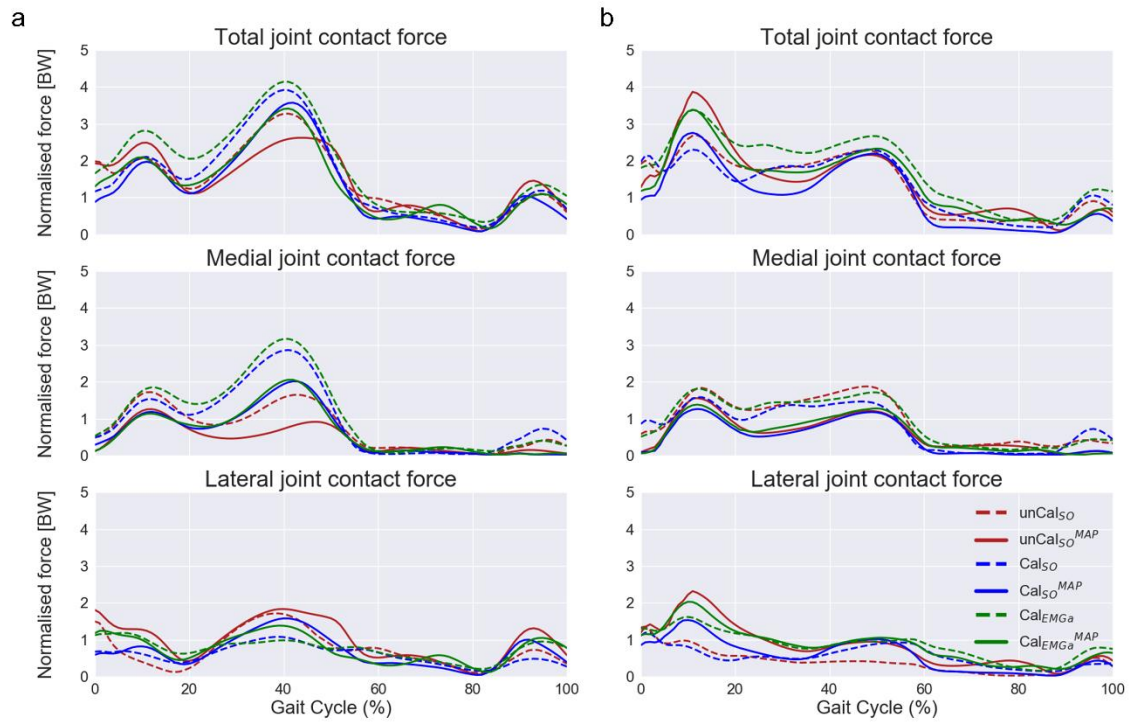


**Figure 35.** Examples of knee JCF profiles estimated using the 6 developed NMSK models, for a TD child (a) and a CP child (b). Colors discriminate models based on the definition of musculotendon parameters and neural solution (red =  $\text{unCal}_{\text{SO}}$ , blue =  $\text{Cal}_{\text{SO}}$ , green =  $\text{Cal}_{\text{EMGa}}$ ). Line types refers to the musculoskeletal anatomy (solid = personalised in the MAP Client, dashed = scaled generic from OpenSim).

**Table 19.** Physiological plausibility score. For each model, a score up to 6 was assigned based on the number of participants (dots) for whom the selected feature/condition was present/met. Population specific, i.e. for typically developing (TD, blue) and cerebral palsy (CP, red) children, and overall scores per model were calculated. The model associated to the highest score ( $\text{Cal}_{\text{EMGa}}^{\text{MAP}}$ ) was considered to be the most physiologically plausible model.

| Physiologically plausible features |                  |                      |                           |                 |       |    |
|------------------------------------|------------------|----------------------|---------------------------|-----------------|-------|----|
| Model                              | Tracking moments | Tracking excitations | JCFs                      | Correct anatomy | Score |    |
|                                    |                  |                      | Non-zero loading in swing |                 |       |    |
| unCal <sub>SO</sub>                | •••              | -                    | •••                       | -               | 6     | 11 |
|                                    | •••              | -                    | ••                        | -               | 5     |    |
| Cal <sub>SO</sub>                  | •••              | -                    | ••                        | -               | 5     | 10 |
|                                    | •••              | -                    | ••                        | -               | 5     |    |
| Cal <sub>EMGa</sub>                | •••              | •••                  | ••                        | -               | 8     | 15 |
|                                    | •••              | •••                  | •                         | -               | 7     |    |
| unCal <sub>SO</sub> <sup>MAP</sup> | •••              | -                    | •••                       | •••             | 9     | 17 |
|                                    | •••              | -                    | ••                        | •••             | 8     |    |
| Cal <sub>SO</sub> <sup>MAP</sup>   | •••              | -                    | ••                        | •••             | 8     | 14 |
|                                    | •••              | -                    | -                         | •••             | 6     |    |
| Cal <sub>EMGa</sub> <sup>MAP</sup> | •••              | •••                  | •••                       | •••             | 12    | 23 |
|                                    | •••              | •••                  | ••                        | •••             | 11    |    |

TD
CP

Based on the above comparisons (Table 19),  $\text{Cal}_{\text{EMGa}}^{\text{MAP}}$  was deemed to be the NMSK model with the highest level of physiological plausibility. Therefore, its estimates of muscle forces and knee JCFs were used as gold standard in subsequent analyses to identify the individual contribution of each personalised feature on models' outcomes.

Increasing the level of subject-specificity was associated with muscle force and JCF profiles more closely approximating the estimates from  $\text{Cal}_{\text{EMGa}}^{\text{MAP}}$  (Figure 36). For the muscle forces, calibration of musculotendon parameters only minimally affected the models' predictions (~5%,  $p = 0.104$ ). However, a ~20% significant increment ( $p < 0.001$ ) in  $R^2$  values was observed when switching neural solution from static optimisation to an EMG-assisted approach. Similar effects were visible on the RMSE values, which became

considerably smaller by using EMG-assisted approaches as opposed to static optimisation ( $p < 0.006$ ). Significantly lower RMSE were obtained in the CP population ( $p = 0.022$ ). The level of personalisation also affected total JCF estimates. Switching neural solution significantly improved the level of agreement with  $\text{Cal}_{\text{EMG}a}^{\text{MAP}}$  predictions ( $p = 0.036$ ). On the other hand, calibrating MTU parameters did not lead to significant improvements in the  $R^2$  ( $p = 0.529$ ).

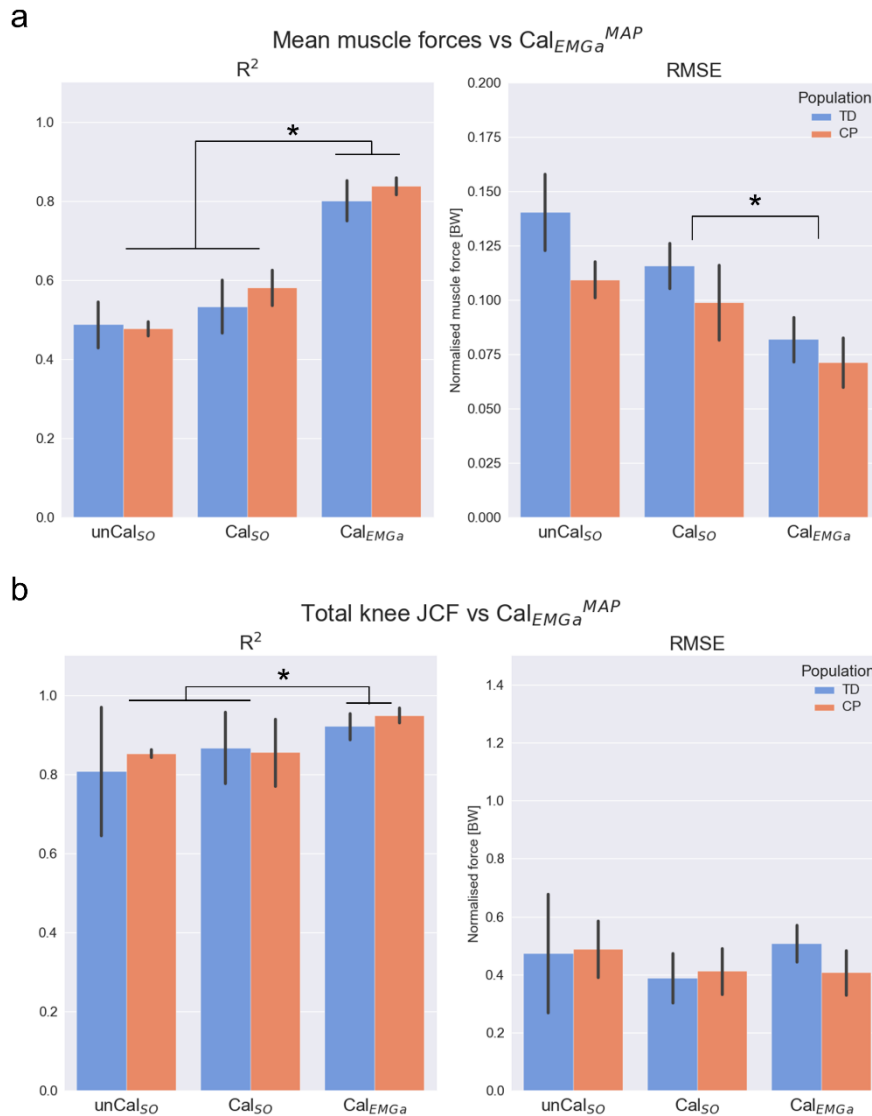


**Figure 36.** Comparison of (a) muscle forces and (b) total knee JCF estimates between models. The level of personalisation was incrementally increased by (1) calibrating musculotendon parameters in CEINMS (unCal<sub>SO</sub> to Cal<sub>SO</sub>), and (2) switching neural solution (Cal<sub>SO</sub> to Cal<sub>EMG<sub>a</sub></sub>). Estimates from the most physiologically plausible model, i.e.  $\text{Cal}_{\text{EMG}a}^{\text{MAP}}$ , were used as gold standard, since no experimental data were available. \* indicate statistically significant differences.

In terms of characteristic peaks of total JCF, Cal<sub>SO</sub> models generally produced lower estimates compared to unCal<sub>SO</sub> and Cal<sub>EMGa</sub>, while Cal<sub>EMGa</sub><sup>MAP</sup> produced the lowest estimates overall (Figure 37).

The agreement between medial JCFs estimated by Cal<sub>EMGa</sub><sup>MAP</sup> and the other models was very high (Figure 38a). The mean R<sup>2</sup> values were larger than 0.87 for all models and across populations, while the RMSE was consistently smaller than 0.5 BW. Nonetheless, unCal<sub>SO</sub> and Cal<sub>SO</sub> showed a significantly lower level of agreement with Cal<sub>EMGa</sub><sup>MAP</sup> compared to Cal<sub>EMGa</sub> (p = 0.036). However, the RMSEs were smaller for Cal<sub>SO</sub> than Cal<sub>EMGa</sub> (p < 0.01). On the lateral compartment of the knee joint the agreement with Cal<sub>EMGa</sub><sup>MAP</sup> was lower than on the medial side, for all models (Figure 38b). The level of personalisation had a significant main effect (p = 0.006), in which the R<sup>2</sup> were significantly higher using a calibrated EMG-informed model compared to unCal<sub>SO</sub> (p < 0.01) and the RMSE were significantly lower switching from static optimisation to EMG-assisted approach (p < 0.047). No differences were detected between populations. Pairwise t-tests in SPM (Figure 39 and Figure 40), conducted separately for each participant, confirmed the above findings. During stance, the medial compartment resulted to be more affected following (i) calibration of MTU parameters and (ii) personalisation of musculoskeletal anatomy (Figure 39a and Figure 40a); while the lateral compartment was mostly affected by the choice of the neural solution (Figure 39b).

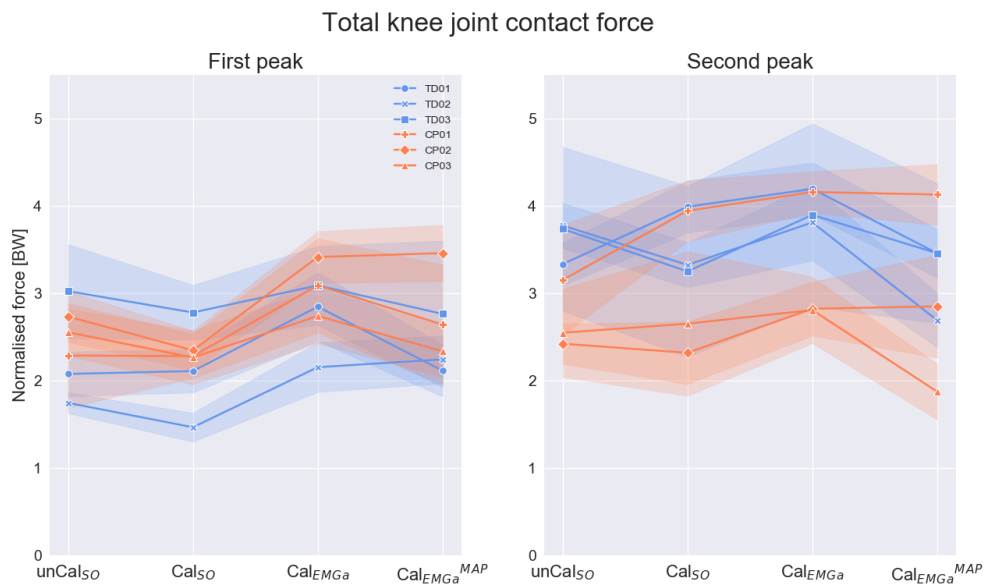


**Figure 37.** Individual peak values for each model and participant. Values are reported as mean (solid line) and standard deviation (shaded area) across 10 walking trials.

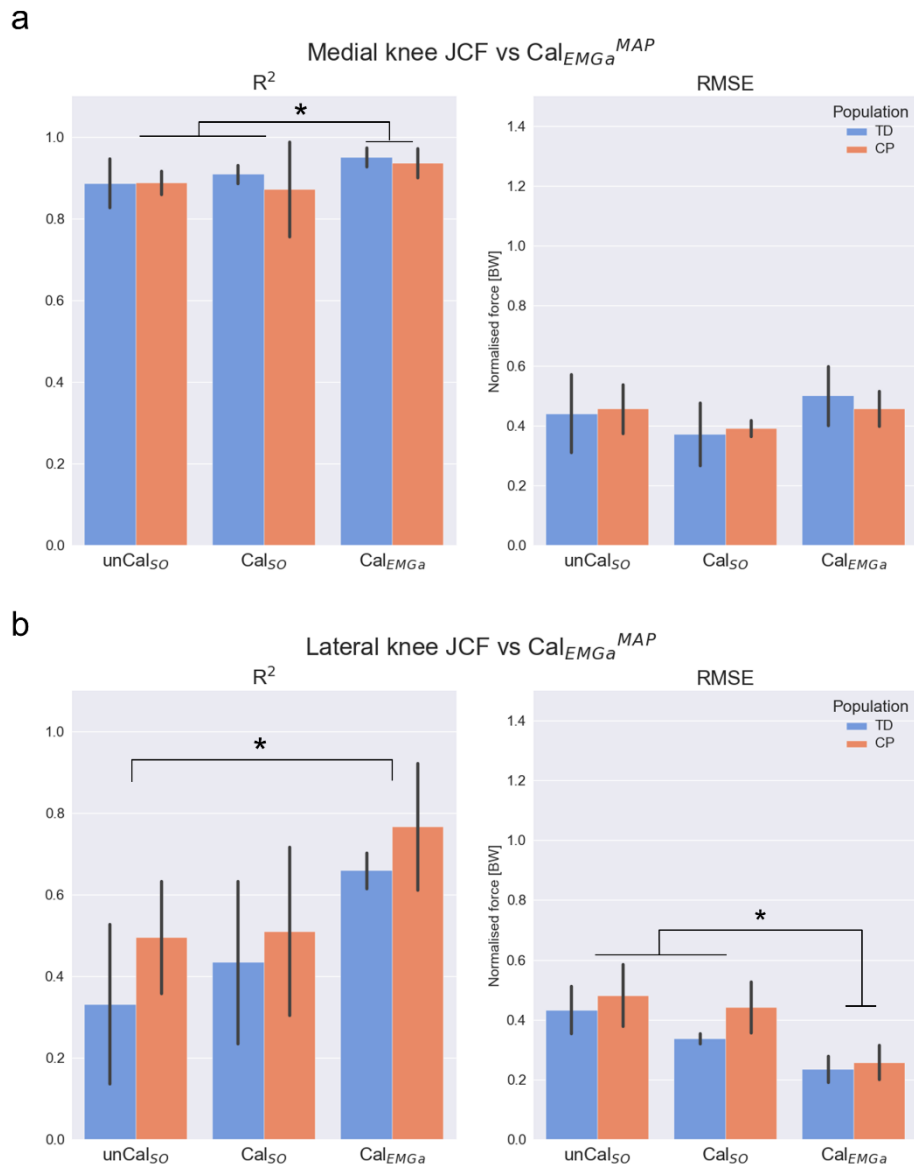


**Figure 38.** Comparison of (a) medial and (b) lateral JCF estimates between models. The level of personalisation was incrementally increased by (1) calibrating musculotendon parameters in CEINMS (unCal<sub>50</sub> to Cal<sub>50</sub>), and (2) switching neural solution (Cal<sub>50</sub> to Cal<sub>EMGa</sub>). Estimates from the most physiologically plausible model, i.e. Cal<sub>EMGa</sub><sup>MAP</sup>, were used as gold standard, since no experimental data were available. \* indicate statistically significant differences.

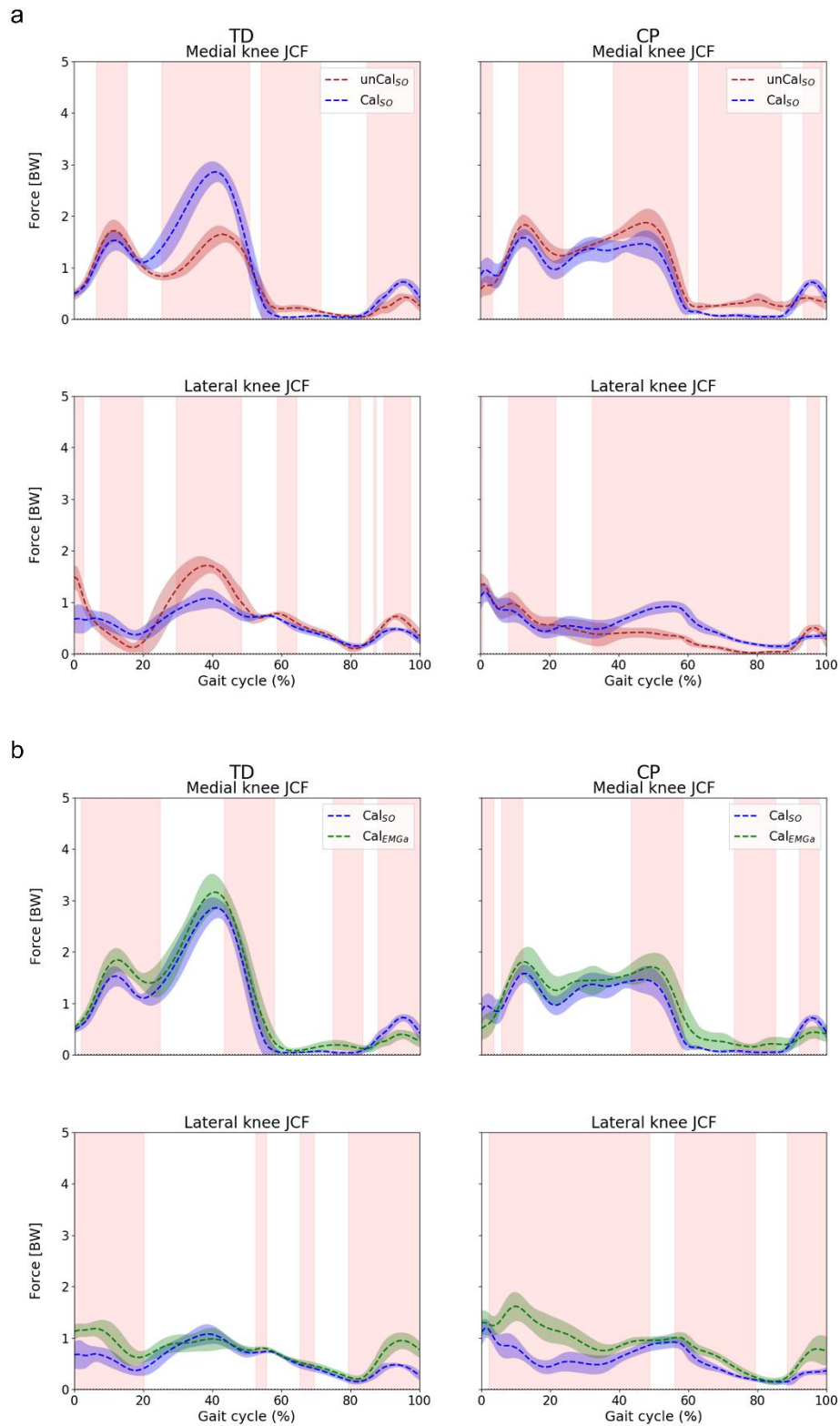


**Figure 39.** Example of medial and lateral joint contact force estimates for one TD and one CP child. Effect of personalising musculotendon parameters (a) and muscle activation patterns (b). Comparisons between unCal<sub>SO</sub>/Cal<sub>SO</sub> and Cal<sub>SO</sub>/Cal<sub>EMGa</sub> models. Red bands indicate significant differences ( $p=0.05$ ).

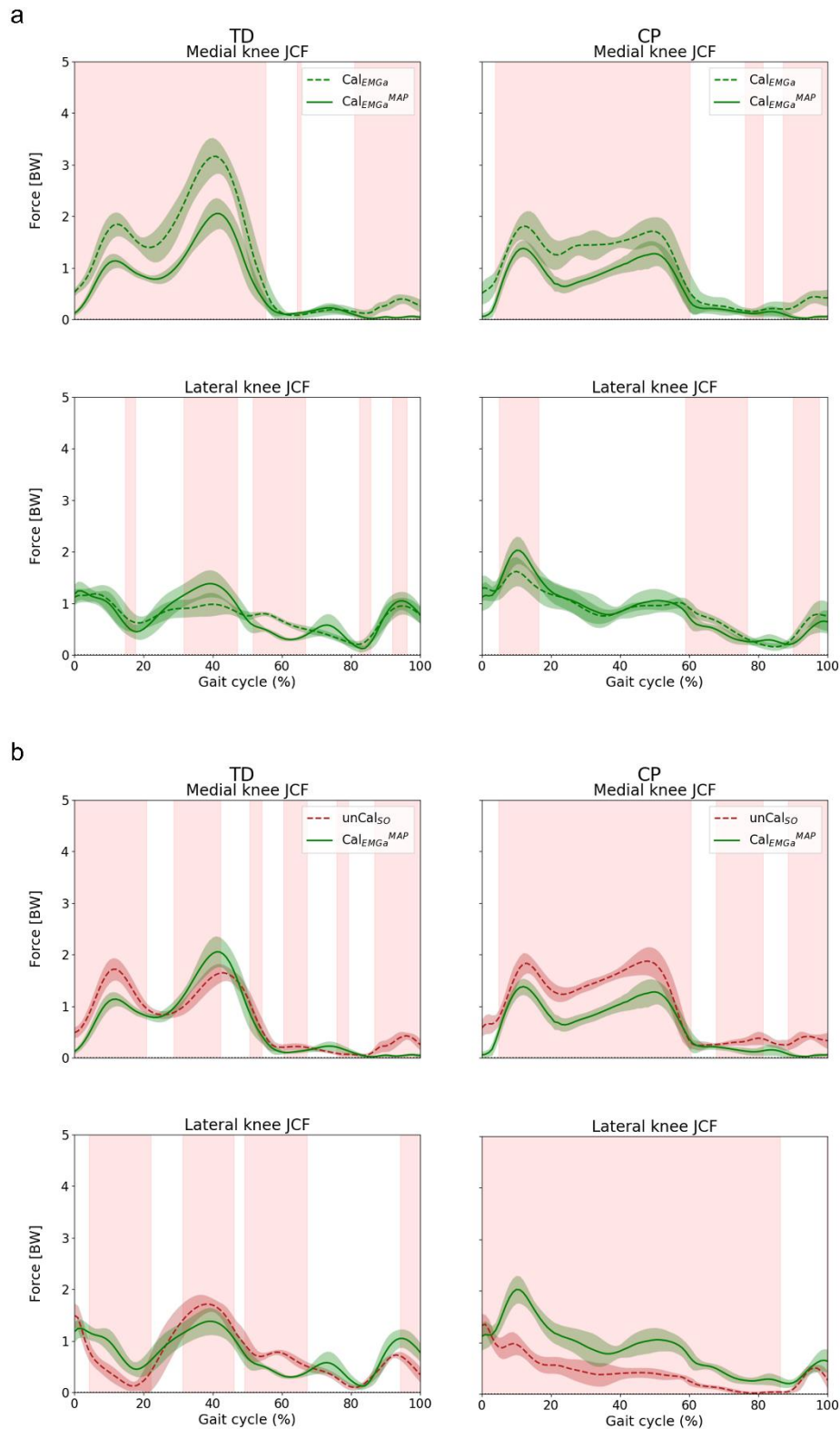


**Figure 40.** Example of medial and lateral joint contact force estimates for one TD and one CP child. Effect of personalising musculoskeletal anatomy (a) and combined effect of different levels of personalisation (b). Comparisons between  $Cal_{EMGa}/Cal_{EMGa}^{MAP}$  and  $unCal_{SO}/Cal_{EMGa}^{MAP}$  models. Red bands indicate significant differences ( $p=0.05$ ).

## Discussion

For the first time, personalised paediatric NMSK models featuring subject-specific bony geometries, muscle pathways, MTU parameters and muscle activation patterns were developed, and employed to estimate knee JCFs during gait in TD and CP populations. Six different models with incremental level of subject-specificity were developed and compared. Among all, the calibrated EMG-assisted NMSK model with personalised musculoskeletal anatomy produced the most physiologically plausible results. Other than accurately representing each individual's anatomy, this model proved to be able (1) to accurately track experimental joint moments and EMG data, and (2) to predict non-zero loading in swing phase. Personalising anatomy and muscle activation patterns more significantly affected muscle forces and knee JCF estimates, i.e. our endpoint variables, compared to calibrating MTU parameters.

In agreement with our first hypothesis, the model with the highest level of personalisation ( $\text{Cal}_{\text{EMG}_a}^{\text{MAP}}$ ) produced the most physiologically plausible internal biomechanics (Table 19). Similar to the other developed models,  $\text{Cal}_{\text{EMG}_a}^{\text{MAP}}$  accurately tracked ankle plantar/dorsiflexion and knee flexion/extension moments. In addition,  $\text{Cal}_{\text{EMG}_a}^{\text{MAP}}$  better tracked experimental EMG data compared to models employing static optimisation. Furthermore, for all participants but one,  $\text{Cal}_{\text{EMG}_a}^{\text{MAP}}$  predicted non-zero knee joint contact loading in swing phase, in line with experimental data from instrumented implants (Fregly et al. 2012a). Moreover, compared to the equivalent generic model employing an EMG-assisted approach ( $\text{Cal}_{\text{EMG}_a}$ ), our most personalised model produced significantly lower estimates of total knee JCF. This is very important. Previous work (Gerus et al. 2013) showed that generic scaled NMSK models may overestimate in-vivo knee JCFs measured with instrumented implants. Last but not least,  $\text{Cal}_{\text{EMG}_a}^{\text{MAP}}$  was anatomically and physiologically more accurate than  $\text{Cal}_{\text{EMG}_a}$  as it featured subject-specific image-based bony geometries and muscle attachments morphed from the SOMSO anatomical model (compared to generic musculoskeletal anatomies).

Increasing the level of personalisation significantly affected muscle force and JCFs estimates. The agreement with  $\text{Cal}_{\text{EMG}_a}^{\text{MAP}}$  results was higher when MTU parameters and/or neural solution were progressively personalised (Figure 36). However, some distinctions need to be drawn. For instance, calibrating MTU parameters appeared to have little impact on mean muscle forces, total and medial joint contact force estimates (Figure 36 and Figure

38). Nonetheless, lateral contact forces were significantly affected (Figure 35 and Figure 38b). However, and importantly, switching neural solution from static optimisation to an EMG-assisted approach considerably improved muscle force tracking ( $R^2 \sim 0.8$ , +20% from Calso models. Figure 36a) and lateral knee JCF tracking (Figure 38b), enabling the identification of abnormal profiles in the CP participants (Figure 39b). In addition, personalising the musculoskeletal anatomy had the greatest impact on joint contact forces (Figure 40a). All MAP generated models produced significantly lower JCFs estimates than the corresponding generic scaled models (Figure 40a), and their ability to track muscle forces was also improved (by 5-10%).

Personalising the musculoskeletal anatomy resulted in lower JCF estimates, particularly in the medial compartment of the knee joint. This is consistent with previous work, where personalised geometries have been associated to lower estimates of contact force, which more closely approximated experimental data from an instrumented implant (Gerus et al. 2013). In the present study, personalised musculoskeletal anatomies featured image-based bony geometries, muscle attachments morphed from the SOMSO anatomical model, physiologically and physically plausible pathways and MTU kinematics, and personalised joint contact points. Particularly, the location of medial and lateral contact points determined the intercondylar distance, which is denominator in the equation solved to compute JCFs (Equation 3). In MAP Client generated models, the contact points were located where tibia and femur were the closest. With the model in default position, i.e. with all joint angles set to 0, an algorithm identified the node on each tibial plateau with shortest Euclidean distance to the corresponding femoral condyle. In contrast, the scaled generic OpenSim models contact point location was defined via regression equations based on adult MRI data (Figure 41). However, adult and paediatric bones may differ in shape and size. Therefore, what may be valid for an adult population may not be applicable to children. This resulted in larger intercondylar distances on MAP generated models compared to generic scaled models (Table 20); possibly explaining our research findings on JCF estimates.

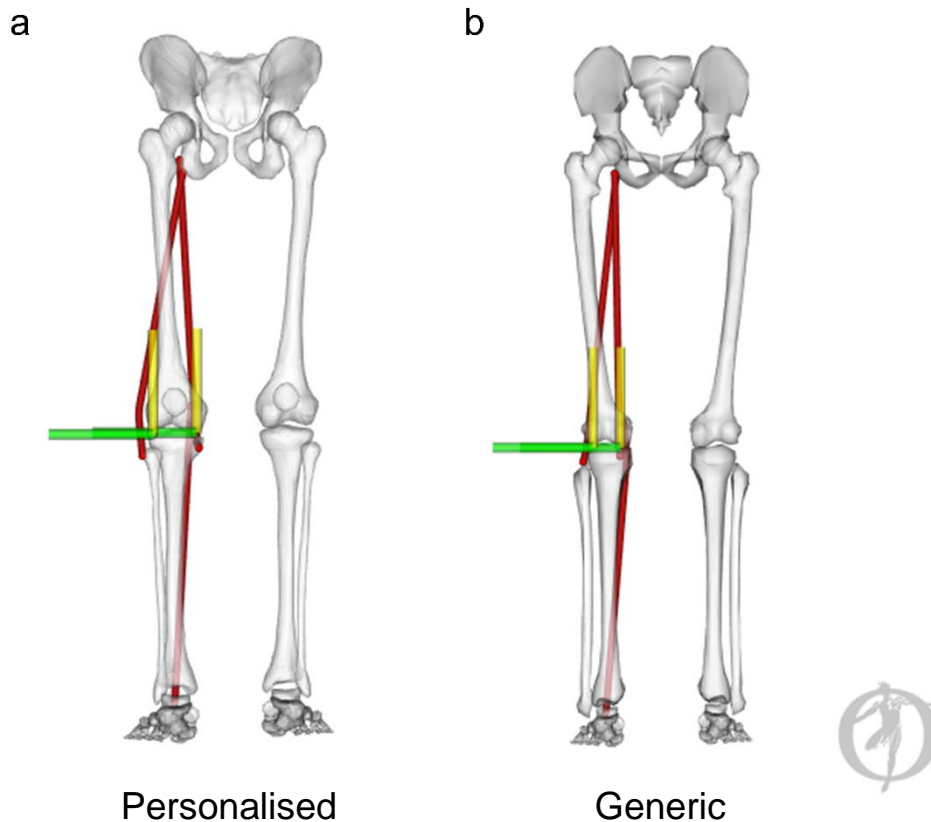


**Figure 41.** Personalised (a) versus scaled generic (b) anatomy showing how medial and lateral contact points were further apart on MAP models.

**Table 20.** Intercondylar distance, in generic scaled and personalised anatomies.

| Intercondylar distance [m] | Subject |       |       |       |       |       |
|----------------------------|---------|-------|-------|-------|-------|-------|
|                            | TD01    | TD02  | TD03  | CP01  | CP02  | CP03  |
| <b>Generic</b>             | 0.033   | 0.027 | 0.026 | 0.023 | 0.036 | 0.031 |
| <b>MAP</b>                 | 0.053   | 0.045 | 0.046 | 0.043 | 0.057 | 0.049 |

This study had some limitations. First, personalised and generic musculoskeletal anatomies featured two different knee joint mechanisms. However, to reduce kinematics discrepancies between models, which could affect JCF predictions, adduction/abduction and internal/external rotation DOFs on the base model were locked, to only allow knee flexion/extension as in the MAP generated models. This resulted in comparable knee joint kinematics and kinetics. Second, although the personalisation of MTU pathways aimed to produce physiologically plausible MTU kinematics, the resulting moment arms and MTU lengths curves reflected patterns observed in cadaveric studies. These may not necessarily

describe the MTU kinematics of a child. Larger than normal moment arms or increased muscle lengths due to the definition of suboptimal wrapping surfaces may have been produced, which could have affected the final estimates. Nonetheless, visual checks were performed, and inaccuracies were manually corrected. Hence, the use of wrapping surfaces resulted in more physically plausible MTU pathways. In-bone penetrations, which are observed in scaled generic models employing via-points to constrain muscle paths, were removed. However, personalised MTU pathways were not validated against *in vivo* data. A thorough investigation of the effects of MSK anatomy personalisation on MTU kinematics, and consequently on muscle forces and joint contact forces, is yet to be conducted. Third, calibration parameters were not standardised for all participants. For TD03 and CP01, who were the smallest children in the studied population (and identical twin sisters), different calibration ranges in CEINMS were used to ensure proper muscle functioning. Instead of a  $\pm 5\%$  variation, calibration allowed for a  $\pm 10\%$  change for both OFL and TSL values. Fourth, the studied population included only three children per group (CP and TD) due to the amount of work required to develop the thirty-six NMSK models. Nonetheless, to confirm the research findings and to determine whether increasing the level of model personalisation may be more beneficial for pathological populations compared to TD children, the methods proposed in this study should be applied to a larger cohort. Last, although this thesis focussed on the knee joint, we acknowledge that individuals with CP experience altered joint loading at the ankle and hip joints (Morrell et al. 2002). Therefore, a comprehensive evaluation (of the three joints) using the levels of personalisation defined in this thesis would provide a more detailed and informative picture of all CP-related effects on gait. Future work should therefore aim to extend the methods hereby presented to both the ankle and hip joints.

## Conclusions

Personalisation is important to generate physiologically plausible NMSK models. Particularly, neural solution and musculoskeletal anatomy play a key role, by allowing to capture atypical muscle activation patterns and to properly characterise joint geometries and muscle pathways. Nonetheless, when working on small paediatric populations, calibration of MTU parameters may be required. Linearly scaled and tuned values may be not physiologically plausible, thus hindering proper muscle function. By generating a subject-specific model with personalised bony geometries, muscle pathways, MTU parameters and muscle activation patterns, we demonstrated the need for implementing different levels of

personalisation at once to produce more physiologically plausible estimates. Although (1) more robust ways to assess the physiological plausibility of a NMSK model should be sought after and (2) automated workflows to generate fully personalised NMSK models are required, the proposed workflow represent the first step towards this goal. More importantly, we showed that personalisation may be introduced using open-source and freely available software, such as OpenSim, CEINMS and the MAP Client.

# CHAPTER 7

---

## General discussion

This chapter first summarises and highlights the major scientific contributions that stem from the work presented in this thesis. The summary is followed by discussion of general modelling and clinical implications with a focus on how the present work may help improve clinical management of individuals with CP. Finally, the general limitations associated with the methodology and future directions are considered.

### Thesis summary

The overarching aim of this thesis was to develop personalised neuromusculoskeletal models of healthy paediatric populations and children with CP. To this end, the thesis comprised of three independent studies. The first study highlighted the need for personalised musculotendon parameters and muscle activation patterns to characterise CP. The second study identified an optimal workflow for accurate reconstruction of paediatric lower limb bones using the Musculoskeletal Atlas Project (MAP) Client. The third study had twofold aims. First, to develop paediatric NMSK models with high level of personalisation. Second, to determine which personalised feature(s), i.e. muscle parameters, neural solution or musculoskeletal anatomy had the largest effect on muscle and knee joint contact force (JCF) estimates.

Study one (Chapter 4) investigated how the personalisation of (i) muscle activation patterns, (ii) optimal fiber and tendon slack lengths, and (iii) maximal isometric force values affected muscle forces and knee JCF estimates during the stance phase of the gait cycle in TD and CP children. Two, 13 years old, identical twin brothers (one TD and one with unilateral spastic CP) were enrolled in the study. The unique recruitment enabled an optimal age- and size-match between participants, increasing the validity of comparative findings. Both children underwent three-dimensional gait assessment and MRI scanning. For each

participant, four NMSK models with increasing level of personalisation were developed and compared. The results showed that the use of static optimisation to synthesise muscle excitations was associated with poor tracking of EMG data, which resulted in similar muscle activation patterns between TD and CP children. Hence, differences in muscle and JCF estimates due to CP were masked. Moreover, personalisation of OFL and TSL enabled more physiologically plausible knee JCF profiles, while updating the maximal isometric force values had a little impact on the final estimates. We concluded that personalisation of muscle parameters and muscle activation patterns is essential while studying neuromuscular disorders.

In study two (Chapter 5) different pipelines, i.e. combination of methods, to generate personalised paediatric lower limb bony geometries for NMSK modelling applications were developed and compared. Medical imaging and motion capture data from eighteen TD children were used to inform the bone reconstruction process. Within the open-source MAP Client we developed ten different pipelines combining linear and non-linear scaling methods, host- and local-mesh fitting techniques. Different levels of imaging data sparsity were tested. For further comparisons, linearly scaled generic OpenSim bony geometries were also generated. Reconstruction accuracy was quantified by computing the Jaccard index, the root mean square distance error and the Hausdorff distance between each reconstructed bone and the corresponding segmented geometry. In addition, hip joint centre locations were extracted and compared. The distance between left and right HJCs were also computed and compared (i) against MRI measurements and (ii) markers based measurements (i.e. Harrington regression equation). We found that (1) for children smaller than 145 cm, non-linear scaling methods might produce abnormal geometries, (2) paediatric lower limb bones can be accurately reconstructed from (sparse) medical imaging datasets, and (3) the Harrington regression equation may inaccurately estimate HJC distance. Based on the research findings from this study, the following guidelines to accurately reconstruct paediatric lower limb bones were proposed: (1) to combine linear scaling methods and mesh fitting techniques for optimal results, (2) to prefer linear over non-linear scaling methods when medical images are not available, (3) not to employ non-linear scaling to reconstruct bones for paediatric populations smaller than 145 cm.

In study three (Chapter 6), personalised paediatric NMSK models with high level of subject-specificity were developed. Motion capture and MRI data were employed to progressively personalise a generic OpenSim NMSK model to determine the individual

effect of (i) personalised musculoskeletal anatomies, (ii) personalised musculotendon parameters and (iii) personalised muscle activation patterns on muscle forces and knee JCFs estimated during walking in three TD and three CP children. Thirty-six NMSK models were thus developed (i.e. six for each participant). The physiological plausibility of each model was quantified by scoring each models ability (1) to track experimental joint moments and EMG data, (2) to estimate non-zero loading in the swing phase of gait and (3) to accurately represent each participant's anatomy. Consequently, the most personalised model was deemed to reproduce the most physiologically plausible internal biomechanics. Consequently, the estimates of muscle forces and knee JCFs computed using this model were used as the 'gold standard' to compare and to assess the performance of the remaining models. Personalisation of neural solution and musculoskeletal anatomy appeared to affect muscle forces and knee JCF estimates more than the calibration of MTU parameters. Specifically, switching neural solution significantly affected lateral compartment loading, while implementing subject-specific anatomies led to reduced JCF estimates on the medial compartment of the knee joint. Nonetheless, calibrating OFL and TSL values could significantly impact on lateral JCF estimates.

## **General modelling implications**

Biomechanical simulations of gait, or other activities of daily living, are commonly performed using linearly scaled generic NMSK models. Despite being easy to implement and rapid to generate, such generic models can produce physiologically implausible results that might lead to erroneous interpretation of a patient's internal biomechanics. Inaccuracies become more apparent when working on paediatric populations; particularly in the study of neuromuscular disorders (e.g. CP). For these reasons, more complex and personalised NMSK models are now becoming popular (Bosmans et al. 2014; Gerus et al. 2013; Hoang et al. 2019; Hoang et al. 2018; Modenese et al. 2018; Saxby et al. 2016; Scheys et al. 2011b; Scheys et al. 2008b; Steele et al. 2012; van der Krogt et al. 2016; Veerkamp et al. 2019; Wesseling et al. 2019). However, due to the niche skillset and specialised software required for model personalisation, the use of personalised models is currently limited to research.

Indeed, employing EMG-informed approaches (Lloyd and Besier 2003; Pizzolato et al. 2015; Sartori et al. 2012) to resolve the muscle redundancy problems is of primary importance in the study of neuromuscular disorders. In line with previous literature (Hoang et al. 2019; Kainz et al. 2019; Veerkamp et al. 2019), results from this thesis showed that

EMG-informed models may produce more physiologically plausible muscle activation patterns, and muscle force estimates; particularly for children with CP. Moreover, experimental EMG data from the major lower limb muscles (i.e. hamstrings, quadriceps, and triceps surae muscles) are routinely collected during gait assessments, as these provide valuable information on muscle coordination. Hence, EMG-informed approaches may be readily implemented in clinical practice. In addition, when the number of EMG sensors is limited, additional muscle activation patterns may be digitally reconstructed via synergy based methods (Bianco et al. 2017; Steele et al. 2015). This approach may be particularly helpful to study small paediatric populations, for whom (1) the identification of muscles may be difficult and (2) cross-talk may affect recorded signals. The evidence presented in this thesis supports the use of EMG-informed approaches for children with CP, however, the use of EMG-informed approaches may not be required to study healthy cohorts. For the latter, it may be fair to assume that the central nervous system aims to optimise muscle recruitment in order to minimise energy consumption during daily living tasks.

Implementing personalised anatomical structures (i.e. bones and muscle pathways) has several implications on biomechanical simulations (Bosmans et al. 2014; Gerus et al. 2013; Kainz et al. 2017a; Lenaerts et al. 2008; Scheys et al. 2008b). However, the process to generate subject-specific bony geometries is often costly and time consuming. To facilitate and to expedite the generation of personalised bony geometries, in this thesis paediatric lower limb bones were generated via the open-source MAP Client. Automated workflows were defined to standardise procedures. Alternatively, personalised anatomies may be generated using novel mesh fitting techniques (Oberhofer et al. 2019), which require the definition of only few landmarks as opposed to sparse or full segmentations to produce accurate reconstructions. Expensive licensed software packages to process medical images may no longer be needed and a considerable amount of processing time may be saved. Further improvements may result from the definition of a paediatric database, as accurate reconstructions would be possible simply providing motion capture data. This would impact more significantly on the study of children presenting with bony deformities, which are not modelled in (scaled) generic geometries and which may not be accurately morphed using current methods. Clinical management would also benefit from the use of personalised anatomies. In paediatric clinical motion analysis, marker-based measurements are currently the gold standard (i.e. Harrington regression equation). However, these methods may be prone to large errors, primarily due to inappropriate marker placement. Furthermore, custom

made interventional tools (i.e., plates and cutting guides) may be designed to fit subject-specific bony geometries, possibly enhancing surgical precision.

In NMSK models, personalisation of muscle-tendon parameters, such as OFL and TSL, may significantly affect muscle function. Linearly scaled values, which are commonly implemented, may lead to non-physiological muscle behaviour. Errors are maximised on paediatric populations, as these are considerably smaller than the initial template models. Since these parameters are difficult to measure *in vivo*, if experimental data are not available, (1) a morphometric scaling to ensure that force-length-velocity relationship is respected (Modenese et al. 2016; Winby et al. 2008) and (2) a calibration step based on EMG data to constrain values within physiological limits (Hoang et al. 2018; Pizzolato et al. 2015; Serrancolí et al. 2016) should be performed. Personalisation of MTU parameters appears to affect the lateral knee JCF profiles. Therefore, for those populations for whom lateral knee loading estimates may be used to inform surgery (i.e. knee osteoarthritis patients), NMSK models should include personalised OFL and TSL values. Nonetheless, personalisation of MTU parameters may have a lesser impact on the final models' estimates, compared to the personalisation of musculoskeletal anatomy and neural solution. Further studies on larger populations should be conducted to confirm the research findings.

## **Implications for children with CP**

Clinical management of CP is currently informed by clinical assessment and results from three-dimensional motion analysis. The clinical assessment generally includes measures of joint range of motion and static bone alignment, spasticity, and strength. Unfortunately, many of these common clinical tests correlate poorly with results from three-dimensional motion analysis (Desloovere et al. 2006), which can make interpretation and subsequent recommendation for patient management difficult. Nonetheless, results such as these are not necessarily counter-intuitive. It is conceivable that patients would respond differently to the external forces applied during the physical exam compared with the challenge of bipedal locomotion. If the patient's goal is to improve gait, combining accurate patient specific anatomical measures from medical imaging (e.g. MRI, CT, and ultrasound) with motion capture data may enable clearer interpretation of factors contributing to gait impairment. For example, a patient specific NMSK model could inform whether a muscle is approaching its strength and/or length tension capacity, if a spastic response has impeded typical kinematics or if a joint is experiencing sub-optimal loading. Biomechanical simulations employing

NMSK models may enable a better understanding of the mechanisms behind the pathology. Several internal parameters (i.e., muscle forces and JCFs), which cannot be readily measured *in vivo* (Herzog et al. 1991), may in fact be estimated *in silico* (i.e., with computer simulations). As such, NMSK models may provide clinicians with valuable information to guide the decision making process (Arnold and Delp 2005). However, commonly used generic NMSK models do have some limitations that may make them unsuitable to accurately represent healthy paediatric populations, let alone children with CP.

To this end, personalised paediatric NMSK models may be developed, using the workflow proposed in this thesis. This involves several steps, which are mostly performed in open-source and freely available software. Within the MAP Client, a generic NMSK model may be personalised to feature image-based and anatomically accurate musculoskeletal anatomies. The recommended combination of statistical shape modelling and mesh fitting techniques makes the bones reconstruction process time- and cost-efficient. Yet, to achieve optimal results a minimum of 6 hours of computational time may be required. To avoid non-physiological in-bone penetrations, muscle pathways may be subsequently personalised introducing wrapping surfaces, whose original size, orientation and location may be further optimised using a particle swarm optimisation routine. The resulting model is thus ready for biomechanical simulations. Nonetheless, if muscle forces and JCFs are sought after, a morphometric scaling may be required to adjust OFL and TSL parameters in order to ensure physiological muscle function. To model CP-related abnormalities, further changes may be imposed by scaling muscle maximal isometric force, OFL and TSL values with information from medical imaging data and/or literature. In addition, muscle parameters can be constrained within physiological ranges via calibration in CEINMS, which employs experimental EMG data and joint torques to refine the original values. Finally, to detect abnormal muscle activity an EMG-assisted approach in CEINMS should be preferred over static optimisation methods to solve for muscle forces.

The work presented in this thesis had further (in)direct implications, which extended outside the domain of biomechanical simulations. In fact, if we think of *in silico* models as tools to perform virtual surgeries (e.g., to simulate tendon transfer or osteotomies) in order to identify the optimal treatment for each patient, the use of scaled generic models seems counterintuitive. Generic NMSK models do not carry enough subject-specific information to discriminate between a successful and an unsuccessful intervention (e.g. when performing a virtual osteotomy). Similar considerations may apply to the use of generic models for

predictive simulations. Predictive simulations are a powerful tool to test the potential effects of surgeries on gait parameters without requiring any experimental data (Ong et al. 2019; Pitto et al. 2019). For this reason, they are becoming increasingly popular. Nonetheless simplistic or generic models are commonly employed (Fox et al. 2009; Mansouri et al. 2016) which, at present, limit the application of predictive modelling to treatment based selection (e.g. injection with botulinum toxin versus muscle lengthening) for general CP populations, rather than informing personalised surgeries.

## **Challenges for clinical implementation**

Translation of patient specific NMSK models into clinical practice presents a number of challenges. For instance, niche skill set are required to develop and to customise a NMSK model, as different software are to be used for each step and current workflows are yet to be fully automated.

Second, model personalisation is a very time-consuming process. Depending on the number of features to be personalised and the source of data employed (i.e., experimental work, literature or previous models), the overall time consumption may range from few minutes to linearly scale a generic model to several hours to generate NMSK models with a high level of personalisation. Approximately 30 hours were required to develop models with personalised bony geometries, muscle pathways, and tuned and calibrated MTU parameters. These included (i) time invested for data collection (~2.5 hours), (ii) six to seven hours for data processing (i.e., medical imaging segmentation and motion capture data cleaning and filtering) and (iii) 21 hours of computational time (i.e., for bones reconstruction, optimisation of MTU pathways wrapping surfaces, model calibration and execution). It must be noted that personalised anatomies were generated from full manual bone segmentations using a combination of statistical shape modelling and mesh fitting techniques. However, novel approaches (Oberhofer et al. 2019), which do not require segmentations, are now available to expedite bone reconstructions. Alternatively, upon the availability of a paediatric medical imaging dataset, motion capture based methods may also be employed to accurately and rapidly (~15-30 minutes) reconstruct lower limb bones. Thus, almost twelve hours, between MRI data acquisition, processing and bone reconstruction, could be saved.

Third, model personalisation is associated to high costs that primarily arise from the acquisition and processing of medical imaging data. For the purposes of this thesis, full lower limb and dedicated high-resolution knee joint MRI scans were acquired. Muscle

volumes and bony geometries, which were respectively used to personalise maximal isometric force values and to inform the morphing process in the MAP Client, were manually segmented in Mimics, a licensed package software. However, recent work (Modenese et al. 2018) suggested that the methods employed to scale generic maximal isometric muscle forces have little effect on the final estimates of a NMSK model. Therefore, medical imaging information on muscles may be redundant. Moreover, machine learning methods may soon enable the automatic segmentation of body structures on medical images (Cunningham et al. 2017), thus eliminating the need for specific licensed package for image data processing.

Last, there is currently no gold standard for modelling. Consequently, there is no consensus on the experimental data to be acquired. Standardising the customisation process would help clarify what type of data is needed, or at least what is the minimum amount of data required to implement a desired level of personalisation. To this end, the workflows proposed in this thesis may represent a first step in this direction. Nonetheless, although this thesis aimed to investigate the individual effect of different levels of personalisation, more robust sensitivity analyses should be conducted to define priorities.

## **Further limitations**

Due to the methods and assumptions underpinning the development of personalised NMSK models, this thesis work had a number of limitations. Within the respective chapter, each individual study limitations have been detailed. However, there are some additional methodological and practical limitations which require further considerations.

Within this thesis, muscles were modelled as Hill-type actuators, which arguably provide a simplistic representation of muscle-tendon dynamics. Despite their simplicity, Hill-type models proved to perform similarly to more complex models (e.g., Huxley models) in biomechanical simulations (Leamire et al., 2016), and are consequently widely accepted in biomechanics. Moreover, these models only require a limited number of parameters to be defined. In addition, all NMSK models developed in this thesis implemented elastic tendons (in CEINMS), and optimised muscle parameters to ensure physiological muscle behaviour (i.e., force-length and force-velocity curves were respected)(Modenese et al., 2017).

Tuned (Modenese et al. 2016; Winby et al. 2008) and EMG-calibrated (Hoang et al. 2019; Pizzolato et al. 2015; Veerkamp et al. 2019) MTU parameters were referred to as personalised parameters, although there was no experimental validation. The reason for this

was that it is not trivial to measure these parameters *in vivo* (Herzog et al. 1991; Panizzolo et al. 2016; Sartori et al. 2017b). Moreover, the proposed approach to personalise MTU parameters ensured physiological muscle behaviour and allowed to accurately track experimental muscle excitations. As such, the personalisation of MTU parameters hereby employed appeared to be a valid alternative to experimental measures, and surely an improvement compared to scaled generic values.

Moreover, the proposed NMSK models featured simplified knee joints, which were represented as 1-DOF or 3-DOFs mechanisms. Simplified joint mechanisms are commonly used in NMSK modelling, due to their easy implementation, but they may not be able to fully describe the complex *in vivo* joint kinematics. More complex multi-DOFs mechanisms have been proposed (Barzan et al. 2019; da Luz et al. 2017; Guess et al. 2014; Marra et al. 2015; Thelen et al. 2014). These rely on segmented medical imaging data to be characterised, which increased the complexity of their implementation. Hence, the benefits of using complex joint mechanisms may not counterbalance the time and cost investment to implement them.

Additionally, only surface EMG data were experimentally collected. Consequently, the use of EMG-assisted approaches was limited by the number of acquired EMG signals. To overcome this limitation, additional muscle excitations were mapped from the experimental EMG data, under the assumption that muscles sharing the same innervation have similar activation patterns (Sartori et al. 2012). Nonetheless, the activity of hip actuators was not collected via surface electromyography, nor it could be mapped from other experimental muscle excitations. Static optimisation methods were used instead, possibly underestimating the contribution of hip muscles to the (stance phase of the) gait cycle.

Finally, EMG data were acquired only on one side for all participants. While muscle activity in TD populations can be reasonably considered symmetrical, such assumption may not be valid for children with CP who often present with bilateral deficiency and non-symmetrical EMG signals. This was the case of two of the 3 children with CP enrolled in Study 3. Contrarily, the twin with CP enrolled in Study 1 was hemiplegic. Hence, due to the limited availability of EMG sensors and to the young age of our participants, it was decided to collect comprehensive data on the (most) affected or dominant side. Instrumenting both legs would have probably resulted in the children walking non-naturally.

## Technical advancement provided by this thesis

In this thesis personalised paediatric NMSK models with increasing level of subject-specificity were developed using user-friendly, and mostly, open-source software (i.e. OpenSim, CEINMS and the MAP Client). The final model ( $\text{Cal}_{\text{EMGa}}^{\text{MAP}}$ ) featured subject-specific image-based musculoskeletal anatomies, tuned and calibrated musculotendon parameters and personalised muscle activation patterns. This model resulted to be the most physiologically plausible among all tested models. Not only did it accurately track experimental joint moments and EMG data, as the other EMG-assisted models, but it also featured personalised musculoskeletal anatomy and estimated non-zero contact loads in swing phase for most participants. More importantly,  $\text{Cal}_{\text{EMGa}}^{\text{MAP}}$  was the first ever MAP Client generated model to be used for biomechanical simulations of gait, leading the way on the use of the MAP Client to develop fully functional and personalised NMSK models. At the same time, it must be noted that  $\text{Cal}_{\text{EMGa}}^{\text{MAP}}$  could have not been developed if study two was not conducted. Methods and pipelines available in the MAP Client to generate subject-specific image-based bony geometries, which produced accurate reconstructions of adult bones from minimal imaging data (Suwarganda et al. 2019), produced abnormally shaped paediatric lower limb bones for children smaller than 145 cm. Therefore, alternative pipelines, which enabled to reach levels of accuracy comparable to previously reported adult results (Bahl et al. 2019; Nolte et al. 2016; Suwarganda et al. 2019) were developed and tested.

## Future directions

Several ideas and directions for future research work stemmed from the difficulties encountered throughout the development of this thesis and the limitations associated with each study.

Future work should focus on the simplification of the proposed workflows to develop and to personalise paediatric NMSK models for biomechanical simulations. This is currently a major drawback of the methods described in this thesis, which substantially limits their translation from research to clinical settings. To this end, the creation of a paediatric medical imaging database would certainly be beneficial. Neural networks could be trained on the images and segmented data and later on employed to automatically segment bones and other tissues (e.g. cartilage, ligaments, muscles), on collected medical images, drastically reducing

the time required to generate subject-specific skeletal models and the room for human error. Manual segmentations may in fact be associated to inter- and intra-subject variability. Data from a large and heterogeneous (in terms of height, mass, age and sexual maturation) paediatric cohort, comprising both typically developing and pathological populations, should be included in the database. This would further enable the generation of mean shape paediatric models for bones and other tissues and the identification of population based principal components, which would allow for fast (~15 minutes compared to 1-2 hours per bone) and accurate reconstructions within the MAP Client using non-linear scaling methods.

Collecting experimental EMG data on children of small stature is not trivial. Due to the limited area over which the electrodes can be placed, the risk to record signals from neighbouring muscles (i.e., cross-talk) is very high. This could have an impact on muscle forces and JCFs estimates when EMG-informed approaches are used. Future work should investigate alternative methods to map additional muscle excitations from limited experimental EMG data. For example, muscle synergies may be employed to digitally reconstruct muscle activation patterns provided a minimal amount of experimental EMG signals. Recently, synergy-based methods have been employed to study pathological populations (Bianco et al. 2017), with promising results. These methods may also be employed to digitally reconstruct the muscle activation patterns of CP children from data collected on the contralateral (and healthy) side or on typically developing paediatric populations.

The methods proposed in this thesis to personalise MTU parameters enabled to produce physiologically plausible values. Nonetheless, there was no guarantee that the implemented values accurately characterised the muscles of children with CP. Morphological and mechanical properties, which are altered in spastic muscles (Barber et al. 2011; Barrett and Lichtwark 2010; Wren et al. 2010), may have not been implemented. Moreover, the tendon properties were potentially not accounted for. This was due to the lack of information to personalise the above features. Freehand 3D ultrasound (3DUS) technology can be used to extract *in vivo* information, with relatively minimal training. To date, freehand 3DUS imaging has been used to characterise musculotendinous tissues in healthy and pathological populations (Barber et al. 2009; Nuri et al. 2017; Nuri et al. 2018; Obst et al. 2014), including the triceps surae muscles in children with CP (Obst et al. 2017). Morphological features and mechanical stiffness of the tendon may be estimated with freehand 3DUS technology and consequently implemented in NMSK models.

## Conclusions

In conclusion, this thesis proposed a workflow to develop personalised paediatric NMSK models of typically developing populations and children with CP and assessed the contribution of different levels of model personalisation on the final estimates of muscle forces and JCFs. Guidelines to accurately reconstruct paediatric lower limb bones were further suggested. For the first time a personalised paediatric NMSK model with high level of personalisation was developed, mostly employing free and open-source software, and used to estimate knee joint contact forces during walking. This model was shown to demonstrate the most physiologically plausible characteristics among the several tested models and produced the lowest estimates of knee JCFs overall. By providing information on internal biomechanical parameters that cannot be measured *in vivo*, the development and use of personalised NMSK models may enable more informed delivery of preventative or corrective personalised treatments.

# Appendix A

---

This Appendix to Chapter 4 presents tables and pictures providing additional information on the demographics, marker placement, experimental data input to the simulations, each model's tracking ability and musculotendon (MTU) parameters variation after calibration in CEINMS.

**Table 21.** Demographics of participants. Two identical twin brothers of comparable size and weight were enrolled in this study. The co-contraction index (CCI) was computed between knee flexors (i.e., SM, BF, MG, LG) and extensors (i.e. VL, VM, RF) muscles and defined in agreement with previous work (Knarr et al. 2012) as:  $(EMG_{flex} + EMG_{ext}) \frac{\min(EMG_{flex}, EMG_{ext})}{\max(EMG_{flex}, EMG_{ext})}$ , where  $EMG_{flex/ext}$  is the summed normalised linear envelope of the knee flexors/extensors. Values are reported as mean±standard deviation across the four processed trials.

|                    | TD        | CP  |
|--------------------|-----------|---|
| <b>Age [years]</b> | 13        | 13  |
| <b>Height [m]</b>  | 1.69      | 1.72  |
| <b>Mass [Kg]</b>   | 59.5      | 59  |
| <b>CCI</b>         | 0.13±0.03 | 0.17±0.02                                       |
| <b>Diagnosis</b>   | -         | Unilateral (left)<br>spastic CP<br>True equinus |

**Table 22.** Markers placement. Name and location of the 51 retro reflective MRI compatible markers placed on anatomical landmarks over the trunk, pelvis, thigh, shank and foot segments.

| <b>Body segment</b> | <b>Marker name</b> |       | <b>Anatomical landmark</b>         |
|---------------------|--------------------|-------|------------------------------------|
| Back                |                    | C7    | 7 <sup>th</sup> Cervical Vertebra  |
|                     |                    | T10   | 10 <sup>th</sup> Thoracic Vertebra |
|                     |                    | CLAV  | Clavicle                           |
|                     |                    | STRN  | Sternum                            |
|                     |                    | RBAK  | Right thorax                       |
| Pelvis              | LASI               | RASI  | Anterior superior iliac spine      |
|                     | LIC                | RIC   | Lateral iliac crest                |
|                     | LPSI               | RPSI  | Posterior superior iliac spine     |
| Knee                | LKNE               | RKNE  | Lateral femoral condyle            |
|                     | LPAT               | RPAT  | Patella                            |
|                     | LMKNE              | RMKNE | Medial femoral condyle             |
|                     | LLTC               | RLTC  | Lateral tibial trochanter          |
|                     | LTTUB              | RTTB  | Tibial tuberosity                  |
|                     | LMTTC              | RMTTC | Medial tibial trochanter           |
| Foot                | LANK               | RANK  | Lateral malleolus                  |
|                     | LHEE               | RHEE  | Calcaneus                          |
|                     | LMMAL              | RMMAL | Medial malleolus                   |
|                     | LMT1               | LMT1  | Big toe                            |
|                     | LTOE               | RTOE  | 2 <sup>nd</sup> toe                |
|                     | LMT5               | RMT5  | 5 <sup>th</sup> toe                |
| Thigh               | LTHI               | RTHI  | Thigh                              |
|                     | LTH1               | RTH1  | Thigh 1                            |
|                     | LTH2               | RTH2  | Thigh 2                            |
|                     | LTH3               | RTH3  | Thigh 3                            |
| Shank               | LTIB               | RTIB  | Tibia                              |
|                     | LTB1               | RTB1  | Tibia 1                            |
|                     | LTB2               | RTB2  | Tibia 2                            |
|                     | LTB3               | RTB3  | Tibia 3                            |

**Table 23.** Knee joint moments and muscle excitations tracking ability of different NMSK models. Values (i.e.  $R^2$  and RMSE) are reported as mean across three trials  $\pm$  standard deviation (SD). For muscles excitations, results are reported as mean values of 12 individual MTUs (Table 7).

|           |                              | <b>Knee Joint Moments</b> |             |              |             |
|-----------|------------------------------|---------------------------|-------------|--------------|-------------|
|           |                              | <b>R<sup>2</sup></b>      |             | <b>RMSE</b>  |             |
|           |                              |                           | <b>(SD)</b> | <b>Nm/Kg</b> | <b>(SD)</b> |
| <b>TD</b> | <b>unCalso</b>               | 0.944                     | (0.074)     | 0.027        | (0.015)     |
|           | <b>unCalEMGa</b>             | 0.973                     | (0.017)     | 0.023        | (0.006)     |
|           | <b>CalEMGa</b>               | 0.986                     | (0.004)     | 0.022        | (0.003)     |
|           | <b>CalEMGa<sup>MRI</sup></b> | 0.958                     | (0.019)     | 0.032        | (0.002)     |
| <b>CP</b> | <b>unCalso</b>               | 0.992                     | (0.008)     | 0.023        | (0.015)     |
|           | <b>unCalEMGa</b>             | 0.984                     | (0.011)     | 0.035        | (0.008)     |
|           | <b>CalEMGa</b>               | 0.964                     | (0.014)     | 0.053        | (0.005)     |
|           | <b>CalEMGa<sup>MRI</sup></b> | 0.973                     | (0.017)     | 0.044        | (0.009)     |

|           |                              | <b>Muscle Excitations</b> |             |              |             |
|-----------|------------------------------|---------------------------|-------------|--------------|-------------|
|           |                              | <b>R<sup>2</sup></b>      |             | <b>RMSE</b>  |             |
|           |                              |                           | <b>(SD)</b> | <b>% max</b> | <b>(SD)</b> |
| <b>TD</b> | <b>unCalso</b>               | 0.226                     | (0.098)     | 0.195        | (0.079)     |
|           | <b>unCalEMGa</b>             | 0.691                     | (0.235)     | 0.071        | (0.043)     |
|           | <b>CalEMGa</b>               | 0.792                     | (0.189)     | 0.064        | (0.050)     |
|           | <b>CalEMGa<sup>MRI</sup></b> | 0.728                     | (0.221)     | 0.062        | (0.039)     |
| <b>CP</b> | <b>unCalso</b>               | 0.221                     | (0.193)     | 0.208        | (0.068)     |
|           | <b>unCalEMGa</b>             | 0.637                     | (0.253)     | 0.081        | (0.035)     |
|           | <b>CalEMGa</b>               | 0.710                     | (0.272)     | 0.074        | (0.044)     |
|           | <b>CalEMGa<sup>MRI</sup></b> | 0.623                     | (0.255)     | 0.079        | (0.035)     |

**Table 24.** Segmented muscle volumes. Muscle volumes manually segmented on full lower limb MRI scans. Five muscles (in bold) presented with substantial volume reductions between participants (i.e., volume difference > 22.5%, accounting for volume reduction by 20% + segmentation error 2.5%). Please refer to Table 7 for muscle acronyms.

| Muscle | Volume [cm <sup>3</sup> ] |        |              |
|--------|---------------------------|--------|--------------|
|        | TD                        | CP     | Δ%           |
| MG     | 240,67                    | 177,01 | <b>26,45</b> |
| LG     | 101,30                    | 77,88  | <b>23,12</b> |
| SOL    | 375,15                    | 365,42 | 2,59         |
| TA     | 87,50                     | 74,41  | 14,97        |
| SM     | 177,97                    | 146,83 | 17,49        |
| ST     | 150,78                    | 117,94 | 21,78        |
| BFSH   | 85,38                     | 81,59  | 4,47         |
| BFLH   | 168,19                    | 138,96 | 17,38        |
| SAR    | 139,13                    | 118,86 | 14,57        |
| TFL    | 89,13                     | 52,41  | <b>41,20</b> |
| GRA    | 107,45                    | 81,17  | <b>24,45</b> |
| VL     | 462,04                    | 467,26 | -1,13        |
| VI     | 239,88                    | -      | -            |
| VM     | 277,13                    | 263,87 | 4,77         |
| RF     | 216,54                    | 166,14 | <b>23,27</b> |

**Table 25.** Muscle maximal isometric force values. Comparison between generic values ( $Cal_{EMGa}$ ) and MRI based values ( $Cal_{EMGa}^{MRI}$ ).

**Table S4**

| Muscle | Maximal Isometric Force [N] |                    |      |
|--------|-----------------------------|--------------------|------|
|        | $Cal_{EMGa}$                | $Cal_{EMGa}^{MRI}$ |      |
|        |                             | TD                 | CP   |
| MG     | 1558                        | 2459               | 3270 |
| LG     | 683                         | 935                | 1321 |
| SOL    | 3549                        | 4994               | 5445 |
| TA     | 905                         | 512                | 479  |
| SM     | 1288                        | 1254               | 1022 |
| ST     | 410                         | 440                | 556  |
| BFSH   | 804                         | 264                | 252  |
| BFLH   | 896                         | 835                | 694  |
| SAR    | 156                         | 159                | 123  |
| TFL    | 233                         | 576                | 491  |
| GRA    | 162                         | 165                | 208  |
| VL     | 1871                        | 2751               | 2999 |
| VI     | 1365                        | 1398               | 1365 |
| VM     | 1294                        | 1569               | 1586 |
| RF     | 1169                        | 1003               | 1311 |

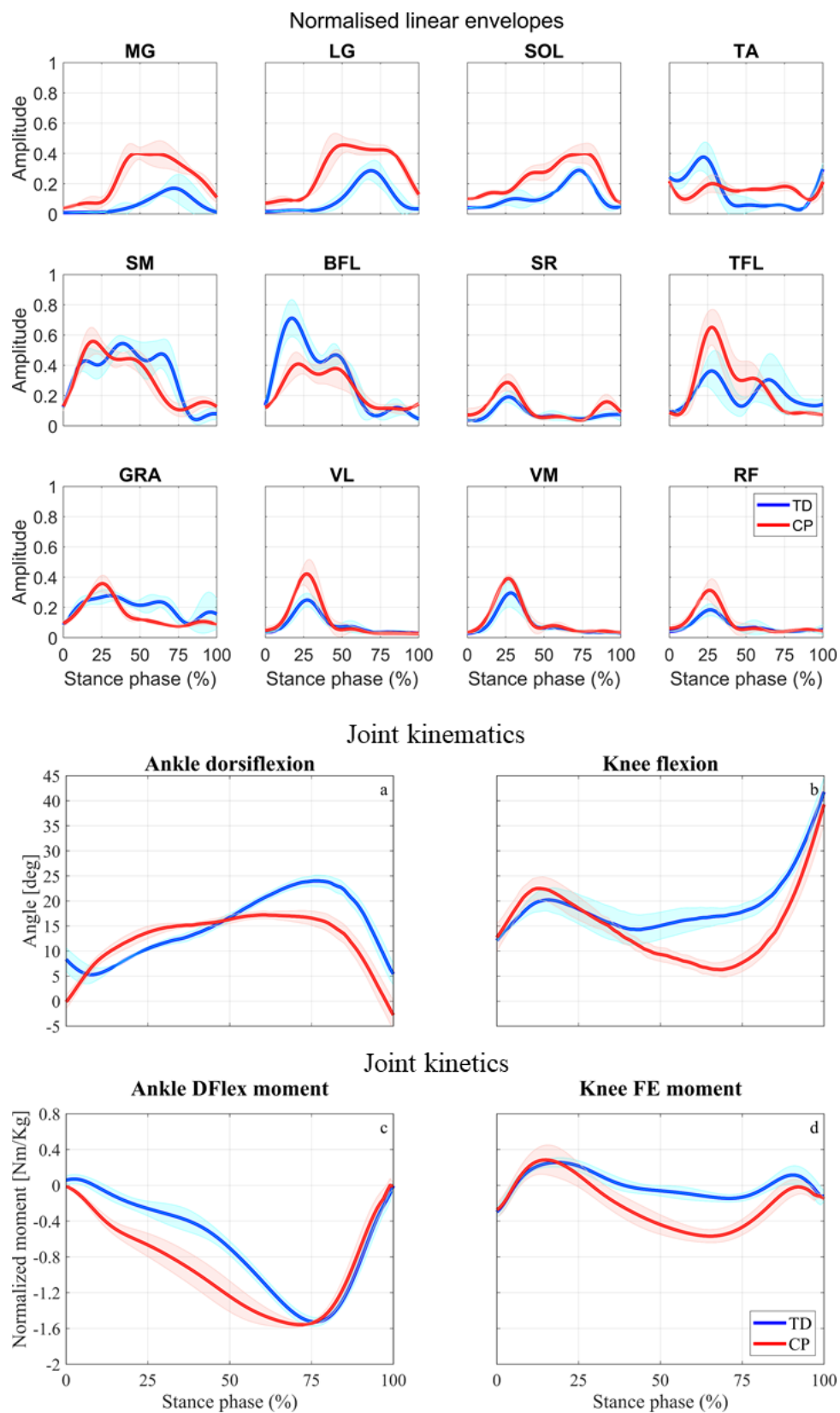


**Figure 42.** Input data for simulations. Normalised linear envelopes of collected EMG data (top), Inverse Kinematics and Inverse Dynamics results at the ankle (a, c) and knee joint (b, d) for both participants (blue = TD, red = CP).

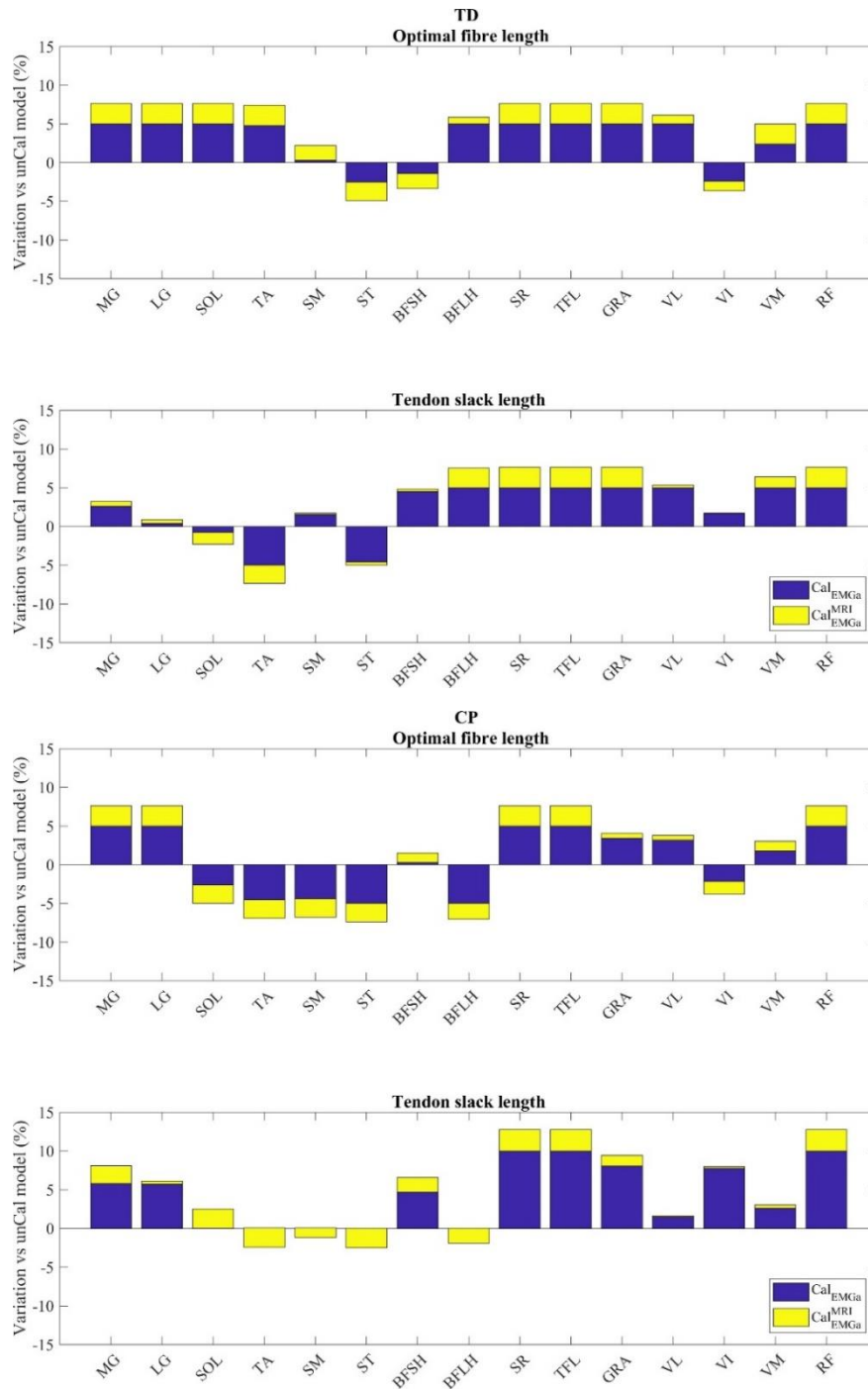


**Figure 43.** MTU parameters after calibration in CEINMS. Percent variation of optimal fibre and tendon slack lengths values following calibration in CEINMS (blue =  $Cal_{EMGa}$  vs  $unCal_{EMGa}$ , yellow =  $Cal_{EMGa}^{MRI}$  vs  $Cal_{EMGa}$ ). Note that when developing  $Cal_{EMGa}$ , for both conditions (i.e., CP and TD), the initial values (i.e. as per  $unCal_{EMGa}$  model) of OFL were allowed to vary up to  $\pm 5\%$ . On the other hand, TSL bounds were set differently depending on the condition:  $\pm 5\%$  for TD child,  $\pm 10\%$  for CP child. These values were further calibrated,  $\pm 2.5\%$  after adjusting maximal isometric forces in model  $Cal_{EMGa}^{MRI}$ .

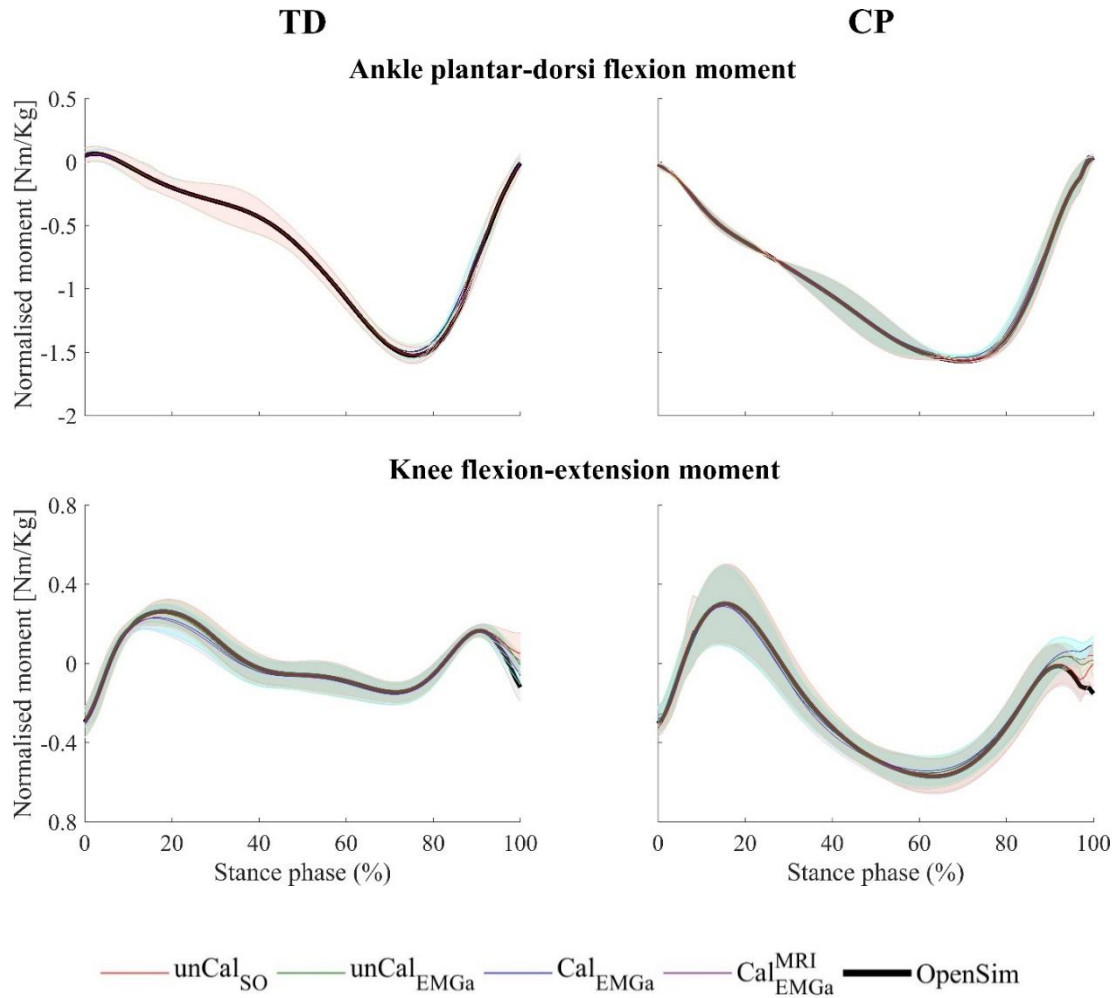


**Figure 44.** Experimental joint moment tracking. Ankle and knee joint moments predicted using the four developed NMSK models in comparison to the values experimentally computed via Inverse Dynamics in OpenSim (black bold line) for both twins (TD on the left, CP on the right).

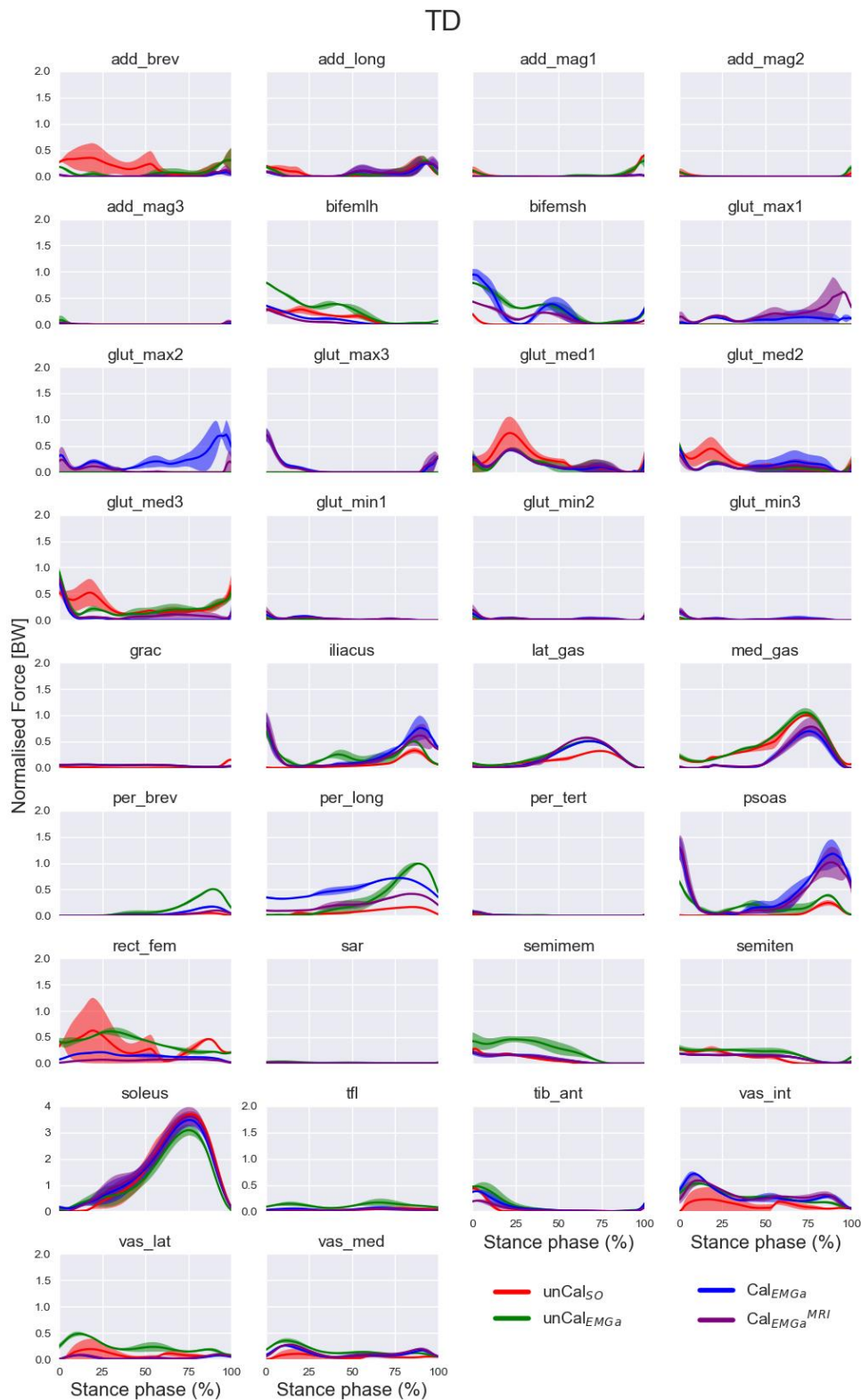


**Figure 45.** Estimated muscle forces for the 34 modelled MTUs. Forces are reported as mean normalised values (solid line)  $\pm$  standard deviation (shaded areas) across 3 trials (red = unCal<sub>SO</sub>, green = unCal<sub>EMGa</sub>, blue = Cal<sub>EMGa</sub> and purple = Cal<sub>EMGa</sub><sup>MRI</sup>) for the TD twin.

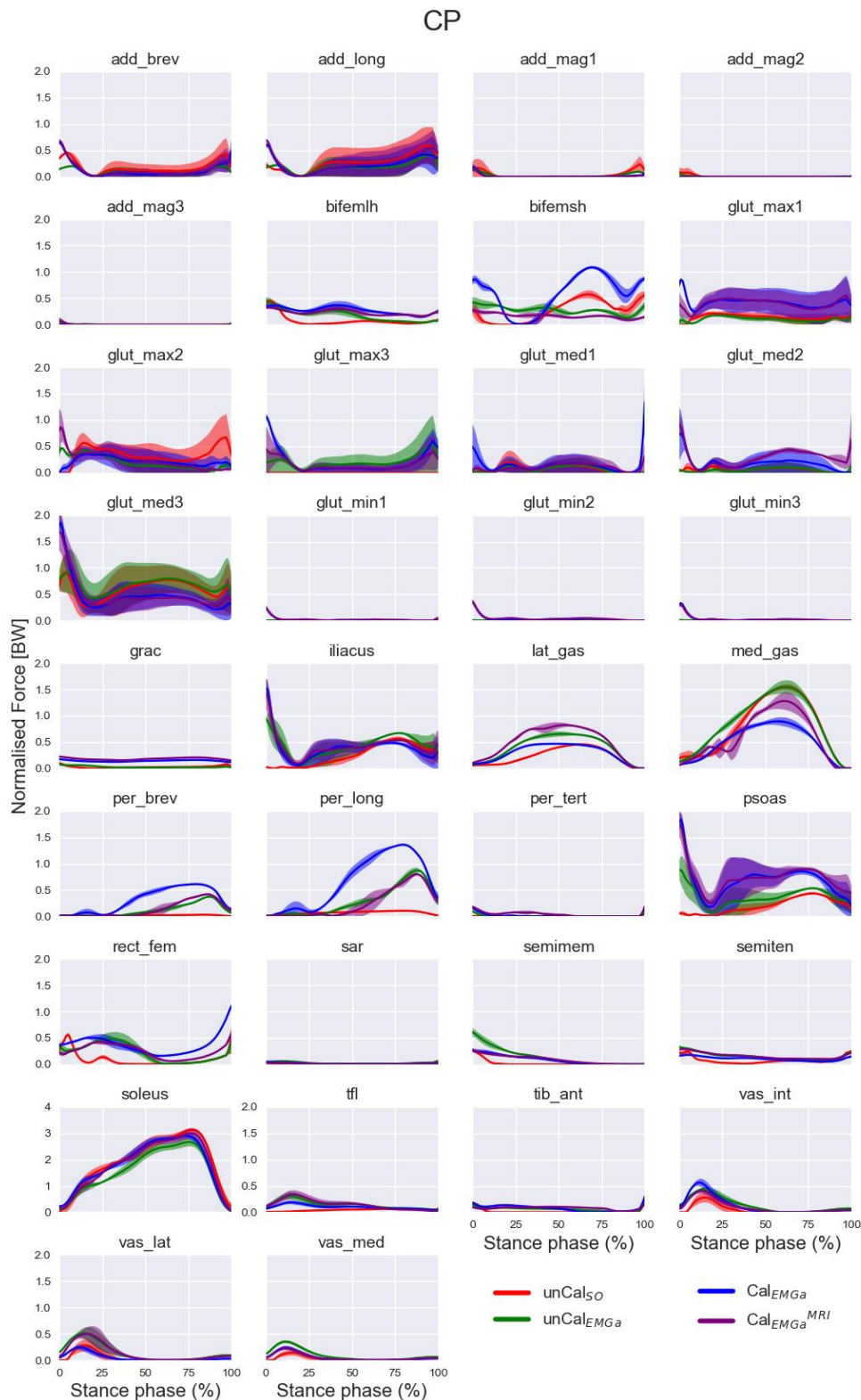


**Figure 46.** Estimated muscle forces for the 34 modelled MTUs. Forces are reported as mean normalised values (solid line)  $\pm$  standard deviation (shaded areas) across 3 trials (red = unCal<sub>SO</sub>, green = unCal<sub>EMGa</sub>, blue = Cal<sub>EMGa</sub> and purple = Cal<sub>EMGa</sub><sup>MRI</sup>) for the twin with CP.

## Appendix B

---

### **Rationale for the choice of 0.7 as scaling factor for optimal fibre length in muscles affected by CP**

Contracted muscles, typical in CP, are characterised by reduced volumes and increased *in vivo* sarcomere length (Lieber et al. 2004; Mathewson and Lieber 2015; Mathewson et al. 2015; Smith et al. 2011). Particularly, the amount of over-stretch in sarcomeres appears to be related to the severity of the pathology (Smith et al. 2011) : children classified as GMFCS III-IV have longer sarcomeres compared to their mildly affected (GMFCS I-II) peers. Across muscles and individuals, on average, the sarcomeres of muscles affected by CP were found to be 1.4 ( $= \frac{3.69 \mu m}{2.63 \mu m} = \frac{\overline{l_{CP}^{sarcc}}}{\overline{l_{TD}^{sarcc}}$ ) times longer than in correspondent healthy muscles (Lieber et al. 2004; Mathewson et al. 2015; Smith et al. 2011). Consequently, if the length of muscle fibres does not change due to CP, but the sarcomeres length increases (Mathewson et al. 2015), the number of sarcomeres in series is lower in affected muscles. Therefore, the optimal fibre length is shorter. Precisely, the amount of shortening is inversely related to the increase in sarcomere length:

$$\frac{\overline{l_{CP}^{sarcc}}}{\overline{l_{TD}^{sarcc}}} = 1.4 \rightarrow \frac{OFL_{CP}}{OFL_{TD}} = \frac{1}{1.4} = 0.71 \approx 0.7$$

Where  $\overline{l^{sarcc}}$  and  $\overline{OFL}$  are the mean *in vivo* sarcomere and optimal fibre lengths respectively.

Consequently, in our NMSK models for CP, we selected 0.7 as starting scaling factor for the OFL values. Each initial value was then allowed to change by  $\pm 5\%$  (i.e.  $0.665 \div 0.735$ ) during a calibration process in CEINMS, aiming to personalise muscle parameters based on the actual EMG data collected from the subject.



# Appendix C

This Appendix to Chapter 5 presents tables providing additional information on the effects of bone geometry personalisation for musculoskeletal modelling applications.

**Table 26.** Difference in femur neck-shaft angle between MRI segmentations and bone reconstructions for the 18 participants, listed in order of height. Three-dimensional angles were computed in 3-Matic (Materialise, Leuven, BE) between the principal axis of two cylinders fitted to neck and shaft of the femoral geometry, respectively. P0 = linearly scaled OpenSim generic bones, P1 = linearly scaled MAP generic geometries, P2 = non-linearly scaled MAP generic geometries, P9 = most accurate MAP reconstructions (see results).

| <b>Subject<br/>[ID]</b> | <b>P0<br/>[deg]</b> | <b>P1<br/>[deg]</b> | <b>P2<br/>[deg]</b> | <b>P9<br/>[deg]</b> |
|-------------------------|---------------------|---------------------|---------------------|---------------------|
| <b>TD01</b>             | 9.05                | 10.05               | 7.95                | 2.94                |
| <b>TD02</b>             | 3.53                | 0.51                | 2.79                | 0.39                |
| <b>TD03</b>             | 7.17                | 8.51                | 5.67                | 5.47                |
| <b>TD04</b>             | 11.90               | 7.77                | 0.56                | 1.67                |
| <b>TD05</b>             | 18.53               | 11.36               | 15.56               | 2.66                |
| <b>TD06</b>             | 9.58                | 2.76                | 0.95                | 0.03                |
| <b>TD07</b>             | 0.24                | 0.06                | 2.06                | 2.75                |
| <b>TD08</b>             | 15.36               | 15.04               | 7.87                | 1.80                |
| <b>TD09</b>             | 11.01               | 11.18               | 8.14                | 4.17                |
| <b>TD10</b>             | 5.78                | 1.11                | 1.92                | 2.08                |
| <b>TD11</b>             | 19.12               | 9.60                | 12.28               | 1.96                |
| <b>TD12</b>             | 8.82                | 3.81                | 0.02                | 1.33                |
| <b>TD13</b>             | 10.69               | 3.45                | 0.37                | 7.14                |
| <b>TD14</b>             | 8.40                | 4.46                | 3.74                | 1.63                |
| <b>TD15</b>             | 1.82                | 2.47                | 1.20                | 2.82                |
| <b>TD16</b>             | 13.20               | 4.59                | 5.76                | 4.36                |
| <b>TD17</b>             | 4.94                | 3.24                | 0.93                | 1.40                |
| <b>TD18</b>             | 2.67                | 0.88                | 2.40                | 3.96                |
| <b>Mean(SD)</b>         | 8.99(5.25)          | 5.60(4.31)          | 4.45(4.29)          | 2.70(1.73)          |

**Table 27.** Knee and ankle joint axis orientation with respect to the global coordinate system (MRI coil). Joint axes were defined according to ISB recommendations, based on anatomical landmarks. Angles were computed from the corresponding rotation matrix and are reported as mean values across the 18 participants, for five of the 21 developed pipelines (i.e., P0, P1, P2, P7 and P9). MRI = manual segmentations (gold standard), P0 = linearly scaled OpenSim generic bones, P1 = linearly scaled MAP generic geometries, P2 = non-linearly scaled MAP generic geometries, P7/9 = most accurate MAP reconstructions.

| <b>Angle<br/>[deg]</b> | <b>MRI</b> | <b>P0</b> | <b>P1</b> | <b>P2</b> | <b>P7</b> | <b>P9</b> |
|------------------------|------------|-----------|-----------|-----------|-----------|-----------|
| <b>Knee</b>            | 119.74     | 117.41    | 116.84    | 119.53    | 120.47    | 115.85    |
| <b>Ankle</b>           | 114.37     | 107.10    | 120.72    | 121.39    | 115.71    | 120.26    |

# Appendix D

This Appendix to Chapter 6 presents the level of agreement in joint kinematics and kinetics between generic scaled and MAP generated OpenSim models.

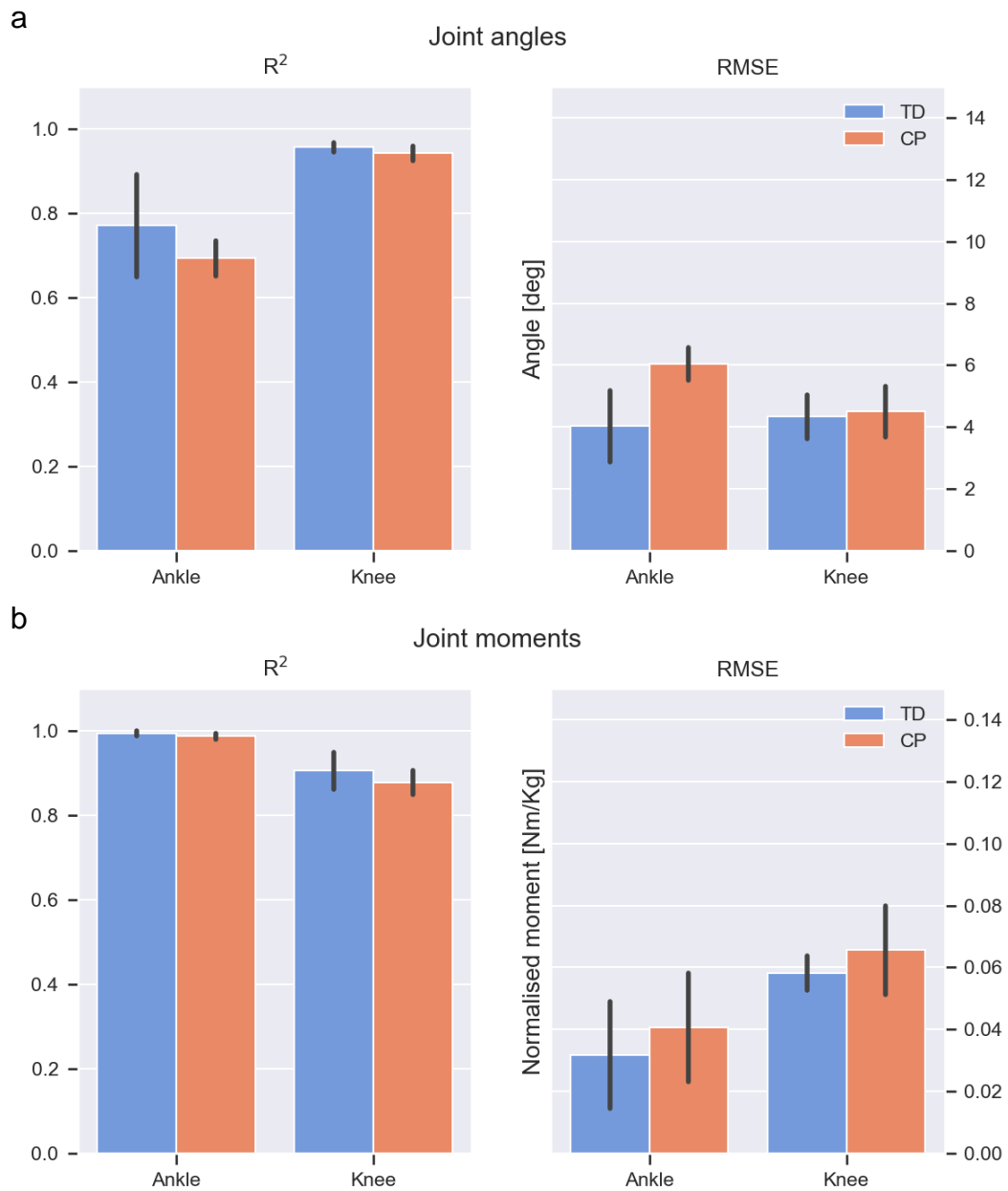


**Figure 47.** Joint angles and moments comparison between a generic scaled and a MAP generated OpenSim model. The level of agreement was quantified computing the  $R^2$  and root mean square error (RMSE) between models' estimates.



# References

---

- Abel MF, Damiano DL, Pannunzio M, Bush J (1999) Muscle-tendon surgery in diplegic cerebral palsy: functional and mechanical changes *Journal of Pediatric Orthopaedics* 19:366-375
- Ackland DC, Robinson D, Redhead M, Lee PVS, Moskaljuk A, Dimitroulis G (2017) A personalized 3D-printed prosthetic joint replacement for the human temporomandibular joint: From implant design to implantation *Journal of the Mechanical Behavior of Biomedical Materials* 69:404-411
- Aiona MD, Sussman MD (2004) Treatment of spastic diplegia in patients with cerebral palsy: Part II *Journal of Pediatric Orthopaedics B* 13:S13-38
- Anderson FC, Pandy MG (2001a) Dynamic Optimization of Human Walking *Journal of Biomechanical Engineering* 123:381-390
- Anderson FC, Pandy MG (2001b) Static and dynamic optimization solutions for gait are practically equivalent *J Biomech* 34:153-161
- Arnold AS, Blemker SS, Delp SL (2001) Evaluation of a Deformable Musculoskeletal Model for Estimating Muscle–Tendon Lengths During Crouch Gait *Annals of Biomedical Engineering* 29:263-274
- Arnold AS, Delp SL (2005) Computer modeling of gait abnormalities in cerebral palsy: application to treatment planning *Theoretical Issues in Ergonomics Science* 6:305-312
- Arnold AS, Salinas S, Asakawa DS, Delp SL (2000) Accuracy of Muscle Moment Arms Estimated from MRI-Based musculoskeletal Models of the Lower Extremity *Computer aided surgery* 5:108-119
- Arnold EM, Hamner SR, Seth A, Millard M, Delp SL (2013) How muscle fiber lengths and velocities affect muscle force generation as humans walk and run at different speeds *The Journal of Experimental Biology* 216:2150-2160

- Arnold EM, Ward SR, Lieber RL, Delp SL (2010) A model of the lower limb for analysis of human movement *Annals of biomedical engineering* 38:269-279
- Bahl JS et al. (2019) Statistical shape modelling versus linear scaling: Effects on predictions of hip joint centre location and muscle moment arms in people with hip osteoarthritis *J Biomech* 85:164-172
- Bar-On L et al. (2013) A clinical measurement to quantify spasticity in children with cerebral palsy by integration of multidimensional signals *Gait & posture* 38:141-147
- Bar-On L, Molenaers G, Aertbeliën E, Monari D, Feys H, Desloovere K (2014) The relation between spasticity and muscle behavior during the swing phase of gait in children with cerebral palsy *Research in Developmental Disabilities* 35:3354-3364
- Bar-On L, Molenaers G, Aertbeliën E, Van Campenhout A, Feys H, Nuttin B, Desloovere K (2015) Spasticity and its contribution to hypertonia in cerebral palsy *Biomed Res Int* 2015:10 pages
- Barber L, Barrett R, Lichtwark G (2009) Validation of a freehand 3D ultrasound system for morphological measures of the medial gastrocnemius muscle *J Biomech* 42:1313-1319
- Barber L, Barrett R, Lichtwark G (2011) Passive muscle mechanical properties of the medial gastrocnemius in young adults with spastic cerebral palsy *J Biomech* 44:2496-2500
- Barber L, Barrett R, Lichtwark G (2012) Medial gastrocnemius muscle fascicle active torque-length and Achilles tendon properties in young adults with spastic cerebral palsy *J Biomech* 45:2526-2530
- Barber L, Hastings-Ison T, Baker R, Kerr Graham H, Barrett R, Lichtwark G (2013) The effects of botulinum toxin injection frequency on calf muscle growth in young children with spastic cerebral palsy: a 12-month prospective study *Journal of Children's Orthopaedics* 7:425-433
- Barrett RS, Lichtwark GA (2010) Gross muscle morphology and structure in spastic cerebral palsy: a systematic review *Dev Med Child Neurol* 52:794-804

- Barzan M (2019) Development of subject-specific tibiofemoral and patellofemoral joint kinematic models for children and adolescents with recurrent patellar dislocation Ph D thesis, Griffith University
- Barzan M et al. (2019) Development and validation of subject-specific pediatric multibody knee kinematic models with ligamentous constraints *J Biomech* 93:194-203
- Bax M et al. (2005) Proposed definition and classification of cerebral palsy, April 2005 *Developmental Medicine & Child Neurology* 47:571-576
- Baxter JR, Farber DC, Hast MW (2019) Plantarflexor fiber and tendon slack length are strong determinates of simulated single-leg heel raise height *J Biomech* 86:27-33
- Beals RK (2001) Treatment of knee contracture in cerebral palsy by hamstring lengthening, posterior capsulotomy, and quadriceps mechanism shortening *Developmental Medicine & Child Neurology* 43:802-805
- Bell K, Ounpuu S, DeLuca P, Romness M (2002) Natural progression of gait in children with cerebral palsy *Journal of Pediatric Orthopaedics* 22:677-682
- Bergmann G, Bender A, Dymke J, Duda G, Damm P (2016) Standardized Loads Acting in Hip Implants *PloS one* 11:e0155612
- Besl PJ, McKay ND (1992) A method for registration of 3-D shapes *IEEE Transactions on Pattern Analysis and Machine Intelligence* 14:239-256
- Bianco NA, Patten C, Fregly BJ (2017) Can Measured Synergy Excitations Accurately Construct Unmeasured Muscle Excitations? *Journal of Biomechanical Engineering* 140:10 pages
- Blemker SS, Asakawa DS, Gold GE, Delp SL (2007) Image-based musculoskeletal modeling: applications, advances, and future opportunities *Journal of Magnetic Resonance Imaging* 25:441-451
- Bohannon RW, Smith MB (1987) Interrater Reliability of a Modified Ashworth Scale of Muscle Spasticity *Physical Therapy* 67:206-207
- Bosmans L, Jansen K, Wesseling M, Molenaers G, Scheys L, Jonkers I (2016) The role of altered proximal femoral geometry in impaired pelvis stability and hip control during CP gait: A simulation study *Gait & posture* 44:61-67

- Bosmans L, Valente G, Wesseling M, Van Campen A, De Groot F, De Schutter J, Jonkers I (2015) Sensitivity of predicted muscle forces during gait to anatomical variability in musculotendon geometry *J Biomech* 48:2116-2123
- Bosmans L, Wesseling M, Desloovere K, Molenaers G, Scheys L, Jonkers I (2014) Hip contact force in presence of aberrant bone geometry during normal and pathological gait *Journal of Orthopaedic Research* 32:1406-1415
- Boyd RN, Graham HK (1999) Objective measurement of clinical findings in the use of botulinum toxin type A for the management of children with cerebral palsy *European Journal of Neurology* 6:s23-s35
- Buchanan TS, Shreeve DA (1996) An Evaluation of Optimization Techniques for the Prediction of Muscle Activation Patterns During Isometric Tasks *Journal of Biomechanical Engineering* 118:565-574
- Campbell AC, Alderson JA, Lloyd DG, Elliott BC (2009) Effects of different technical coordinate system definitions on the three dimensional representation of the glenohumeral joint centre *Medical & Biological Engineering & Computing* 47:543-550
- Cans C (2000) Surveillance of cerebral palsy in Europe: a collaboration of cerebral palsy surveys and registers *Developmental Medicine & Child Neurology* 42:816-824
- Cappozzo A, Catani F, Della Croce U, Leardini A (1995) Position and orientation in space of bones during movement: anatomical frame definition and determination *Clinical biomechanics* 10:171-178
- Carbone V, van der Krogt MM, Koopman HF, Verdonschot N (2016) Sensitivity of subject-specific models to Hill muscle-tendon model parameters in simulations of gait *J Biomech* 49:1953-1960
- Carleton AD (2018) A weighted vector method for morphing muscle via-points in subject-specific OpenSim models using the MAP Client
- Castle ME, Reyman TA, Schneider M (1979) Pathology of spastic muscle in cerebral palsy *Clinical orthopaedics and related research* 142:223-232

- Chang FM, Rhodes JT, Flynn KM, Carollo JJ (2010) The role of gait analysis in treating gait abnormalities in cerebral palsy *The Orthopedic Clinics of North America* 41:489-506
- Chao EYS, Armiger RS, Yoshida H, Lim J, Haraguchi N (2007) Virtual interactive musculoskeletal system (VIMS) in orthopaedic research, education and clinical patient care *Journal of Orthopaedic Surgery and Research* 2
- Cook RE, Schneider I, Hazlewood ME, Hillman SJ, Robb JE (2003) Gait analysis alters decision-making in cerebral palsy *Journal of Pediatric Orthopaedics* 23:292-295
- Cootes TF, Taylor CJ, Cooper DH, Graham J (1995) Active Shape Models-Their Training and Application *Computer Vision and Image Understanding* 61:38-59
- Correa TA, Baker R, Graham HK, Pandy MG (2011) Accuracy of generic musculoskeletal models in predicting the functional roles of muscles in human gait *J Biomech* 44:2096-2105
- Crenna P (1998) Spasticity and 'Spastic' Gait in Children with Cerebral palsy *Neuroscience & Biobehavioral Reviews* 22:571-578
- Crenna P (1999) Pathophysiology of lengthening contractions in human spasticity: a study of the hamstring muscles during locomotion *Pathophysiology* 5:283-297
- Crowninshield RD, Brand RA (1981) A physiologically based criterion of muscle force prediction in locomotion *J Biomech* 14:793-801
- Cunningham RJ, Harding PJ, Loram ID (2017) Real-Time Ultrasound Segmentation, Analysis and Visualisation of Deep Cervical Muscle Structure *IEEE Transactions on Medical Imaging* 36:653-665
- da Luz SB, Modenese L, Sancisi N, Mills PM, Kennedy B, Beck BR, Lloyd DG (2017) Feasibility of using MRIs to create subject-specific parallel-mechanism joint models *J Biomech* 53:45-55
- Damiano DL (1993) Reviewing Muscle Cocontraction *Physical & Occupational Therapy In Pediatrics* 12:3-20

- Damiano DL, Alter KE, Chambers H (2009) New clinical and research trends in lower extremity management for ambulatory children with cerebral palsy *Physical medicine and rehabilitation clinics of North America* 20:469-491
- Damiano DL, Martellotta TL, Sullivan DJ, Granata KP, Abel MF (2000) Muscle force production and functional performance in spastic cerebral palsy: Relationship of cocontraction *Archives of Physical Medicine and Rehabilitation* 81:895-900
- Damiano DL, Quinlivan JM, Owen BF, Payne P, Nelson KC, Abel MF (2002) What does the Ashworth scale really measure and are instrumented measures more valid and precise? *Developmental Medicine & Child Neurology* 44:112-118
- Damsgaard M, Rasmussen J, Christensen ST, Surma E, de Zee M (2006) Analysis of musculoskeletal systems in the AnyBody Modeling System Simulation Modelling Practice and Theory 14:1100-1111
- Dao TT, Tho M-CHB (2018) A Systematic Review of Continuum Modeling of Skeletal Muscles: Current Trends, Limitations, and Recommendations *Applied Bionics and Biomechanics* 2018:17 pages
- De Groote F, Kinney AL, Rao AV, Fregly BJ (2016) Evaluation of Direct Collocation Optimal Control Problem Formulations for Solving the Muscle Redundancy Problem *Annals of Biomedical Engineering* 44:2922-2936
- Delp SL et al. (2007) OpenSim: open-source software to create and analyze dynamic simulations of movement *IEEE transactions on biomedical engineering* 54:1940-1950
- Delp SL, Loan JP, Hoy MG, Zajac FE, Topp EL, Rosen JM (1990) An interactive graphics-based model of the lower extremity to study orthopaedic surgical procedures *IEEE Transactions on Biomedical engineering* 37:757-767
- Delp SL, Statler K, Carroll NC (1995) Preserving plantar flexion strength after surgical treatment for contracture of the triceps surae: A computer simulation study *Journal of Orthopaedic Research* 13:96-104
- DeLuca PA (1991) Gait analysis in the treatment of the ambulatory child with cerebral palsy *Clinical orthopaedics and related research* 264:65-75

- DeLuca PA, Davis III RB, Öunpuu S, Rose S, Sirkin R (1997) Alterations in surgical decision making in patients with cerebral palsy based on three-dimensional gait analysis *Journal of Pediatric Orthopaedics* 17:608-614
- Demers MS, Pal S, Delp SL (2014) Changes in tibiofemoral forces due to variations in muscle activity during walking *Journal of Orthopaedic Research* 32:769-776
- Desloovere K, Molenaers G, Feys H, Huenaerts C, Callewaert B, Van de Walle P (2006) Do dynamic and static clinical measurements correlate with gait analysis parameters in children with cerebral palsy? *Gait & posture* 24:302-313
- Devaprakash D, Weir GJ, Dunne JJ, Alderson JA, Donnelly CJ (2016) The influence of digital filter type, amplitude normalisation method, and co-contraction algorithm on clinically relevant surface electromyography data during clinical movement assessments *J Electromyogr Kinesiol* 31:126-135
- Duda GN, Brand D, Freitag S, Lierse W, Schneider E (1996) Variability of femoral muscle attachments *J Biomech* 29:1185-1190
- Dzialo CM, Pedersen PH, Simonsen CW, Jensen KK, de Zee M, Andersen MS (2018) Development and validation of a subject-specific moving-axis tibiofemoral joint model using MRI and EOS imaging during a quasi-static lunge *J Biomech* 72:71-80
- Eckstein F, Burstein D, Link TM (2006) Quantitative MRI of cartilage and bone: degenerative changes in osteoarthritis *NMR in Biomedicine* 19:822-854
- Elder GCB, Bsc GS, Pt KC, Msc DW, Marshall A, Leahey L (2003) Contributing factors to muscle weakness in children with cerebral palsy *Developmental Medicine & Child Neurology* 45:542-550
- Falisse A, Bar-On L, Desloovere K, Jonkers I, De Groote F (2018) A spasticity model based on feedback from muscle force explains muscle activity during passive stretches and gait in children with cerebral palsy *PloS one* 13:e0208811
- Falisse A, Van Rossom S, Jonkers I, De Groote F (2017) EMG-Driven Optimal Estimation of Subject-SPECIFIC Hill Model Muscle-Tendon Parameters of the Knee Joint Actuators *IEEE transactions on bio-medical engineering* 64:2253-2262

- Fasano V, Broggi G, Barolat-Romana G, Sguazzi A (1978) Surgical treatment of spasticity in cerebral palsy *Pediatric Neurosurgery* 4:289-305
- Fernandez J, Zhang J, Heidlauf T, Sartori M, Besier T, Röhrle O, Lloyd D (2016) Multiscale musculoskeletal modelling, data–model fusion and electromyography-informed modelling *Interface Focus* 6:20150084
- Fernandez JW, Mithraratne P, Thrupp SF, Tawhai MH, Hunter PJ (2004) Anatomically based geometric modelling of the musculo-skeletal system and other organs *Biomech Model Mechanobiol* 2:139-155
- Filho MC, Yoshida R, Carvalho Wda S, Stein HE, Novo NF (2008) Are the recommendations from three-dimensional gait analysis associated with better postoperative outcomes in patients with cerebral palsy? *Gait Posture* 28:316-322.
- Fleuren JFM, Voerman GE, Erren-Wolters CV, Snoek GJ, Rietman JS, Hermens HJ, Nene AV (2010) Stop using the Ashworth Scale for the assessment of spasticity *Journal of Neurology, Neurosurgery & Psychiatry* 81:46-52
- Foran JR, Steinman S, Barash I, Chambers HG, Lieber RL (2005) Structural and mechanical alterations in spastic skeletal muscle *Developmental Medicine & Child Neurology* 47:713-717
- Ford KR, van den Bogert J, Myer GD, Shapiro R, Hewett TE (2008) The effects of age and skill level on knee musculature co-contraction during functional activities: a systematic review *Br J Sports Med* 42:561-566
- Fox AS, Carty CP, Modenese L, Barber LA, Lichtwark GA (2018) Simulating the effect of muscle weakness and contracture on neuromuscular control of normal gait in children *Gait & posture* 61:169-175
- Fox MD, Reinbolt JA, Öunpuu S, Delp SL (2009) Mechanisms of improved knee flexion after rectus femoris transfer surgery *J Biomech* 42:614-619
- Franci R, Parenti-Castelli V, Belvedere C, Leardini A (2009) A new one-DOF fully parallel mechanism for modelling passive motion at the human tibiotalar joint *J Biomech* 42:1403-1408

- Fregly BJ, Besier TF, Lloyd DG, Delp SL, Banks SA, Pandy MG, D'Lima DD (2012a) Grand challenge competition to predict in vivo knee loads *Journal of Orthopaedic Research* 30:503-513
- Fregly BJ, Boninger ML, Reinkensmeyer DJ (2012b) Personalized neuromusculoskeletal modeling to improve treatment of mobility impairments: a perspective from European research sites *Journal of neuroengineering and rehabilitation* 9
- Frisk RF, Lorentzen J, Nielsen JB (2019) Contribution of corticospinal drive to ankle plantar flexor muscle activation during gait in adults with cerebral palsy *Experimental Brain Research* 237:1457-1467
- Frost HM (2003) Bone's mechanostat: a 2003 update *The Anatomical Record Part A: Discoveries in Molecular, Cellular, and Evolutionary Biology* 275:1081-1101
- Fry NR, Gough M, Shortland AP (2004) Three-dimensional realisation of muscle morphology and architecture using ultrasound *Gait & posture* 20:177-182
- Gage JR (1983) Gait analysis for decision-making in cerebral palsy *Bulletin of the Hospital for Joint Diseases Orthopaedic Institute* 43:147-163
- Gage JR (1990) Surgical treatment of knee dysfunction in cerebral palsy *Clinical Orthopaedics and Related Research* 253:45-54
- Gage JR (2009) The identification and treatment of gait problems in cerebral palsy vol 180-181. vol Book, Whole. Mac Keith Press, London
- Galea C et al. (2019) Cerebral palsy trends in Australia (1995–2009): a population-based observational study *Developmental Medicine & Child Neurology* 61:186-193
- Gao F, Zhao H, Gaebler-Spira D, Zhang LQ (2011) In vivo evaluations of morphologic changes of gastrocnemius muscle fascicles and achilles tendon in children with cerebral palsy *American Journal of Physical Medicine & Rehabilitation* 90:364-371
- Garijo N, Verdonschot N, Engelborghs K, Garcia-Aznar JM, Perez MA (2017) Subject-specific musculoskeletal loading of the tibia: Computational load estimation *Journal of the Mechanical Behavior of Biomedical Materials* 65:334-343
- Garner BA, Pandy MG (2003) Estimation of musculotendon properties in the human upper limb *Annals of Biomedical Engineering* 31:207-220

- Gasparutto X, Dumas R, Jacquelin E (2012) Multi-body optimisation with deformable ligament constraints: influence of ligament geometry *Computer methods in biomechanics and biomedical engineering* 15 Suppl 1:191-193
- Gerus P, Rao G, Berton E (2015) Ultrasound-based subject-specific parameters improve fascicle behaviour estimation in Hill-type muscle model *Computer methods in biomechanics and biomedical engineering* 18:116-123
- Gerus P et al. (2013) Subject-specific knee joint geometry improves predictions of medial tibiofemoral contact forces *J Biomech* 46:2778-2786
- Gough M (2009) Does botulinum toxin prevent or promote deformity in children with cerebral palsy? *Developmental Medicine & Child Neurology* 51:89-90
- Gough M, Shortland AP (2012) Could muscle deformity in children with spastic cerebral palsy be related to an impairment of muscle growth and altered adaptation? *Dev Med Child Neurol* 54:495–499
- Graham HK, Selber P (2003) Musculoskeletal aspects of cerebral palsy *The Journal of Bone and Joint Surgery British volume* 85-B:157-166
- Granata KP, Ikeda AJ, Abel MF (2000) Electromechanical delay and reflex response in spastic cerebral palsy *Archives of Physical Medicine and Rehabilitation* 81:888-894
- Guess TM, Stylianou AP, Kia M (2014) Concurrent prediction of muscle and tibiofemoral contact forces during treadmill gait *Journal of biomechanical engineering* 136:021032-021032
- Haeufle DFB, Günther M, Bayer A, Schmitt S (2014) Hill-type muscle model with serial damping and eccentric force–velocity relation *J Biomech* 47:1531-1536
- Hainisch R, Gfoehler M, Zubayer-UI-Karim M, Pandy MG (2012) Method for determining musculotendon parameters in subject-specific musculoskeletal models of children developed from MRI data *Multibody System Dynamics* 28:143-156
- Handsfield GG, Meyer CH, Abel MF, Blemker SS (2015) Heterogeneity of muscle sizes in the lower limbs of children with cerebral palsy *Muscle & Nerve* 53:933-945

- Handsfield GG, Meyer CH, Hart JM, Abel MF, Blemker SS (2014) Relationships of 35 lower limb muscles to height and body mass quantified using MRI *J Biomech* 47:631-638
- Hanna SE, Rosenbaum PL, Bartlett DJ, Palisano RJ, Walter SD, Avery L, Russell DJ (2009) Stability and decline in gross motor function among children and youth with cerebral palsy aged 2 to 21 years *Dev Med Child Neurol Suppl* 51:295-302
- Harrington ME, Zavatsky AB, Lawson SEM, Yuan Z, Theologis TN (2007) Prediction of the hip joint centre in adults, children, and patients with cerebral palsy based on magnetic resonance imaging *J Biomech* 40:595-602
- Hayashi D, Roemer FW, Guermazi A (2016) Imaging for osteoarthritis *Annals of Physical and Rehabilitation Medicine* 59:161-169
- Heine R, Manal K, Buchanan TS (2003) Using Hill-Type Muscle Models and EMG Data in a Forward Dynamic Analysis of Joint Moment *Journal of Mechanics in Medicine and Biology* 03:169-186
- Heller MO, Taylor WR, Perka C, Duda GN (2003) The influence of alignment on the musculo-skeletal loading conditions at the knee *Langenbeck's Archives of Surgery* 388:291-297
- Herzog W, Read LJ, ter Keurs HEDJ (1991) Experimental determination of force—length relations of intact human gastrocnemius muscles *Clinical biomechanics* 6:230-238
- Hicks J, Arnold A, Anderson F, Schwartz M, Delp S (2007) The effect of excessive tibial torsion on the capacity of muscles to extend the hip and knee during single-limb stance *Gait & posture* 26:546-552
- Hicks JL, Uchida TK, Seth A, Rajagopal A, Delp SL (2015) Is my model good enough? Best practices for verification and validation of musculoskeletal models and simulations of movement *Journal of Biomechanical Engineering* 137:020905
- Hill AV (1938) The heat of shortening and the dynamic constants of muscle *Proceedings of the Royal Society of London Series B - Biological Sciences* 126:136-195
- Hoang HX, Diamond LE, Lloyd DG, Pizzolato C (2019) A calibrated EMG-informed neuromusculoskeletal model can appropriately account for muscle co-contraction in

- the estimation of hip joint contact forces in people with hip osteoarthritis *J Biomech* 83:134-142
- Hoang HX, Pizzolato C, Diamond LE, Lloyd DG (2018) Subject-specific calibration of neuromuscular parameters enables neuromusculoskeletal models to estimate physiologically plausible hip joint contact forces in healthy adults *J Biomech* 80:111-120
- Hong J, Hipp JA, Mulkern RV, Jaramillo D, Snyder BD (2000) Magnetic Resonance Imaging Measurements of Bone Density and Cross-Sectional Geometry Calcified Tissue International 66:74-78
- Hösl M, Böhm H, Arampatzis A, Döderlein L (2015) Effects of ankle-foot braces on medial gastrocnemius morphometrics and gait in children with cerebral palsy *Journal of children's orthopaedics* 9:209-219
- Jan MM (2006) Cerebral Palsy: Comprehensive Review and Update *Annals of Saudi Medicine* 26:123-132
- Johnson D, Damiano D, Abel M (1997) The evolution of gait in childhood and adolescent cerebral palsy *Journal of Pediatric Orthopaedics* 17:392-396
- Johnson DL, Miller F, Subramanian P, Modlesky CM (2009) Adipose Tissue Infiltration of Skeletal Muscle in Children with Cerebral Palsy *The Journal of Pediatrics* 154:715-720
- Jonkers I, Stewart C, Spaepen A (2003) The study of muscle action during single support and swing phase of gait: clinical relevance of forward simulation techniques *Gait & posture* 17:97-105
- Kadaba MP, Ramakrishnan HK, Wootten ME (1990) Measurement of lower extremity kinematics during level walking *Journal of Orthopaedic Research* 8:383-392
- Kainz H, Carty CP, Maine S, Walsh HPJ, Lloyd DG, Modenese L (2017a) Effects of hip joint centre mislocation on gait kinematics of children with cerebral palsy calculated using patient-specific direct and inverse kinematic models *Gait & posture* 57:154-160

- Kainz H, Carty CP, Modenese L, Boyd RN, Lloyd DG (2015) Estimation of the hip joint centre in human motion analysis: a systematic review *Clinical biomechanics* 30:319-329
- Kainz H, Goudriaan M, Falisse A, Huenaerts C, Desloovere K, De Groote F, Jonkers I (2018) The influence of maximum isometric muscle force scaling on estimated muscle forces from musculoskeletal models of children with cerebral palsy *Gait & posture* 65:213-220
- Kainz H et al. (2019) Selective dorsal rhizotomy improves muscle forces during walking in children with spastic cerebral palsy *Clinical biomechanics* 65:26-33
- Kainz H, Hoang HX, Stockton C, Boyd RR, Lloyd DG, Carty CP (2017b) Accuracy and Reliability of Marker-Based Approaches to Scale the Pelvis, Thigh, and Shank Segments in Musculoskeletal Models *Journal of Applied Biomechanics* 33:354-360
- Kainz H, Modenese L, Lloyd D, Maine S, Walsh H, Carty C (2016) Joint kinematic calculation based on clinical direct kinematic versus inverse kinematic gait models *J Biomech* 49:1658-1669
- Kautz SA, Neptune RR, Zajac FE (2000) General coordination principles elucidated by forward dynamics: minimum fatigue does not explain muscle excitation in dynamic tasks *Motor control* 4:75-80; discussion 97-116 .
- Keith RCM, Mackenzie ICK, Polani PE (1959) Definition of Cerebral Palsy *Developmental Medicine & Child Neurology* 1:23-23
- Killen BA (2019) Muscular stabilisation of the knee and development of automated and tuned subject specific musculoskeletal models for gait simulations Ph D thesis, Griffith University
- Knarr BA, Higginson JS (2015) Practical approach to subject-specific estimation of knee joint contact force *J Biomech* 48:2897-2902
- Knarr BA, Zeni JAJ, Higginson JS (2012) Comparison of electromyography and joint moment as indicators of co-contraction *J Electromyogr Kinesiol* 22:607-611
- Koman LA, Smith BP, Balkrishnan R (2003) Spasticity Associated with Cerebral Palsy in Children *Pediatric Drugs* 5:11-23

- Konrath JM, Vertullo CJ, Kennedy BA, Bush HS, Barrett RS, Lloyd DG (2016) Morphologic Characteristics and Strength of the Hamstring Muscles Remain Altered at 2 Years After Use of a Hamstring Tendon Graft in Anterior Cruciate Ligament Reconstruction *The American Journal of Sports Medicine* 44:2589-2598
- Krčah M, Székely G, Blanc R Fully automatic and fast segmentation of the femur bone from 3D-CT images with no shape prior. In: 2011 IEEE International Symposium on Biomedical Imaging: From Nano to Macro, 2011. pp 2087-2090
- Krigger KW (2006) Cerebral palsy: an overview *American Family Physician* 73:91-100
- Kruse A, Schranz C, Svehlik M, Tilp M (2017) Mechanical muscle and tendon properties of the plantar flexors are altered even in highly functional children with spastic cerebral palsy *Clinical biomechanics* 50:139-144
- Lampe R, Grassl S, Mitternacht J, Gerdesmeyer L, Gradinger R (2006) MRT-measurements of muscle volumes of the lower extremities of youths with spastic hemiplegia caused by cerebral palsy *Brain and Development* 28:500-506
- Lance JW (1980) Pathophysiology of spasticity and clinical experience with baclofen. *Spasticity: disordered motor control*. Lance, J.W., Feldman, R.G., Young, R.R. and Koella, W.P., Eds., Chicago
- Lee EH, Nather A, Goh J, Teng B, Bose K (1985) Gait analysis in cerebral palsy *Annals of the Academy of Medicine, Singapore* 14:37-43
- Lenaerts G, De Groote F, Demeulenaere B, Mulier M, Van der Perre G, Spaepen A, Jonkers I (2008) Subject-specific hip geometry affects predicted hip joint contact forces during gait *J Biomech* 41:1243-1252
- Leonard CT, Hirschfeld H, Forssberg H (1991) The development of independent walking in children with cerebral palsy *Developmental Medicine & Child Neurology* 33:567-577
- Lerner ZF, DeMers MS, Delp SL, Browning RC (2014) How tibiofemoral alignment and contact Locations Affect Predictions of Medial and Lateral Tibiofemoral Contact Forces *J Biomech* 48:644-650

- Li L, Tong KY, Hu XL, Hung LK, Koo TTK (2009) Incorporating ultrasound-measured musculotendon parameters to subject-specific EMG-driven model to simulate voluntary elbow flexion for persons after stroke *Clinical biomechanics* 24:101-109
- Lichtwark G, Farris D, Chen X, Hodges P, Sanchez G, Delp S (2017) The variable relationship between sarcomere number and fascicle length when measured in vivo in human lower limb muscle *Journal of Science and Medicine in Sport* 20:56
- Lieber RL, Runesson E, Einarsson F, Fridén J (2003) Inferior mechanical properties of spastic muscle bundles due to hypertrophic but compromised extracellular matrix material *Muscle & Nerve* 28:464-471
- Lieber RL, Steinman S, Barash IA, Chambers H (2004) Structural and functional changes in spastic skeletal muscle *Muscle & Nerve* 29:615-627
- Lloyd DG, Besier TF (2003) An EMG-driven musculoskeletal model to estimate muscle forces and knee joint moments in vivo *J Biomech* 36:765-776
- Lorentzen J, Willerslev-Olsen M, Hüche Larsen H, Farmer SF, Nielsen JB (2019) Maturation of feedforward toe walking motor program is impaired in children with cerebral palsy *Brain* 142:526-541
- Lu TW, O'Connor JJ (1999) Bone position estimation from skin marker co-ordinates using global optimisation with joint constraints *J Biomech* 32:129-134
- Ma J (2008) Dixon techniques for water and fat imaging *Journal of Magnetic Resonance Imaging* 28:543-558
- Manal K, Buchanan TS (2003) A Numerical Method for Estimating Tendon Slack Length 2003:235-236
- Manal K, Buchanan TS (2004) Subject-Specific Estimates of Tendon Slack Length: A Numerical Method *Journal of Applied Biomechanics* 20:195-203
- Mansouri M, Clark AE, Seth A, Reinbolt JA (2016) Rectus femoris transfer surgery affects balance recovery in children with cerebral palsy: A computer simulation study *Gait & posture* 43:24-30

- Mantoan A, Pizzolato C, Sartori M, Sawacha Z, Cobelli C, Reggiani M (2015) MOtoNMS: A MATLAB toolbox to process motion data for neuromusculoskeletal modeling and simulation Source Code for Biology and Medicine 10:1-14
- Mantoan A, Reggiani M (2015) BOPS v0.9.
- Marra MA, Vanheule V, Fluit R, Koopman BH, Rasmussen J, Verdonchot N, Andersen MS (2015) A subject-specific musculoskeletal modeling framework to predict in vivo mechanics of total knee arthroplasty Journal of Biomechanical Engineering 137:020904
- Martelli S, Calvetti D, Somersalo E, Viceconti M (2015) Stochastic modelling of muscle recruitment during activity Interface focus 5:20140094-20140094
- Mathewson MA, Lieber RL (2015) Pathophysiology of muscle contractures in cerebral palsy Physical Medicine and Rehabilitation Clinics of North America 26:57-67
- Mathewson MA, Ward SR, Chambers HG, Lieber RL (2015) High resolution muscle measurements provide insights into equinus contractures in patients with cerebral palsy Journal of Orthopaedic Research 33:33-39
- McIntyre S, Morgan C, Walker K, Novak I (2011) Cerebral Palsy—Don't Delay Developmental Disabilities Research Reviews 17:114-129
- Melhem E, Assi A, El Rachkidi R, Ghanem I (2016) EOS(®) biplanar X-ray imaging: concept, developments, benefits, and limitations Journal of children's orthopaedics 10:1-14
- Merletti R, Rau G, Disselhorst-Klug C, Stoffel K, Stegemen D, Hagg G (2006) The SENIAM Project. <http://www.seniam.org/>.
- Meyer AJ, Eskinazi I, Jackson JN, Rao AV, Patten C, Fregly BJ (2016) Muscle Synergies Facilitate Computational Prediction of Subject-Specific Walking Motions Frontiers in Bioengineering and Biotechnology 4:77
- Meyer AJ, Patten C, Fregly BJ (2017) Lower extremity EMG-driven modeling of walking with automated adjustment of musculoskeletal geometry PloS one 12:e0179698

- Millard M, Uchida T, Seth A, Delp SL (2013) Flexing computational muscle: modeling and simulation of musculotendon dynamics *Journal of biomechanical engineering* 135:021005
- Mockford M, Caulton JM (2010) The Pathophysiological Basis of Weakness in Children With Cerebral Palsy *Pediatric Physical Therapy* 22:222-233
- Modenese L, Ceseracciu E, Reggiani M, Lloyd DG (2016) Estimation of musculotendon parameters for scaled and subject specific musculoskeletal models using an optimization technique *J Biomech* 49:141-148
- Modenese L, Montefiori E, Wang A, Wesarg S, Viceconti M, Mazzà C (2018) Investigation of the dependence of joint contact forces on musculotendon parameters using a codified workflow for image-based modelling *J Biomech* 73:108-118
- Mohr M, Lorenzen K, Palacios-Derflingher L, Emery C, Nigg BM (2018) Reliability of the knee muscle co-contraction index during gait in young adults with and without knee injury history *J Electromyogr Kinesiol* 38:17-27
- Moissenet F, Cheze L, Dumas R (2014) A 3D lower limb musculoskeletal model for simultaneous estimation of musculo-tendon, joint contact, ligament and bone forces during gait *J Biomech* 47:50-58
- Molenaers G, Van Campenhout A, Fagard K, De Cat J, Desloovere K (2010) The use of botulinum toxin A in children with cerebral palsy, with a focus on the lower limb *Journal of children's orthopaedics* 4:183-195
- Morrell DS, Pearson JM, Sauser DD (2002) Progressive Bone and Joint Abnormalities of the Spine and Lower Extremities in Cerebral Palsy *RadioGraphics* 22:257-268
- Morris C (2007) Definition and classification of cerebral palsy: a historical perspective *Developmental Medicine & Child Neurology* 49:3-7
- Mortenson PA, Eng JJ (2003) The Use of Casts in the Management of Joint Mobility and Hypertonia Following Brain Injury in Adults: A Systematic Review *Physical Therapy* 83:648-658
- Murray WM, Arnold AS, Salinas S, Durbhakula MM, Buchanan TS, Delp SL Building biomechanical models based on medical image data: An assessment of model

- accuracy. In: Wells WM, Colchester A, Delp S (eds) *Medical Image Computing and Computer-Assisted Intervention — MICCAI'98*, Berlin, Heidelberg, 1998. Springer Berlin Heidelberg, pp 539-549
- Navacchia A, Kefala V, Shelburne KB (2017) Dependence of Muscle Moment Arms on In Vivo Three-Dimensional Kinematics of the Knee *Annals of biomedical engineering* 45:789-798
- Nielsen JB (1998) Co-contraction of antagonistic muscles in man *Danish medical bulletin* 45:423-435
- Nielsen JB, Petersen NT, Crone C, Sinkjaer T (2005) Stretch Reflex Regulation in Healthy Subjects and Patients with Spasticity *Neuromodulation: Technology at the Neural Interface* 8:49-57
- Noble JJ, Chruscikowski E, Fry NRD, Lewis AP, Gough M, Shortland AP (2017) The relationship between lower limb muscle volume and body mass in ambulant individuals with bilateral cerebral palsy *BMC Neurology* 17:223
- Noble JJ, Fry NR, Lewis AP, Keevil SF, Gough M, Shortland AP (2014) Lower limb muscle volumes in bilateral spastic cerebral palsy *Brain & development* 36:294-300
- Nolte D, Tsang CK, Zhang KY, Ding Z, Kedgley AE, Bull AM (2016) Non-linear scaling of a musculoskeletal model of the lower limb using statistical shape models *J Biomech* 49:3576-3581
- Novak I et al. (2013) A systematic review of interventions for children with cerebral palsy: state of the evidence *Dev Med Child Neurol* 55:885-910
- Nuri L, Obst SJ, Newsham-West R, Barrett RS (2017) The tendinopathic Achilles tendon does not remain iso-volumetric upon repeated loading: insights from 3D ultrasound *The Journal of Experimental Biology* 220:3053-3061
- Nuri L, Obst SJ, Newsham-West R, Barrett RS (2018) Three-dimensional morphology and volume of the free Achilles tendon at rest and under load in people with unilateral mid-portion Achilles tendinopathy *Experimental Physiology* 103:358-369

- O'Brien TD, Reeves ND, Baltzopoulos V, Jones DA, Maganaris CN (2010) In vivo measurements of muscle specific tension in adults and children *Experimental Physiology* 95:202-210
- O'Shea TM (2008) Diagnosis, treatment, and prevention of cerebral palsy *Clinical obstetrics and gynecology* 51:816-828
- Oberhofer K, Lorenzetti S, Mithraratne K (2019) Host Mesh Fitting of a Generic Musculoskeletal Model of the Lower Limbs to Subject-Specific Body Surface Data: A Validation Study *Applied Bionics and Biomechanics* 2019:8 pages
- Oberhofer K, Stott NS, Mithraratne K, Anderson IA (2010) Subject-specific modelling of lower limb muscles in children with cerebral palsy *Clinical biomechanics* 25:88-94
- Obst S, Boyd R, Read F, Barber L (2017) Quantitative 3-D Ultrasound of the Medial Gastrocnemius Muscle in Children with Unilateral Spastic Cerebral Palsy *Ultrasound in Medicine & Biology* 43:2814-2823
- Obst SJ, Newsham-West R, Barrett RS (2014) In Vivo Measurement of Human Achilles Tendon Morphology Using Freehand 3-D Ultrasound *Ultrasound in Medicine and Biology* 40:62-70
- Odding E, Roebroek ME, Stam HJ (2006) The epidemiology of cerebral palsy: incidence, impairments and risk factors *Disabil Rehabil* 28:183-191
- Oei L, Koromani F, Rivadeneira F, Zillikens MC, Oei EHG (2016) Quantitative imaging methods in osteoporosis *Quantitative Imaging in Medicine and Surgery* 6:680-698
- Ong CF, Geijtenbeek T, Hicks JL, Delp SL (2019) Predicting gait adaptations due to ankle plantarflexor muscle weakness and contracture using physics-based musculoskeletal simulations *PLOS Computational Biology* 15:e1006993
- Oskoui M, Coutinho F, Dykeman J, Jetté N, Pringsheim T (2013) An update on the prevalence of cerebral palsy: a systematic review and meta-analysis *Developmental Medicine & Child Neurology* 55:509-519
- Palisano R, Rosenbaum P, Walter S, Russell D, Wood E, Galuppi B (1997) Development and reliability of a system to classify gross motor function in children with cerebral palsy *Developmental Medicine & Child Neurology* 39:214-223

- Panizzolo FA, Maiorana AJ, Naylor LH, Dembo LG, Lloyd DG, Green DJ, Rubenson J (2016) Muscle size explains low passive skeletal muscle force in heart failure patients PeerJ 4:e2447
- Papageorgiou E, Nieuwenhuys A, Vandekerckhove I, Van Campenhout A, Ortibus E, Desloovere K (2019) Systematic review on gait classifications in children with cerebral palsy: An update Gait & posture 69:209-223
- Papavasiliou AS (2009) Management of motor problems in cerebral palsy: A critical update for the clinician European Journal of Paediatric Neurology 13:387-396
- Parmar B et al. (2010) Characterization of controlled bone defects using 2D and 3D ultrasound imaging techniques Physics in medicine and biology 55:4839-4859
- Passmore E, Graham HK, Pandy MG, Sangeux M (2018) Hip- and patellofemoral-joint loading during gait are increased in children with idiopathic torsional deformities Gait & posture 63:228-235
- Pataky TC (2012) One-dimensional statistical parametric mapping in Python Computer methods in biomechanics and biomedical engineering 15:295-301
- Pellikaan P et al. (2014) Evaluation of a morphing based method to estimate muscle attachment sites of the lower extremity J Biomech 47:1144-1150
- Pitcher C, Elliott C, Valentine J, Stannage K, Williams S, J. Shipman P, Reid S (2018) Muscle morphology of the lower leg in ambulant children with spastic cerebral palsy Muscle & Nerve 58:818-823
- Pitcher CA, Elliott CM, Panizzolo FA, Valentine JP, Stannage K, Reid SL (2015) Ultrasound characterization of medial gastrocnemius tissue composition in children with spastic cerebral palsy Muscle & Nerve 52:397-403
- Pitto L et al. (2019) SimCP: A Simulation Platform to Predict Gait Performance Following Orthopedic Intervention in Children With Cerebral Palsy Frontiers in Neurorobotics 13:54
- Pizzolato C, Lloyd DG, Barrett RS, Cook JL, Zheng MH, Besier TF, Saxby DJ (2017) Bioinspired Technologies to Connect Musculoskeletal Mechanobiology to the

- Person for Training and Rehabilitation *Frontiers in Computational Neuroscience* 11:96
- Pizzolato C, Lloyd DG, Sartori M, Ceseracciu E, Besier TF, Fregly BJ, Reggiani M (2015) CEINMS: A toolbox to investigate the influence of different neural control solutions on the prediction of muscle excitation and joint moments during dynamic motor tasks *J Biomech* 48:3929-3936
- Pollock G (1962) Surgical treatment of cerebral palsy *Bone & Joint Journal* 44:68-81
- Prilutsky BI, Zatsiorsky VM (2002) Optimization-based models of muscle coordination *Exercise and sport sciences reviews* 30:32-38
- Prosser LA, Lee SCK, VanSant AF, Barbe MF, Lauer RT (2010) Trunk and Hip Muscle Activation Patterns Are Different During Walking in Young Children With and Without Cerebral Palsy *Physical Therapy* 90:986-997
- Rajamani KT, Styner MA, Talib H, Zheng G, Nolte LP, Gonzalez Ballester MA (2007) Statistical deformable bone models for robust 3D surface extrapolation from sparse data *Medical Image Analysis* 11:99-109
- Reed EB, Hanson AM, Cavanagh PR (2015) Optimising muscle parameters in musculoskeletal models using Monte Carlo simulation *Computer methods in biomechanics and biomedical engineering* 18:607-617
- Reinbolt JA, Haftka RT, Chmielewski TL, Fregly BJ (2007) Are patient-specific joint and inertial parameters necessary for accurate inverse dynamics analyses of gait? *IEEE transactions on bio-medical engineering* 54:782-793
- Report of the Australian Cerebral Palsy Register, Birth Years 1993-2006 (February, 2013).
- Richards RE, Andersen MS, Harlaar J, van den Noort JC (2018) Relationship between knee joint contact forces and external knee joint moments in patients with medial knee osteoarthritis: effects of gait modifications *Osteoarthritis and cartilage* 26:1203-1214
- Rosenbaum P et al. (2007) A report: the definition and classification of cerebral palsy April 2006 *Developmental Medicine & Child Neurology* 109:8-14

- Rosenbaum P, Stewart D (2004) The world health organization international classification of functioning, disability, and health: a model to guide clinical thinking, practice and research in the field of cerebral palsy *Seminars in Pediatric Neurology* 11:5-10
- Rutz E, Baker R, Tirosh O, Romkes J, Haase C, Brunner R (2011) Tibialis anterior tendon shortening in combination with Achilles tendon lengthening in spastic equinus in cerebral palsy *Gait & posture* 33:152-157
- Sancisi N, Parenti-Castelli V (2011) A New Kinematic Model of the Passive Motion of the Knee Inclusive of the Patella *Journal of Mechanisms and Robotics* 3:041003-041003-041007
- Sancisi N, Zannoli D, Parenti-Castelli V, Belvedere C, Leardini A (2011) A one-degree-of-freedom spherical mechanism for human knee joint modelling *Proceedings of the Institution of Mechanical Engineers, Part H: Journal of Engineering in Medicine* 225:725-735
- Sangeux M, Armand S (2015) Kinematic Deviations in Children with Cerebral Palsy. In: *Orthopedic Management of Children With Cerebral Palsy: A Comprehensive Approach*. Nova Science Publishers Inc., p 567
- Sangeux M, Marin F, Charleux F, Tho MCHB (2009) In vivo personalized finite element modelling of the knee joint derived from MRI images *European Journal of Computational Mechanics* 18:81-92
- Sartori M, Farina D, Lloyd DG (2014) Hybrid neuromusculoskeletal modeling to best track joint moments using a balance between muscle excitations derived from electromyograms and optimization *J Biomech* 47:3613-3621
- Sartori M et al. (2017a) Toward modeling locomotion using electromyography-informed 3D models: application to cerebral palsy *Wiley Interdisciplinary Reviews: Systems Biology and Medicine* 9:e1368
- Sartori M, Reggiani M, Farina D, Lloyd DG (2012) EMG-Driven Forward-Dynamic Estimation of Muscle Force and Joint Moment about Multiple Degrees of Freedom in the Human Lower Extremity *PloS one* 7:e52618

- Sartori M, Rubenson J, Lloyd DG, Farina D, Panizzolo FA (2017b) Subject-Specificity via 3D Ultrasound and Personalized Musculoskeletal Modeling. In: Ibáñez J, González-Vargas J, Azorín JM, Akay M, Pons JL (eds) *Converging Clinical and Engineering Research on Neurorehabilitation II: Proceedings of the 3rd International Conference on NeuroRehabilitation (ICNR2016)*, October 18-21, 2016, Segovia, Spain. Springer International Publishing, Cham, pp 639-642
- Saxby DJ et al. (2016) Tibiofemoral contact forces during walking, running and sidestepping *Gait & posture* 49:78-85
- Scheys L, Desloovere K, Spaepen A, Suetens P, Jonkers I (2011a) Calculating gait kinematics using MR-based kinematic models *Gait & posture* 33:158-164
- Scheys L, Desloovere K, Suetens P, Jonkers I (2011b) Level of subject-specific detail in musculoskeletal models affects hip moment arm length calculation during gait in pediatric subjects with increased femoral anteversion *J Biomech* 44:1346-1353
- Scheys L, Jonkers I, Loeckx D, Maes F, Spaepen A, Suetens P *Image Based Musculoskeletal Modeling Allows Personalized Biomechanical Analysis of Gait*. In: Harders M, Székely G (eds) *Biomedical Simulation*, Berlin, Heidelberg, 2006. Springer Berlin Heidelberg, pp 58-66
- Scheys L, Loeckx D, Spaepen A, Suetens P, Jonkers I (2009) Atlas-based non-rigid image registration to automatically define line-of-action muscle models: A validation study *J Biomech* 42:565-572
- Scheys L, Spaepen A, Suetens P, Jonkers I (2008a) Calculated moment-arm and muscle-tendon lengths during gait differ substantially using MR based versus rescaled generic lower-limb musculoskeletal models *Gait & posture* 28:640-648
- Scheys L, van Campenhout A, Spaepen A, Suetens P, Jonkers I (2008b) Personalized MR-based musculoskeletal models compared to rescaled generic models in the presence of increased femoral anteversion: effect on hip moment arm lengths *Gait & posture* 28:358-365
- Schless S-H, Hanssen B, Cenni F, Bar-On L, Aertbeliën E, Molenaers G, Desloovere K (2018) Estimating medial gastrocnemius muscle volume in children with spastic

- cerebral palsy: a cross-sectional investigation *Developmental Medicine & Child Neurology* 60:81-87
- Scholtes VAB, Becher JG, Beelen A, Lankhorst GJ (2006) Clinical assessment of spasticity in children with cerebral palsy: a critical review of available instruments *Developmental Medicine & Child Neurology* 48:64-73
- Schroeder AS et al. (2009) Muscle biopsy substantiates long-term MRI alterations one year after a single dose of botulinum toxin injected into the lateral gastrocnemius muscle of healthy volunteers *Movement Disorders* 24:1494-1503
- Schwartz M, Lakin G (2003) The effect of tibial torsion on the dynamic function of the soleus during gait *Gait & posture* 17:113-118
- Sellier E, Platt MJ, Andersen GL, Krägeloh-Mann I, De La Cruz J, Cans C, Surveillance of Cerebral Palsy N (2016) Decreasing prevalence in cerebral palsy: a multi-site European population-based study, 1980 to 2003 *Developmental Medicine & Child Neurology* 58:85-92
- Serrancolí G, Kinney AL, Fregly BJ, Font-Llagunes JM (2016) Neuromusculoskeletal Model Calibration Significantly Affects Predicted Knee Contact Forces for Walking *Journal of biomechanical engineering* 138:0810011-08100111
- Seth A et al. (2018) OpenSim: Simulating musculoskeletal dynamics and neuromuscular control to study human and animal movement *PLOS Computational Biology* 14:e1006223
- Shao Q, Bassett Dn Fau - Manal K, Manal K Fau - Buchanan TS, Buchanan TS (2009) An EMG-driven model to estimate muscle forces and joint moments in stroke patients *Computers in Biology and Medicine* 39:1083-1088
- Sharma N, Aggarwal LM (2010) Automated medical image segmentation techniques *Journal of medical physics* 35:3-14
- Sherman MA, Seth A, Delp SL What is a moment arm? Calculating muscle effectiveness in biomechanical models using generalized coordinates. In: *Proceedings of the ASME Design Engineering Technical Conferences. ASME Design Engineering Technical Conferences, 2013.*

- Shortland A (2017) Skeletal Muscle Structure in Spastic Cerebral Palsy. In: Handbook of Human Motion. pp 1-15
- Smith LR, Lee KS, Ward SR, Chambers HG, Lieber RL (2011) Hamstring contractures in children with spastic cerebral palsy result from a stiffer extracellular matrix and increased in vivo sarcomere length *J Physiol* 589:2625-2639
- Smithers-Sheedy H et al. (2016) A special supplement: findings from the Australian Cerebral Palsy Register, birth years 1993 to 2006 *Developmental Medicine & Child Neurology* 58:5-10
- Sprague JB (1992) Surgical management of cerebral palsy *Orthopaedic Nursing* 11:11-19
- Steele KM, DeMers MS, Schwartz MH, Delp SL (2012) Compressive tibiofemoral force during crouch gait *Gait & posture* 35:556-560
- Steele KM, Munger ME, Peters KM, Shuman BR, Schwartz MH (2019) Repeatability of electromyography recordings and muscle synergies during gait among children with cerebral palsy *Gait & posture* 67:290-295
- Steele KM, Rozumalski A, Schwartz MH (2015) Muscle synergies and complexity of neuromuscular control during gait in cerebral palsy *Developmental Medicine & Child Neurology* 57:1176-1182
- Steele KM, Shuman BR, Schwartz MH (2017) Crouch severity is a poor predictor of elevated oxygen consumption in cerebral palsy *J Biomech* 60:170-174
- Steinbok P (2006) Selection of treatment modalities in children with spastic cerebral palsy *Neurosurgical Focus FOC* 21:1-8
- Steinbok P (2007) Selective dorsal rhizotomy for spastic cerebral palsy: a review *Child's Nervous System* 23:981-990
- Surveillance of Cerebral Palsy in Europe (SCPE) Scientific report 1998 - 2018 (November, 2018).
- Suwarganda EK et al. (2019) Minimal medical imaging can accurately reconstruct geometric bone models for musculoskeletal models *PloS one* 14:e0205628

- Thelen DD, Riewald SA, Asakawa DS, Sanger TD, Delp SL (2003a) Abnormal coupling of knee and hip moments during maximal exertions in persons with cerebral palsy *Muscle & Nerve* 27:486-493
- Thelen DG, Anderson FC, Delp SL (2003b) Generating dynamic simulations of movement using computed muscle control *J Biomech* 36:321-328
- Thelen DG, Won Choi K, Schmitz AM (2014) Co-simulation of neuromuscular dynamics and knee mechanics during human walking *Journal of biomechanical engineering* 136:021033-021033
- Theroux MC, DiCindio S (2014) Major surgical procedures in children with cerebral palsy *Anesthesiology clinics* 32:63-81
- Thomason P, Baker R Fau - Dodd K, Dodd K Fau - Taylor N, Taylor N Fau - Selber P, Selber P Fau - Wolfe R, Wolfe R Fau - Graham HK, Graham HK (2011) Single-event multilevel surgery in children with spastic diplegia: a pilot randomized controlled trial *The Journal of Bone and Joint Surgery American volume* 93:451-460
- Touyama M, Touyama J, Toyokawa S, Kobayashi Y (2016) Trends in the prevalence of cerebral palsy in children born between 1988 and 2007 in Okinawa, Japan *Brain and Development* 38:792-799
- Treece GM, Gee AH, Prager RW, Cash CJC, Berman LH (2003) High-definition freehand 3-D ultrasound *Ultrasound in Medicine & Biology* 29:529-546
- Trompetto C, Marinelli L, Mori L, Pelosin E, Curra` A, Molfetta L, Abbruzzese G (2014) Pathophysiology of Spasticity: Implications for Neurorehabilitation *Biomed Res Int* 2014:8 pages
- Valente G, Crimi G, Vanella N, Schileo E, Taddei F (2017) nmsBuilder: Freeware to create subject-specific musculoskeletal models for OpenSim *Computer Methods and Programs in Biomedicine* 152:85-92
- Valente G, Pitto L, Stagni R, Taddei F (2015) Effect of lower-limb joint models on subject-specific musculoskeletal models and simulations of daily motor activities *J Biomech* 48:4198-4205

- Valente G et al. (2014) Are subject-specific musculoskeletal models robust to the uncertainties in parameter identification? *PloS one* 9:e112625
- Vallat R (2018) Pinguin: statistics in Python *Journal of Open Source Software* 3:1026
- van der Krogt MM, Bar-On L, Kindt T, Desloovere K, Harlaar J (2016) Neuro-musculoskeletal simulation of instrumented contracture and spasticity assessment in children with cerebral palsy *Journal of neuroengineering and rehabilitation* 13
- van der Krogt MM, Delp SL, Schwartz MH (2012) How robust is human gait to muscle weakness? *Gait & posture* 36:113-119
- van der Krogt MM, Doorenbosch CA, Becher JG, Harlaar J (2009) Walking speed modifies spasticity effects in gastrocnemius and soleus in cerebral palsy gait *Clinical biomechanics* 24:422-428
- van der Krogt MM, Doorenbosch CAM, Becher JG, Harlaar J (2010) Dynamic spasticity of plantar flexor muscles in cerebral palsy gait *Journal of rehabilitation medicine* 42:656-663
- van Drongelen S, Dreher T, Heitzmann DW, Wolf SI (2013) Gait patterns in twins with cerebral palsy: similarities and development over time after multilevel surgery *Research in Developmental Disabilities* 34:1595-1601
- van Naarden Braun K, Doernberg N, Schieve L, Christensen D, Goodman A, Yeargin-Allsopp M (2016) Birth Prevalence of Cerebral Palsy: A Population-Based Study *Pediatrics* 137:1-9
- Vaughan C, Bowsher K, Sussman M (1992) Spasticity and gait: knee torques and muscle co-contraction. In: Sussman M (ed) *The Diplegic Child: Evaluation and Management*. American Academy of Orthopaedic Surgeons Rosemont, IL, pp 45-58
- Veerkamp K, Schallig W, Harlaar J, Pizzolato C, Carty CP, Lloyd DG, van der Krogt MM (2019) The effects of electromyography-assisted modelling in estimating musculotendon forces during gait in children with cerebral palsy *J Biomech* 92:45-53
- Verrotti A, Greco R, Spalice A, Chiarelli F, Iannetti P (2006) Pharmacotherapy of Spasticity in Children With Cerebral Palsy *Pediatric Neurology* 34:1-6

- Wang KK, Novacheck TF, Rozumalski A, Georgiadis AG (2019) Anterior Guided Growth of the Distal Femur for Knee Flexion Contracture: Clinical, Radiographic, and Motion Analysis Results *Journal of Pediatric Orthopaedics* 39:e360-e365
- Ward SR, Kingsbury T, Winters T, Lieber KM, Braun J, Eng CM, Lieber RL Scaling of Joint Mechanics and Muscle Architecture in the Human Knee. In: American Society of Biomechanics Meeting, Stanford University, California., 2007.
- Ward SR, Smallwood LH, Lieber RL Scaling of human lower extremity muscle architecture to skeletal dimensions. In: ISB XXth Congress, Cleveland, Ohio, 2005.
- Weijjs WA, Hillen B (1985) Cross-sectional areas and estimated intrinsic strength of the human jaw muscles *Acta morphologica Neerlando-Scandinavica* 23:267-274
- Wesseling M, Bosmans L, Van Dijck C, Vander Sloten J, Wirix-Speetjens R, Jonkers I (2019) Non-rigid deformation to include subject-specific detail in musculoskeletal models of CP children with proximal femoral deformity and its effect on muscle and contact forces during gait *Computer methods in biomechanics and biomedical engineering* 22:376-385
- Whitney DG, Singh H, Miller F, Barbe MF, Slade JM, Pohlig RT, Modlesky CM (2017) Cortical bone deficit and fat infiltration of bone marrow and skeletal muscle in ambulatory children with mild spastic cerebral palsy *Bone* 94:90-97
- Williams SA, Reid S, Elliott C, Shipman P, Valentine J (2013) Muscle volume alterations in spastic muscles immediately following botulinum toxin type-A treatment in children with cerebral palsy *Developmental Medicine & Child Neurology* 55:813-820
- Winby CR, Lloyd DG, Besier TF, Kirk TB (2009) Muscle and external load contribution to knee joint contact loads during normal gait *J Biomech* 42:2294-2300
- Winby CR, Lloyd DG, Kirk TB (2008) Evaluation of different analytical methods for subject-specific scaling of musculotendon parameters *J Biomech* 41:1682-1688
- Winters TF (1987) Gait patterns in spastic hemiplegia in children and young adults *The Journal of Bone and Joint Surgery American* volume 69:437-441

- Wren TA, Cheatwood AP, Rethlefsen SA, Hara R, Perez FJ, Kay RM (2010) Achilles tendon length and medial gastrocnemius architecture in children with cerebral palsy and equinus gait *Journal of Pediatric Orthopaedics* 30:479-484
- Wren TA, Gorton GE, 3rd, Ounpuu S, Tucker CA (2011) Efficacy of clinical gait analysis: A systematic review *Gait & posture* 34:149-153
- Wren TAL, Rethlefsen S, Kay RM (2005) Prevalence of Specific Gait Abnormalities in Children With Cerebral Palsy *Journal of Pediatric Orthopaedics* 25:79-83
- Wu G et al. (2002) ISB recommendation on definitions of joint coordinate system of various joints for the reporting of human joint motion—part I: ankle, hip, and spine *J Biomech* 35:543-548
- Zhang J, Besier T (2017) Accuracy of femur reconstruction from sparse geometric data using a statistical shape model *Computer methods in biomechanics and biomedical engineering* 20:566-576
- Zhang J, Malcolm D, Hislop-Jambrich J, Thomas CDL, Nielsen PMF (2014a) An anatomical region-based statistical shape model of the human femur *Computer Methods in Biomechanics and Biomedical Engineering: Imaging & Visualization* 2:176-185
- Zhang J et al. The MAP Client: User-Friendly Musculoskeletal Modelling Workflows. In: Bello F, Cotin S (eds) *Biomedical Simulation*, Cham, 2014b. Springer International Publishing, pp 182-192